ARL 69-0089

CONDENSATION OF METAL VAPOR IN A SUPERSONIC CARRIER GAS

P. M. SHERMAN
D. D. McBRIDE
T. CHMIELEWSKI
T. H. PIERCE
E. OKTAY

THE UNIVERSITY OF MICHIGAN
DEPARTMENT OF AEROSPACE ENGINEERING
ANN ARBOR, MICHIGAN

JUNE 1969

Contract No. AF33(615)-67c-1197
Project No. 7116

AEROSPACE RESEARCH LABORATORIES
OFFICE OF AEROSPACE RESEARCH
UNITED STATES AIR FORCE
WRIGHT-PATTERSON AIR FORCE BASE, OHIO

FOREWORD

This Final Report was prepared on work done under Contract AF 33(615)-67c-1197 between Aerospace Research Laboratory, Office of Aerospace Research, United States Air Force and The University of Michigan. It was first under the technical cognizance of Mr. E. Stephens of the Thermo-Mechanics Research Laboratory of ARL and then under the technical cognizance of Mr. S. Hasinger of the Energetics Research Laboratory, ARL.

ABSTRACT

A study of the condensation of metal vapor in an inert carrier gas was made with primary emphasis on the size of the particles formed and the location of the onset of the condensation. Superheated zinc vapor was generated in a hotshot wind tunnel in a helium carrier gas and expanded in a converging-diverging nozzle. Static pressure measurements were made to determine the location of the onset of condensation. A sampling method was developed and used to determine the size of the condensed particles. An exploding wire arrangement was also used in a few additional studies and condensed platinum and other metal particles were obtained. A few measurements were also made of the condensation of argon.

It was found that decelerating a skimmed part of the nozzle flow by mixing with air at matched pressure was an effective way of sampling. Electron microscope analysis of the particles sampled showed a narrow distribution of sizes with 80% of the particles having diameters within a 100 $\mathring{A}$ range, and a peak number of particles about 135 $\mathring{A}$ in diameter. The amount of supercooling before onset of condensation was found to be approximately 430^{o}K (measured along the isentrope) over a range of zinc mass fractions of .35 to .70 for saturation partial pressure of zinc between 10 psia and 70 psia. Pitot pressure was found to be a function of the size of the pitot tube up to a critical diameter.

A classical non-equilibrium liquid drop analysis predicted values of both particle size and condensation onset in moderately good agreement with the measurements. The analysis was also used to determine the qualitative effects of rate of expansion, amount of carrier gas and molecular weight of carrier gas.

An equilibrium analysis yielded useful algebraic approximations for conditions far downstream of the onset of condensation.

TABLE OF CONTENTS

LIST OF ILLUSTRATIONS

NOMENCLATURE

$\bar{A}$	area ratio (A/A*)
$\bar{A}_{eff}$	effective area ratio
C_v	Specific heat at constant volume
E	energy
e	specific energy
f	mass fraction of inert carrier gas (helium)
g	mass fraction of vapor condensed
J	nucleation rate
L	latent heat (of vaporization or sublimation depending upon T) of condensable vapor (zinc)
p	pressure
p'_o	pitot pressure
q	mass fraction of uncondensed vapor
R	universal gas constant
T	temperature
ΔT	supersaturation temperature decrement measured along isentrope ($T_{sat} - T_{onset}$)
t	time
V	arc chamber volume
x	station in nozzle measured from throat
y	mass fraction of condensable vapor in stagnation chamber

α	ratio of molecular weights (μ_v/μ_a)
γ	specific heat ratio
κ	mass fraction of condensable vapor (zinc) in chamber
μ	molecular weight
Φ	particle size distribution function (see Section II-B)

Subscripts

a	inert carrier gas
c	stagnation chamber condition
ch	arc chamber charge condition (prior to arc heating)
f	frozen expansion
o	stagnation values
nr	no relaxation condition (see SectionIII)
sat	condition where expansion isentrope crosses saturation curve
z	zinc
v	condensable vapor (except for C_v; see above)
∞	saturated vapor condition

Miscellaneous

$\overline{(\,)}$	nondimensionalized by stagnation chamber condition (except for $\bar{A}$; see above)

I. INTRODUCTION

When a superheated vapor is expanded in a nozzle the initial decrease in the pressure and temperature can be regarded as isentropic. In general the vapor pressure curve (in the p-T plane) is steeper than the isentropic curve and the expanding vapor will at some point become saturated (Wegener and Mack[1] give an excellent discussion of this). If the expansion is rapid and the gaseous mixture is relatively "clean", sufficient surface will not exist for the condensation necessary to maintain equilibrium ($p_v = p_\infty$) and a supersaturated vapor ($p_v > p_\infty$) will result. As the supersaturation continues to increase small droplets will be formed from the vapor through a process of spontaneous (homogeneous) self-nucleation[2]. As the nucleation rate increases, a point is usually reached where enough droplets exist to provide the surface necessary for the faster condensation through particle growth required to return the vapor to equilibrium, and the supersaturated state "collapses". The point at which this collapse begins (as determined by a noticeable departure of the vapor properties from their isentropic values) is herein called the condensation onset point. Subsequent to this collapse a negligible number of new droplets will be formed and the existing particles will continue to grow until the supply of vapor is exhausted.

Condensation in general has been the subject of considerable research through the past several years. Several comprehensive reviews of both theoretical and experimental research exist. (The reader is referred in particular to Ref. 1, 3, and 4a). Much of the early work understandably involved the condensation of steam[5,6,7,8]. However, with the observation of condensation in a supersonic wind tunnel, much of the emphasis was switched to air, water vapor in air, and nitrogen. The earlier investigations, at the California Institute of Technology, by Head[9] on water vapor in air, Willmarth and Nagamatsu[10] on nitrogen, and Buhler[11] on air, warrant special mention. Considerable theoretical work on nucleation theory has recently been summarized and reviewed by Courtney[4b]. An early study of condensation in hypersonic wind tunnel flows was completed by Daum[12]. Several other studies were made of hypersonic flows, but most of them were made for the purpose of establishing operating limits of specific wind tunnels and, as a result, much of the available data overlaps. Recent research, at the Massachusetts Institute of Technology by Duff[13], and Kremmer and Okurounmu[14], has extended the data to include carbon dioxide and ammonia. However, the ability to predict, a priori, condensation conditions for any given system is still highly questionable.

Almost all of the work done has been for one-component flow or a minute amount of vapor in a carrier gas and has dealt with condensation of non-metals

having surface tensions, latent heats, molecular weights, and vapor pressures which are widely different from those of the metals. Since all the above factors have considerable effect upon the condensation process, extrapolation of the limited existing data to a flow comprised of comparable quantities of condensable vapor and carrier gas is questionable, and especially so when the condensable vapor is a metal.

Condensing metal vapors have enjoyed some recent interest[15, 16, 17, 18] due to several newly developed applications. The use of metal vapors as the working fluid in turbines shows distinct advantages[15]. However, the condensation of these metal vapors would markedly affect such things as turbine efficiency, blade erosion, etc. When metal additives are employed in chemical rocket engines, condensation rates of the metallic oxides are a factor in determining combustion rates, while condensed particle size and energy release exert a significant influence on the amount of thrust generated. Metal vapor condensation is used to produce the chargeable particles of a colloidal EHD Energy Convertor[19] and the condensation of a metal or metallic compound has been proposed as a method of producing the extremely small and numerous particles which make up the working fluid in a colloidal-electrostatic rocket engine[20]. The use of liquid metals in connection with nuclear reactors also has condensation problems associated with it. As can be seen, many of these applications require a knowledge of the size of the particles formed in the

condensation process (or the number of particles formed, which can of course be directly inferred from the particle size distribution for a given total amount of condensate). Almost all of the previous condensation work, both theoretical and experimental, has been concerned, however, with the onset of condensation and its effect on the flow parameters rather than with particle size.

Most of the work that has concerned itself with particle size measurement can be generally classed into three basic groups: (1) light scattering[21,22], (2) particle separation[23,24,25], and (3) particle sampling[20]. The light scattering techniques generally assume a monodispersion and result in a mean particle diameter. Techniques yielding polydisperse size distributions by angular scattering distributions have not yet been proved. Particle separation techniques have been used mostly for large particle sizes (order of 1μ diameter). Thomann[23], however, inferred very small ice crystal sizes (approximately 14 $\mathring{A}$ diameter) from a pitot tube separation technique. The collection of some particles on a blunt body placed directly in a Mach 2 flow has also been done[20]. The dearth of significant experimental data is understandable in light of the complexity of the problem. However, the number of significant problems presently in need of reliable experimental data on metal vapor condensation phenomena certainly warrants an extensive effort in this field.

The purpose of this research was primarily the determination of (1) the size of the particles formed in the condensation of a rapidly expanding metal vapor—inert carrier gas mixture and (2) the point at which the onset of condensation

occurred. Measurements were accomplished in two separate phases. The particle size was determined by a sampling procedure followed by electron microscope analysis. The onset point was found by determining the point in the nozzle where the static pressure deviated from its "frozen" expansion (no condensation) value. Both equilibrium and non-equilibrium condensation analyses were made.

II. EXPERIMENTAL ARRANGEMENT AND PROCEDURE

A. WORKING FLUID

One problem which arises in the study of metal vapor is the production of the extreme conditions of temperature (at reasonable pressure), necessary to obtain the superheated conditions required. The choice of metal vapor and carrier gas therefore depended largely upon their suitability for laboratory measurements. Figure 1 shows the saturation curves for several metals. Toxity and high chemical activity make the use of some of the metals unfeasible. Zinc was chosen as one metal with fewer difficulties than most. It has a saturation temperature at reasonable pressures that is not inordinately high and it has physical properties wh ich are well behaved. It is well-behaved in both gaseous and condensed phases. It has constant, or near constant, specific heats, ratio of specific heats, and latent heat along with well known and reliable physical data (such as vapor pressure) which make analysis of results much easier and comparison of theory and experiment much more meaningful (since fewer approximations must be made). The low vaporization temperature meant that it would remain superheated at lower temperatures and thus operation problems would be minimized by minimizing energy transfer into the stagnation chamber. Zinc has the added advantage of structural strength and convenient handling and machining properties which make possible the use of the test metal as part of the arc chamber electrode

arrangement in the form of the fuse-switch (see Appendix A) which could withstand certain electromagnetic forces for given time periods and which could be readily handled and machined.

Helium was chosen as a carrier gas because it is light, inert, monatomic and will not condense at the temperatures commonly reached in the laboratory.

For most of the studies made, the metal vapor was generated in the University of Michigan hotshot wind tunnel facility[28] (Appendix A). (An exploding wire arrangement (Appendix H) was also employed.) The tunnel is capable of storing up to approximately 1.5×10^7 in.-lb of energy in the energy storage coil. The energy is transferred to the working fluid at efficiencies of the order of 50%.

The specific energy e necessary to heat, at constant volume, a mixture of metal and gas to a final temperature T_f, vaporizing the metal in the process, can be approximated by[27]:

$$e = C_{v_c} (T_f - T_{ch}) + (1 - f) L_{ch} \qquad \text{(II. 1)}$$

where the mixture constant volume specific heat C_{v_c} is defined by:

$$C_{v_c} = f C_{v_a} + (1 - f) C_{v_v} \qquad \text{(II. 2)}$$

For a given volume V, the total energy E required to reach a final pressure p_f and temperature T_f is

$$E = \frac{p_f Ve}{RT_f} \frac{\mu_v}{1 - f + f\alpha} \qquad \text{(II. 3)}$$

The total energy required to raise a zinc-helium mixture from $298^{o}K$ to $5000^{o}K$, and 5000 psia in a volume of 65 $in.^3$ (tunnel arc chamber) is shown in Fig. 2 as a function of helium mass fraction f.

It can be seen that the amount of energy required for moderate operating conditions, lies between 4×10^5 and 8×10^5 in. -lb depending upon the amount of zinc vaporized. Thus, the hotshot is easily capable of furnishing the energy for the operating conditions necessary to obtain the required superheated zinc vapor-helium mixture. In addition, the hotshot provided a ready means of introducing the zinc vapor into the flow by means of the arcing process employed to transfer the energy from the main coil to the working fluid.

B. SAMPLING FOR PARTICLE SIZE STUDY

A nominal Mach 25 (helium) nozzle was used for the particle sampling phase of the experiment in the tunnel. A sketch of the Mach 25 nozzle installation is shown in Fig. 3. It is a conical nozzle with a total included angle of 15^{o}. The throat insert is of beryllium copper with a throat diameter of approximately

.10 in. Due to erosion the throat diameter increased approximately .001 in. during each run and, in fact, over a period of 15 runs increased from .102 in. to .121 in. The throat size was considered constant during any one run due to the small variation. The nozzle is protected from the arc by a baffle with a centerbody on the downstream side, employed to reduce the volume of the region between the baffle and the throat. The nozzle has an exit diameter of 3.25 in. and exhausts into an evacuated 20 in. diameter test section which connects to a vacuum tank with a volume of approximately 400 ft^3.

It was not feasible to fabricate static pressure taps along the wall of this nozzle. Therefore to obtain the static pressure of the jet at the exit of the nozzle (or in the near vicinity), a carefully machined extension with three static pressure ports was employed. An extension made of epoxy was also used.

High sensitivity schlieren pictures and light emission pictures were taken of the flow field between the nozzle exit and the entrance slit to the sampler. They showed no indications of any flow disturbances in this region. (The schlieren system used was a 20 ft focal length double-pass parallel arrangement of extremely high sensitivity[28].)

The primary concern in determining the size distribution of the very small, high speed, condensed particles lay in the obvious requirement that the method must not alter the results. At the very outset of this experiment, it seemed that light-scattering techniques presented the easiest means of obtaining this

goal. However, it soon became evident that there were problems and uncertainties involved in light-scattering methods and unless uniform size particles are assumed, the results appear ambiguous. The most promising and straightforward alternative to present itself was simply catching the particles and measuring them.

The sampler, described in detail in Appendix C, skimmed a portion of the flow through a narrow inlet slit, decelerated the stream of helium and zinc particles by mixing with air at matched pressure and "caught" and spread the solid zinc particles on a strip of mica tape (precoated with a 160 $\mathring{A}$ carbon layer) attached to a rotating cylinder.

Following the collection the mica strip was carefully removed from the collector cylinder and was then analyzed under an optical microscope to determine the exact locations of the samples. It was found, surprisingly, that optical microscope observations correlated closely with later electron microscope observations with respect to density of deposit, damage to tape, and relative size of particles (surprising since there are over two orders of magnitude difference between the magnification of the optical and the electron microscope). The optical inspection of the tape was accomplished on a Unitron Inverted Metallographic Binocular Microscope under a magnification of approximately 1200X. This sample location analysis was then checked against an independent determination of sample location based upon the oscillograph record of cylinder orientation with time given by the magnetic pickup signals

described in Appendix B. It should be noted that, as shown in Fig. C-8, samples taken (when using the rotating shutter version of the sampler) are arranged in a definite order with respect to each other, and an optical inspection of the tape need only determine which sample was taken first for all other sample times to be definitely fixed for a given cylinder speed. This determination was made by a simple comparison between the optical inspection of the tape and the location diagram shown in Fig. C-8 (i.e. only one deposit order made sense). This qualitative determination of sample order was checked against a determination made by analysis of the timing "blips" on the oscillograph record.

The mica strip was then labeled and sent to the electron microscope laboratory for photomicrographs as described in Appendix C.

Upon receipt of the photomicrographs, they were inspected qualitatively with respect to results from other runs and with an eye toward possible improvements in sampling technique, etc. If the sampling was successful and good quality photomicrographs resulted, the particle size distribution was determined. To represent the size distribution graphically, a normalized function Φ was defined such that the integral of the function over a given particle diameter range will yield the fraction of particles having diameters within that range. The curve was determined by actual measurement of each particle on the photograph. The particles were classified according to size—e.g., all particles having diameters between 0.06 and 0.08 photograph inches were

assigned to the 0.07 in. (96 Å for a magnification of 132,000) class. The number of particles in each class was normalized by the total number of particles counted and then divided by the diameter span of the class. This yielded one point on the distribution curve. Figure 24 is an example of particle size distribution determined from these counts. Other methods of plotting the data were also used (see Fig. 25).

C. STATIC PRESSURE MEASUREMENT FOR CONDENSATION ONSET

A Mach 5 (helium) nozzle (see Fig. 4) was designed for making static pressure measurements and was fabricated from beryllium copper. This nozzle has a .1294 in. diameter throat, a total included angle of 7.45°, and a .389 in. exit diameter. These dimensions were chosen, (1) to give approximately the same blowdown rate as with the Mach 25 nozzle, (2) to provide sufficient space for the transducer mountings while keeping the nozzle as short as possible to minimize boundary layer, and (3) to maintain underexpansion when exhausting to atmosphere in order to minimize the chance of boundary layer separation near the nozzle exit. Nine static pressure taps are located along the 2 in. length of its supersonic portion according to Table 1. A stagnation pressure tap is located just upstream of the throat at a diameter of .500 in. Although stagnation pressure was measured at the arc chamber, this pressure measurement was deemed necessary due to the configuration of the arc chamber downstream closure assembly (see Fig. 5) used in conjunction with the Mach 5 nozzle. There existed the possibility of a

stagnation pressure loss through the baffle arrangement and through the ruptured diaphragm. However, in almost all runs, both hot and cold, the two stagnation pressures were found to agree within experimental error limits, i.e. within approximately 3%. Also, neither pressure measurement was consistently higher or lower than the other, again indicating that any discrepancy was due to experimental error.

Figure B-2 shows the nozzle installed in the arc chamber with all transducers installed and connected. Figure 7 is a photograph of the complete setup. The light sources are for the purpose of illuminating the flow field (providing the light for scattering by the condensed particles) for the Fastax pictures (such as that shown in Fig. 34).

The method used for obtaining location of onset of condensation was the determination of the location at which the nozzle static pressure deviates from its isentropic or "frozen" expansion value. This method has the disadvantage that either a large number of pressure taps are necessary or a relatively high degree of uncertainty must be accepted due to pressure tap spacing. While a large number of taps are feasible on a steady state device (since they can be connected to a multiple manometer bank or similar device), the cost becomes prohibitive on a short duration blowdown facility requiring an expensive transducer and related electronic devices for each tap.

The static pressures (non-dimensionalized by the chamber pressure) were plotted against the effective area ratios (e.g. see Fig. 31) determined from

pitot pressure measurements* (see Section III). The uncertainty mentioned above can be seen in Fig. 31, where it is noted the condensation onset point can be anywhere between an area ratio of 1.76 and 2.26.

D. PITOT PRESSURE MEASUREMENT FOR DETERMINATION OF EFFECTIVE AREA RATIO

It has been argued[1] that at lower Mach numbers, condensation has little effect upon the pitot pressure and that, therefore, pitot pressure can be used as a valid indicator of effective area ratio. The way in which pitot pressure can be used for this purpose is shown in Section III.A and Appendix G. Such a determination of effective area ratio made it possible to distinguish boundary layer effects on static pressure from those due to condensation.

In a "frozen" supersonic flow the pitot pressure is simply the stagnation pressure downstream of a normal shock; this shock is the bow shock created by the pitot itself. In most cases the size of the pitot probe is irrelevant; however, in a flow containing condensed particles, its size becomes of major importance since it affects the degree of revaporization of the particles downstream of the bow shock. These particles will always tend to revaporize if they were created by condensation (i.e., if the vapor was superheated at any point upstream such as in the stagnation chamber). The temperature will

---

*In one run the boundary layer was determined from nozzle pressures taken far upstream where it was assumed there was no condensation. This method was necessitated by a pitot failure.

increase downstream of the shock finally reaching the original chamber temperature while there is a stagnation pressure loss. Since the slope dp/dT of almost all saturation curves is positive, the vapor returns to conditions further "to the right" of the saturation curve or at a higher degree of superheat than before.

The gas or vapor surrounding these particles will experience a sudden increase in temperature and decrease in velocity upon passing through the shock while the particles themselves will experience some thermal and momentum lag[29, 30]. Calculations (see Appendix E) show that the adjustment downstream of the shock to the final equilibrium state between the gas and the vapor (i.e., the "relaxation"), resulting from particle revaporization and momentum transfer, is characterized by an increase in stagnation pressure.

It is therefore necessary either to completely analyze this region or to measure the stagnation pressure either close enough to the shock that no relaxation will have taken place or far enough from the shock that the flow will have returned to equilibrium. Of course, the latter method is by far the simpler. This can be accomplished either by the use of a "shock holder" or by simply making the probe of such a diameter that the bow shock will be located far enough upstream of the pitot. In this experiment pitot probes varying in diameter from .008 in. to .375 in. were used to determine the variation of pitot pressure with pitot tube diameter (i.e. bow shock detachment).

Figure 8 shows how the pitot pressure varies with pitot diameter. A diameter of .125 in. was selected as the minimum pitot diameter consistent with the assumption of equilibrium behind the pitot shock. It had been hoped that a lower "knee" to the curve could be found indicating the point at which no relaxation at all had occurred, but technical difficulties associated with the miniature sizes and accompanying lag times made this impossible. When using the larger pitot probes, the transducers could be located as much as 4 in. away from the entrance to the tube without causing significant lag (the inside diameter of the tubes was approximately .032 in.); but such was not the case with the small pitots. In fact the measurement of pressure with the .008 in. diameter pitot caused considerable difficulty. To minimize the lag time problem the pitot tube was epoxied directly to the transducer after the transducer had been "degassed" and filled with a low vapor pressure liquid, n-dibutylphthalate (see Fig. 8), to substantially reduce its internal volume. This method met with only moderate success and further development of the technique was abandoned in favor of using the much more easily obtained equilibrium pitot pressure.

Since the experimentation with pitot sizes was performed at the exit of the Mach 25 nozzle, a somewhat smaller diameter was considered conservative for use with the Mach 5 nozzle. The four major influencing differences between the two nozzles would all tend to make the .125 diameter conservative for the Mach 5 case:

(1) At the lower exit Mach number the particles have less chance to grow. This would result in smaller particle size and therefore faster revaporization and relaxation.

(2) The lower velocity would result in the particles travelling less distance during any revaporization time.

(3) The higher temperature of the particles at the lower Mach number results in less heat transfer necessary to vaporize them.

(4) At the lower Mach number the shock detachment distance is greater for any given size pitot resulting in more distance in which relaxation can take place.

Throughout the remainder of this report, "pitot pressure" will be used (unless otherwise stated) to describe the stagnation pressure downstream of a normal shock where complete revaporization of the condensed mass is assumed and the flow has returned to an equilibrium state.

III. THEORETICAL ANALYSES

A. SATURATED EQUILIBRIUM EXPANSION

It appeared from earlier work (see Appendix G) that far downstream of condensation, there was an approach to pressures close to those which would exist for a saturated equilibrium expansion. This was substantiated by perusal of previous measurements of static pressure along nozzle walls as well as calculations. For conditions far downstream of the location of onset of condensation, then, a solution of the equations for the saturated equilibrium expansion becomes useful. The equations for a two component condensing flow are derived in Appendix D. A computer program to numerically integrate the equations (which permitted the use of a variable latent heat) was developed and solutions for the values of the parameters used in the experimental measurements were obtained.

Figure 9 shows the effects of condensation on the flow parameters (in terms of vapor mass fraction and pressures—non-dimensionalized by the chamber pressure) as a function of the area ratio for one typical set of stagnation chamber conditions. The frozen flow expansion is also shown for reference.

There are curves for three "pitot" pressures in Fig. 9. The top two are important to this study because they show the difference between the pitot pressure for a condensing flow p_o' (assuming total relaxation of the flow between the bow shock and the pitot) and that for a non-condensing or frozen

flow p_{o_f}'. The lowest of the three curves is of some interest and represents that "pitot" pressure $p_{o_{nr}}$' which should be recorded if no relaxation took place downstream of the pitot shock. It would represent the theoretical lower limit that a pitot probe might ever read and, as such, establishes where the lower "knee" to the curve shown in Fig. 7 should be (as discussed in Section II. D).

The other two pressure curves in Fig. 9 represent the static pressure p in condensing and non-condensing flows. The small "bump" due to condensate solidification is apparent. The remaining curve shows how the mass fraction of vapor decays in a condensing flow.

The pitot pressure p_o' is often used at low Mach numbers as an indicator of effective area ratio[1] (or boundary layer displacement thickness) due to its insensitivity to condensation in the flow. The possibility of extrapolating this concept to large amounts of metal vapor condensing in relatively high Mach number flows led to an analysis of the effect of condensation on the pitot pressure as well as to its effect on the static pressure. The fact that condensation affects the two pressures differently permitted a solution for carrier gas mass fraction f (Appendix G).

Figures 10 and 11 show the variation of these two pressures as a function of the mixture concentration (with chamber temperature as a parameter) at two widely different area ratios (corresponding to the exit area of the Mach 5 and the Mach 25 nozzles respectively).

Figure 10 indicates that at large area ratios, even though the pitot pressure is much less sensitive to condensation than is the static pressure, it still deviates considerably from its "frozen" value (i.e., from its value at f = 1). In fact, at typical conditions (p_c = 2500 psia, T_c = 2500°K, f = .25, $\bar{A}$ = 800), p_o' is 22% higher than p_{o_f}'. This discrepancy would lead to a 17% error in the determination of $\bar{A}_{eff}$ if that determination assumed $p_o' = p_{o_f}'$. If f were determined using $\bar{A}_{eff}$, it would be calculated as .30 or 25% higher than the true value. For this reason the graphical interpolation method set forth in Appendix G was necessary in place of the simple assumption, $p_o' = p_{o_f}'$.

At much smaller area ratios as in Fig. 11, the deviation of p_o' from p_{o_f}' is not as great (only 9.5% in this case) but would still be considered significant.

Therefore, it seems that in a condensing metal vapor, the pitot pressure is much less sensitive to the condensation than is the static pressure, but is still too sensitive to allow the approximation $p_o' = p_{o_f}'$.

Figures 10 and 11 show that pitot pressure is quite insensitive at all area ratios to both stagnation chamber temperature and flow composition in that a 12% change in either of these parameters would cause, at most, a change of 3% in $\bar{p}_o'$. Pitot and static pressure when non-dimensionalized by stagnation chamber pressure were both found to be almost completely independent of chamber pressure. At the large exit area ratio of the Mach 25 nozzle, the static pressure is almost independent of chamber temperature but is quite

sensitive to the flow composition. It was this combination of factors that allowed the determination of mass fraction and chamber temperature as outlined in Appendix G.

Figure 12 shows the way in which the effect of differences in stagnation temperature on nozzle pressure decreases as the equilibrium expansion proceeds to larger area ratios. The plot remains unchanged for stagnation chamber pressures between 1750 psia and 5500 psia. The approximate departure of temperature and pressure from a frozen isentropic expansion over a wide range of mass fractions, area ratios and stagnation chamber pressures and temperatures is shown in Fig. 13. If pressure is measured, temperature can immediately be approximated from the curve.

It was found that if the latent heat is approximated by a constant, the equilibrium equations can be integrated (Appendix D) to give a single transcendental equation in T and $\overline{A}$ (see Eq. (D.21)). For a given area ratio of interest, the transcendental equation may then be solved (either by iterative or graphical methods) for T. Solving for the other flow variables follows algebraically.

The main advantage of this integrated solution is the fact that the flow properties may be obtained at some given area ratio, without a stepwise integration from the saturation point (i.e., it was not necessary to solve for the complete nozzle flow field to obtain a solution at a given downstream area ratio). While it is much simpler than the exact solution, which has to be numerically

integrated from the saturation point to the point under consideration, the integrated solution (Eq. (D. 21)) has the disadvantage of requiring graphs or iteration. However, if the point under consideration is far enough downstream of the saturation point that it may be assumed all of the condensation has taken place, and if also the temperature may be assumed small in comparison to the chamber temperature (i.e., $T/T_c \ll 1$), then the equation becomes even simpler, of the form, $T = k_1(\bar{A})^{k_2}$, where k_1 and k_2 are constants which depend upon the flow and fluid properties (see Eq. (D. 28)).

Each of the equilibrium solutions mentioned above, Eq. (D. 21) and Eq. (D. 28), are shown in Fig. 14 for the stagnation chamber conditions: $p_c = 4500$ psia, $T_c = 4500^{\circ}K$, $f = 0.4$. The "frozen" flow solution is also shown for reference. Three sets of curves are shown—the upper set represents the non-dimensional temperature $\overline{T}$; the middle set represents the non-dimensional static pressure $\overline{p}$; and the lower set represents the mass fraction of uncondensed vapor q. If the latent heat used is "adjusted" at each area ratio calculated for the change in local temperature, the integrated solution is very close to the exact solution as indicated in Fig. 14.

The solution obtained from Eq. (D. 28) indicates what might have been expected concerning the region of validity. The plot of q at the bottom of Fig. 14 shows that the condensation is essentially complete by an area ratio of 20. Downstream of this point all solutions are quite close to each other.

It can also be seen from Fig. 14 that the mass fraction of uncondensed vapor (calculated from Eq. (D.19) using temperatures resulting from Eq. (D.28)) is quite large in the region where the asymptotic equation (D.28) is not valid. This indicates that if it is not known whether condensation is essentially complete at an area ratio of interest (i.e., whether Eq. (D.28) would be valid), the temperature may be calculated using Eq. (D.28), then q calculated with Eq. (D.19) would determine whether all the vapor had condensed and therefore whether the equation was valid.

B. DISCONTINUOUS CONDENSATION AND VAPORIZATION

The maximum increase in static pressure which would occur at a point in a nozzle as a result of the onset of condensation was determined by assuming that all the vapor condensed at a point in the nozzle does so in a discontinuity such that downstream of the discontinuity saturation conditions exist (sometimes called "condensation shock"). A similar approach was used to determine pitot pressure p_o', by considering the total process as one in which the flow of a gas-vapor-condensate mixture passes through a normal shock wave and subsequent total vaporization of the condensate occurs with thermal and momentum equilibration of the two components.

The equations governing each of the above processes are derived with their solutions indicated in Appendix E. It should be noted that the solutions given here are dissimilar to the classical condensation-shock theory previously

presented[1], not only due to the fact that a two-component system is treated here, but also in that no assumption is made here that the mass of the gaseous part of the flow can be considered unchanged.

Figure 15 shows $\bar{p}$ - $\bar{A}$ curves for a frozen isentropic and an equilibrium expansion along with a locus of the pressures downstream of a condensation jump at the given area ratio. Each point on this locus represents conditions downstream of a different condensation jump. It can be seen that the solution for condensation at a discontinuity yields higher pressures than does the equilibrium solution. Further, the percentage increase in pressure difference between the two solutions increases with the amount of supersaturation (defined as the ratio p_v/p_∞) preceding the condensation jump. However, it may also be seen that the two pressures do not become significantly different until an area ratio of about 10 where the vapor in the equilibrium expansion is within approximately 15% of being totally condensed (i.e., until the "knee" of the equilibrium expansion curve is reached).

Figure 15 also shows the mass fraction of uncondensed vapor downstream of the condensation discontinuity as compared to that for a saturated equilibrium expansion. It can be seen that even though the pressure is higher for the case of a discontinuity, less vapor must be condensed to reach these pressures and satisfy saturation downstream of the discontinuity.

C. NON-EQUILIBRIUM EXPANSION

While having been under increasing attack recently, the classical theory still seems to have the greatest "success" in matching experimental data from nozzle flows[21, 33, 35, 36]. It provides a basis for comparison with, and extrapolation of, experimental data. It also provides in a qualitative manner prediction of the effects of different flow parameters on the condensation process. A program for the solution of the non-equilibrium condensation of a vapor in non-condensing carrier gas expanding through a nozzle therefore was written and is described in Appendix F. The classical liquid drop nucleation model which yields a nucleation rate equation in terms of a "critical" drop size was used. The value of the surface tension was taken as a function of drop size[37] through the Tolman constant related to the intermolecular distance in the liquid drop. Although there is some disagreement on surface tension correction for small radii, this correction seems to be generally regarded as the best available[15, 23] and is somewhat substantiated by experiment[21, 36]. The particle size measurement was used to approximate the Tolman constant within the appropriate limits.

The growth rate equation used for comparison with the present experimental results was one given by Hill[35] with the following two approximations: (1) the droplet temperature was assumed equal to the equilibrium saturation temperature T_∞ corresponding to the vapor partial pressure, and (2) the droplet pressure was assumed equal to the vapor partial pressure (i.e., the droplet is considered to be large enough to allow neglect of the surface tension contribution).

To determine the effect of the growth rate equation on the resultant solution, other growth rate expressions were also considered (Appendix F). Figure 16 shows how onset of condensation (roughly at the peak J) is delayed by slower growth rates. As would be expected the faster the growth, the more sudden or narrow is the region of collapse of supersaturation.

The program developed (using Eq. (F. 64)) was used to determine the effects of the amount of (mass fraction) and molecular weight of the non-condensing carrier gas on the condensation process. All calculations assumed accommodation coefficients of one. Helium, argon, and xenon as carrier gas for zinc vapor were considered with the stagnation conditions of the vapor held constant. The nozzle geometry was held constant to that of the Mach 5 nozzle.

The primary effects of the carrier gas appears to be the result of the carrier gas acting as a sink for the latent heat released by the condensation. That is, it acts to cool the flow. Therefore, for a carrier gas such as helium with a very high specific heat, the more carrier gas the faster the accumulation of condensate—once condensation has started. This can be seen in Fig. 17. Figure 18 shows similar results for constant mass fraction of carrier gas but different molecular weights.

An additional effect of the carrier gas results from the change in velocity of the gas mixture before onset of condensation. The lower the molecular weight of the mixture at a given point in the nozzle, the higher the velocity.

Therefore when helium is the carrier gas, a higher mass fraction of helium means a lower residence time in the nozzle, or a faster expansion, or delayed onset. This can be seen in Fig. 19. Figure 20 shows the same effect for constant mass fraction of carrier gas but different molecular weights. Figure 21 shows the same effects in the $\bar{p}$-x plane. Changing the mass fraction of xenon makes almost no difference in the condensation process since the molecular weight of xenon is not different enough from that of zinc.

The effect of change in nozzle expansion angle was also considered. A change in nozzle cone half-angle from 7.5^{o} to 3.5^{o} made almost no change in the area ratio at which onset occurred. This was also true for a change in nozzle size. (The throat area, hence the scale of the expansion was changed by a factor of four.) Both changes did show a difference in drop size downstream, however. A decrease in nozzle angle and an increase in nozzle scale both make for a decrease in the rate of change of the properties of the flow. The change in nozzle angle changed drop size by almost a factor of two, while the increase in scale resulted in an approximate 30% increase in drop size.

In general, the lower the partial pressure of the vapor at the saturation point the slower the growth and the smaller the particles resulting far downstream. For a constant saturation partial pressure, particle size decreases slightly with increased mass fraction of carrier gas lighter than the vapor, as a result of the cooling effect of the carrier gas.

IV. EXPERIMENTAL RESULTS

A. PARTICLE SIZE

Figure 22 is an electron microscope photograph of a collection of particles obtained through methods outlined in Section II and Appendix C. The magnification is 132,000X or 1.0 in. on the photograph represents approximately 1925 Å. The condensed zinc particles appear round and dark. The background grain structure is the chromium layer used for shadowing. Each particle has a light oblong "tail" extending toward the lower right. This is the shadow cast by the particle in the chromium evaporated over the sample at an angle to the surface. The length of the shadow shows the height of the particle above the collection surface. It can be seen that the particles are indeed not only round but also close to spherical in shape. The size range is quite narrow (i.e. there seem to be no particles less than 60 Å—approximately .03 photograph inches—and none greater than 250 Å—approximately .13 photograph inches). That this is not due to the picture's small range of field can be seen in Fig. 23 which is a lower magnification (33,000X) photograph of the same sample. Here the lack of large particles becomes quite apparent.

The particle size distribution curve for the sample shown in Fig. 22 is given in Fig. 24. , the distribution function defined in Section II.B is plotted against particle size. It can be seen to peak at a particle diameter of 135 Å, meaning this was the most prevalent particle size. While plotting the data in

this manner gives a very good qualitative description of the size distribution, the only quantitative data that can be easily obtained from it is the peak particle diameter and the approximate width of the distribution. The results were also plotted in the manner of Fig. 25 to give a quantitatively more descriptive evaluation. (This curve is simply the integral of the distribution curve.) It may be readily seen that the median diameter was 140 Å. As was indicated above, the curve is quite narrow with only 10% of the total number of particles having diameters greater than 195 Å and 10% having diameters less than 95 Å (i.e., 80% of the particles have diameters within a 100 Å range). This narrow distribution of condensate drop sizes about a median size agrees qualitatively (i.e., except for a particle size scale factor) with previous theoretical work[21] and experiments[23]. (These references deal with the condensation of water vapor in air which yields much smaller particle sizes.)

A comparison was made between the experimental curve and one obtained from the non-equilibrium calculations described in Section III.C and Appendix F. The agreement was found to be quite good—especially the agreement between the peak diameters and the median diameters. As can be seen in Fig. 24 and Fig. 25, the calculated curve peaks at 155 Å; its median diameter is 165 Å, while the "80% limits" fall at 140 Å and 200 Å giving only a 60 Å range of diameters. The difference in heights of the two distribution curves is only due to the narrower distribution of the calculated sizes.

Figure 22 has been discussed at length due mainly to its relatively high quality and optimum particle density (i.e., enough particles for a very good statistical sample but not so many that they obscure one another). The size distribution of another sample taken during that same run (80514), but much earlier (11.5 msec), is shown in Fig. 26. For comparison the distribution of the sample taken at 22.4 msec (Fig. 22) is included. The 11.5 msec collection peaks at 125 Å (quite close to the same diameter as at 22.4 msec). However, the curve is characterized by a "bump" extending from a diameter of approximately 150 Å to 250 Å. The reason for the more than normal preponderance of particles in this size range at this sampling time is not clear. However, the fact that the chamber temperature was still quite high (3935°K) and the arc was still established suggests the possibility of ionization effects. Heterogeneous condensation (i.e., condensation on foreign nuclei—such as ions) is usually characterized by earlier onset and therefore larger particles, and therefore could account for the "bump" in the curve. It should be noted that in the absence of this "bump" the curve is quite similar to the 22.4 msec curve.

Figure 27 is the size distribution curve for a particle sample taken during Run 80115, but at similar stagnation conditions as those of Run 80514. It can be seen to compare well with the experimental distribution curve of Run 80514, establishing a semblance of repeatability to the results previously discussed.

Due to the exploratory and developmental nature of the study, the quantity of "good" data was limited even though over 30 runs were actually made. Eighty percent of all particles collected in all runs were between 70 and 200 Å.

Particle samples were also taken at various locations downstream of the exit of the Mach 5 nozzle. The two locations yielding the most interesting results were the rear of the pitot sting, facing downstream, and approximately 6 ft downstream of the nozzle exit, facing upstream. The samples were, of necessity, time-integrated over the length of the run. For the sample obtained on the rear of the sting, the distribution of particle sizes is plotted in Fig. 28. The curve shows no "peak" as such. It is evident the distribution is strongly skewed toward the smaller diameters, but this was expected due to the placement of the sample. (The small particles would be much more likely to be "trapped" in the wake of the sting and be deposited on the sting surface.) The major observation that can be made is that the particles are the same order of size as those found when using the sampler. Figure 29 shows that the sample obtained far downstream includes considerable agglomeration. Almost no single small particles were collected. This demonstrates one problem in any particle sampling method that did not obtain the particles directly from an undisturbed free stream (e.g., such as "sweeping" a receiver tank following a run). While no particle measurements were attempted, the photograph suggests pre-agglomeration particle sizes on the order of 130 Å (.08 photograph inches) which is in close agreement to those obtained with the sampler using the Mach 25 nozzle.

In any collecting device, the question of collector efficiency is always raised. In this case, since no analysis was made concerning the total number of particles collected, the question became not "what is the efficiency?", but rather, "how does the efficiency vary with particle size?" It was therefore necessary to obtain a reasonable estimate of whether the size distribution obtained from the rotating collector tape was indeed representative of the size distribution of particles entering the sampler. To accomplish this, samples were taken from elsewhere inside the sampler during each run.

One location (Fig. C-1) was on the inside wall of the sampler, placed approximately on the centerline so that if particles were being "thrown" from the collector cylinder, they would be caught at this point. The size distribution curve from this sample is shown in Fig. 30 and can be seen to be very similar to the collector's distribution curve of Fig. 24. (Both samples were taken during the same run.) Side wall samples taken during other runs yielded similar results. Although these samples were "time-integrated" (i.e., taken over the duration of the run rather than at a discrete time), it is still reasonable to assume that, since their distribution curves were similar to those obtained on the collector cylinder, collection was not weighted toward any particular size. The distribution curves obtained should therefore be representative of the free stream particle size distribution.

The size distribution curves drawn from the experimental data are believed to be valid representations of the condensed flow to within a maximum possible

error of $\pm$ 20 Å of particle diameter. This range of uncertainty derives from the measurement of the particle size. Experience has indicated that it is possible to read and repeat particle size measurements within a .02 in. range on a 132,000X photomicrograph. This corresponds to a possible error of $\pm$ 20 Å.

One of the first questions to arise in a study of particle size concerns agglomeration. The region in which agglomeration could exert an effect on particle size is that distance extending from the saturation point, where particles first begin to be formed, to the particle solidification point, beyond which particles stuck together could be seen in the photomicrographs of the collected particles. In the present study the total residence time of a particle in this region is typically only 13 μsec. Since the particles are quite small (of the order of 150 Å in diameter) it can be assumed there would be no velocity lag[26]; all the particles would expand with the gas. If every particle collision resulted in coagulation, Brownian movement of the particles relative to each other could cause the number of particles to decrease by a factor of two during the 13 μsec[38]. This would result in a 25% increase in particle diameter. However, since the assumption that every collision results in coagulation is very conservative the agglomeration process should tend to be considerably slower than this maximum amount[39]. In this study, agglomeration effects were neglected.

B. CONDENSATION ONSET

Although the study of condensation onset was relegated primarily to the Mach 5 nozzle, the question of onset did arise early in the study in connection with the Mach 25 nozzle. The concern at that time was whether the condensed particles being sampled originated in the nozzle or in the sampler, after the flow had been decelerated.

Even though an expanding vapor becomes supersaturated, it is not evident, a priori, that homogeneous condensation will occur. The possibility exists that if the vapor is expanded too rapidly, the nucleation process cannot produce "enough" nuclei to cause collapse of the supersaturated state, or if the vapor density is "too low", the nucleation rate will never reach a sufficient level to cause collapse. Both conditions would result in a frozen expansion.

While preliminary calculations, based upon classical nucleation theory, indicated that condensation would occur in the nozzle, the theory in its present state of development was not considered reliable enough to furnish absolute proof one way or the other. Therefore, to establish the fact that the condensation did, indeed, take place in the nozzle, Fastax photographs were taken perpendicular to a 1/8 in. light beam traversing the flow between the exit of the nozzle and the sampler. Sufficient scattered light was seen from $t \doteq 1$ msec throughout the run to establish the fact that condensation was occurring inside the nozzle during that time.

As mentioned previously, the measurement of static pressure was used to determine the location of condensation onset in the Mach 5 nozzle. Figure 31 shows a typical expansion curve obtained during the study. The static pressure (non-dimensionalized by the chamber pressure) is plotted against effective area ratio. The "frozen isentropic" expansion and the nonequilibrium solution (Appendix F) are shown for comparison. As can be seen, the location of the onset point cannot be determined more accurately than the pressure tap spacing. In this case, it can only be said that onset occurs between an area ratio of 1.76 (where the experimental point still lies on the frozen expansion curve) and 2.26 (where the experimental point has definitely departed in the direction of the equilibrium curve). These two outside limits correspond to $\bar{p}$'s of 0.090 and 0.054 or, using Dalton's Law (Eq. (D.6) with q = (1 - f), since at onset no condensation has yet taken place), to zinc partial pressures p_z of 12.9 and 7.7 psia.

While a p vs. $\bar{A}$ plot is fine for studying the manner in which onset occurs, the p-T coordinates are of interest in the comparison of results of different expansions. The nozzle expansion of the zinc vapor before condensation may be considered isentropic and as such p_z vs. T is represented by a straight line of slope $(\gamma/\gamma - 1)$ when plotted on a log-log scale. The position of the line is determined by the chamber conditions, p_{c_z} and T_c. Figure 32 shows a summary of the onset data obtained for zinc vapor in helium.

Within the accuracy the apparatus dictates, the onset "points" seem to yield a definite onset curve which is characterized by an almost constant separation

(at constant pressure) from the saturation curve. A common method of defining the amount of supersaturation at onset is by means of the "supersaturation temperature decrement" ΔT, defined as the difference between the temperature at which the flow isentrope crosses the saturation curve and the temperature at which onset of condensation occurs. One interesting feature of the measurement is that ΔT for the conditions considered here is found to be almost constant at $430^{\circ}K$ over the range of conditions considered. The onset points computed are also shown and indicate reasonable agreement. Similar results were obtained using argon in helium (Appendix I), where the ΔT found appeared to be approximately $20^{\circ}K$ over a range of argon saturation point pressures between 7 psia and 300 psia.

Figure 33 shows the same set of onset data with constant nucleation rate curves and computed onset points superposed. The nucleation rate curves were calculated from Eq. (F.49) and (F. 50) (Appendix F).

Quite some time ago, Head[9] proposed that the attainment of an approximate nucleation rate of $J \doteq 10^{18}$ (drops/in.^{3}-sec) (calculated according to Eq. (F.49) and (F. 50)) typifies the onset of condensation in water vapor. He justified this argument on both theoretical and experimental grounds. More recently, it has been shown[33] that this figure also serves to indicate onset in nitrogen and that calculations indicate the figure may be good for pure copper vapor also. The onset point in zinc vapor expanding in helium carrier gas however, seems to be typified by a nucleation rate lying between 10^{20} and 10^{25} (drops/in.^{3}-sec).

Figure 34 shows light scattered from condensed particles in the flow leaving the nozzle.

It has long been known that ionized particles will act as condensation nuclei in a supersaturated vapor. This is the underlying principle of the Wilson Cloud Chamber. Thus, due to the relatively low ionization potentials of metals and the very high temperatures reached in the arc chamber, the possible effect on condensation of ionization in the arc chamber is certainly a question which cannot be overlooked. Solbes and Kerrebrock[17] have shown that non-equilibrium ionization effects on nucleation and condensation are minor in potassium at temperatures below $2000^{o}K$ at 1 atmosphere. A simple equilibrium ionization calculation on potassium vapor at these conditions yields an ionized mass fraction of 2.7×10^{-5}. Due to zinc's much higher ionization potential, stagnation conditions of 4650 psia and $4650^{o}K$, at a zinc mass fraction of .75, are necessary to obtain a comparable ionization level. However, most of the measurements of particle size were made at stagnation pressures and temperatures approximately half that value. At the typical chamber conditions of 2500 psia, $2500^{o}K$, and a .75 zinc mass fraction, the ionized mass fraction of zinc is only 6.8×10^{-10}. Thus the equilibrium ionization level at stagnation conditions is five orders of magnitude less than an equilibrium level would be in the potassium case. Since the higher density in the zinc flow would tend to minimize the non-equilibrium ionization downstream of the chamber, it seems

reasonable that ionization, in toto, can be assumed to be negligible. Earlier in the run when the temperatures are high and the arc is still established, it is not clear what the ionization level would be.

It is felt that contamination did not play a strong role in influencing any of the major findings of this study. The fact that the heavily eroded center electrode was made of zinc and that there was no evidence that the other end of the arc column established itself at any one point (other than the zinc fuse) would lend credence to the assumption that the only significant "contaminant" was zinc (it should be noted that hotshot contamination usually derives from only one electrode and the fuse, which were made of pure (99.99+%) zinc in this case). Further, considerable supersaturation of zinc vapor during the expansion indicates negligible effects from contamination since contamination would have tended to cause a saturated expansion.

V. SUMMARY OF RESULTS

The study made was primarily of the condensation of a metal vapor as it is expanded in a nozzle in the presence of a noncondensing inert carrier gas. Zinc was the metal vapor employed for most of the measurements made with helium as the carrier gas. During measurements, stagnation chamber pressures ranged from 1300 to 4000 psia while chamber temperatures varied from 1600 to 4000^{o}K. Helium mass fractions varied between 0.2 and 0.7. Two major objectives were set: to determine the size of the particles formed, and to locate the point at which noticeable condensation first occurred. In the accomplishment of these objective, analyses of both equilibrium and non-equilibrium condensation in a two-component mixture were made.

The more important results of this study are presented below.

1. The pitot pressure in a condensing flow varies with the size of the pitot tube up to a critical diameter. This diameter is determined by the minimum shock standoff distance that allows sufficient distance for the condensate to revaporize and the flow to reach thermal and dynamic equilibrium.
2. A particle sampler, which decelerates the extremely high speed flow emanating from a hypersonic nozzle, by mixing with air at the same static pressure is an effective means of collecting very small particles while they are still held in suspension in the carrier gas.

3. An analytical study of the equilibrium expansion of a condensable vapor-inert carrier gas mixture yielded the following results:

   a. When the condensing vapor constitutes a sizeable portion of the expanding mixture, the assumption that the pitot pressure is the same as it would be with no condensation becomes invalid.

   b. Far downstream of the region in which the condensation initially occurs, both the static pressure ratio p/p_c and the pitot pressure ratio p_o'/p_c were quite insensitive to both chamber pressure and temperature. The pitot pressure ratio was insensitive, while the static pressure ratio was quite sensitive, to the helium mass fraction.

   c. Under the assumptions that the latent heat is constant with temperature, the condensation has been completed, and the temperature is small compared to the stagnation temperature, the equilibrium equations reduce to a simple algebraic relation between T and $\overline{A}$.

4. The measured particle size distribution was found in general to be quite narrow, with 80% of the particles having diameters within a 100 Å range. The distribution curve peaked at a diameter of 135 Å indicating the majority of particles clustered about that size.

5. The particle size distribution seemed to be relatively insensitive to stagnation conditions, for the range of conditions considered.

6. The condensation onset locus is characterized by a constant 430°K supersaturation temperature decrement ($T_{sat} - T_{onset}$). This value seemed to remain constant over the range of stagnation conditions considered.

7. The experimentally determined particle size and onset locus provided data which has served to set parameters for use of the classical non-equilibrium condensation theory. The theory then gave moderate agreement with the measurements. It was also used to determine the effects of quantity and molecular weight of carrier gas on the condensation process and to extend the present condensation results to other flow conditions. The analysis yielded the following results for the chamber conditions considered:

   a. The higher the mass fraction of carrier gas of low molecular weight (helium) or the lower the molecular weight of carrier gas (at constant mass fraction), the faster is the accumulation of condensate following onset of condensation but the greater is the supercooling and the smaller the particles far downstream.

   b. The area ratio at which onset occurs is not very sensitive to the nozzle expansion angle (over a factor of two in nozzle angle) or to the change in nozzle scale (over a factor of two in nozzle scale).

c. The size of particles far downstream depends primarily on the conditions at the saturation point. For a constant saturation point the size changes almost inversely with change in nozzle angle. The size increases about 30% for an increase in nozzle scale of two.

APPENDIX A. THE UNIVERSITY OF MICHIGAN'S HOTSHOT WIND TUNNEL AND DESIGN OF THE ARC-INITIATING FUSE-SWITCH

NOMENCLATURE

A	cross-sectional area of fuse
a	see Fig. A-9
B	electromagnetic field strength
C_1, C_2, C_3, C_4	integration constant
C_P	specific heat
C_{P_f}	specific heat of fuse
E	modulus of elasticity
F	force distribution on fuse
F_L	force distribution at tip of fuse
F_0	force distribution at clamp end of fuse
I	current; moment of inertia
I_2	current through co-axial buss and fuse
I_{T_S}	main buss bar final current
I_{T_t}	main buss bar current as function of time
K	experimental constant
k	conversion coefficient
L, ℓ	see Fig. A-9
M	moment on fuse; mass
M_f	mass of fuse
P	effective load at tip of fuse

R	see Fig. A-9; Resistance
R_c	resistance of co-axial buss
R_{f_r}	resistance of fuse at reference temperature T_r
R_{f_T}	resistance of fuse as function of temperature
R_s	resistance of main transfer switch
r	see Fig. A-9
T	temperature
T_A	temperature of fuse at main switch opening (at time, $t = \tau$)
T_B	temperature of fuse at breakage (at time, $t = t_B$)
T_i	initial temperature of fuse
T_r	reference temperature
T_o	"zero resistance" temperature
t	time
t_B	time from main switch opening to fuse breakage
V	shear force on fuse
x	see Fig. A-9
y	deflection of fuse

δ	mass density of fuse
Θ	slope of fuse
$\theta, \theta_1, \theta_2$	see Fig. A-9
μ	permeability of free space
ρ	resistivity of fuse
τ	current buildup time
ϕ	see Fig. A-9

The University of Michigan Hotshot Wind Tunnel is an impulse-type, blowdown wind tunnel of the induction driven type. A plan view of the laboratory layout is shown in Fig. A-1. The major components are the energy supply system (see Fig. A-2), the arc chamber, test section, and vacuum tank with pumping system (see Fig. A-3) and the instrument-control room enclosure (see Fig. A-4). A detailed description of this facility can be found in Ref. A1. A very brief description is given here.

BRIEF DESCRIPTION OF TUNNEL FACILITY

Large amounts of energy are needed to obtain the necessary high temperature for metal vaporization or high velocities. This energy is obtained by storing it over a long period of time and discharging it over a short period of time. The energy is first obtained from a 150 hp electric motor and stored as kinetic energy in a heavy flywheel capable of storing up to 20×10^6 joules when driven at its maximum speed of 10,000 rpm. This flywheel is connected to the rotor of a unipolar generator so that when the field voltage in the generator is turned on, a current is built up in the main coil circuit (see Fig. A-5) establishing a magnetic field about the coil. In 3 sec—the approximate time to reach peak coil current—switch S_2 is opened, transferring the total current to the arc chamber electrode part of the circuit. Switch S_3 is a fuse-switch designed to carry current until switch S_2 is

completely open. The buildup of electromagnetic forces on S_3, combined with the decrease in its strength due to resistance heating, force it to open after a given time. This initiates an arc resulting in a high voltage and rapid dissipation of the current in the arc column.

The constant volume arc-heating of the gas in the arc chamber causes its pressure and temperature to increase until a diaphragm upstream of the nozzle throat ruptures. The gas then expands through the nozzle either to the atmosphere or into an evacuated test section. A baffle in the arc chamber shields the throat from the arc column and prevents large particles from entering the nozzle.

The arc chamber (see Fig. A-6) consists of three shells of Potomac "A" (Allegheny Ludlum Corporation) steel, prestressed to withstand the high stress concentration located at the three holes in its wall (a pressure relief passage, a transducer port, and a charge gas port). The inner shell is prestressed compressively to balance part of the tensile stress caused by the loading pressure. The resulting chamber is capable of containing 80,000 psi at a safety factor of 2. The interior is cylindrical in shape with a volume of approximately 65 $in.^3$

FUSE-SWITCH DESIGN

The unit shown as S_3 in Fig. A-5 is not really what is conventionally considered either a fuse or a switch. It is a bar, installed

parallel with the electrodes, which was initially designed to break in such a manner that the contact points at the break widely separate very rapidly, initiating an arc across the electrodes. For the initial fuse design and development and for all subsequent experiments outside the area of zinc condensation, copper was chosen as the bar material due to its low resistivity. However, for the zinc-in-helium condensation tests, zinc was chosen for the fuse-switch (hereafter referred to simply as the fuse) for the obvious purpose of introducing zinc vapor into the helium charge gas. The center electrode material was also changed from copper to zinc. In addition, if the arc could be encouraged to remain for a longer period of time between the broken fuse ends, it was assumed that a maximum amount of zinc would be vaporized and copper vapor contamination (from the chamber-liner-outer-electrode that, due to practical considerations, remained copper) could be held to a minimum. Since the fuse as mentioned above, tended to separate widely upon breakage, the zinc fuse was designed with a thick root (see Fig. A-7). This tended to keep the broken fuse tip close to the center electrode which, in turn, kept the arc column between the zinc fuse tip and the zinc center electrode for a longer period of time. The bar must be designed to carry part of the current during the relatively long (approximately 3 sec) current buildup in the coil as well as the total current for the short time necessary to allow the main transfer switch S_2 to open completely.

The time between the opening of the main switch S_2 and the breaking of the fuse S_3 is of critical importance. If the fuse breaks pre-maturely, the main switch may not be completely open and an arc may be maintained across the main switch itself, while a late opening fuse allows a waste of energy by dissipation through the circuit resistance. A delay time of 25 msec was chosen for optimum performance.

The method of calculating fuse size to give a certain breakage time was as follows:

Figure A-8 shows the fuse installation configuration in the arc chamber and Fig. A-9 shows a schematic of this configuration. The repulsive force distribution between the two bars in the electromagnetic field generated by the current is given by [A2]:

$$F = I \int_0^{\ell} B d\ell \qquad (A.1)$$

where

$$B = \frac{\mu I}{4\pi} \int_0^{a} \frac{\sin \theta \, dx}{r^2} \qquad (A.2)$$

(In Eq. (A.2), μ is the permeability of free space and I is the current through the bars.) Now:

$$dx \sin \theta = r d\theta$$

and

$$r \sin \theta = R + \ell \sin \phi$$

therefore,

$$r = \frac{R + \ell \sin \phi}{\sin \theta}$$

Substituting this into Eq. (A.2) and noting that as x varies between 0 and a, θ varies between θ_1 and θ_2.

$$B = \frac{\mu I}{4\pi} \int_{\theta_1}^{\theta_2} \frac{\sin \theta \, d\theta}{R + \ell \sin \phi} \qquad (A.3)$$

$$= \frac{\mu I}{4\pi (R + \ell \sin \phi)} \left[- \cos \theta \right]_{\theta_1}^{\theta_2} \qquad (A.4)$$

It can be seen from Fig. A-9 that

$$\cos \theta_2 = - \frac{\ell \cos \phi}{\sqrt{(R + \ell \sin \phi)^2 + (\ell \cos \phi)^2}}$$

$$\cos \theta_1 = \frac{a - \ell \cos \phi}{\sqrt{(a - \ell \cos \phi)^2 + (R + \ell \sin \phi)^2}}$$

Therefore, from Eq. (A. 1) and (A. 4):

$$F = \frac{I^2 \mu}{4\pi} \int_0^{\ell} \frac{\ell \cos \phi}{(R + \ell \sin \phi) \sqrt{(R + \ell \sin \phi)^2 + (\ell \cos \phi)^2}}$$

$$+ \frac{a - \ell \cos \phi}{(R + \ell \sin \phi) \sqrt{(a - \ell \cos \phi)^2 + (R + \ell \sin \phi)^2}} \, d\ell \qquad \text{(A. 5)}$$

The equation assumes the fuse to be of curved cross-section (the center of curvature being at the centerline of the center electrode) and of infinitely small thickness.

If the fuse is considered to be a beam, rigidly clamped at one end, the situation can be approximated by a one-dimensional beam model. Equation (A. 5) can be numerically integrated to give a force distribution similar to that in Fig. A-10. Approximating this distribution by the linear force distribution shown in Fig. A-11 simplifies the problem considerably.

The beam equations are as follows:

Load: $$F = F_0 + \frac{F_L - F_0}{L} x \qquad \text{(A. 6)}$$

Shear: $$V = \int F \, dx$$

$$= F_0 x + \frac{F_L - F_0}{2L} x^2 + C_1 \qquad \text{(A. 7)}$$

Moment: $M = \int V\,dx$

$$= \frac{F_0}{2}x^2 + \frac{F_L - F_0}{6L}x^3 + C_1 x + C_2 \qquad \text{(A.8)}$$

Slope: $\Theta = \int \frac{M}{EI}\,dx$ (A.9)

$$= \frac{1}{EI}\left[\frac{F_0}{6}x^3 + \frac{F_L - F_0}{24L}x^4 + \frac{C_1}{2}x^2 + C_2 x + C_3\right]$$

Deflection: $y = \int \Theta\,dx$

$$= \frac{1}{EI}\left[\frac{F_0}{24}x^4 + \frac{F_L - F_0}{120L}x^5 + \frac{C_1}{6}x^3 + \frac{C_2}{2}x^2 + C_3 x + C_4\right] \qquad \text{(A.10)}$$

The boundary conditions on the beam are given by:

at $x = L$, $V = 0$ $M = 0$ at $x = 0$, $\Theta = 0$ $y = 0$

Applying these boundary conditions, the constants are found:

$$C_1 = \frac{F_L + F_0}{2}L \qquad C_2 = \frac{2F_L + F_0}{6}L^2$$

$$C_3 = 0 \qquad C_4 = 0$$

Thus Eq. (A.10) becomes

$$y = \frac{1}{EI}\left[\frac{F_0}{24}x^4 + \frac{F_L - F_0}{120\,L}x^5 - \frac{F_L + F_0}{12}Lx^3 + \frac{2F_L + F_0}{12}L^2x^2\right] \quad (A.11)$$

and the deflection at the tip of the beam is

$$y_L = \frac{11F_L + 4F_0}{120\,EI}L^4 \quad (A.12)$$

This deflection due to a linear force distribution across the beam can now be equated to the deflection caused by a single load P at the tip of the beam. The load P required to satisfy this equation can then be considered to be the effective force tending to break the fuse at the tip.

For an end loaded cantilever beam, the deflection at the tip is

$$y_L = \frac{PL^3}{3\,EI} \quad (A.13)$$

Equating Eq. (A.12) and (A.13) and solving for P:

$$P = \frac{11F_L + 4F_0}{40}L \quad (A.14)$$

The numerical constants for the fuse configuration used are:

$L = 3.2$ cm $\qquad R = 1.6$ cm

$a = 4.8$ cm $\qquad \phi = 39^o$

and, $\mu = 4\pi \times 10^{-7}$ h/m. Using these values in Eq. (A.5) and (A.14)

gives a value for P as a function of current.

$$P = .1548\ I^2 \times 10^{-7}\ \text{lbs}$$

where the current I is in amperes.

Preheating of Fuse Prior to Main Switch Opening

When an electric current flows through a resistance, the temperature of the material increases according to the relationship

$$k\ I^2\ R\ dt = M\ C_p\ dT \qquad \text{(A.15)}$$

When I is the current in amperes, R is the resistance in ohms, t is the time in seconds, M is the mass in grams, C_p is the specific heat in calories per gram-^oC, and T is the temperature in ^oC, the constant k is equal to 0.2389.

A schematic drawing of the parallel circuit of the arc chamber prior to the opening of the main switch is shown in Fig. A-12. From the figure it is seen that

$$I_2 = \frac{I_{T_t}\ R_s}{R_s + R_c + R_{f_T}} \qquad \text{(A.16)}$$

Equation (A.15) when applied to heating of the fuse becomes

$$.2389\ I_2^2\ R_{f_T}\ dt = M_f\ C_{P_f}\ dT \qquad \text{(A.17)}$$

Now, the fuse resistance as a function of temperature is obtained from the following considerations.

The resistance of most metals decreases with temperature at a rate which is practically linear and if extrapolated would give a resistance of zero at some temperature T_o (see Fig. A-13). Therefore, if the resistance of the fuse at temperature T is R_{f_T} and the resistance of the fuse at some reference temperature T_r is R_{f_r}, then

$$R_{f_T} = \frac{T - T_o}{T_r - T_o} R_{f_r} \tag{A.18}$$

Assuming a linear buildup of current with time, the main time dependent buss bar current I_{T_t} can be considered to be a linear ratio of the final desired buss bar current I_{T_s}. Thus, considering τ to be the total time for current buildup,

$$I_{T_t} = \frac{t}{\tau} I_{T_s} \tag{A.19}$$

Combining Eq. (A.16), (A.17), (A.18), and (A.19) and rearranging gives:

$$.2389\left(\frac{I_{T_s}^{\,2} R_s^{\,2} R_{f_r}}{\tau^2}\right) t^2\, dt = M_f C_{P_f}\left[\frac{(R_s + R_c)^2 (T_r - T_o)}{(T - T_o)}\right.$$

$$\left. + 2(R_s + R_c) R_{f_r} + \left(\frac{T - T_o}{T_r - T_o}\right) R_{f_r}^{\,2}\right] dT \qquad \text{(A.20)}$$

Integrating Eq. (A.20) between the limits $0 \leq t \leq \tau$ and $T_i \leq T \leq T_A$, where T_i is the initial temperature of the fuse at $t = 0$, and T_A is the temperature of the fuse at main switch opening, and assuming C_{P_f} constant, gives:

$$\frac{.2389}{3} R_s^{\,2} R_{f_r} \tau I_{T_s}^{\,2} = M_f C_{P_f}\left\{(R_s + R_c)^2 (T_r - T_o) \ln \frac{T_A - T_o}{T_i - T_o}\right. \qquad \text{(A.21)}$$

$$\left. + \left[2(R_s + R_c) R_{f_r} - \frac{T_o R_{f_r}^{\,2}}{T_r - T_o}\right](T_A - T_i) + \frac{R_{f_r}^{\,2}}{T_r - T_o}\left(\frac{T_A^{\,2}}{2} - \frac{T_i^{\,2}}{2}\right)\right\}$$

Both the mass of the fuse M_f and the reference resistance R_{f_r} are functions of the length L and the cross-sectional area A of the fuse and may be represented as follows:

$$M_f = \delta\, LA$$

$$R_{f_r} = \rho \frac{L}{A}$$

where δ is the mass density of the fuse material and ρ is the resistivity of the fuse material. Equation (A. 21) now becomes:

$$.0796\, R_s^2\, \rho\, \tau\, I_{T_s}^2 = \delta A^2 C_{P_f} \left\{ (R_s + R_c)^2 (T_r - T_o) \ln \frac{T_A - T_o}{T_i - T_o} \right.$$

$$+ \left[2(R_s + R_c)\, \rho \frac{L}{A} - \frac{T_o\, \rho^2 L^2}{A^2 (T_r - T_o)} \right] (T_A - T_i)$$

$$\left. + \frac{\rho^2 L^2}{A^2 (T_r - T_o)} \left(\frac{T_A^2}{2} - \frac{T_i^2}{2} \right) \right\} \qquad \text{(A. 22)}$$

Fuse Heating After Main Switch Opening

The process for finding the temperature of the fuse at breakage is essentially the same as for finding the temperature at the opening of the main switch with the following exceptions:

1) The current is assumed constant at a value of I_{T_s}.
2) There is now no parallel circuit; therefore, I_{T_s} is the current passing through the fuse.

Equation (A.20) becomes:

$$.2389\, I_{T_s}^{\,2} R_{f_r}\, dt = M_f\, C_{P_f} \frac{T_r - T_o}{T - T_o}\, dT \qquad (A.23)$$

and integrating between the limits $T_A \leq T \leq T_B$, where t_B is the time from main switch opening to fuse breakage and T_B is the temperature of the fuse at breakage, gives:

$$.2389\, I_{T_s}^{\,2} R_{f_r}\, t_B = M_f\, C_{P_f} (T_r - T_o) \ln \frac{T_B - T_o}{T_A - T_o} \qquad (A.24)$$

or

$$t_B = \frac{M_f\, C_{P_f} (T_r - T_o)}{.2389\, I_{T_s}^{\,2} R_{f_r}} \ln \frac{T_B - T_o}{T_A - T_o} \qquad (A.25)$$

However, from experimental results it was found that the time to breakage was slightly longer than predicted. To allow for this discrepancy an empirical constant K is introduced into Eq. (A.25) giving:

$$t_B = \frac{K\, M_f\, C_{P_f} (T_r - T_o)}{:2389\, I_{T_s}^{\,2} R_{f_r}} \ln \frac{T_B - T_o}{T_A - T_o} \qquad (A.26)$$

and in terms of ρ, δ, L, and A:

$$t_B = \frac{K\delta A^2 C_{P_f} (T_r - T_o)}{.2389\, I_{T_s}^{\,2}\, \rho} \ln \frac{T_B - T_o}{T_A - T_o} \qquad (A.27)$$

Equations (A.22) and (A.27) are independent equations containing five variables—I_{T_s}, A, T_A, t_B, and T_B. The third relation needed is provided in the dependence of the breaking temperature T_B upon the rupture stress of the fuse material; i.e.

$$T_B = f(P/A) \qquad (A.28)$$

This relationship can be plotted from existing data for any fuse material and with Eq. (A.22) and (A.27) form a set of equations yielding a relationship between the breakage time t_B and the buss bar current I_{T_s} for any fuse cross-sectional area.

Design of the Zinc Fuse

The zinc fuse was designed using the above procedure but keeping in mind that zinc evaporation after fuse breakage was desired (whereas copper evaporation was not). The constants associated with the zinc fuse are:

$R_c = 70 \times 10^{-6}\ \Omega$ $\qquad$ $T_o = -250^{\circ}C$

$R_s = 15 \times 10^{-6}\ \Omega$ $\qquad$ $\delta = 7.13\ gm/cm^3$

$\rho = 5.88 \times 10^{-6}\ \Omega\ cm$ $\qquad$ $C_{P_{zn}} = .095\ cal/gm^{\circ}C$

$T_r = 0^{\circ}C$ $\qquad$ $\tau = 1.5\ sec$

$K = 1.7$

Using these values and Eq. (A.22), the graph shown in Fig. A-14 was drawn. Equation (A.27) was then used with the relationship, Eq. (A.28), depicted in Fig. A-15, and with Fig. A-14 to give the family of curves shown in Fig. A-16 giving fuse breakage time as a function of fuse cross-sectional area for varying buss bar current.

After the fuse size was determined on any given run, the fuse was made oversize and a hole was drilled at the desired breakage point (see Fig. A-7) to adjust the cross-sectional area and to assure that the fuse would break at that point.

Testing of the Zinc Fuse

Although the zinc fuse was of the same general configuration as the experimentally proven copper fuse, its performance was evaluated by simple tests outside the arc chamber. These tests were made for two major purposes: (1) to determine the reliability of the delay time prediction and (2) to ascertain, if possible, the mode of fuse breakage; i.e. determine whether a substantial amount melted before breakage or whether the fuse broke while still essentially solid.

Two tests were made with the sample fuses connected between the two external electrodes shown in Fig. A-17. The external electrodes were used because they are much simpler to use than the arc chamber. Although the electrode shape is not the same as that in the arc chamber, the current path is quite similar and therefore the electromagnetic force on the fuse is representative of that occurring in the arc chamber. Because of the "rail" configuration of these test electrodes, as soon as the fuse breaks the arc transfers to the electrodes and is rapidly swept away from the fuse by the electromagnetic force on the arc column. This action tends to preserve the breaking configuration of the fuse permitting a meaningful evaluation of its breaking condition after the test.

A Fastax high speed motion picture camera (operating at a speed of approximately 1400 frames/sec) was used to photograph, simultaneously, the fuse and the main transfer switch. The fuse delay time was determined by studying these pictures.

During the first fuse test, the buss bar current was 47,000 amperes and the measured delay time was 15 msec. This compared favorably with the 11 msec value predicted by the calculations. Since a longer delay time was desired to reduce the possibility of arcing at the main switch, a second test was made with a fuse designed to delay 40 msec at 40,000 amperes. The measured delay time was 48 msec, again agreeing well with the predicted value.

The pictures from the first test revealed nothing about the manner in which the fuse broke. An improved camera placement for the second test resulted in the sequence of pictures shown in Fig. A-18. The fuse appeared to melt at the edges and around the center hole before breaking. Subsequent examination of the fuse breakage point revealed a smooth, melted appearance at these locations. However, a crystalline structure elsewhere along the break indicated a mechanical break due to the reduced tensile strength of the zinc at the elevated temperatures.

A third test was made with the fuse in its normal location inside the arc chamber, but with the downstream end of the arc chamber left open. A delay time of 37 msec, at a buss bar current of 39,000 amperes, was achieved. This agreed well with the calculated value of 43 msec. On the basis of this final test, the zinc fuse was considered satisfactory for use in metal condensation studies in the hotshot.

APPENDIX B. INSTRUMENTATION AND PROCEDURES

Any hypersonic blowdown type wind tunnel presents many problems in data acquisition due to the short run times and extremities of conditions to be measured. Pressure measurements taken during this research work varied from approximately 5000 psi to as low as .002 psi, depending upon the pressure to be measured. Since any one pressure measurement could vary an order of magnitude during the typical 30 msec run time, a measurement lag time of a msec or less was a necessity. Due to these stringent lag time requirements, transducers had to be kept quite small to enable their placement very close to the pressure sources.

These are but a few of the special problems connected with a hotshot type tunnel, but serve to point out that the instrumentation requirements are widely different from those of a "steady-state" device. This appendix describes the instrumentation and methods associated with the University of Michigan's Hotshot Wind Tunnel Facility with special emphasis on the requirements of this research work.

RECORDING EQUIPMENT

Almost all measurements and timing signals were recorded on a CEC (Consolidated Electrodynamics Corporation) Recording Oscillograph Model S-119. This is a 50 channel recorder which has a maximum recording speed of 100 in./sec. For quantitatively important, rapidly changing measurements such as pressure, high performance

fluid damped galvanometers, CEC Type 362, were generally used. These galvos have a flat (5%) frequency response range of 0-2500 Hz.

Flow visualization data was recorded on a Wollensak Fastax 16 mm High Speed Motion Picture Camera at framing rates in the neighborhood of 1000 to 2000 frames/sec depending upon the application.

CARRIER AMPLIFIER SYSTEM

The Hotshot Tunnel is equipped with three Plug-In Model SCAS-1002A-R 20 KC Carrier Amplifier Systems, each containing one SOP-5001A-P Oscillator Power Supply Module and four SCA-1003A-P 20 KC Carrier Amplifier Modules. Two of the power supplies were slaved to the first so that only one oscillator was used, thus preventing signal voltage modulation arising from carrier frequency beating between oscillators. These carrier amplifiers provided the core of the pressure measuring facilities described below.

TIMING DEVICES

Position and speed of both the sampler collector cylinder and the outer "shutter" cylinder were determined from the output of Electromation Model 3030 Magnetic Proximity Pickups. A metallic protrusion connected to a cylinder passed one of these pickups once per revolution disturbing the magnetic field of the pickup and generating a voltage pulse.

In the linear shutter sampler, the time of sampling was determined accurately by means of a light beam shining through a small hole in

the shutter housing and impinging on a light sensitive voltaic cell. The hole was placed so that the shutter broke the light beam at the same instant the sample was taken.

A small neon bulb inside the Fastax provided the time correlation between the Fastax movie frames and the oscillograph record. A simple 60 Hz square wave generator (see Fig. B-1) provided the voltage to fire the neon bulb, thus exposing an interrupted streak along the edge of the film which could be accurately correlated with the square wave signal recorded on the oscillograph record.

Two Eagle Model HM Seven Channel Multiflex Reset Timers programmed the firing of the tunnel and sequential operation of all recorders, cameras, etc.

TRANSDUCERS

Stagnation Chamber Pressure

Originally the arc chamber stagnation pressure was measured with a Baldwin-Lima-Hamilton Type GP 10,000 psi bonded strain gage pressure transducer driven by a carrier amplifier. This transducer was later replaced by a Kistler Model 603H 15,000 psi piezoelectric transducer which has an unfiltered rise time of the order of 1 μsec. In addition to the faster transducer response time, the small physical size of the Kistler transducer and its seismic mass acceleration compensation make it possible to locate it approximately 6 in. closer to

the pressure source. The charge produced by the transducer was converted to voltage in a Kistler Model 566 Charge Amplifier. A Kintel Model 111 BF/ER-3107 Wideband DC Amplifier boosted this output to the level necessary (24 ma full scale) to drive the fluid damped galvanometer in the CEC Recorder.

It was found that the pressure curve resulting from the Kistler was approximately 1 msec faster (using fuse breakage, i.e. arc voltage rise, as a time reference) in rising than a typical pressure curve resulting from the Baldwin gauge; however, the pressure decay curves (from 10 msec to 30 msec) were quite similar and seemed to indicate that the Baldwin gauge suffered no lag time difficulties during this part of the run. Since this is the part of the run which has been considered the "good" part (after the arc has quenched) and which has thus been used for the major portions of any analysis, all previous data obtained with the Baldwin gauge were considered valid.

In the onset measurement phase of the program, a stagnation pressure measurement was made just upstream of the Mach 5 nozzle throat. This measurement was made with a Schaevitz-Bytrex Model HFH 5000 psi semiconductor strain gage pressure transducer. This model has a rise time in the μsec range and, in fact, is recommended for blast measurements as well as static pressure applications. The transducer was used in conjunction with a temperature compensation module and was driven by a carrier amplifier.

Pitot Pressures

At the exit of the Mach 25 nozzle the pitot pressure was approximately 12 psia. This allowed measurement with Hidyne variable reluctance transducers used in conjunction with carrier amplifiers.

A pitot pressure of approximately 600 psia at the exit of the Mach 5 nozzle was measured with a Kistler Model 601 piezoelectric transducer installed as shown in Fig. B-2. The electric charge produced by the transducer was converted to voltage in a Kistler Model 566 Charge Amplifier and boosted through a Kistler Model 567A Power Amplifier to the level necessary (24 ma) to drive the fluid damped galvo in the recorder.

The transducer was installed in a stiff support whose only connection with the pitot sting, besides the heavy arc chamber, was a pressure tube and was installed vertically so that the pressure sensing element was perpendicular to the expected axial vibration of the arc chamber. This was deemed necessary since the Model 601 transducer has no acceleration compensation.

The pitot (see Fig. B-3) was constructed of .125 in. O.D. stainless steel tubing with a .028 in. wall thickness. It was reduced to an outer diameter of .090 at the leading edge. This smaller diameter (.090 in.) was advisable due to the small exit diameter of the Mach 5 nozzle. A "debris catcher" was brazed onto the aft end of the pitot

after a small piece of mylar from the ruptured diaphragm entered and subsequently plugged the pitot during a preceding run (the photograph in Fig. B-2 was taken prior to this modification).

Static Pressures

The Mach 5 nozzle contained nine static pressure taps. The seven higher pressures were measured with Microsystems Model 1003 Pressure Transducers. These transducers are of the flush diaphragm type with semiconductor strain gages bonded directly to the diaphragm in a full-bridge circuit. The rise time of these transducers is again in the μsec range. They were all driven by carrier amplifiers.

The lower two pressures were measured with Hidyne W Series 30 psid transducers of the variable reluctance type. These transducers are very rugged and versatile with a rise time of less than 1 msec at the pressure encountered in this experiment. They also were driven by carrier amplifiers. A constant reference pressure of approximately 15 psig was applied to these transducers to increase their null or zero level to cause the transducers to operate closer to 0 psid in a more linear range.

Hidyne variable reluctance transducers were also used for all static pressure measurements taken in conjunction with the particle sampling phase of the program, in which the Mach 25 nozzle was used with a free jet vacuum test section. In all cases a high vacuum

reference was applied on one side of the diaphragm. Since this vacuum was kept below 2×10^{-3} torr (i.e., 0.2% of the minimum .02 psia encountered), the differential pressures measured by the Hidynes were considered to be absolute pressures. The pressures measured were:

Nozzle Exit Pressure

This pressure usually ranged from .03 to .07 psia during the useable part of a run. It was obtained with either a 0.1 psid Hidyne HR Series Transducer or a 0.25 psid Hidyne W Series Transducer whose output was amplified to give full scale galvo deflection at a pressure of 0.1 psid.

Receiver Pressure

This pressure, ranging from .02 to .07 psia, was initially measured with a 0.1 psid Ultradyne Model S-40 variable reluctance transducer. However, it was found that while Ultradyne claimed a rise time of 75-150 μsec, it was, in fact, closer to 10 msec. Subsequently 0.5 psid Hidyne P Series variable reluctance transducers were used. The output was amplified to give full scale galvo deflection at 0.1 psid. This series of transducers has been discontinued by Hidyne in favor of the more easily cleaned W Series; however, they seemed to perform very ably in this application.

Sampler Pressure

The sampler pressure was measured by two transducers—one set at .05 psia full scale and the other at 3 psia. This wide range was made

necessary by the rapid and extreme change in pressure (from .02 to approximately 1 psia) when the inside of the sampler was opened to atmospheric pressure at t ≐ 40 msec. Again Hidyne transducers were used—a 0.1 psid HR Series and a 3 psid W Series.

The above mentioned practice of using highly amplified high pressure transducers to measure low pressures is a common practice necessitated by economic factors. If a choice has to be made between purchasing a high or a low pressure transducer for general purposes, it must be considered that a high pressure transducer can measure low pressures through suitable amplification while the reverse is not true. In general it has been found that an amplification factor of 5 is obtainable without too many problems and a factor of 10 is possible. However, the higher the amplification, the less reliable the transducer signals become. Noise, calibration factor, and zero drift are the problems most frequently encountered in connection with this amplification. One of the major, contributing factors seems to be the heat generated by the excitation current passing through the transducer element resistance. Under the low pressures encountered there is no heat convection from the transducer casing and it becomes quite hot causing slight irregularities (such as zero shift) in the signal voltage. These become troublesome when highly amplified. Eventually an equilibrium is reached, but delaying a run to this point is not only inconvenient but also injects a degree of uncertainty into the pressure readings.

This uncertainty is due to the fact that during a run the ambient pressure—and therefore amount of heat convection from the transducer—varies considerably and rapidly. A possible solution to this problem would be the addition of water jackets around the transducers with water piped in and out through flexible tubing similar to that used for the transducer pressure connections. It is felt these could be made quite simple to fabricate and use, and would insure a constant temperature throughout calibration and the run.

Current and Voltage

Current measurement is made by means of a Halltron HR-31 Current Transducer. It is a solid state device producing a voltage proportional to the magnetic field generated by the current flowing through a nearby conductor and therefore proportional to that current.

The arc voltage is obtained from a small coil placed inside the hotshot main energy storage coil so that the collapsing magnetic field produces a current proportional to the arc voltage, L (di/dt).

CALIBRATION PROCEDURES

The calibration procedures for the pressure transducers were quite different for the two separate phases of the condensation program due to the use of the vacuum receiver tank in the particle collection phase. The transducers inside the vacuum tank were extremely inaccessible and as a result had to be calibrated in their installed position. The easiest way to accomplish this was by simply varying

the vacuum in the tank from 0 to atmospheric pressure while maintaining a high vacuum reference on one side of the differential pressure transducer. The main difficulty in this method lay in the fact that all transducers (including those with a sensitive 0.1 psid range) would be subjected to these pressures. Therefore to keep from overpressuring some transducers while calibrating others, a bypass system had to be incorporated. Figure B-4 shows a schematic of this reference-bypass system. When higher capacity pressure transducers were being calibrated, the sensitive transducers and low pressure manometers were closed to the high vacuum reference and bypassed to vacuum tank pressure on both sides.

The high vacuum reference system consists of a chamber of approximately 0.3 ft^3, a small CVC water cooled diffusion pump and a mechanical pump. A McLeod gauge with a refrigerated trap acts as a primary reference while an NRC Alphatron Type 530 Vacuum Gauge serves as a continuous monitor of reference vacuum. This reference was kept at or below 2×10^{-3} torr and thus for all practical purposes could be assumed to be an absolute zero reference.

Three manometers were used for calibration purposes:

1. A mercury filled U-tube manometer was used for all calibrations above 1 psid. A 1 in. column of dibutylphthalate was introduced into each leg of the mercury manometer and

served to keep the tube clean, provide a clear mercury meniscus, and raise the pressure at the meniscus above the vapor pressure of the mercury.

2. A U-tube manometer filled with dibutylphthalate served as a calibration standard for pressures below 1 psid.
3. An inclined manometer using dibutylphthalate as the indicating fluid could be used at pressures below 0.2 psid; however, this manometer was rarely employed due to its extremely slow response time.

Since the Mach 5 nozzle exhausted to atmosphere, the calibration technique used on its two Hidyne transducers was much simpler and amounted merely to applying a pressure on the "high" side of the transducer and measuring the pressure with a deadweight calibrated bourdon tube gauge.

All of the strain gage transducers (Microsystems, Schaevitz-Bytrex, and Baldwin-Lima-Hamilton) were calibrated on a deadweight tester (Ashcroft Model 1305-B-50). At this time reference calibration signals were applied to the amplifiers so they could later be used alone to determine the calibration of the amplifier system by itself. Thus, if the sensitivity of the transducer remained constant, the application of this reference calibration signal would be sufficient to calibrate the complete transducer system. This, in fact, was found to be the case by repeated deadweight calibrations.

The Kistler transducers were calibrated in much the same way using the deadweight tester and nulling the transducer output with an external voltage source. In this way a voltage vs. pressure curve can be obtained and subsequent voltage applications suffice for a very accurate calibration. This is the procedure recommended by Kistler Corporation and was found to work extremely well. Subsequent deadweight calibrations gave voltage-pressure curves which agreed within 2.3%.

All calibrations were made as close to the run as procedures permitted and when possible both pre-run and post-run calibrations were made.

ESTIMATE OF EXPERIMENTAL ERROR

CEC Recording Errors

The CEC traces recorded during an actual run can be read to $\pm$ .02 in. or $\pm$ 1% of full scale (2 in.) deflection. It should be noted that as the pressure decays, the possible percentage error increases due to the fixed reading error. Thus, when the pressure is sufficient to deflect the galvo full scale the reading error will be $\pm$ 1.0%, while at 1/4 full scale deflection, the error will be 4.0%.

The galvanometer was considered absolutely accurate in recording the current flowing through it. This conclusion was reached on the basis of unrecorded day by day experience in their use. CEC specifies a flat frequency response to within 5% up to 2500 Hz for the galvos

used. By exercising care in providing the galvo with a proper amount of electrical damping, this figure can be reduced to 2% up to 2800 Hz. Since most of the signals measured could be considered to be d.c. and even the most rapidly varying signals were in the vicinity of only 1000 Hz, it was assumed that the frequency response was perfectly flat.

Pressure Measurements

The stagnation pressure Kistler transducer was found to vary less than 2.3% over all calibrations and was therefore considered repeatable within this limit, or in other words, to have a "system calibration error" of $\pm$ 1.15%. This error would have to be added to the CEC "reading error."

The pitot pressure Kistler transducer was found to be accurate to within $\pm$ 1% on calibrations, while the Schaevitz-Bytrex transducer remained within an error range of $\pm$ 2%.

When the Baldwin transducer was used, it was pressure calibrated before each run and was considered to have a system calibration error of $\pm$ 1%.

The Microsystems transducers exhibited various system calibration errors as follows:

Transducer No.	Pressure Range	Error
3	0-100 psi	$\pm$ 3.2% of reading
4	0-100 psi	$\pm$ 1.7% of reading
5	0-200 psi	$\pm$ 1.9% of reading

6	0-300 psi	± 1.7% of reading
7	0-1000 psi	± 2.5% of reading
8	0-1000 psi	± 4.1% of reading
9	0-2500 psi	± 3.0% of reading

The Hidyne transducers were considered to have a possible system calibration error of ± 5% of full scale reading. This figure was arrived at on the basis of continued use and experience with these transducers. The major factors contributing to this large error estimate are excitation current heating effects and hysteresis. The heating effects are discussed above in the section on static pressure transducers. The hysteresis effect which could be calibrated statically, cannot be determined in a dynamic situation without more sophisticated dynamic calibration methods and equipment, and thus had to be estimated.

APPENDIX C. SAMPLING AND ELECTRON MICROSCOPE TECHNIQUES

SAMPLER DESIGN AND DEVELOPMENT

The particles entering the sampler had to be decelerated, prior to "catching" them, in some way which would decrease their kinetic energy while keeping their temperature low enough to prevent revaporization. The very narrow slit at the leading edge of the sampler (shown in Fig. C-1) produced a narrow free jet just inside the sampler. The entrance slit in the housing was large compared to the radius of curvature of the razor blades used as beam splitters. Figure C-2 shows a photomicrograph of a cross section of the razor blade. It can be seen that the radius of curvature of the edge was less than 2.4×10^{-5} in., which, when compared to the minimum slit opening used (6×10^{-3} in.), was small enough to be considered perfectly sharp. The included angle presented to the flow was 45° (i.e., the flow impinging on the sampler was required to deflect 22.5°), and the minimum Mach number for a maximum turning angle of 22.5° is only 2.3 (in helium). As a result of this there was no possibility of the starting shock's not being swallowed when the sampler pressure is controlled. By matching the ambient pressure in the sampler to the static pressure of the jet, the jet was perfectly expanded, thus eliminating the possibility of strong shocks. Since the Reynolds number at the sampler inlet was of order 500 (based on the slit width), it was reasonable to assume a turbulent jet[C1]. As the jet issued into the quiescent surrounding gas, it was decelerated gradually by turbulent viscous mixing. The particle collection was accomplished approximately 750 "slit-widths" downstream of the entrance slit.

Abramovich[C2] outlines a method for determining the variation in velocity and temperature along the axis of a nonisothermal, two-dimensional, compressible gas jet in a stationary medium. This is a semi-empirical method in which Abramovich uses a "mixing length" to arrive at a general equation for jet spreading, the constants for the equation being supplied from experiment. Experimental data of various researchers confirm the "universality" of profiles of dimensionless velocity and stagnation temperature in turbulent compressible jets. Abramovich matched polynomials to these experimental profiles and, using the empirical jet spreading equation, obtained his results. His procedure when applied to axially symmetric jets has been verified experimentally to be quite accurate as far as 100 diameters downstream.

His method was used, with one modification, to determine the velocity and temperature variation along the axis of the jet in the sampler. The modification consisted of using a density ratio ($\overline{\rho} = \rho_{amb}/\rho_{jet}$), in preference to Abramovich's temperature ratio ($\theta = T_{jet}/T_{amb}$), to include the effect of the heavy zinc particles in the helium flow (his temperature ratio was derived from a density ratio by assuming matching pressures and molecular weights). A further assumption was that the jet was perfectly expanded (i. e. , $p_{jet} = p_{amb}$) in the sampler (even though at times there was some deviation from this condition).

These assumptions, coupled with the extrapolation to 750 "diameters" (approximately five times the verified region of validity), certainly open

the method to question. However, since the substitution of $\overline{\rho}$ for θ is a conservative assumption (i. e., the use of $\overline{\rho}$ instead of θ leads to a higher velocity at any given point) and, since the extrapolation is over the region where velocity and temperature are varying least, it is felt that the results should be indicative of the physical situation.

As an indication of the validity of substituting $\overline{\rho}$ for θ in the equations, a comparison was made against a solution found by Abramovich for a two phase jet of atomized water in air. Abramovich's solution directly accounted for the solid particles but was necessarily extremely idealized in all other respects and was also very difficult and tedious. A solution of the same problem, ignoring the solid particles but using $\overline{\rho}$ in place of θ, agreed perfectly with his solution (see Fig. C-3), indicating that substitution of $\overline{\rho}$ for θ effectively accounts for the solid particles in the flow.

Figure C-4 shows the results obtained for the sampler using this method. For a typical set of chamber conditions the upper curves give the temperature and velocity (both non-dimensionalized by their initial values) as a function of the number of "slit-widths" downstream of the entrance slit. The lower plot shows a family of curves which represent the amount of zinc which would be revaporized by passing through a normal shock at the given location (it was assumed just enough zinc would revaporize to saturate the mixture downstream of the shock). It can be seen that the particles are effectively decelerated when the receiver

pressure is matched to the jet pressure (i. e., $p_{amb} = p_{jet} \doteq 900\ \mu$ Hg). However, if the ambient pressure were kept quite low there would not be sufficient viscous deceleration, and subsequent strong shocks, particle revaporization, and mica tape damage would probably result. This expected result was confirmed by Fastax photographs of the region immediately in front of the sampling cylinder. (A window in the bottom of the sampler was used to obtain the photographs.) In one run with ambient pressure held to less than 5μ Hg, emitted light from this region indicated the presence of a strong shock. The mica tape in this run suffered severe damage (craters and holes), and no particles, as such, were distinguishable. No emitted light was detectable when the pressure was raised to approximately $900\,\mu$ Hg.

Due to the large amount of zinc in the flow, the particles had to be collected over a very short period of time and spread over a large area to enable analysis by means of a transmitted beam electron microscope. To accomplish this, a rotating cylinder collector was used in conjunction with a shutter arrangement.

Two different types of shutters were used; a solenoid actuated linear shutter and a rotating shutter. In both, the principle was quite similar to the focal plane shutter used in a camera.

Linear Shutter

Figure C-5 shows a schematic of the experimental arrangement used with this shuttering technique.

An aluminum shutter moved vertically in a triangular shaped housing. Both the shutter and the housing had openings in them which, when aligned, allowed the flow to pass through and impinge on the collector cylinder.

Figures C-6 and C-7 show a mica tape just after a hotshot. In Fig. C-6 the tape is still attached to the cylinder collector and in Fig. C-7 it has been removed and labeled for electron microscope analysis. In this particular run the density of the collected zinc particles was too high to be analyzed in the dark region (it was generally found that if the deposit could be seen by the naked eye, it was too dense for analysis). However the pictures give an excellent example of the pattern left by the impinging zinc particles.

There were two inherent disadvantages in this shuttering arrangement: (1) only one collection could be made during each run and (2) only 1/4 in. (the length of the opening in the shutter housing) of the flow was sampled (i. e. these eliminated a location-resolved, time-resolved sampling of the beam and resulted in only one point of information in time and location for each run). A rotating shutter arrangement circumvented both of these disadvantages and in addition provided a much "cleaner" inlet configuration.

Rotating Shutter

The rotating shutter design allowed a sampling across the entire width of the jet while collecting particles at several distinct times during the run and therefore at different stagnation conditions. Figure

C-1 is a schematic of this sampling apparatus. Two concentric cylinders—a hollow exterior "shutter" cylinder with two opposite openings extending the full axial length, and a solid interior "collector" cylinder with attached sampling tape—were driven through a gear arrangement by a 12 volt d.c. motor. The gear sizes were selected to give a collector speed of 5 1/4 times that of the shutter. In this way the deposits of zinc on the inner cylinder were spaced 225^{o} apart allowing eight spaced deposits before there was any overlap (see Fig. C-8). Since the shutter rotated at approximately 3000 rpm, this allowed 80 msec of run time before overlapping occurred.

At 30 msec the arc chamber relief dump valve opened ending the useful part of the run. Although the stagnation pressure dropped quite sharply at this time, flow out of the chamber continued for a long period of time. To prevent this undesired flow from entering the sampler and causing "overlap" on previously collected samples, the interior pressure of the sampler was increased immediately following the run (i.e. at 40 msec). This was accomplished by connecting the sampler with the atmospheric pressure outside the vacuum tank and controlling the flow through this line with a solenoid actuated vacuum valve. The arc voltage trace was used as a time reference by employing this voltage (obtained from a small coil placed inside the hotshot main power coil)

as trigger input to a single beam, dual time base Tektronix Oscilloscope, Model 545A. The scope then produced two gate signals; one (gate B) was concurrent with the input voltage and the other (gate A) could be delayed any desired amount. This gate B voltage was used as input to a simple silicon-controlled rectifier circuit (see Fig. C-9) which switched current to the valve solenoid. As the response time of the solenoid valve was approximately 40 msec, the pressure in the housing started to rise immediately following the run. This created a reverse flow out of the inlet slit and prevented the contamination of the sampler interior.

The system was found to be very efficient when, on one run, the valve triggered prematurely opening the sampler to atmospheric pressure prior to the start of the run. The resulting perfectly clean sample tape proved the blockage efficiency of the interior pressure to the flow.

A plenum in the form of a 4 in. diameter x 30 ft long tube opened into the rear of the sampler. This extra volume was sufficient to prevent the entering gas sample from raising the pressure inside the housing during the first 40 msec.

ELECTRON MICROSCOPE TECHNIQUES

When the particles collected are too small to be seen under an optical microscope, an electron microscope must be employed. The instrument used was of the transmitted beam type where the beam must

pass through the surface to be examined. At least part of the surface must then be transparent to the beam. As mentioned earlier, in the case of the examination of small particles, the collection must then be sparse.

The procedure employed was based on the use of mica strips as a supporting surface. The mica was cleaved along lattice surfaces so that it was microscopically smooth and very thin. It was placed in an evaporator where a layer of carbon approximately 160 $\mathring{A}$ thick was deposited on it by evaporation and surface condensation at very low pressure. Such a carbon film was transparent to the electron beam. A much thicker layer would have been opaque, while a much thinner layer would have been structurally weak. The carbon coated mica was fastened to the collection cylinder in the sampler by means of tape with adhesive on both sides.

After the particles were collected, the mica strip was placed back in the evaporator where the surface was "shadowed" by evaporation of a thin film of chromium deposited at an angle to the surface. Chromium is opaque to the electron beam so that the shadows created permitted three-dimensional analysis of the particles photographed. The higher a particle stood above the collection surface, the longer was the shadow.

Copper grids consisting of a 1/8 in. diameter ring with a copper gauze or mesh mounted on it provided the ultimate support for the film to be examined in the electron microscope. The film, consisting of carbon layer plus particles plus chromium layer, was removed from each

piece of the mica, which had been cut to grid size, by floating it off the mica in water. As the film floated on the water a copper grid was placed under it and the specimen was ready to be placed in the microscope and photographed.

The above procedure was developed after several other approaches were first used. Instead of mica, a layer of Biodine, and earlier a layer of collodion were used. These support surfaces had two disadvantages. They were difficult to remove from the carbon film, since it had to be removed by dissolving in an extractor, and in addition, both of these backings yielded a rough background surface so that very small particles might not have been detected.

The use of the copper grids, coated with carbon, directly mounted on the sampler met with virtually no success, primarily because of the difficulty of keeping the grids glued to the sampler surface. The carbon films with no back support except the copper grid also tended to tear.

APPENDIX D. DERIVATION AND SOLUTIONS OF THE SATURATED EQUILIBRIUM EXPANSION EQUATIONS

NOMENCLATURE

$\bar{A}$	area ratio (A/A_{throat})
a	matrix element defined by Eq. (D. 9)
B	vapor saturation curve constant (Eq. (D. 18))
C_p	specific heat at constant pressure
f	mass fraction of inert carrier gas
L	latent heat (of vaporization or sublimation depending upon T)
$\dot{m}$	mass flow rate per unit of throat area
p	pressure
q	mass fraction of uncondensed vapor
R	universal gas constant
T	temperature
u	velocity
α	ratio of molecular weights (μ_v/μ_a)
β	parameter defined by Eq. (D. 25)
Γ	parameter defined by Eq. (D. 24)
γ	specific heat ratio
Δ	determinant of [A] matrix in Eq. (D.9)
δ	parameter defined by Eq. (D. 26)
θ	parameter defined by Eq. (D. 20)
μ	molecular weight

ξ	parameter defined by Eq. (D. 26)
ρ	density
ϕ	integration constant defined by Eq. (D. 13)

Subscripts

a	property of inert carrier gas
i	property at some known reference point (e. g. saturation point)
c	property defined at chamber conditions
v	property of condensible vapor

Superscripts

	derivative with respect to T

Wegener and Mack[D1] derive the one-dimensional equilibrium flow equations for a two-component mixture of a condensable vapor in an inert carrier gas. The simplifying assumptions are: (1) the condensed phase is uniformly distributed throughout the expanding two-component mixture, (2) the condensed phase has the same velocity and temperature as the mixture, (3) the gaseous components are assumed thermally and calorically perfect, (4) the flow is considered to be steady, and (5) the density of the condensed phase is much greater than the density of the vapor phase allowing neglect of its volume. The equations are, as usual, the conservation equations and the equation of state; but an added equation is necessary in this case due to the added variable associated with the unknown amount of condensate. This equation may be supplied by the requirement that the condensable vapor and its condensed phase remain in equilibrium (i.e., the vapor must expand along its coexistence or saturation curve). The Clausius-Clapeyron equation for this saturation curve, used in conjunction with Dalton's Law to relate the partial pressures, supplies the necessary relationship.

RUNGE-KUTTA NUMERICAL INTEGRATION

The full set of equations in their differential form are:

Conservation of Mass: $$\frac{d\rho}{\rho} + \frac{du}{u} + \frac{d\bar{A}}{\bar{A}} = 0 \qquad \text{(D.1)}$$

Conservation of Momentum: $$u\,du + \frac{dp}{\rho} = 0 \qquad \text{(D.2)}$$

Conservation of Energy:

$$u\,du + C_{p_c}\,dT - d[L(1 - f - q)] = 0 \qquad \text{(D. 3)}$$

Equation of State:

$$\frac{dp}{p} - \frac{d\rho}{\rho} - \frac{dT}{T} - \frac{dq}{q + f\alpha} = 0 \qquad \text{(D. 4)}$$

Clausius-Clapyron Equation:

$$\frac{dp_v}{p_v} - \frac{L\mu_v}{RT}\frac{dT}{T} = 0 \qquad \text{(D. 5)}$$

Dalton's Law:

$$p_v = \frac{q}{q + f\alpha}\,p \qquad \text{(D. 6)}$$

or,

$$\frac{dp}{p} - \frac{dp_v}{p_v} + \frac{dq}{q}\,\frac{f\alpha}{q + f\alpha} = 0 \qquad \text{(D. 7)}$$

Equation (D. 7) combines readily with Eq. (D. 5) and the singularity at $q = 0$ (indicating complete condensation of the vapor phase) is removable by multiplying through by q:

$$q\,\frac{dp}{p} - q\,\frac{L\mu_v}{RT}\,\frac{dT}{T} + f\alpha\,\frac{dq}{q + f\alpha} = 0 \qquad \text{(D. 8)}$$

Relating these differentials to an increment of area ratio $d\bar{A}$ and using the notation $(\ )' \equiv d(\ )/d\bar{A}$, Eq. (D. 1)-(D. 4), and (D. 8) form a set of five ordinary nonlinear differential equations. Expressed in matrix form these equations are:

$$\begin{bmatrix} 0 & 0 & a_{13} & a_{14} & 0 \\ a_{21} & 0 & 0 & a_{24} & 0 \\ 0 & a_{32} & 0 & a_{34} & a_{35} \\ a_{41} & a_{42} & a_{43} & 0 & a_{45} \\ a_{51} & a_{52} & 0 & 0 & a_{55} \end{bmatrix} \begin{bmatrix} p' \\ T' \\ \rho' \\ u' \\ q' \end{bmatrix} = \begin{bmatrix} -\frac{1}{A} \\ 0 \\ 0 \\ 0 \\ 0 \end{bmatrix} \qquad \text{(D. 9a)}$$

where:

$$a_{13} = \frac{1}{\rho} \qquad a_{14} = \frac{1}{u}$$

$$a_{21} = \frac{1}{\rho} \qquad a_{24} = u$$

$$a_{32} = C_{p_c} - (1 - f - q)\frac{dL}{dT} \qquad a_{34} = u \qquad a_{35} = L \qquad \text{(D. 9b)}$$

$$a_{41} = \frac{1}{p} \qquad a_{42} = -\frac{1}{T} \qquad a_{43} = -\frac{1}{\rho} \qquad a_{45} = -\frac{1}{q + f\alpha}$$

$$a_{51} = \frac{q}{p} \qquad a_{52} = -\frac{qL\mu_v}{RT^2} \qquad a_{55} = \frac{f\alpha}{q + f\alpha}$$

This set of equations can be solved by determinants to give:

$$p' = -\frac{1}{A\Delta}(a_{24}\,a_{32}\,a_{43}\,a_{55} - a_{24}\,a_{35}\,a_{43}\,a_{52})$$

$$T' = -\frac{1}{A\Delta}(a_{21}\,a_{34}\,a_{43}\,a_{55} + a_{24}\,a_{35}\,a_{43}\,a_{51})$$

$$\rho' = -\frac{1}{A\Delta}(a_{21}\,a_{34}\,a_{45}\,a_{52} + a_{24}\,a_{32}\,a_{45}\,a_{51} + a_{24}\,a_{35}\,a_{41}\,a_{52} - a_{21}\,a_{34}\,a_{42}\,a_{55} - a_{24}\,a_{32}\,a_{41}\,a_{55} - a_{24}\,a_{35}\,a_{42}\,a_{51}) \quad \text{(D.10)}$$

$$u' = -\frac{1}{A\Delta}(a_{21}\,a_{35}\,a_{43}\,a_{52} - a_{21}\,a_{32}\,a_{43}\,a_{55})$$

$$q' = -\frac{1}{A\Delta}(-a_{21}\,a_{34}\,a_{43}\,a_{52} - a_{24}\,a_{32}\,a_{43}\,a_{51})$$

where Δ is the determinant of the A matrix.

When arranged in this manner, the equations are very amenable to solution by a Runge-Kutta method numerical integration on a digital computer. The initial conditions may be supplied most easily at the saturation point, but, of course, may be furnished at any arbitrary starting point such as downstream of a condensation "shock".

(Note: A minor problem occurs at the triple point where the latent heat has a discontinuity due to the heat of fusion (see Fig. D-1). This difficulty was circumvented by approximating the discontinuity by a ramp function and cutting the integration step size in that region by an order of magnitude for a slow integration through this ramp.)

The major disadvantage of this type of solution lies in the necessity of integrating all the way from a known point to obtain the flow parameters at any downstream point (i.e. it is necessary to solve the equations along the complete nozzle to obtain the exit conditions).

ANALYTICAL SOLUTION FOR CONSTANT LATENT HEAT

If the latent heat can be considered constant, the momentum and energy equations may be analytically integrated as pointed out by Goldin[D2]. Combining Eq. (D.2)-(D.4), and (D.8) and rearranging gives:

$$\frac{T\,dq - q\,dT}{T^2} = f\alpha\frac{dT}{T^2} - \frac{C_{p_c}}{L}\frac{dT}{T} - \frac{Rf}{\mu_a L}\frac{dq}{q} \qquad (D.11)$$

The left-hand side of this equation may be recognized as the differential of q/T. Thus, integrating Eq. (D.11) and evaluating the constant of integration ϕ at any point i where both T and q are known (such as the saturation point), gives:

$$\phi T + \frac{C_{p_c}}{L} T \ln T + \frac{Rf}{\mu_a L} T \ln q + q + f\alpha = 0 \qquad (D.12)$$

where

$$\phi = -\frac{1}{T_i}(q_i + f\alpha) - \frac{C_{p_c}}{L}\ln T_i - \frac{Rf}{\mu_a L}\ln q_i \qquad (D.13)$$

Equation (D. 1) is still available to determine the relationship to nozzle flow. In integrated form it is

$$\rho u \overline{A} = \dot{m} \tag{D. 14}$$

Integrating Eq. (D. 3) for a constant L and evaluating the constant of integration at stagnation conditions gives

$$u = \sqrt{2[C_{p_c} (T_c - T) + L (1 - f - q)]} \tag{D. 15}$$

The integrated equation of state,

$$p = (q + f\alpha) \rho \frac{R}{\mu_v} T \tag{D. 16}$$

combines with Eq. (D. 6) to give

$$p_v = q \rho \frac{R}{\mu_v} T \tag{D. 17}$$

which is recognizable as simply the equation of state of the uncondensed vapor phase.

Integration of the Clausius-Clapyron equation produces a constant of integration B which is a property of the vapor and must be determined by experimental vapor pressure data. The integrated equation is then

$$p_v = \exp\left(B - \frac{L\mu_v}{RT}\right) \tag{D. 18}$$

Combining Eq. (D.14), (D.15), and (D.17), and squaring gives a quadratic equation in q which can be solved to yield:

$$q = -\frac{L}{\theta} + \sqrt{\frac{L^2}{\theta^2} + \frac{2}{\theta}\left[C_{p_c}(T_c - T) + L(1 - f)\right]} \qquad (D.19)$$

where

$$\theta = \left(\frac{\dot{m}RT}{\mu_v p_v \bar{A}}\right)^2$$

or, using Eq. (D.18),

$$\theta = \left(\frac{\dot{m}RT}{\mu_v \bar{A}}\right)^2 \exp\left[2\left(\frac{L\mu_v}{RT} - B\right)\right] \qquad (D.20)$$

By combining Eq. (D.12) and (D.19), a single transcendental equation in T and $\bar{A}$ results, which may be solved by an iterative numerical technique or by graphing:

$$\frac{C_{p_c}}{L} T \ln\frac{T}{T_i} + \frac{Rf}{\mu_a L} T \ln\left\{\frac{-L + \sqrt{L^2 + 2\theta\left[C_{p_c}(T_c - T) + (1 - f)L\right]}}{q_i \theta}\right\}$$

$$+ q + f\alpha - \frac{T}{T_i}(q_i + f\alpha) = 0 \qquad (D.21)$$

SIMPLIFIED SOLUTION FOR FULLY CONDENSED FLOW

Downstream of the condensation regime (i.e. for very small values of q), an approximate explicit solution for T as a function of $\bar{A}$ exists. This "fully-condensed" regime may be defined as one in which the following relations hold:

$$\frac{q}{f\alpha} \ll 1 \quad , \quad \frac{L^2}{\theta} \ll 1 \quad , \quad \frac{T^2}{\left[T_c + \frac{(1-f)\,L}{C_{p_c}}\right]^2} \ll 1 \tag{D.22}$$

Using the first two assumptions, algebraic manipulation on Eq. (D.21) yields:

$$T = \left\{ \frac{\mu_v \sqrt{2\left[C_{p_c}\,(T_c - T) + L\,(1-f)\right]}}{q_i\,\dot{m} R T_i^{\Gamma} \exp\left[\frac{L\mu_v}{RT_i}\left(\frac{q_i + f\alpha}{f\alpha}\right) - B\right]}\,\bar{A} \right\}^{1/(1-\Gamma)} \tag{D.23}$$

where

$$\Gamma = \frac{\gamma_a}{\gamma_a - 1} + \frac{1-f}{f\alpha}\frac{\gamma_v}{\gamma_v - 1} \tag{D.24}$$

Letting,

$$\beta = \left\{ \frac{\mu_v \sqrt{2\left[C_{p_c}\,T_c + (1-f)\,L\right]}}{q_i\,\dot{m} R T_i^{\Gamma} \exp\left[\frac{L\mu_v}{RT_i}\left(\frac{q_i + f\alpha}{f\alpha}\right) - B\right]}\,\bar{A} \right\}^{1/(1-\Gamma)} \tag{D.25}$$

Eq. (D. 23) can be written:

$$T = \beta \left[1 - \frac{T}{T_c + \frac{(1 - f)\, L}{C_{p_c}}} \right]^{1/[2(1-\Gamma)]}$$

The second term on the right-hand side may be expanded in a binomial series. Letting,

$$\delta = \frac{T}{T_c + \frac{(1 - f)\, L}{C_{p_c}}} \quad , \quad \xi = \frac{1}{2(1 - \Gamma)} \tag{D. 26}$$

the series becomes:

$$(1 - \delta)^{\xi} = 1 - \xi\delta + \frac{\xi(\xi - 1)}{2!}\delta^2 - \frac{\xi(\xi - 1)(\xi - 2)}{3!}\delta^3 + \ldots$$

If the last of the assumptions (Eq. (D. 22)) is now made, then δ is small enough that the terms of order greater than 1 may be neglected, and

$$(1 - \delta)^{\xi} \doteq 1 - \xi\delta$$

or,

$$\left[1 - \frac{T}{T_c + \frac{(1 - f)\, L}{C_{p_c}}} \right]^{1/[2(1-\Gamma)]} \doteq 1 - \frac{T}{2(1 - \Gamma)\left[T_c + \frac{(1 - f)\, L}{C_{p_c}} \right]}$$

Substituting back into Eq. (D.23) and simplifying, the equation for T becomes, finally:

$$T = \left\{ \left[\frac{\mu_v \sqrt{2[C_{p_c} T_c + (1 - f) L]}}{q_i \dot{m} R T_i^{\Gamma} \exp\left[\frac{L\mu_v}{RT_i} \left(\frac{q_i + f\alpha}{f\alpha} \right) - B \right]} \bar{A} \right]^{1/(\Gamma-1)} + \frac{1}{2(1 - \Gamma) \left[T_c + \frac{(1 - f) L}{C_{p_c}} \right]} \right\}^{-1} \tag{D.27}$$

Of course, far downstream of onset, when the temperature becomes so small that it may be neglected completely in relation to $[T_c + (1 - f) L/C_{p_c}]$, the equation becomes simply

$$T = \left\{ \frac{\mu_v \sqrt{2[C_{p_c} T_c + (1 - f) L]}}{q_i \dot{m} R T_i^{\Gamma} \exp\left[\frac{L\mu_v}{RT_i} \left(\frac{q_i + f\alpha}{f\alpha} \right) - B \right]} \bar{A} \right\}^{1/(1-\Gamma)} \tag{D.28}$$

APPENDIX E. DERIVATION AND SOLUTION OF DISCONTINUOUS CONDENSATION OR VAPORIZATION EQUATIONS

NOMENCLATURE

B	vapor saturation curve constant
C_p	specific heat at constant pressure
f	mass fraction of inert carrier gas
L	latent heat (of vaporization or sublimation depending upon T)
p	pressure
q	mass fraction of uncondensed vapor
R	universal gas constant
T	temperature
u	velocity
α	ratio of molecular weights (μ_v/μ_a)
γ	specific heat ratio
μ	molecular weight
ρ	density
Φ	parameter defined by Eq. (E. 6)

Subscripts

a	property of inert carrier gas
c	property defined at chamber conditions
v	property of condensable vapor
1	property defined just upstream of discontinuity
2	property defined just downstream of discontinuity

The "condensation shock" solution is treated by Wegener and Mack[E1] for a one component flow. The solution given here, while being similar in principle, is necessarily different in execution due to the fact that it is for a mixture of two gases, one condensable and one inert. Also, the solution has been kept perfectly general to allow its use for either a "condensation jump" (a discontinuous heat addition through condensation) or a "vaporization shock" (a discontinuous heat subtraction in conjunction with a normal shock).

The solution assumes: (1) the flow is steady and one-dimensional, (2) the gaseous components are thermally and calorically perfect, (3) in the two phase mixture, the particles and gaseous components have equal temperatures and equal velocities, and (4) the density of the condensed phase is much greater than the density of the gaseous phase allowing neglect of its volume, and (5) the latent heat is constant.

The governing equations are simply the difference equations across a discontinuity at constant area:

Conservation of Mass:
$$\rho_1 u_1 = \rho_2 u_2 \tag{E.1}$$

Conservation of Momentum:
$$p_1 + \rho_1 u_1^2 = p_2 + \rho_2 u_2^2 \tag{E.2}$$

Conservation of Energy:
$$C_{p_c} T_1 + \frac{u_1^2}{2} + q_1 L = C_{p_c} T_2 + \frac{u_2^2}{2} + q_2 L \tag{E.3}$$

Equation of State:

$$p_2 = (f + q_2)\,\rho_2 \frac{R}{\mu_2} T_2 \tag{E.4}$$

A simultaneous solution of these equations yields:

$$p_2 = \frac{-\Phi_2 \pm \sqrt{\Phi_2^{\,2} - 4\Phi_1\Phi_3}}{2\Phi_1} \tag{E.5}$$

where,

$$\Phi_1 = \frac{1}{2\rho_1^{\,2} u_1^{\,2}}\left[1 - \frac{2\gamma_c}{\gamma_c - 1}\left(\frac{1 - f + f\alpha}{q_2 + f\alpha}\right)\right]$$

$$\Phi_2 = \frac{p_1 + \rho_1 u_1^{\,2}}{\rho_1^{\,2} u_1^{\,2}}\left[\frac{\gamma_c}{\gamma_c - 1}\left(\frac{1 - f + f\alpha}{q_2 + f\alpha}\right) - 1\right] \tag{E.6}$$

$$\Phi_3 = \frac{(p_1 + \rho_1 u_1^{\,2})^2}{2\rho_1^{\,2} u_1^{\,2}} - C_{p_c} T_1 - \frac{u_1^{\,2}}{2} - (q_1 - q_2)\,L$$

In Eq. (E.5) the sign of the radical will be (+) if the discontinuity contains only condensation or evaporation and (-) if a normal shock is also present. The stagnation chamber value of the specific heat ratio γ_c can be evaluated from the relationship given by Goldin[E2]:

$$\gamma_c = \gamma_v\left[\frac{\frac{\gamma_a}{\gamma_v}\left(\frac{\gamma_v - 1}{\gamma_a - 1}\right) f\alpha + 1 - f}{\left(\frac{\gamma_v - 1}{\gamma_a - 1}\right) f\alpha + 1 - f}\right] \tag{E.7}$$

A simultaneous solution of Eq. (E. 1), (E. 2), and (E. 4) yields T_2:

$$T_2 = \frac{\mu_v p_2 (p_1 - p_2 + \rho_1 u_1^2)}{R \rho_1^2 u_1^2 (q_2 + f\alpha)} \tag{E.8}$$

The downstream mass fraction of zinc vapor q_2 can be supplied by requiring that the flow return to saturated equilibrium downstream of the discontinuity. The integrated Clausius-Clapyron relationship between the pressure and temperature of a saturated vapor, used in conjunction with Dalton's Law of partial pressures yields the equation for satisfying this condition:

Clausius-Clapyron Equation:
$$p_{2_\infty} = \exp\left(B - \frac{L\mu_v}{RT_2}\right) \tag{E.9}$$

Dalton's Law:
$$p_{2_v} = \frac{q_2}{q_2 + f\alpha} p_2 \tag{E.10}$$

A solution may now be found by solving Eq. (E. 5), (E. 8), (E. 9), and (E. 10) for incremental jumps of q_2 until $p_{2_v} = p_{2_\infty}$, a simple task using any digital computer.

When the discontinuity is a normal shock in a condensed flow whose stagnation conditions are superheated, total revaporization may be expected. In this case the solution is closed form since $q_2 = 1 - f$, and p_2 is thus specified completely in terms of the upstream properties.

Note: If it is desired to release the assumption of constant latent heat, Eq. (E. 3), (E. 6), and (E. 9) must be changed in the above discussion:

$$C_{p_c} T_1 + \frac{u_1^2}{2} - (1 - f - q_1) L_1 = C_{p_c} T_2 + \frac{u_2^2}{2} - (1 - f - q_2) L_2 \qquad (E.3')$$

$$\Phi_3 = \frac{(p_1 + \rho_1 u_1^2)^2}{2\rho_1^2 u_1^2} - C_{p_c} T_1 - \frac{u_1^2}{2} - q_1 L_1 + q_2 L_2 + (1 - f)(L_1 - L_2) \qquad (E.6')$$

$$P_{2_\infty} = \exp B - \frac{L_2 \mu_v}{R T_2} \qquad (E.9')$$

In addition to incrementing q_2 until $P_{2_v} = P_{2_\infty}$, the solution now requires that at each increment of q_2 some type of iteration be performed on L_2 since $L_2 = L(T_2)$ and L_2 must be used in the calculation of T_2.

APPENDIX F. EQUATIONS FOR THE COMPUTER SOLUTION OF NON-EQUILIBRIUM CONDENSATION

NOMENCLATURE

A	Nozzle area
A_t	Area of throat
C_L	Specific heat of liquid
C_p	Initial average specific heat of mixture
Cp_c	Specific heat at constant pressure of carrier gas
Cp_v	Specific heat at constant pressure of vapor
Cv_c	Specific heat at constant volume of carrier gas
Cv_v	Specific heat at constant volume of vapor
E_{ic}	The energy of the carrier molecules impinging on a liquid drop
E_{iv}	The energy of the vapor molecules impinging on a liquid drop
ΔE	The net increase in energy between reflected and impinging molecules striking a liquid drop
ΔE_c	The net increase in energy between the reflected and impinging carrier molecules striking a liquid drop
ΔE_v	The net increase in energy between the reflected and impinging vapor molecules striking a liquid drop
f	The fraction of vapor molecules which strike a liquid drop that condenses
g	The mass fraction of the condensed liquid
g_+	The mass fraction of the condensate at the triple point
g_-	The mass fraction of the condensate at the triple point for the solid
h	The enthalpy per unit mass
h_c	The enthalpy per unit mass of the carrier gas
h_L	The enthalpy per unit mass of the liquid
h_v	The enthalpy per unit mass of the vapor
J	The nucleation rate

T_s	The saturation temperature corresponding to p_v
T_o	The initial stagnation gas temperature
u	The gas velocity
W 18	Constant in equation for σ_∞ defined by Eq. (F. 80)
W 19	Constant in equation for σ_∞ defined by Eq. (F. 80)
W 20	Constant in equation for ρ_L defined by Eq. (F. 81)
W 21	Constant in equation for ρ_L defined by Eq. (F. 81)
W 42	Constant in equation for L defined by Eq. (F. 83)
W 43	Constant in equation for L defined by Eq. (F. 83)
W 44	Constant in equation for L defined by Eq. (F. 83)
W 45	Constant in equation for L defined by Eq. (F. 82)
W 46	Constant in equation for L defined by Eq. (F. 82)
X_c	The mass fraction of the non-condensing gas
x	The distance downstream from the throat
Δx	The increment in x used in S; also equal to the integration increment used in computer program
y	The initial mass fraction of the vapor
α_c	The thermal accommodation coefficient of the carrier gas to the surface of the condensate
α_v	The thermal accommodation coefficient of the vapor on the surface of its own liquid
β	The constant factor included in the equation for J in the program to allow for modification of nucleation rate
γ	The average specific heat ratio of the mixture
γ_c	The specific heat ratio of the carrier gas
γ_v	The specific heat ratio of the vapor
γ_o	The average initial specific heat ratio of the mixture, (i. e., γ with g = 0)
δ	The constant in Tolman's equation for σ (Eq. F. 50)

k	Boltzman's constant
L	The latent heat
L_+	The latent heat of the liquid at the triple point
L_-	The latent heat of the solid at the triple point
ΔL	The difference between L_- and L_+
M	Mach number
m_D	The mass of a drop
$\dot{m}$	The mass rate of flow
N_A	Avogadro's number
p	The pressure of the gas mixture
p_c	The partial pressure of the carrier gas
p_D	The pressure at drop surface
p_v	The partial pressure of the vapor
p_{vs}	The saturation pressure of the vapor corresponding to T
p_z	The partial pressure of zinc
p_{zo}	The initial stagnation partial pressure of zinc
p_o	The initial stagnation pressure of the mixture
r	The radius of a liquid drop
r^*	The critical drop radius
r'	The integrated value of dr/dx from the saturation point
R_u	Universal gas constant
R_{AV}	The average gas constant of the vapor and carrier gas mixture
R_{AV_O}	The initial stagnation gas constant of the vapor and carrier gas, (i. e. , R_{AV} with g = 0)
R_{th}	The radius of the throat of the nozzle
S	The sum in the equation for g; defined in Eq. (F. 75)
T	The gas temperature
T_D	The temperature of the droplet

μ_c	The molecular weight of the carrier gas
μ_v	The molecular weight of the vapor
ρ	The total density of the mixture
ρ_c	The density of the carrier gas
ρ_L	The density of the liquid
ρ_L'	The density of the condensate referred to the total volume
ρ_v	The density of the vapor
ρ_o	The initial stagnation density of the mixture
σ	The surface tension
σ_∞	The surface tension of a flat surface
θ	The nozzle half angle
ξ	A variable defining the point in the nozzle where a given drop was formed

Subscripts

i	Indicates the current calculation point, x, in the nozzle
j	The integer assigned to each calculation point in the nozzle
k	The integer of the calculation point at $x-\Delta x_i$, (i. e., $k = i - 1$)

Theoretical analyses of non-equilibrium condensation have been confined in the past to pure vapors or extremely small fractions of vapor in a carrier gas. The problem of a vapor in a carrier gas where the two components are comparable fractions of the flow has not been previously considered. A treatment of the latter problem is presented here. The solution is restricted to a straight walled conical nozzle with condensation restricted to taking place downstream of the sonic throat. Variations in physical properties such as latent heat, liquid density and surface tension were provided for in the computer solution. Since it had been previously found[F1] that the correction to surface tension for droplet size has a strong effect, such a correction[F2] was included in the analysis.

Solutions for frozen isentropic flow as well as for the saturated equilibrium expansion were included in the computer program developed for the non-equilibrium condensation problem. These serve as convenient comparisons.

FLOW EQUATIONS

The equations describing one dimensional steady flow in a nozzle are well known and have been derived by many authors[F3, F4]. They represent a general set of equations and may be written for two component flows with condensation. For this particular investigation in which a non-condensing gas (carrier gas), and a condensing gas (vapor),

are present along with the liquid state, this set of equations must be expanded to include the mass fraction of each species and to include the effects of the vapor's condensing.

These equations and those to follow contain many inherent assumptions. They are:

1. One dimensional, steady, inviscid flow.
2. No external heat transfer.
3. The gases are perfect gases.
4. The liquid drops formed have the same velocity as the flow.
5. The liquid drops formed do not contribute to the pressure.
6. The volume of the condensed phase is negligible when compared to the total volume.
7. The vapor and its condensate are uniformly distributed.
8. Changes in the entropy of mixing are neglected.

The continuity equation takes its usual form and can be written

$$\rho u A = \dot{m} \tag{F.1}$$

where in this case ρ is the total density of the mixture, u is the velocity, A is the nozzle area, and $\dot{m}$ is the mass rate of flow. The density is defined

$$\rho \equiv \rho_c + \rho_v + \rho_L' \tag{F.2}$$

where ρ_c is the density of the carrier gas, ρ_v is the density of the vapor and ρ_L' is the density of the condensate referred to the total volume. The density of the individual species can be referenced to the total density by defining their mass fraction. The mass fraction of the carrier gas is defined

$$X_c \equiv \rho_c/\rho \tag{F.3}$$

Since the carrier does not condense, X_c is also the initial mass fraction, i.e. a constant. The mass fraction of the condensate at any point is defined

$$g \equiv \rho_L'/\rho \tag{F.4}$$

and the mass fraction of the vapor at any point is

$$y - g \equiv \rho_v/\rho \tag{F.5}$$

where y is the initial mass fraction of the vapor. By virtue of their definitions X_c and y are related by

$$X_c + y = 1 \tag{F.6}$$

The momentum equation is

$$\rho u \, du = - dp \tag{F.7}$$

where p is the pressure.

The equation of state can be written

$$p = \rho R_{AV} T \tag{F.8}$$

where T is the temperature and R_{AV} is the average gas constant of the mixture

$$R_{AV} \equiv \left(\frac{X_c}{\mu_c} + \frac{y - g}{\mu_v} \right) R_u \tag{F.9}$$

where R_u is the universal gas constant, μ_v and μ_c are the molecular weights of the vapor and carrier gas, respectively. Equation (F.9) assumes the condensate does not contribute to the total pressure. That is

$$p = p_c + p_v \tag{F.10}$$

where p_v and p_c are the partial pressures of the vapor and carrier gas, respectively. For an ideal gas mixture

$$p_c = \rho_c \frac{R_u}{\mu_c} T \tag{F.11}$$

$$p_v = \rho_v \frac{R_u}{\mu_v} T \tag{F.12}$$

Substituting Eq.(F.9) into Eq.(F.8) the equation of state becomes

$$p = \rho \left(\frac{X_c}{\mu_c} + \frac{y - g}{\mu_v} \right) R_u T \tag{F.13}$$

which could have been obtained by substituting Eq.(F. 3),(F. 5), (F. 11), and (F. 12) into Eq. (F. 10).

The energy equation is given by

$$d (h + u^2/2) = 0 \tag{F.14}$$

where h is the enthalpy per unit mass of the mixture. The following expression for h was derived by Wegener[F5]

$$h = X_c h_c + (y - g) h_v + g h_L \tag{F.15}$$

where h_c, h_v, and h_L are the enthalpies of the carrier gas, vapor and condensate respectively, and where

$$h_L(T) \equiv h_v(T) - L(T) - C_L(T - T_D) \qquad \text{(F.16)}$$

where L is the latent heat at the temperature of the gas mixture, C_L is the specific heat of the condensate and T_D is the temperature of the droplet. In Eq. (F.16) the term, $-C_L(T - T_D)$, represents the change in enthalpy which would decrease the temperature of the drop from T_D to T. This is very nearly equal to the difference between the latent heat released at temperature, T, and that at temperature, T_D. Thus Eq. (F.16) can be written

$$h_L = h_v - L(T_D) \qquad \text{(F.17)}$$

Substituting Eq. (F.17) into Eq. (F.15) gives

$$h = X_c h_c + y h_v - g L(T_D) \qquad \text{(F.18)}$$

Dropping the temperature notation from L on the understanding hence-forth $L = L(T_D)$ the conservation of energy equation may be written

$$d\,(u^2/2 + X_c h_c + y h_v - g L) = 0 \qquad \text{(F.19)}$$

Taking the differential

$$u\,du + X_c\,dh_c + y\,dh_v\ 1\ d(gL) = 0 \qquad \text{(F.20)}$$

Since we are assuming a perfect gas with constant specific heats

$$dh_c = C_{p_c}\, dT \tag{F.21}$$

$$dh_v = C_{p_v}\, dT \tag{F.22}$$

where C_{p_c} and C_{p_v} are the specific heats at constant pressure of the carrier and vapor, respectively. Substituting into Eq. (F.20)

$$u\, du + (X_c\, C_{p_c} + y\, C_{p_v})\, dT - d(gL) = 0 \tag{F.23}$$

However, the initial ("frozen" flow) specific heat, C_p, is

$$C_p \equiv X_c\, C_{p_c} + y\, C_{p_v} \tag{F.24}$$

Equation (F.23) then becomes

$$u\, du + C_p\, dT - d(gL) = 0 \tag{F.25}$$

A more convenient form of Eq. (F.25) can be obtained by differentiating the last term, assuming $dT_D/dT \cong 1$

$$u\, du + (C_p - g dL/dT_D)\, dT - L dg = 0 \tag{F.26}$$

A useful form of the energy equation can be obtained by integrating Eq. (F.25). Using the chamber conditions as the initial point

$$\int_0^u u\,du + C_p \int_{T_o}^{T} dT - \int_0^{gL} d(gL) = 0 \qquad \text{(F. 27)}$$

The latent heat generally has a discontinuity at the triple point thus, if T_D is less than the triple point temperature, Eq. (F. 27) should actually be written

$$\int_0^u u\,du + C_p \int_{T_o}^{T} dT - \int_0^{g_+L_+} d(gL) - \int_{g_-L_-}^{gL} d(gL) = 0 \qquad \text{(F. 28)}$$

where the plus (+) sign represents the value at the triple point for the liquid and the minus (-) sign represents the value at the triple point for the solid. Completing the integral and noting $g_+ = g_-$, Eq. (F. 28) becomes

$$\frac{u^2}{2} + C_p (T - T_o) + g_+ \Delta L - gL = 0 \qquad \text{(F. 29)}$$

where T_D is less than the triple point temperature,

$$\Delta L \equiv L_- - L_+ \qquad \text{(F. 30)}$$

and where T_D is greater than the triple point temperature

$$\Delta L \equiv 0 \qquad \text{(F. 31)}$$

In addition to the integral form of the energy equation the differential form of the continuity equation and equation of state are useful. Logarithmically differentiating Eq. (F. 1) and (F. 13) they become

$$\frac{d\rho}{\rho} + \frac{du}{u} + \frac{dA}{A} = 0 \tag{F. 32}$$

$$\frac{dp}{p} = \frac{d\rho}{\rho} + \frac{dT}{T} - \frac{dg}{\frac{\mu_v}{X_c \frac{\mu_v}{\mu_c}} + y - g} \tag{F. 33}$$

Consistent with the assumption of a perfect gas the specific heats, C_{p_c} and C_{p_v}, were calculated from the relationship

$$C_{p_v} = \frac{\gamma_v}{\gamma_v - 1} \frac{R_u}{\mu_v} \tag{F. 34}$$

$$C_{p_c} = \frac{\gamma_c}{\gamma_c - 1} \frac{R_u}{\mu_c} \tag{F. 35}$$

where γ_v and γ_c are the ratio of the specific heats of the vapor and carrier gas, respectively. These were taken to be constants.

Although it does not enter the flow calculations, a computation of a local Mach number, M, was included in the program and its output. It was defined

$$M \equiv u/\sqrt{\gamma R_{AV} T} \tag{F. 36}$$

where γ is the average ratio of specific heats, and is given by

$$\gamma = \frac{X_c C_{p_c} + (y - g) C_{p_v}}{X_c C_{v_c} + (y - g) C_{v_v}} \tag{F. 37}$$

C_{v_c} and C_{v_v} are the specific heats at constant volume for the carrier and vapor respectively, and are taken to be

$$C_{v_c} = C_{p_c} - R_u/\mu_c \tag{F.38}$$

$$C_{v_v} = C_{p_v} - R_u/\mu_v \tag{F.39}$$

Consistent with the assumption of a straight walled conical nozzle the cross sectional area is given by

$$A = \pi (R_{th} + x \tan \theta)^2 \tag{F.40}$$

where R_{th} is the radius at the throat and θ is the half angle of the nozzle, which are constants for any given nozzle. The rate of change of A can be obtained by differentiating Eq. (F.40). It is

$$\frac{dA}{dx} = 2\pi \tan \theta (R_{th} + x \tan \theta) \tag{F.41}$$

Upon closer examination of Eq. (F.1, 7, 13, 26, 29, 32, and 33) it is seen that the equations can be written in terms of two unknowns, p and g. The mass fraction of the condensate, g, can be obtained as a function of the distance downstream of the throat, x, and the flow variables from the nucleation and growth rate equations discussed in the next chapter. An integrable equation for dp/dx can be obtained by simultaneously solving and rearranging so that the only differentials

are dA/dx and dg/dx. Using the six above mentioned equations the following equation can be obtained.

$$\frac{dp}{dx} = \frac{-\frac{p}{A}\frac{dA}{dx} + \left\{Lp/\left[T(C_p - gdL/dT_D)\right] - \dot{m}\, R_u\, T/(\mu_v\, uA)\right\}\frac{dg}{dx}}{1 - pA/(u\dot{m}) - puA/\left\{\dot{m}T(C_p - gdL/dT_D)\right\}} \qquad (F.42)$$

To calculate the other variables as functions of p and g special combinations of the equations must be used. Solving Eq. (F.1), (F.8), and (F.29), the velocity is given by

$$u = -C_p\, A\, p/R_{AV}\, \dot{m} + \left[\left\{C_p\, Ap/R_{AV}\, \dot{m}\right\}^2 + 2\, C_p\, T_o + 2gL - 2g_+\, \Delta L\right]^{1/2} \qquad (F.43)$$

Then the density can be calculated from Eq. (F.1) and the temperature from Eq. (F.29).

The expression used to determine $\dot{m}$ was calculated from isentropic relations[F9] at the throat, since condensation has been restricted to taking place downstream of that point.

$$\dot{m} = A_t\, P_t \left[2\, C_p\, (T_o - T_t)\right]^{1/2} / R_{AV_0}\, T_t \qquad (F.44)$$

where R_{AV_0} is R_{AV} calculated with g = 0, and A_t, P_t, and T_t are the area, pressure and temperature at the throat and are given by

$$P_t = P_o \left(\frac{2}{\gamma_o + 1} \right)^{\frac{\gamma_o}{\gamma_o - 1}} \quad ; \quad T_t = \frac{2T_o}{\gamma_o + 1} \quad ; \quad A_t = \pi R_{th}^2 \qquad \text{(F.45-47)}$$

where γ_o is γ calculated with g = 0.

NUCLEATION AND GROWTH EQUATIONS

The classical equation for nucleation rate derived and discussed in Ref. F6 was used for the present calculations.

The assumptions inherent in the use of the equation[F6] are the following:

1. Drops are formed by spontaneous nucleation only.
2. Only drops reaching the critical drop size can exist and grow or effect the flow.
3. The fact that the drops have an ordered velocity does not effect the nucleation process.
4. The drops are spherical.
5. The nucleation process is independent of the presence of the carrier gas (Ref. F10 includes a discussion of this).
6. Thermodynamic equilibrium representation of the vapor properties with the non-equilibrium nucleation process is valid.

7. Saturation pressure corresponds to saturation pressure of a drop of infinite radius.

8. The number of molecules of vapor is not decreased by the nucleation.

The concept of the critical drop size arises from considerations hermodynamic equilibri um. It is defined as that size at which the drop will neither have a tendency to evaporate or grow. This drop size in terms of its radius is given by[F6] the Thompson-Helmholtz equation:

$$r^* = \frac{2\sigma\ \mu_v}{\rho_L\ R_u\ T\ \ell n\ (p_v/p_{v_s})} \qquad \text{(F.48)}$$

where σ is the surface tension, ρ_L is the density of the liquid drop, and p_{v_s} is the equivalent saturation pressure of the vapor at temperature, T.

The nucleation rate, J, which describes the number of critical sized drops formed per unit volume per unit time[F6] is

$$J = \alpha_v \left(\frac{p_v}{kT}\right)^2 \frac{1}{\rho_L}\left[\frac{2\,\mu_v\,\sigma}{\pi N_A}\right]^{1/2} \exp\left(\frac{-4\pi\sigma r^{*2}}{3kT}\right) \qquad \text{(F.49)}$$

where α_v is the thermal accommodation coefficient of the vapor to its liquid.

As can be seen from Eq. (F.48 and F.49), J is a strong function of σ. Tolman's[F2] correction of σ for the drop radius was included in the analysis. This correction is

$$\sigma = \frac{\sigma_\infty}{1 + \frac{\delta}{r^*}} \qquad \text{(F.50)}$$

where σ_∞ is the surface tension of a flat surface and δ is a constant between .5 and 1.2 molecular diameters in the liquid state.

Once the critical sized drop exists in the flow any additional decrease in temperature will cause growth. Thus as the particle traverses the nozzle it will grow. The growth is, of course, effected by the ambient conditions. Various concepts have been used in studying drop growth in an effort to obtain an equation to describe it. Since the validity of any given equation is limited, four equations were chosen to emphasize different aspects. Although the effects on the flow of the four equations were demonstrated, only one was used in studying the effects of the carrier gas.

The following assumptions are common to all the growth rate equations used in this analysis:

1. Drop radius is much less than the local mean free path.
2. There is no agglomeration of the drops.
3. The gas mixture is composed of only pure vapor and pure carrier gas and contains no foreign substance.
4. The growth rate equation is valid when used with the steady flow approximation.

The first growth equation employed was derived by Stever[F7]. It was developed for the condensation of a pure vapor. It assumes in addition to the assumptions above, that the drop temperature is equal to the saturation temperature, T_s, corresponding to p_v and that the evaporation of molecules was neglected. The approach Stever took was to determine the net influx of molecules that would maintain an energy balance between the latent heat released and the energy carried away by the noncondensing molecules in order to maintain $T_D = T_s$. His equation using the steady flow approximation is

$$\frac{dr}{dx} = \frac{\alpha_v p}{L \rho_L u} \left[\frac{2 R_u}{\pi \mu_v T}\right]^{1/2} (T_s - T) \qquad \text{(F.51)}$$

where r is drop radius at any point in the flow. The use of this equation for the two component case implies the approximation that the

presence of the carrier gas has no influence on the drop growth (or an accommodation coefficient of zero for the carrier gas).

In order to incorporate the effects of the carrier gas another growth rate equation using Stever's approach was derived. It, also, assumes $T_D = T_s$ and neglects the evaporation of molecules. It is obtained as follows: The average energy of the molecules impinging on the drop per unit area and time from kinetic theory[F8] is

$$d E_{iv} = p_v \left(\frac{2 R_u T}{\pi \mu_v} \right)^{1/2} \qquad \text{(F.52)}$$

for the vapor. For the carrier it is

$$d E_{ic} = p_c \left(\frac{2 R_u T}{\pi \mu_c} \right)^{1/2} \qquad \text{(F.53)}$$

The impinging molecules will return to the gas a net amount of energy per unit time and area upon reflection which depends upon the degree to which they are accommodated to the temperature of the drop. Since the carrier molecules do not condense, the same number that impinge upon the drop will be reflected. Therefore, the net energy per unit time and area, ΔE_c, which the carrier molecules acquire is

$$\Delta E_c = \alpha_c p_c \left(\frac{2 R_u}{\pi \mu_c T} \right)^{1/2} (T_s - T) \qquad \text{(F.54)}$$

where α_c is the thermal accommodation coefficient of the carrier gas. Some of the vapor molecules, though, will condense and not be reflected. The difference between the reflected and impinging molecules, ΔE_v is

$$\Delta E_v = \alpha_v p_v \left(\frac{2 R_u}{\pi \mu_v T} \right)^{1/2} \left((1 - f) T_s - T \right) \qquad \text{(F.55)}$$

where α_v is the thermal accommodation coefficient of the vapor and f is the fraction of the impinging molecules which condense.

The number of molecules of the vapor impinging on the drop per unit area and time is $p_v / \sqrt{2\pi k \mu_v T / N_A}$. The number which condense is $f p_v \sqrt{2\pi k \mu_v T / N_A}$. Each molecule upon condensing releases an amount of energy = $L \mu_v / N_A$. But in order to maintain the drop temperature = T_s, the net amount of energy transferred per unit area and time, ΔE, by the vapor and carrier gas molecules therefore is:

$$\Delta E = \Delta E_c + \Delta E_v = \frac{f L p_v}{\sqrt{2\pi R_u T / \mu_v}} \qquad \text{(F.56)}$$

Summing Eq. (F.54 and F.55), equating to Eq. (F.56), and solving for f gives

$$f = \frac{\left\{\alpha_v + \alpha_c \frac{p_c}{p_v}\sqrt{\frac{\mu_v}{\mu_c}}\right\} 2 R_u (T_s - T)}{L \mu_v + 2 \alpha_v R_u T_s} \qquad \text{(F. 57)}$$

The increase in the mass of the drop, m_D, per unit time is

$$\frac{dm_D}{dt} = \frac{4\pi r^2 f p_v}{\sqrt{2\pi R_u T/\mu_v}} \qquad \text{(F. 58)}$$

Substituting for Eq. (F. 58) f becomes

$$\frac{dm_D}{dt} = \frac{4\pi r^2 \left(\frac{2 R_u}{\pi \mu_v T}\right)^{1/2} \left\{\alpha_v p_v + \alpha_c p_c \sqrt{\frac{\mu_v}{\mu_c}}\right\}(T_s - T)}{(L + 2 \alpha_v R_u T_s/\mu_v)} \qquad \text{(F. 59)}$$

Since $m_D = \frac{4}{3}\pi r^3 \rho_L$

$$\frac{dm_D}{dt} = 4\pi r^2 \rho_L \frac{dr}{dt} \qquad \text{(F. 60)}$$

Also, from the steady flow approximation dr/dt = u (dr/dx) and Eq. (F. 60) can be written

$$\frac{dm_D}{dt} = 4\pi r^2 u\rho_L \frac{dr}{dx} \qquad \text{(F. 61)}$$

Combining Eq. (F. 59 and F.61) and solving for the drop growth rate, dr/dx, yields

$$\frac{dr}{dx} = \frac{\dfrac{1}{\rho_L\, u}\left(\dfrac{2\,R_u}{\pi\,\mu_v\,T}\right)^{1/2}\left\{\alpha_v\, p_v + \alpha_c\, p_c\sqrt{\dfrac{\mu_v}{\mu_c}}\right\}(T_s - T)}{L + 2\,\alpha_v\, R_u\, T_s/\mu_v} \qquad \text{(F.62)}$$

The use of this equation with the two component condensing flow removes the one-component restriction of Stever's equation. The presence of the carrier gas is accounted for by the term $\alpha_c\, p_c\sqrt{\mu_v/\mu_c}$, but it creates another problem. The problem is determining the correct value for the thermal accommodation coefficient of an inert carrier gas on a liquid drop.

The third and fourth growth rate equations were obtained from similar considerations. Hill[F9] derives an equation for dr/dx which is obtained by considering only the mass flux to and from the drop including the molecules which evaporate. If it is assumed that all the incoming particles condense, the equation can be written

$$\frac{dr}{dx} = \frac{1}{\rho_L\, u}\left[\frac{p_v}{\sqrt{2\pi\,R_u\,T/\mu_v}} - \frac{p_D}{\sqrt{2\pi\,R_u\,T_D/\mu_v}}\right] \qquad \text{(F.63)}$$

where p_D is the pressure of the drop. Two limits of this equation, which depend on the limits of T_D, yield the third and fourth growth rate equation.

$T_D = T_s$ is one limit, and p_D is correspondingly p_v, (if effects of drop curvature are neglected), since any other drop pressure would correspond to some other T_s. Substituting these into Eq. (F.63)

$$\frac{dr}{dx} = \frac{p_v}{\rho_L u}\left(\frac{\mu_v}{2\pi R_u}\right)^{1/2}\left\{\frac{1}{\sqrt{T}} - \frac{1}{\sqrt{T_s}}\right\} \qquad \text{(F.64)}$$

The assumption that $T_D = T_s$ implies that the latent heat raises the temperature of the drop to saturation. This assumption is probably most reasonable, because the critical size drops are formed at $T_D = T_s$, and it would require an efficient transfer of energy away from the drop to decrease the temperature below saturation.

Equation (F.64) was also chosen as the growth rate equation when performing the calculations on the effects of the carrier gas. It was chosen since it yielded results closest to experimental measurements.

The other limit on the drop temperature is the gas temperature. The temperature of the drop would be no less than the gas temperature since the change in phase would tend to raise the temperature of the drop. The drop pressure corresponding to $T_D = T$ is p_{v_s} since this is the corresponding saturation value. Substituting these values for p_D and T_D into Eq. (F.63) yields the fourth growth rate equation

$$\frac{dr}{dx} = \frac{1}{\rho_L u}\left[\frac{\mu_v}{2\pi R_u T}\right]^{1/2}(p_v - p_{v_s}) \qquad \text{(F.65)}$$

Having the relations for J and dr/dx the equation for g can be obtained. Consider any point downstream from the saturation point (i.e., the point at which the flow crosses the saturation curve). At this location drops will be in the process of being formed and there will be drops previously formed and in the process of growing. If this point is labeled x and the point at which a droplet originated is labeled ξ, then the radius of any drop at point x that was formed at point ξ is given by

$$r(x, \xi) = r^*(\xi) + \int_{\xi}^{x} \frac{dr}{dx}\, dx \tag{F.66}$$

where $\xi \leq x$. The mass of a drop formed at ξ is

$$\frac{4\pi}{3} \rho_L \left\{r(x, \xi)\right\}^3 \tag{F.67}$$

The rate at which these drops were formed in the interval $d\xi$ about ξ is

$$J(\xi)\, A(\xi)\, d\xi \tag{F.68}$$

Thus the mass rate of flow crossing x from the drops that were created at ξ is

$$\frac{4\pi}{3} \rho_L \left\{r(x, \xi)\right\}^3 J(\xi)\, A(\xi)\, d\xi \tag{F.69}$$

This compared to the total rate of mass flux represents the mass fraction of these droplets. If, however, mass flow rate from all drops is calculated by considering the contribution from each point ξ. This, when compared to $\dot{m}$, is the mass fraction of condensate at point x. That is

$$g(x) = \frac{4\pi \rho_L}{3\dot{m}} \int_{x_o}^{x} \left\{r(x, \xi)\right\}^3 J(\xi)\, A(\xi)\, d\xi \qquad \text{(F.70)}$$

where x_o is some point where $J = 0$. Taken here to be the saturation point.

A more convenient form of Eq.(F.70) is obtained by differentiating it and approximating the remaining integral. Performing the differentiation

$$\frac{dg(x)}{dx} = \frac{4\pi \rho_L}{\dot{m}} \left\{ \frac{1}{3} J(x)\, A(x) \left\{r^*(x)\right\}^3 + \int_{x_o}^{x} \left\{r(x, \xi)\right\}^2 \frac{dr}{dx} J(\xi)\, A(\xi)\, d\xi \right\} \qquad \text{(F.71)}$$

Noting that dr/dx is not a function of ξ since it is not a function of r but only of the particular point x, and approximating the integral by a sum, Eq.(F.71) becomes

$$\frac{dg}{dx} = \frac{4\pi \rho_L}{\dot{m}} \left\{ \frac{1}{3} J(x)\, A(x) \left\{r^*(x)\right\}^3 + \frac{dr}{dx} \sum_{j=0}^{i} r_j^2\, J_j\, A_j\, \Delta x_j \right\} \qquad \text{(F.72)}$$

where r_j, J_j, A_j and Δx_j replace $r(x, \xi)$, $J(\xi)$, $A(\xi)$ and $d\xi$, respectively, and where i is the number of intervals each one corresponding to a width Δx_j that the distance $x - x_o$ is divided into.

Since dr/dx is not a function of r but only of x Eq. (F.66) can be integrated to give

$$r(x, \xi) = r^*(\xi) + r_i'(x) - r_j'(\xi) \tag{F.73}$$

where r_i' is the integrated value of dr/dx from the point x_o to x and r_j' is the integral of dr/dx from x_o to ξ. In terms of the above notation Eq.(F.73) is

$$r_j = r_j^* + r_i' - r_j' \tag{F.74}$$

Considering just the sum in Eq.(F.72) and substituting for r_j, we have

$$\sum_{j=0}^{i} (r_j^* + r_i' - r_j')^2 J_j A_j \Delta x_j \equiv S \tag{F.75}$$

where i goes from station x_o to station x and j goes from station x_o to ξ. If the point of interest, x, equals x_o this sum must obviously be zero. Defining S to be equal to the value of the sum at point x, i.e., up to i, and S_k to be the value of the sum at $x - \Delta x_i$, i.e. $i - 1 = k$, then their difference is

$$S - S_k = \sum_{j=0}^{k} \left\{ (r_j^* + r_i' - r_j')^2 J_j A_j \Delta x_j - (r_j^{*2} + r_k' - r_j')^2 J_j A_j \Delta x_j \right\}$$

$$+ r_i^{*2} J_i A_i \Delta x_i \qquad \text{(F.76)}$$

or expanding the squares and rearranging

$$S - S_k = r_i^{*2} J_i A_i \Delta x_i + \sum_{j=0}^{k} \left[\left\{ (r_i'^2 - r_i'^2) + 2(r_j^* - r_j')(r_i' - r_k') \right\} \right.$$

$$\left. \times J_j A_j \Delta x_j \right] \qquad \text{(F.77)}$$

or since r_i' and r_k' are invariant with j

$$S = S_k + r_i^{*2} J_i A_i \Delta x_i + (r_i'^2 - r_k'^2) \sum_{j=0}^{k} J_j A_j \Delta x_j$$

$$+ 2(r_i' - r_k') \sum_{j=0}^{k} (r_j^* - r_j') J_j A_j \Delta x_j \qquad \text{(F.78)}$$

The two summations in Eq. (F.78) are easy values to compute, since they can be summed as the calculation goes from point to point downstream. This makes S an easy value to obtain in a calculation since it then becomes the sum of current values and the value it had at the last computation point. Using the subscript notation and substituting S in Eq. (F.72):

$$\frac{dg}{dx} = \frac{4\pi \rho_L}{\dot{m}} \left\{ \frac{1}{3} J_i A_i r_i^{*3} + S \frac{dr}{dx} \right\} \qquad \text{(F. 79)}$$

which, when integrated with respect to x, yields g at any point in the flow. This completes the set of equations needed to describe the flow provided r' is simultaneously calculated by integrating dr/dx.

In the development of the nucleation, growth rate and mass fraction equations several physical properties were introduced as known quantities. These are function of temperature and therefore a means of computing them is provided. This was accomplished by representing them as general curvefit equations to the empirical data. These relations are as follows, where W designates a constant:

the surface tension, $\sigma_\infty = (W18) - (W19)\ T_D$ (F. 80)

the density of the liquid, $\rho_L = (W20) - (W21)\ T_D$ (F. 81)

(σ_∞ and ρ_L are functions of T_D since these are drop properties)

the latent heat, $L = (W45) - (W46)\ T_D$ (F. 82)

where T_D is greater than the temperature of the triple point and:

$$L = (W42) - (W43)\ T_D - (W44)\ T_D^2 \qquad \text{(F. 83)}$$

for T_D less than the temperature at the triple point. The saturation curve for calculating the saturation pressure corresponding to T:

$$p_{v_s} = \exp\left[(W8) - (W9)/T\right] \qquad \text{(F. 84)}$$

above the triple point, and

$$p_{v_s} = \exp\left[(W10) - (W11)/T\right] \tag{F.85}$$

below the triple point.

Likewise for calculating the saturation temperature corresponding to p_v

$$T_s = (W9)/(W8) - \ln p_v \tag{F.86}$$

above the triple point, and

$$T_s = (W11)/(W10) - \ln p_v \tag{F.87}$$

below the triple point.

"FROZEN" ISENTROPIC FLOW EQUATIONS

The calculations of the frozen flow were performed by incrementing the Mach number. Knowing the Mach number, the distance downstream from the throat was calculated by combining the equation for area ratio as a function of Mach number and the equation defining the nozzle area as a function of x. Combining,

$$\frac{A}{A_t} = \frac{1}{M}\left[\frac{2}{\gamma_o + 1}\left(1 + \frac{\gamma_o - 1}{2} M^2\right)\right]^{\gamma_o + 1/2(\gamma_o - 1)} \tag{F.88}$$

with Eq. (F.40), where γ_o is γ defined by Eq. (F. 37) with g = 0 and solving for x yields

$$x = \frac{R_{th}}{\tan\theta}\left\{\frac{1}{\sqrt{M}}\left[\frac{2}{\gamma_o + 1}\left(1 + \frac{\gamma_o - 1}{2} M^2\right)\right]^{\gamma_o + 1/4(\gamma_o - 1)} - 1\right\} \tag{F.89}$$

where the identity $A_t = \pi R_{th}^2$ has been used. The area can then be calculated from Eq. (F.40). The density and temperature are calculated from the stagnation conditions and Mach number, and the velocity from the conservation of energy equation. Finally, knowing T and ρ the pressure and partial pressure of the vapor are obtained using Eq. (F.12 and F.13) with g = 0.

The equations used to initiate the equilibrium and non-equilibrium flows are the same as those used for the non-equilibrium flow with g = 0. A and dA/dx are calculated from Eq. (F.40 and F.41). The velocity is obtained by combining the continuity, ideal gas and energy equations:

$$u = -\frac{\gamma_o}{\gamma_o - 1}\frac{pA}{\dot{m}} + \left\{\left(\frac{\gamma_o}{\gamma_o - 1}\frac{pA}{\dot{m}}\right)^2 + 2 C_p T_o\right\}^{1/2} \qquad \text{(F.90)}$$

Using the continuity and energy equations the density and temperature are calculated. Equation (13) with g = 0 defines the partial pressure of the vapor, and the differential of the pressure is obtained by combining Eq. (1), (7) and the energy equation:

$$\frac{dp}{dx} = \frac{-dA/dx}{A\left\{\frac{1}{\gamma_o p} - \frac{A}{\dot{m}u}\right\}} \qquad \text{(F.91)}$$

This equation when integrated defines p at each point from which the other variables can be calculated.

SATURATED EQUILIBRIUM FLOW EQUATIONS

The requirement of thermodynamic equilibrium provides another equation for use with the flow equations. The equation is the Clausius-Clapeyron relation

$$\frac{dp_v}{dT} = \frac{L\rho_v}{T} \tag{F.92}$$

where it has been assumed that the volume of the liquid is negligible when compared to the volume of the vapor.

The form of the equilibrium flow equations used are obtained by combining and rearranging the equations to obtain the differentials dp/dx and du/dx. dp/dx is obtained by combining Eq. (F.1, 7, 26, 33, 13, 12, 5, and 92) and rearranging. It becomes

$$\frac{dp}{dx} = -\frac{1}{A}\frac{dA}{dx} \Bigg/ \left\{ \frac{1}{p} - \frac{A}{u\dot{m}} - \frac{Au}{T\dot{m}\left[C_p - g\frac{dL}{dT_D}\right]} - \left[\frac{L(y-g)}{T\left[C_p - g\frac{dL}{dT_D}\right]} - \frac{p_v}{p}\right] \right.$$

$$\left. \times \left[1 - \frac{L\,p\,Au\,\mu_v}{\dot{m}\,R_u\,T^2\left[C_p - g\frac{dL}{dT_D}\right]}\right] \Bigg/ \left[\frac{p - p_v + L^2(y-g)\,p\,\mu_v}{T^2\left[C_p - g\frac{dL}{dT_D}\right]}\right] \right\} \tag{F.93}$$

Rearranging Eq. (F.7), du/dx becomes

$$\frac{du}{dx} = \frac{-A}{\dot{m}} \frac{dp}{dx} \tag{F.94}$$

Using Eq. (F.13 and F.29) and solving

$$g = \frac{x_c \mu_v}{\mu_c} + y - (C_p T_o - u^2/2 + g_+ \Delta L)/L - \left\{ \left[\frac{x_c \mu_v}{\mu_c} + y \right. \right.$$

$$\left. - (C_p T_o - u^2/2 + g_+ \Delta L)/L \right]^2 - \frac{p C_p \mu_v}{\rho R_u}$$

$$\left. - \left(\frac{x_c \mu_v}{\mu_c} + y \right) \left(C_p T_o - u^2/2 + g_+ \Delta L \right) / L \right\}^{1/2} \tag{F.95}$$

The temperature, density, partial pressure of the vapor, the area and dA/dx are calculated using Eq. (F.29, 1, 13, 40, and 41).

THE COMPUTER PROGRAM

The complexity of the equations describing the two component condensing flow required numerical methods for solution. This was undertaken by creating a computer program for use with the IBM 360 system at The University of Michigan. The language chosen for the program was FORTRAN II. It was first thought that the later version

of FORTRAN, namely FORTRAN IV, would be used, but for this case its convenience was outweighed by the greater availability of machines accepting FORTRAN II.

In developing the program, the first consideration was to incorporate an integration routine, since the equations had to be solved by a point to point progression down the nozzle while simultaneously integrating dp/dx, dg/dx and dr/dx. The routine chosen was a fourth order Runge-Kutta method. From experience, it was known that the method gave accurate results as long as the change in any one variable over an increment Δx was kept to less than 2%. Thus the integration increment was chosen so as to not exceed this limit for any variable at any point. In addition to insure accuracy all variables were calculated as double precision numbers.

The arrangement and order of calculation in the program was set up as follows:

1. It reads input parameters.
2. It initializes variables and calculates constants.
3. Beginning at the throat, it calculates; the isentropic flow properties in increments of 0.5 Mach number and outputs them if desired. It also, during this calculation, determines the location of the saturation point within that Mach number increment.

4. It re-initializes the flow parameters at the closest 0.5 Mach number upstream of the saturation point or at a Mach number of 1.01 whichever is greater.
5. It integrates a set of isentropic relations downstream up to and including the saturation point while simultaneously calculating the exact location of the saturation point.
6. It initializes the non-equilibrium and equilibrium flow variables at the saturation point.
7. If specified in the input that an equilibrium calculation was so desired, it calculates the derivatives. If not, it skips the equilibrium flow equations.
8. It calculates derivatives for the non-equilibrium flow.
9. It then enters the Runge-Kutta routine with the derivatives and proceeds to integrate the variables and increment x by the amount Δx.
10. At the end of each integration increment it calculates the new value of S (sum of growth parameter) and returns to complete another increment.
11. After a specified number of increments it outputs the non-equilibrium flow variables and the equilibrium flow variables, if so specified.

In keeping with the intent to provide generality to the program the following were chosen as the input parameters. They are written using the nomenclature of the program.

Y	The initial mass fraction of the vapor.
P0	The initial pressure in psia (note: all calculations in program are in c.g.s. units but it was more feasible to input pressure in psia and internally convert it).
T0	The initial temperature in ^{o}K.
TNO	The tangent of the nozzle half angle.
RTH	The radius of the throat, cm.
GAMAC	The specific heat ratio of the carrier.
GAMAV	The specific heat ratio of the vapor.
DELTA	The constant in Tolman's equation -cm.
ALPHAC	The thermal accommodation coefficient of the carrier.
ALPHAV	The thermal accommodation coefficient of the vapor.
WMC	The molecular weight of the carrier in grams/mole.
WMV	The molecular weight of the vapor in grams/mole.
TTR	The triple point temperature in ^{o}K.
PCY	The print cycle ratio e.e., a print out occurs in increments of x = PCY*DX1.
DX1	The integration increment in cm.
XSTOP	The length of the nozzle, cm.
W8	The constant in Eq.(F.84) in ln (dynes/cm^2).

W9 The constant in Eq. (F.84) in ln (dynes/cm^2) ^oK.

W18 The constant in Eq. (F.80) in dynes/cm.

W19 The constant in Eq. (F.80) in dynes/cm ^oK.

W20 The constant in Eq. (F.81) in grams/cm^3.

W21 The constant in Eq. (F.81) in grams/cm^3 ^oK.

W42 The constant in Eq. (F.83) in ergs/gr.

W43 The constant in Eq. (F.83) in ergs/gr ^oK.

W44 The constant in Eq. (F. 83) in ergs/gr $^oK^2$.

W45 The constant in Eq. (F.82) in ergs/gr.

W46 The constant in Eq. (F.90) in ergs/gr ^oK.

W10 The constant in Eq. (F.85) in ln (dynes/cm^2).

W11 The constant in Eq. (F.85) in ln (dynes/cm^2) ^oK.

K1 An indicator determining if echo check of input is desired; 1 is positive, 0 is negative.

K2 An indicator determining if the isentropic flow output is desired; 1 is positive, 0 is negative.

K3 An indicator determining if equilibrium flow is to be calculated; 1 is positive, 0 is negative.

ISTOP The Mach number at which the isentropic flow calculations will stop.

BETA The constant factor included in the equation for J to simulate other nucleation theories.

K4 An indicator determining which growth rate equation will be used in computing the flow. A value of 1 yields Eq. (F. 51); 2 yields Eq. (F. 62); 3 yields Eq. (F. 64); 4 yields Eq. (F. 65).

In summary, the major equations used in the program in the order of their calculations including the isentropic and equilibrium flow equations are given below.

isentropic flow:

$$x = R_{th}/\tan\theta \left\{ \frac{1}{\sqrt{M}} \left[\frac{2}{\gamma_o + 1} \left(1 + \frac{\gamma_1 - 1}{2} M^2 \right) \right]^{\gamma_o + 1/4(\gamma_o - 1)} - 1 \right\} \quad \text{(F.89)}$$

$$A = \pi (R_{th} + x \tan\theta)^2 \quad \text{(F.40)}$$

$$T = \frac{T_o}{1 + \frac{\gamma_o - 1}{2} M^2} \quad \text{(F.96)}$$

$$u = \left[2 C_p (T_o - T) \right]^{1/2} \quad \text{(F.97)}$$

$$\rho = \rho_o \left[1 + \frac{\gamma_o - 1}{2} M^2 \right]^{-1/(\gamma_o - 1)} \quad \text{(F.98)}$$

where ρ_o is the initial density calculated from p_o and T_o,

$$p = \rho R_{AV_o} T \quad \text{(F.13)}$$

$$p_v = \rho y R_u T/\mu_v \quad \text{(F.12)}$$

Isentropic equations in differential form for initializing the equilibrium and non-equilibrium flow:

$$A = \pi (R_{th} + x \tan \theta)^2 \tag{F.40}$$

$$\frac{dA}{dx} = 2\pi \tan \theta (R_{th} + x \tan \theta) \tag{F.41}$$

$$u = - \frac{\gamma_o}{\gamma_o - 1} \frac{pA}{\dot{m}} + \left[\left(\frac{\gamma_o}{\gamma_o - 1} \frac{pA}{\dot{m}} \right)^2 + 2 C_p T_o \right]^{1/2} \tag{F.90}$$

$$T = T_o - u^2/2 C_p \tag{F.97}$$

$$\rho = \dot{m}/uA \tag{F.1}$$

$$\frac{dp}{dx} = \frac{- dA/dx}{A \left\{ \frac{1}{\gamma_o p} - \frac{A}{u\dot{m}} \right\}} \tag{F.91}$$

equilibrium flow:

$$\rho = \dot{m}/uA \tag{F.1}$$

$$g = \frac{X_c \mu_v}{\mu_c} + y - (C_p T_o - u^2/2 + g_+ \Delta L)/L - \left\{ \left[\frac{X_c \mu_v}{\mu_c} + y \right. \right.$$

$$\left. - (C_p T_o - u^2/2 + g_+ \Delta L)/L \right]^2 - \frac{p C_p \mu_v}{\rho R_u} \tag{F.95}$$

$$\left. - \left(\frac{X_c \mu_v}{\mu_c} + y \right) \left(C_p T_o - \frac{u^2}{2} - g_+ \Delta L \right)/L \right\}^{1/2}$$

$$T = T_o - u^2/2\,C_p + (gL - g_+\,\Delta L)/C_p \qquad \text{(F.29)}$$

$$p_v = \frac{\rho(y - g)}{\mu_v} R_u T \qquad \text{(F.12)}$$

$$\frac{dp}{dx} = -\frac{dA}{dx}\frac{1}{A} \Bigg/ \left\{ \frac{1}{p} - \frac{A}{u\dot{m}} - \frac{Au}{T\dot{m}\left\{C_p - g\frac{dL}{dT_D}\right\}} \right.$$

$$\left. - \frac{\left[\frac{L(y - g)}{T\left\{C_p - g\frac{dL}{dT_D}\right\}} - \frac{p_v}{p}\right]\left[1 - \frac{L\,p\,A\,u\,\mu_v}{\dot{m}\,R_u\,T^2\left\{C_p - g\frac{dL}{dT_D}\right\}}\right]}{\frac{p - p_v + L^2\,(y - g)\,p\,\mu_v}{T^2\left\{C_p - g\frac{dL}{dT_D}\right\}}} \right\} \qquad \text{(F.93)}$$

$$\frac{du}{dx} = -\frac{A}{\dot{m}}\frac{dp}{dx} \qquad \text{(F.94)}$$

non-equilibrium flow:

$$u = \frac{C_p\,Ap}{R_{AV}\,\dot{m}} + \left[\left(\frac{C_p\,Ap}{R_{AV}\,\dot{m}}\right)^2 + 2\,C_p T_o + 2\,g\,L - 2\,g_+\,\Delta L\right]^{1/2} \qquad \text{(F.43)}$$

$$T = T_o + (gL - g_+\,\Delta L - u^2/2)/C_p \qquad \text{(F.29)}$$

$$p_v = \rho\frac{y - g}{\mu_v} R_u\,T \qquad \text{(F.12)}$$

$$p_c = p - p_v \tag{F.10}$$

$$r^* = \frac{2\sigma_\infty \mu_v}{R_u \rho_L \ln (p_v/p_{v_s})} - \delta \tag{F.48}$$

where

$$\sigma = \frac{\sigma_\infty}{1 + \frac{\sigma}{r^*}} \tag{F.50}$$

$$J = \alpha_v \beta \left(\frac{p_v}{kT}\right)^2 \frac{1}{\rho_L} \left[\frac{2\mu_v}{\pi N_A}\right]^{1/2} \exp\left(\frac{-4\pi \sigma r^{*2}}{3kT}\right) \tag{F.49}$$

where β has here been inserted for use in the program to simulate other nucleation theories.

Four growth rate equations:

$$\frac{dr}{dx} = \frac{\alpha_v p_v}{L \rho_L u} \left[\frac{2R_u}{\pi \mu_v T}\right]^{1/2} (T_S - T) \tag{F.51}$$

$$\frac{dr}{dx} = \frac{1}{\rho_L u} \left[\frac{2R_u}{\pi \mu_v T}\right]^{1/2} (T_S - T) \left\{\alpha_v p_v + \alpha_c p_c \left(\frac{\mu_v}{\mu_c}\right)^{1/2}\right\} \Big/ \left\{L + 2\alpha_v R_u T_S/\mu_v\right\} \tag{F.62}$$

$$\frac{dr}{dx} = \frac{p_v}{\rho_L u} \left[\frac{\mu_v}{2\pi R_u}\right]^{1/2} \left(\frac{1}{\sqrt{T}} - \frac{1}{\sqrt{T_S}}\right) \tag{F.64}$$

$$\frac{dr}{dx} = \frac{1}{\rho_L u} \left[\frac{\mu_v}{2\pi R_u T}\right]^{1/2} (p_v - p_{v_s}) \tag{F.65}$$

Derivatives:

$$\frac{dg}{dx} = \frac{4\pi \rho_L}{\dot{m}} \left[J_i A_i r_i^{*3}/3 + S \frac{dr}{dx} \right] \tag{F.79}$$

$$\frac{dp}{dx} = \left\{ -\frac{p}{A}\frac{dA}{dx} + \left[Lp / \left\{ T (C_p - g\, dL/dT_D) \right\} - \dot{m} R_u T/(\mu_v uA) \right] \frac{dg}{dx} \right\}$$

$$/ \left\{ 1 - \frac{pA}{u\dot{m}} - puA/\left[\dot{m} T (C_p - g\, dL/dT_D) \right] \right\} \tag{F.42}$$

and

Sum of growth term:

$$S = S_k + r_i^{*2} J_i A_i \Delta x_i + (r_i'^2 - r_k'^2) \sum_{j=0}^{k} J_j A_j \Delta x_j$$

$$+ 2(r_i' - r_k') \sum_{j=0}^{k} (r_j^* - r_j') J_j A_j \Delta x_j \tag{F.78}$$

APPENDIX G. DETERMINATION OF STAGNATION CONDITIONS

NOMENCLATURE

A^*	throat area
$\bar{A}_{eff}$	effective area ratio
C_1	parameter defined by Eq. (G.4)
f	mass fraction of inert carrier gas (helium)
m_z	mass of zinc added to chamber
p	pressure
p_o'	pitot pressure
R	universal gas constant
T	temperature
t	time
V	arc chamber volume
$\dot{w}$	mass flow rate
γ	specific heat ratio
κ	mass fraction of condensable vapor (zinc) in chamber
μ	molecular weight
ρ	density
τ	integration dummy variable
$(\ )_c$	stagnation chamber condition
$\bar{(\ )}$	nondimensionalized by stagnation chamber condition (except for $\bar{A}$; see above)

The chamber pressure was measured continuously during each run (see Appendix B). However, due to the very high temperatures and pressures encountered in the arc chamber there was no way to experimentally measure the temperature in the chamber. It is much too high for thermocouples and the pressures are so high that windows for optical measurements are difficult to make and keep transparent. Thus, stagnation temperature must be inferred either by assuming equilibrium in the arc chamber and computing the temperature from the measured pressure, a known initial density, and a calculated mass flow, or from measurements made in the test section. Both of these methods along with a combination of them were used in the condensation experiments.

MACH 25 NOZZLE

The basic difficulty in determining the stagnation state lay in the presence of the zinc vapor. Unlike the helium charge density the zinc vapor density was not known a priori for the equilibrium calculation of stagnation temperatures. However, by weighing the zinc fuse and center electrode bolt before and after the run along with small pellets of zinc found in the chamber following the run, the amount of zinc "lost" during the run could be determined. If it were then assumed

that all of this lost zinc had been vaporized*, that the zinc vapor had been added to the chamber in a known manner with respect to time†, and that the nozzle flow to the throat was isentropic (this does not assume the blowdown or decay in stagnation conditions is adiabatic), then the stagnation state of the gas-vapor mixture may be calculated. This calculation is based on the pressure measured in the arc chamber as a function of time, as indicated below. The governing equations are:

Equation of State:

$$p_c = \rho_c \frac{R}{\mu_c} T_c \qquad \text{(G.1)}$$

*This, in fact, should be a relatively valid assumption since the zinc required to saturate the mixture is three to five times higher than the amount of zinc "lost". In other words, the vapor represented by the lost zinc would be in a very highly superheated state.

†It was subsequently found that the calculated stagnation temperature (after all the zinc vapor has been assumed to be added) was virtually independent of the manner of zinc addition. It was also found that the calculated equilibrium stagnation temperature was quite insensitive to the total amount of zinc added. The calculated "zinc free" temperature was typically only 10% higher than for the case where the zinc "lost" was assumed totally vaporized.

Nozzle Mass Flow Rate:

$$\dot{w} = A^* \sqrt{\frac{\gamma_c \mu_c}{R}\left(\frac{2}{\gamma_c + 1}\right)^{\frac{\gamma_c+1}{\gamma_c-1}}} \frac{p_c}{\sqrt{T_c}} \qquad (G.2)$$

Conservation of Mass:

$$\frac{d\rho_c}{dt} + \frac{1}{V}\left(\dot{w} - \frac{dm_z}{dt}\right) = 0 \qquad (G.3)$$

Combining Eq. (G.1) with Eq. (G.2) and defining C_1 as

$$C_1 \equiv -\frac{A^*}{2V} \sqrt{\gamma_c \left(\frac{2}{\gamma_c + 1}\right)^{\frac{\gamma_c+1}{\gamma_c-1}}} \qquad (G.4)$$

results in

$$\frac{\dot{w}}{V} = -2C_1 \sqrt{p_c \rho_c} \qquad (G.5)$$

or, with Eq. (G.3),

$$\frac{d\rho_c}{dt} - \frac{1}{V}\frac{dm_z}{dt} - 2C_1 \sqrt{p_c \rho_c} = 0 \qquad (G.6)$$

Defining:

$$\xi_c \equiv \sqrt{\rho_c} \qquad (G.7)$$

Eq. (G.6) becomes:

$$\frac{d\xi_c}{dt} = \frac{1}{2V\xi_c}\frac{dm_z}{dt} + C_1\sqrt{p_c} \qquad (G.8)$$

Since $m_z(t)$ is assumed and $p_c(t)$ is known (measured experimentally) Eq. (G.8) can be numerically integrated to give $\xi_c(t)$ and thus $\rho_c(t)$.

If $\kappa(t)$ is the zinc mass fraction in the chamber at any time t, it can be determined as follows:

$$\kappa(t) \equiv \frac{\text{zinc added - zinc removed}}{\text{(zinc added - zinc removed) + (helium charge - helium removed)}}$$

or

$$\kappa(t) = \frac{m_z - \int_{t_r}^{t} \dot{w}(\tau)\,\kappa(\tau)\,d\tau}{m_z - \int_{t_r}^{t} \dot{w}(\tau)\,\kappa(\tau)\,d\tau + \rho_{ch} V - \int_{t_r}^{t} \dot{w}(\tau)\left[1 - \kappa(\tau)\right]d\tau} \qquad (G.9)$$

or, more simply,

$$\kappa(t) = \frac{m_z - \int_{t_r}^{t} \dot{w}(\tau)\,\kappa(\tau)\,d\tau}{m_z + \rho_{ch} V - \int_{t_r}^{t} \dot{w}(\tau)\,d\tau} \qquad (G.10)$$

Differentiating Eq. (G.10) with respect to t and simplifying yields:

$$\frac{d\kappa(t)}{dt} = \frac{\left[1 - \kappa(t)\right] \frac{dm_z}{dt}}{\left[m_z + \rho_{ch} V - \int_{t_r}^{t} \dot{w}(\tau)\, d\tau\right]} \qquad \text{(G.11)}$$

Equation (G.5) gives $\dot{w}(\tau)$ from the $\rho_c(\tau)$ just calculated, so Eq. (G.11) may be numerically integrated to obtain $\kappa(t)$.

For the above integrations, the zinc addition $m_z(t)$ was assumed to be linear, varying from zero at t = 0 to the total amount of zinc "lost" at the time of arc quenching.

Given, $p_c(t)$, $\rho_c(t)$, and $\kappa(t)$, $T_c(t)$ can be calculated from the equation of state. Figure G1 shows stagnation conditions, determined in this manner, as a function of time for a typical run.

Due to the short times involved in the vaporization of zinc, it was reasonable to consider the possibility of gradients in zinc mass fraction within the chamber. It was therefore desirable that some method other than weight measurement be found to determine the zinc mass fraction in the flow.

It was found through a parametric study of equilibrium condensation (discussed in Section III.A) that after condensation is complete (i.e., there is only a negligible amount of vapor left), the ratio of static pressure to chamber pressure is very nearly independent of

chamber temperature (see Fig. 10) and chamber pressure, but is very sensitive to the initial mass fraction of vapor and, of course, to the area ratio.

It has been shown experimentally[6, 9] (Fig. G2 shows experimental data for condensing steam[6] compared to the calculated equilibrium expansion) and analytically[33] that the static pressure in the flow of a condensing vapor (either with or without an inert carrier gas), far downstream of condensation onset, is very nearly at the level represented by an equilibrium expansion. In the same way, the pitot pressure (which is far less sensitive to condensation) can be predicted if there is a complete return to equilibrium between the pitot shock and the probe (see Section II).

A plot of static pressure vs. pitot pressure (both non-dimensionalized by the chamber pressure) obtained from the equilibrium expansion solution is shown in Fig. G3 for representative stagnation conditions. Also shown is the locus of experimental points for pressures measured near the exit of the nozzle during a typical run. The indicated mass fraction and effective area ratio can easily be determined by graphical interpolation. It was found that the mass fraction determined in this manner was usually within 10% of that found from the simple weight loss calculation (Eq. (G.11)).

MACH 5 NOZZLE

The Mach 5 nozzle presented a different problem due to two factors—the different arc chamber configuration, and the smaller exit area ratio.

The large intermediate volume between the baffle and the nozzle (approximately 10% of the total chamber volume) could be expected to contribute to temperature gradients as well as concentration gradients. This would render as highly questionable a stagnation temperature based on the assumption of temperature equality throughout the chamber.

Since the exit area ratio is quite small, there is a strong probability that the zinc vapor would not be fully condensed by the time it reached the exit. Therefore the static pressure is dependent on both the stagnation temperature and the zinc mass fraction (see Section III.A and Fig. 11).

Due to these two factors, a method for determining stagnation conditions such as that outlined for the Mach 25 nozzle would yield erroneous results for the Mach 5 nozzle. However, a solution presented itself in the many static pressures taken along the nozzle. If it is assumed that equilibrium has been reached at two of the more downstream pressure taps* then both of these pressures will fit only one equilibrium expansion curve. This expansion gives a unique stagnation temperature and zinc concentration. The procedure used to determine this curve is outlined below.

---

*This assumption should be quite good since it has been shown [15, 33] that approach to equilibrium is fast after supersaturation collapses.

For one of the measured static pressures several different reasonable stagnation temperatures were selected. For each temperature, the equilibrium expansion was calculated for varying zinc concentration until the concentration was found which caused the expansion curve to fit the measured pressure. This gave a locus of stagnation temperature-zinc concentration combinations whose equilibrium expansion curves all passed through the given pressure ratio. The same procedure was followed for the other measured pressure and the intersection of the two curves yielded the unique stagnation temperature and zinc mass fraction at that given time in the run.

APPENDIX H. EXPLODING WIRE STUDIES

One means of obtaining a heated metal vapor is by transferring large amounts of energy stored in capacitors to a metal wire and thus quickly vaporizing (or "exploding") it. This is accomplished by using the wire as the load of a low inductance L-R-C circuit. The metal vapor thus produced is a good source of vapor for the study of condensation. The method has the advantage of requiring a relatively small laboratory system. Such a system was used in the development of condensation measurement techniques and also yielded additional information on exploding wire characteristics and particle size.

A picture of the system is shown in Fig. H-1, and a schematic of the circuitry is shown in Fig. H-2. A 14.7 μfd/20KV Sangamo capacitor was used as the energy storage capacitor, and it was charged with a 0-30KV/10ma Sorenson Power Supply to a specified voltage V_o. The circuit inductance and resistance, exclusive of the wire, were approximately 0.50 μhy and 10.76 milliohm respectively. Of this resistance, 2.43 milliohm was contributed by the T and M non-inductive current shunt which was used to measure the current in the circuit as a function of time. The voltage across the wire was measured as a function of time with a P-6015 Tektronix High Voltage Probe. Both the voltage and current traces were recorded on a Type 551 Dual Beam Oscilloscope. The oscilloscope was triggered externally with the voltage signal induced on a pick-up coil which was located in the vicinity of the circuit.

A mechanical "drop-switch" was used to close the circuit. One contact of the switch, which was tied to a string, was dropped manually onto the positive terminal of the capacitor. This type of switch was chosen for the sake of its simplicity. Factors such as the inductance of the switch, and the energy loss in the switch were considered negligible.

The discovery that a "optimum discharge" exists was the outcome of exploratory work on exploding wires undertaken in the study of the condensation of metal vapors. "Optimum discharge" characteristics were reported in Ref. H-1 and described in detail in Ref. H-2. In this type of discharge all of the stored energy of the capacitor is dissipated during the first pulse. Both current and voltage traces decrease rapidly to zero by the end of the pulse, indicating no more energy is left in the capacitor, (see Fig. H-3). The results indicated that the voltage at which the "optimum discharge" takes place is directly proportional to the wire cross-sectional area, and is independent of the wire length.

In connection with the program to measure the size of condensing particles in an expanding metal vapor, measurements of particles from wires vaporized at room conditions were made.

Platinum wire was employed to minimize possible chemical reactions between the metal vapor and the atmosphere. Mica tape with a layer of carbon evaporated over it was used as a collecting surface for collecting particles which can be photographed in an electron microscope.(See appendix C.)

The collection tape was placed at several locations more than 2 in. away from the wire and along the perpendicular to the wire, at the wire mid point. The energy discharged through the wire was varied from just above that required to melt the wire to well above vaporization energy. One and two in. of No. 26 platinum wire was used.

Figure H-4 shows a photomicrograph of platinum particles collected. The collected particles were shadowed with chromium (appendix C). The white "tails" are shadows indicating the height of each particle above the collecting surface. Figure H-5 shows several size distributions measured. In all cases the peak of the distribution of diameters was in the region of approximately 60 $\mathring{A}$. It appeared that as the energy increased, the size distribution shifted to somewhat smaller particles. This might be expected since one would expect higher initial entropy at higher energies with the greater concomitant supercooling which would yield smaller particles. It also appeared that making the collection further away from the wire changes the distribution only slightly.

When the stored energy was reduced to that a little above that required for melting (376 joules/gm.), no particles were collected but the wire did "disappear". A few very large (approximately 1mm) single "drops" were collected near the wire. They represented approximately 75% of the mass of the wire. This suggests that there is little if any vaporization of the wire locally, when there is not much more than enough energy to melt the whole wire.

When the energy employed was increased to above that necessary to vaporize (3370 joules/gm) about 1/2 of the wire, there clearly was some vaporization as indicated by the very few small particles collected which were roughly of the same size as those obtained at high energies.

It appears clear that the particles obtained from condensation in a supersonic nozzle are much more uniform in size than those obtained from the exploding wire. This might be expected since the exploding wire represents a very rapid expansion where nucleation could continue at a high rate for some distance before the drop growth could reduce it effectively. The particles formed early would then be considerably larger than the many particles formed much later.

A small cylindrical chamber with adjustable axial wire holder and nominal Mach 3 nozzle was also built (see reference H-2) for exploratory nozzle pressure measurements. The maximum pressure the chamber was designed for was 1000 psia. It appeared that at this lower stagnation pressure the assumption that equilibrium is reached in the chamber when the flow starts is questionable. Confirmation of thermal equilibrium between the species would have to be made before nozzle pressure data could be interpreted accurately.

Zinc particles which were collected downstream of the nozzle exit did appear to be quite uniform and of diameters the order of that collected from the Mach 5 and Mach 25 nozzles.

APPENDIX I. CONDENSATION OF ARGON

Argon was used to check out the tunnel arrangement for the Mach 5 nozzle static pressure measurements which were used to determine the onset of condensation (see Section II. B). In making these checks, the actual onset of argon under several different conditions was obtained.

Bottles of gas were used to charge a compression chamber which was then used to charge the tunnel stagnation chamber. The work done in charging the chamber increased the temperature of the gas somewhat. A thermocouple port was located at the same axial location as the downstream stagnation pressure tap, approximately one-half inch upstream of the throat. A chromel-constantan thermocouple (Balwin-Lima-Hamilton HT Microminiature Thermocouple Model TCRC-ES-50) with hot junction made up of electrically fused .001 in. diameter wires, was employed to obtain stagnation temperature as a function of time. The response time was found to be less than 1 msec indicating it was negligible compared to the slowly changing conditions of the argon. The stagnation pressure was measured both upstream in the stagnation chamber and also at the location of the thermocouple. The two measurements were found to be the same within the accuracy of the measurement. Static pressure was measured along the nozzle according to the locations in Table 1. The boundary layer thickness was determined from pitot measurement at the exit of the nozzle and the assumption that the rate of

growth would be like that of pure helium. The onset of condensation could be determined only to the accuracy of the transducer spacing (see Section IV. B). A larger than "smooth" increase in the pressure ratio at any transducer at a given time was interpreted as the onset of condensation.

Figure I-1 shows the onset regions obtained for expansions in which saturation point pressures range from approximately 7 psia to about 300 psia. Table I-1 shows the stagnation conditions referred to in the figure.

A comparison of the locus of condensation onset points computed from the classical nonequilibrium condensation solution in Appendix F and the midpoints of the onset regions measured is shown in Fig. I-2. The locus of computed points appears to be a resonable fit for the measurements. It is interesting to note that over the region considered the temperature difference between saturation and onset (measured along the isentrope) remains approximately a constant 20^{o}K.

Table 1

TABLE 1. MACH 5 NOZZLE GEOMETRY

Static Pressure Port Number	Distance from Throat (in.)	Geometric Area Ratio	Isentropic Static Pressure Ratio
9	.0547	1.1132	.25800
8	.1897	1.4188	.14400
7	.3522	1.8358	.08220
6	.5336	2.3645	.04960
5	.7968	3.2505	.02720
4	1.1038	4.4616	.01520
3	1.3712	5.6722	.00995
2	1.6407	7.0395	.00680
1	1.8589	8.2545	.00515
Exit	1.9737	8.9325	.00447
Pitot	2.0214	9.2220	.00424

Throat Diameter = 0.1294 in.

Exit Angle = 7.45^{o}

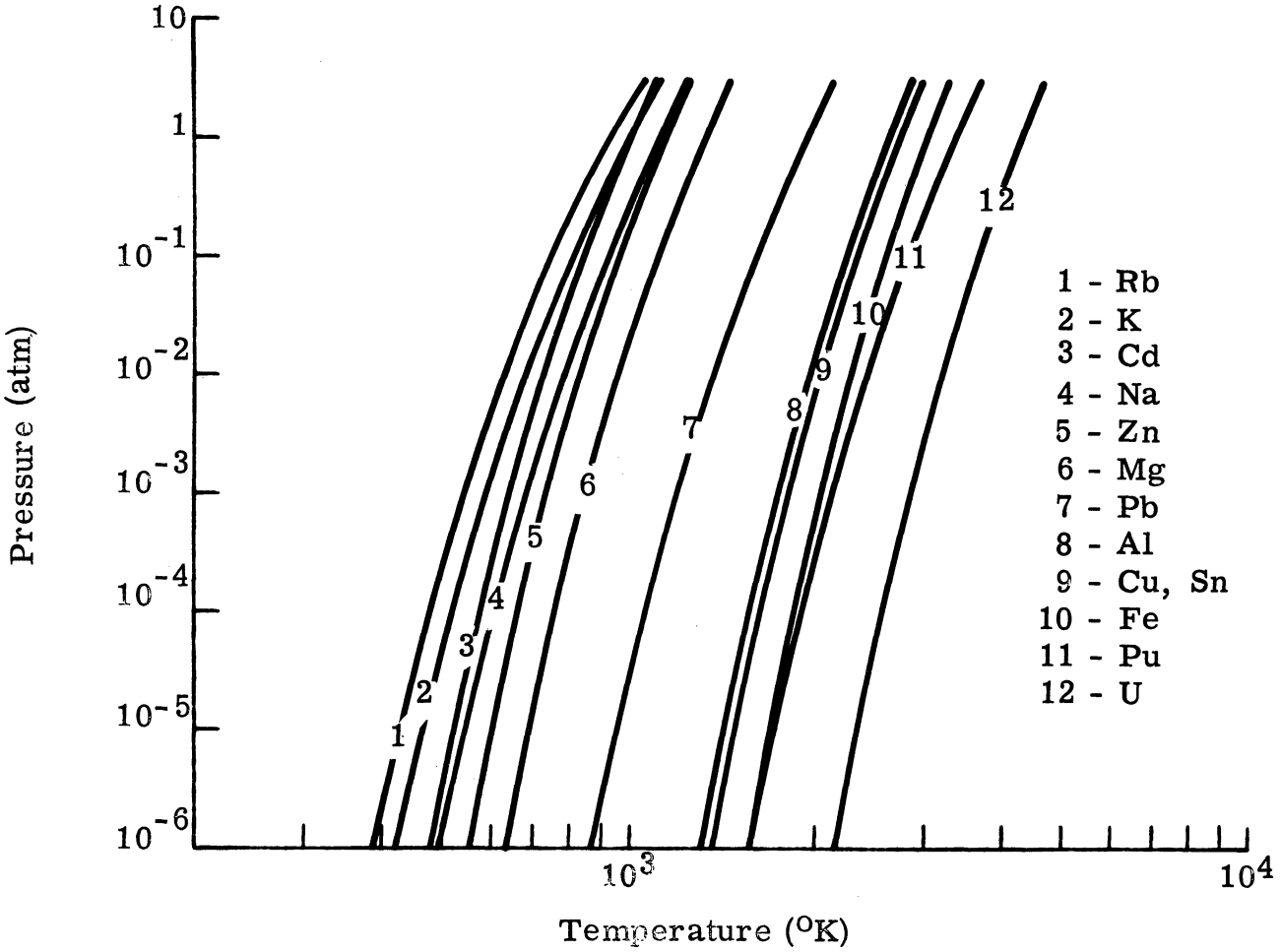

Figure 1. Saturated Vapor Pressure Curves for Various Metals

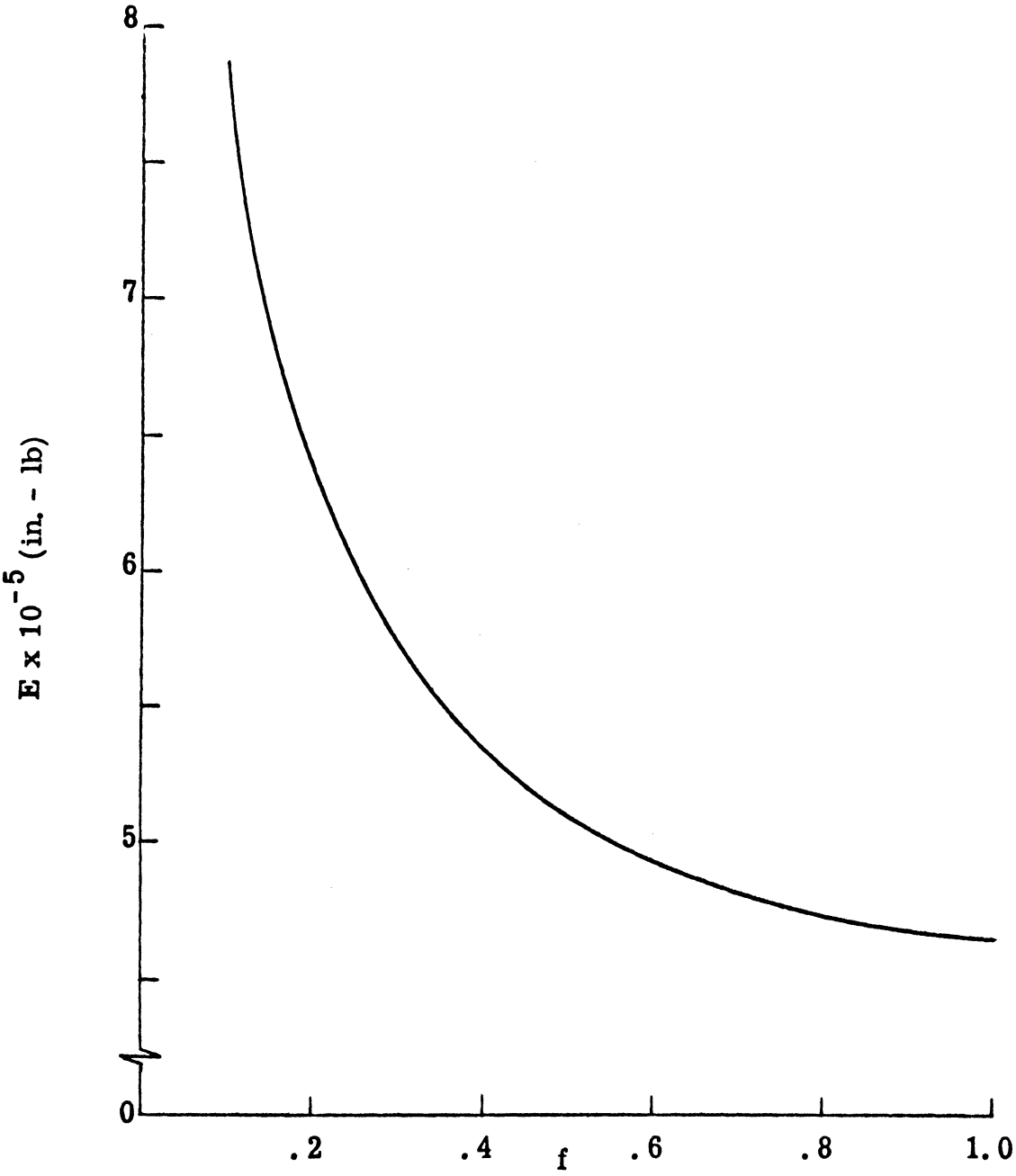

Figure 2. Energy Requirement for Producing a Zinc-Helium Mixture at 5000 psia, 5000 ^{o}K. (Initial Temperature = 298 ^{o}K)

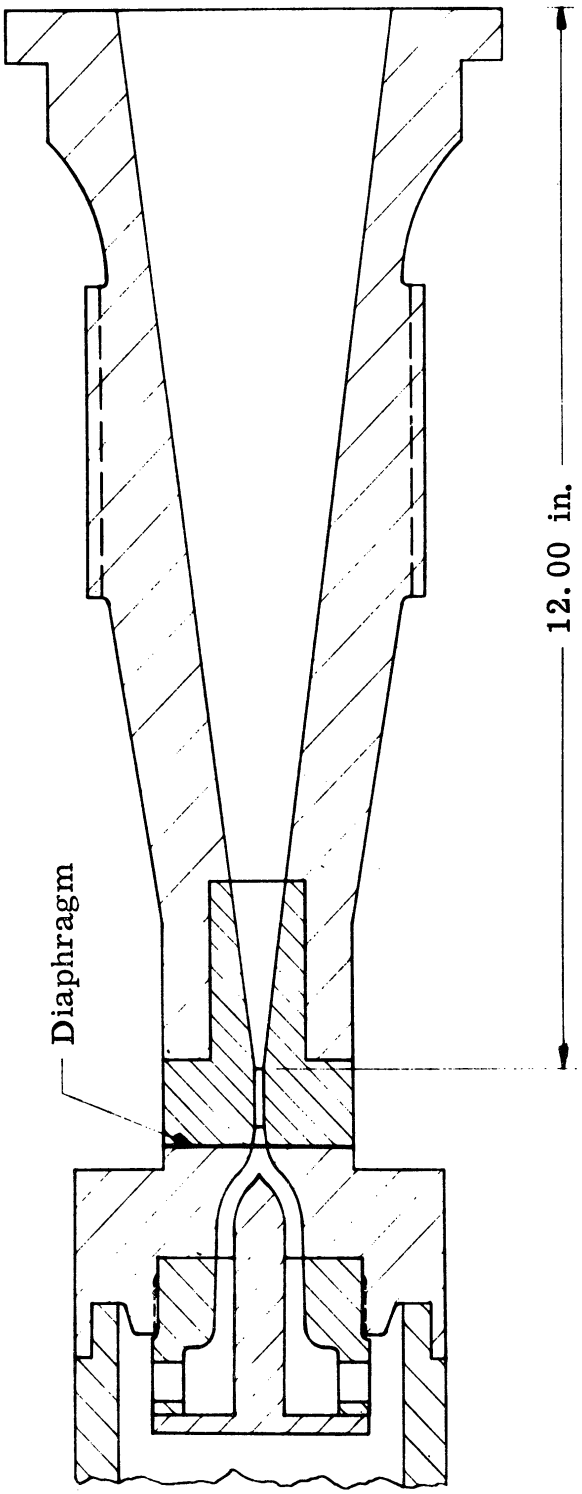

Figure 3. Sketch of Mach 25 Nozzle Installation

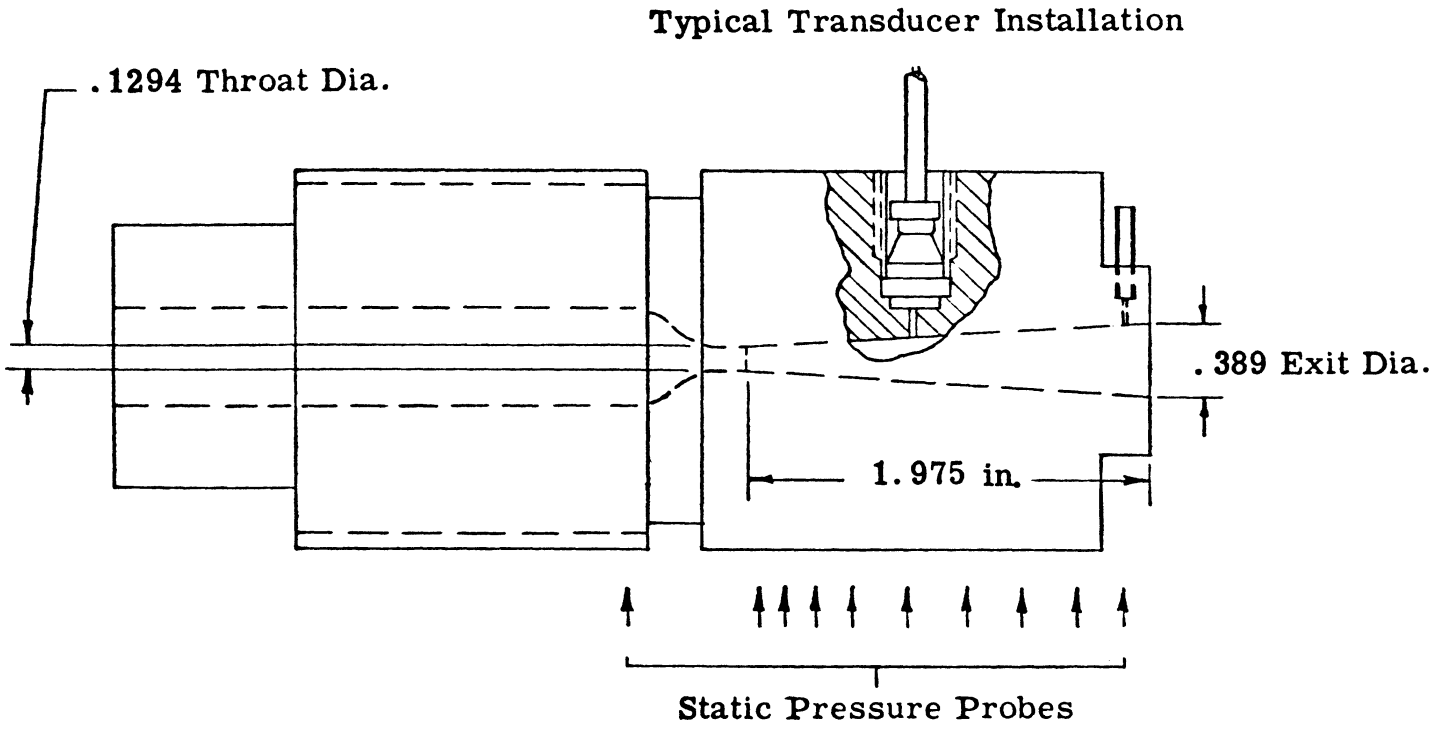

Figure 4. Mach 5 Nozzle

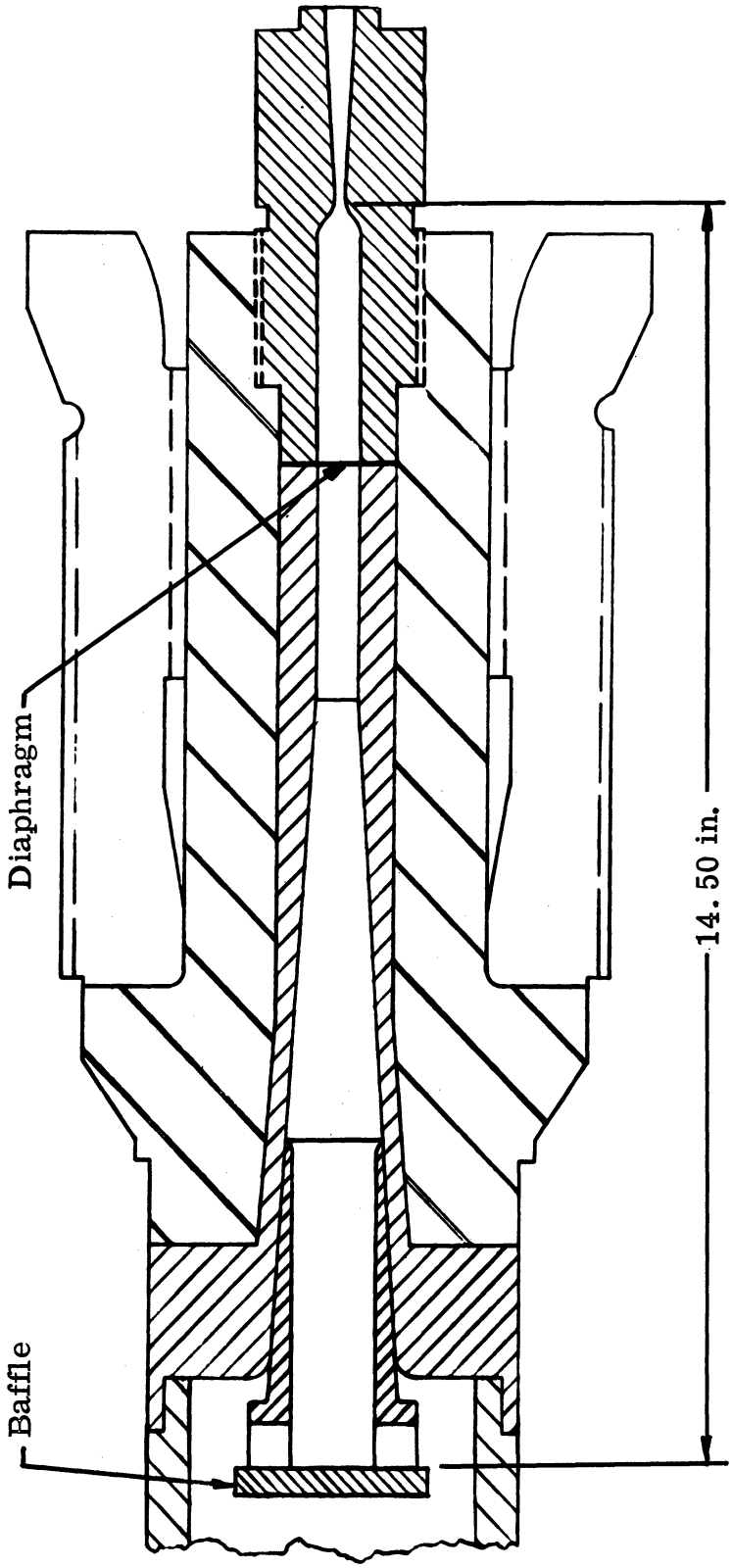

Figure 5. Sketch of Mach 5 Nozzle Installation

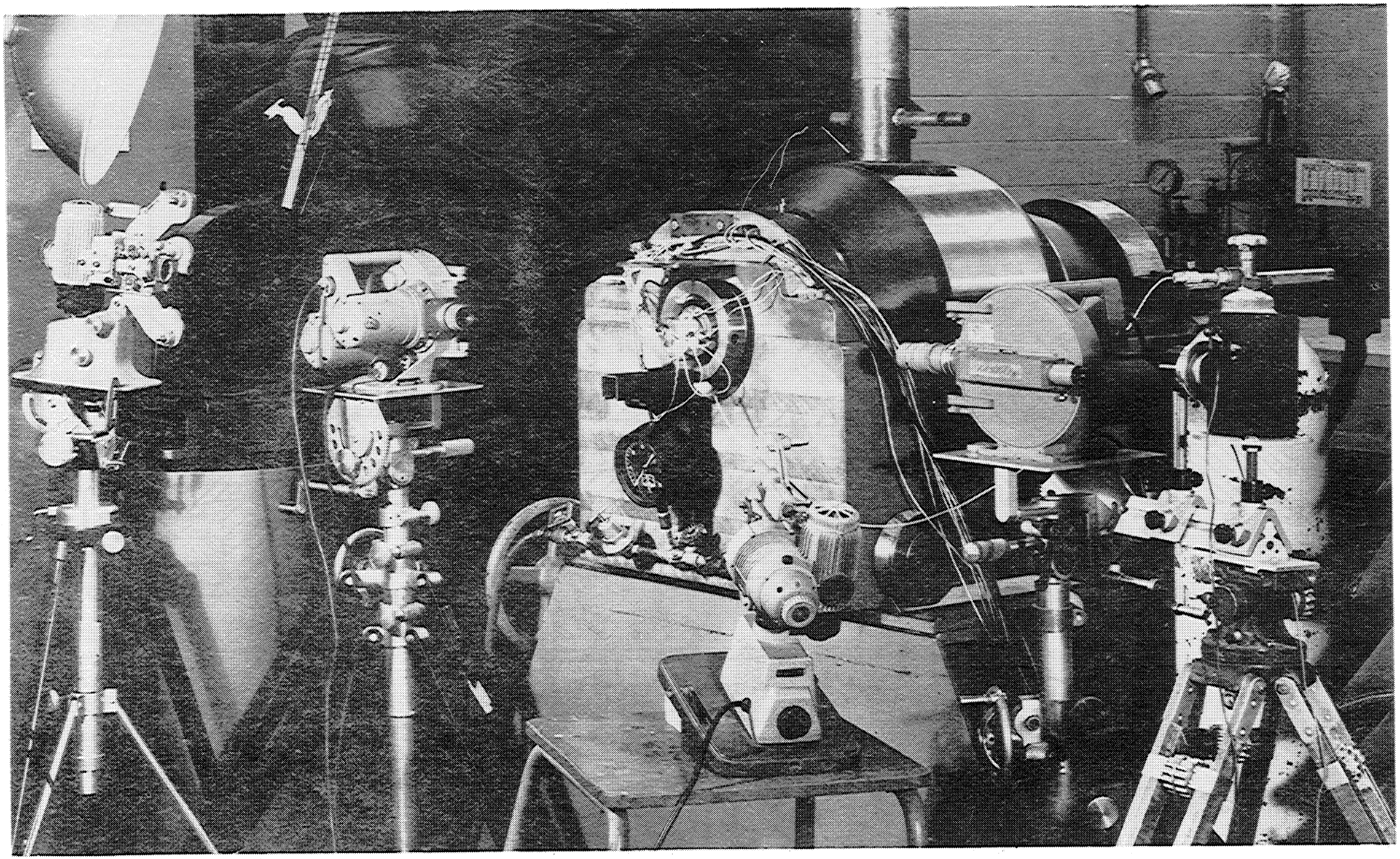

Figure 6. Static Pressure Measurement Experimental Setup

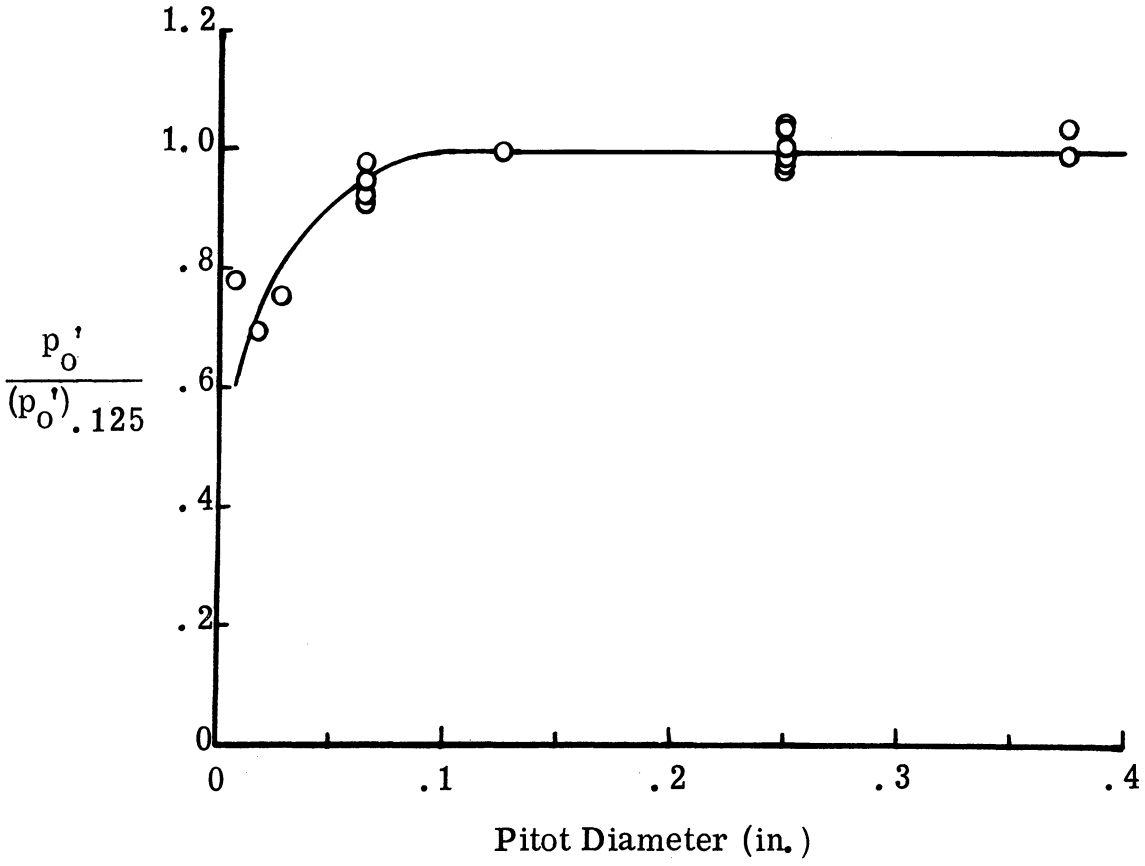

Figure 7. Pitot Pressure Dependence upon Pitot Tube Diameter

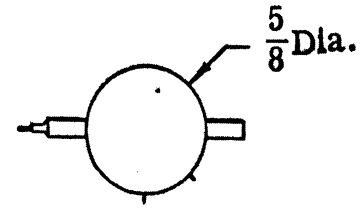

Actual Size of
Transducer and
Pitot Assembly

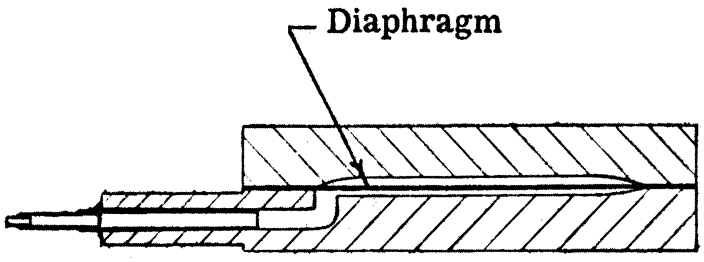

4X Section Showing Pitot
Installed in Transducer

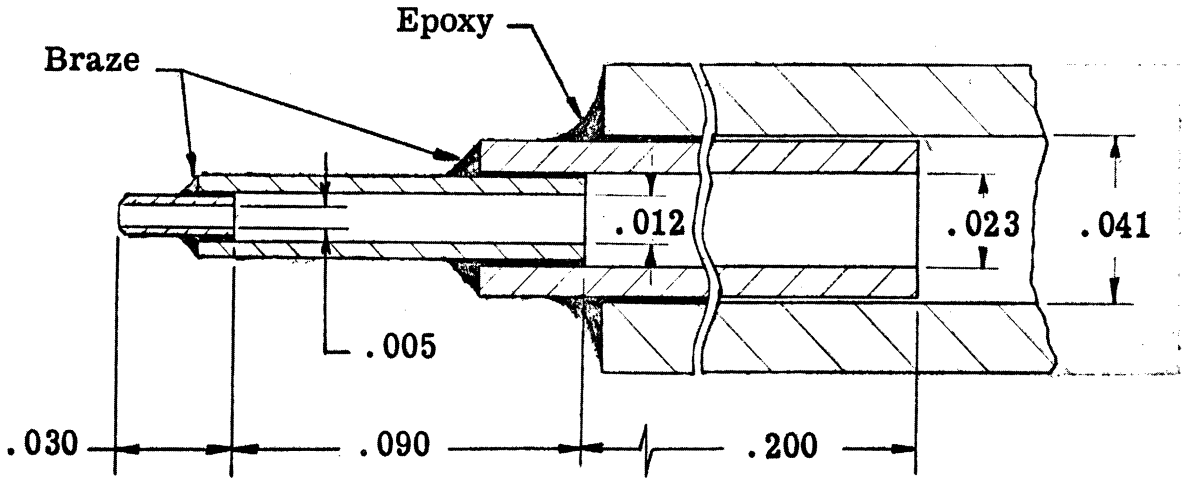

20X Section of Pitot Tube

Figure 8. Miniature Pitot Tube Configuration

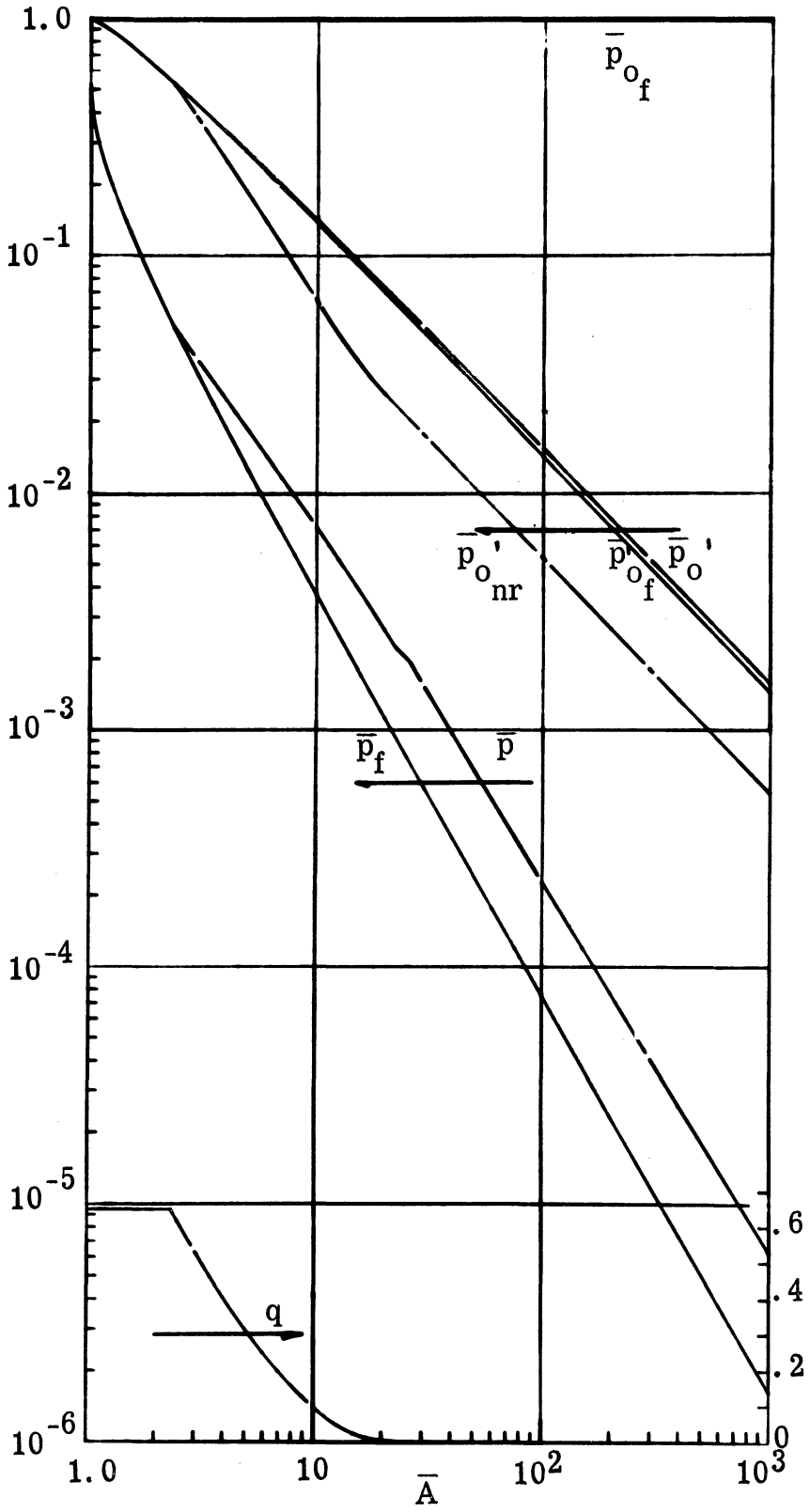

Figure 9. Saturated Equilibrium Expansion ("Exact Solution") (p_c = 4000 psia, T_c = 4000°K, f = 0.35)

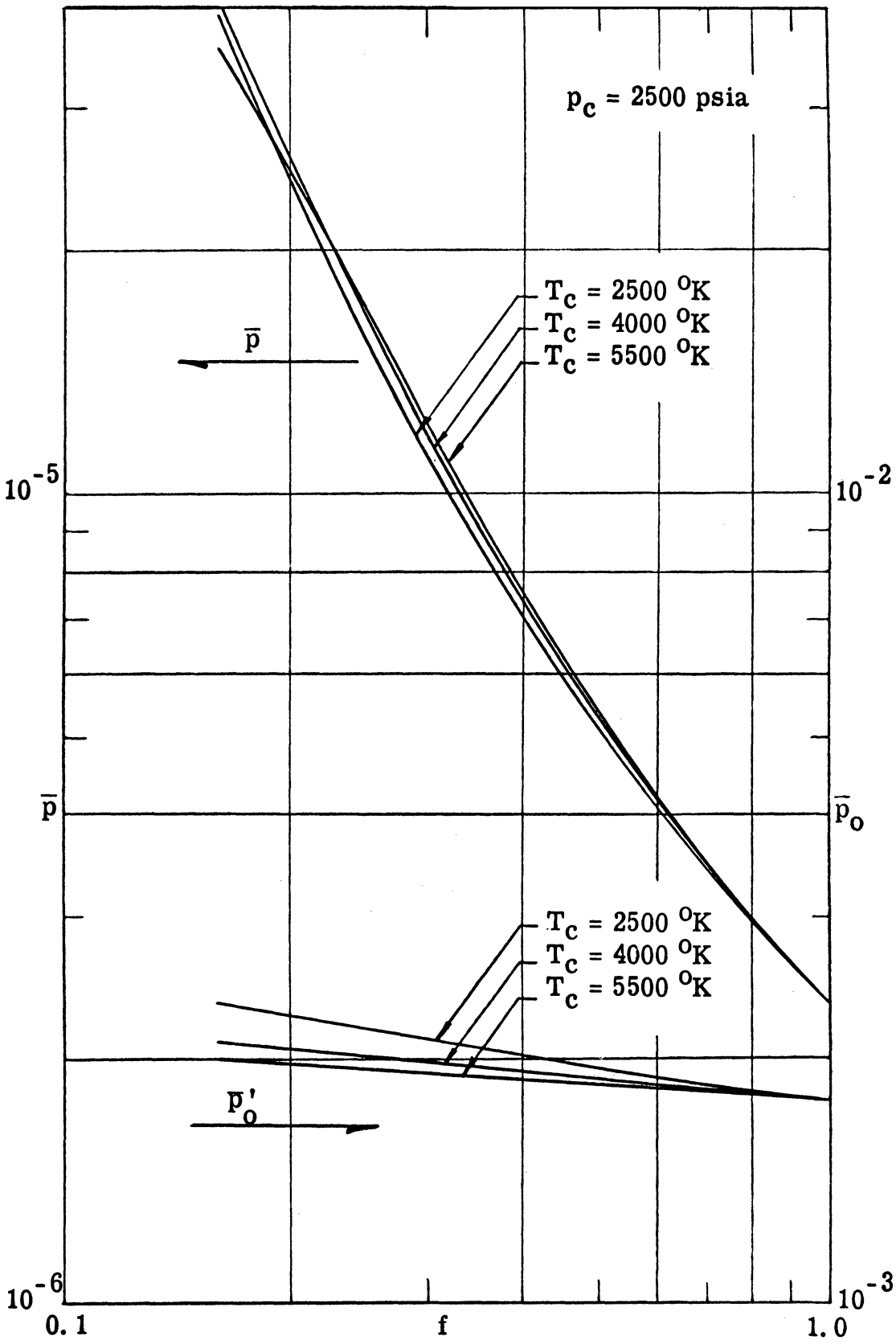

Figure 10. Static Pressure and Pitot Pressure as a Function of Carrier Gas Mass Fraction ($\bar{A}$ = 800).

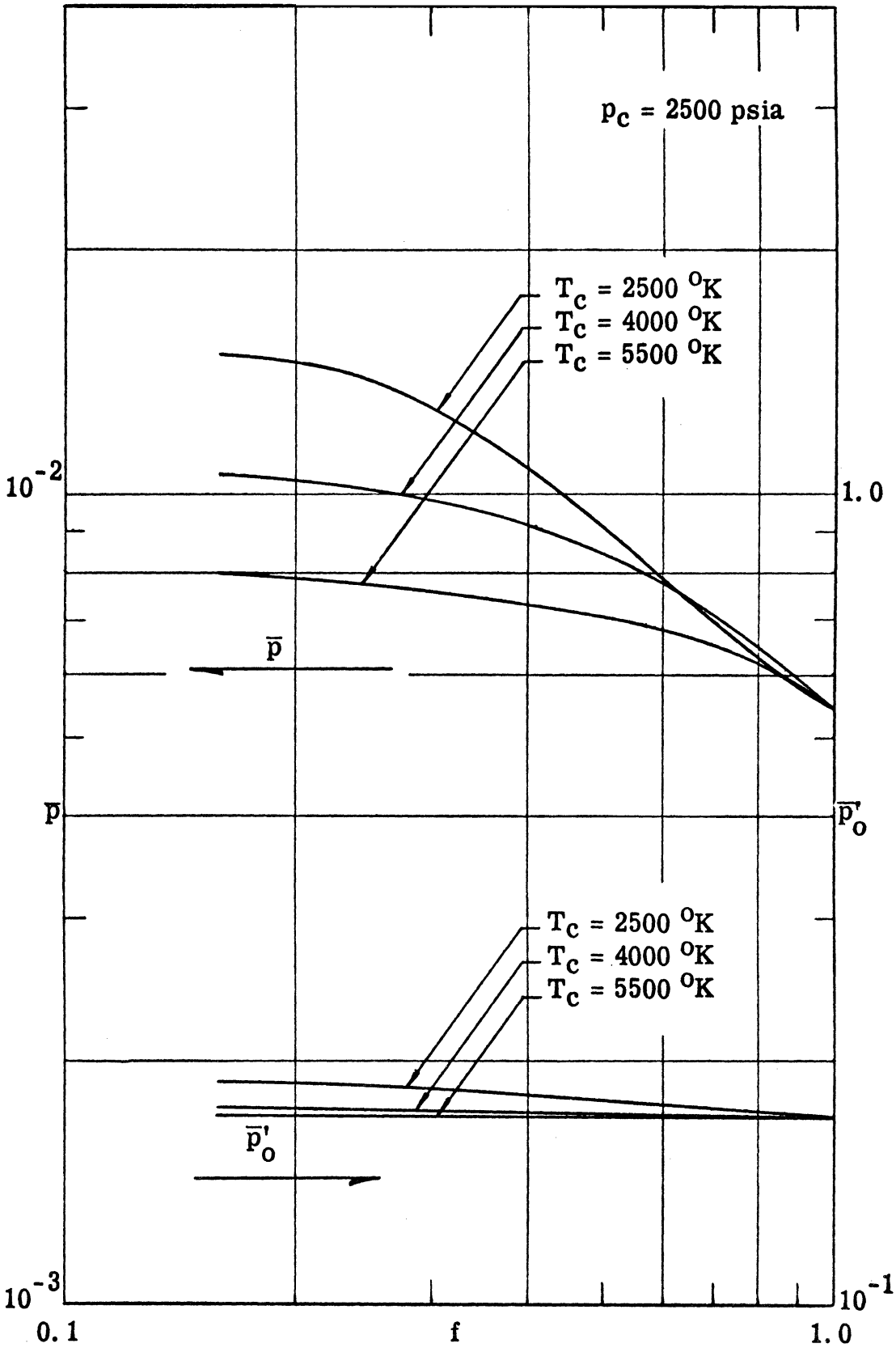

Figure 11. Static Pressure and Pitot Pressure as a Function of Carrier Gas Mass Fraction ($\bar{A}$ = 8).

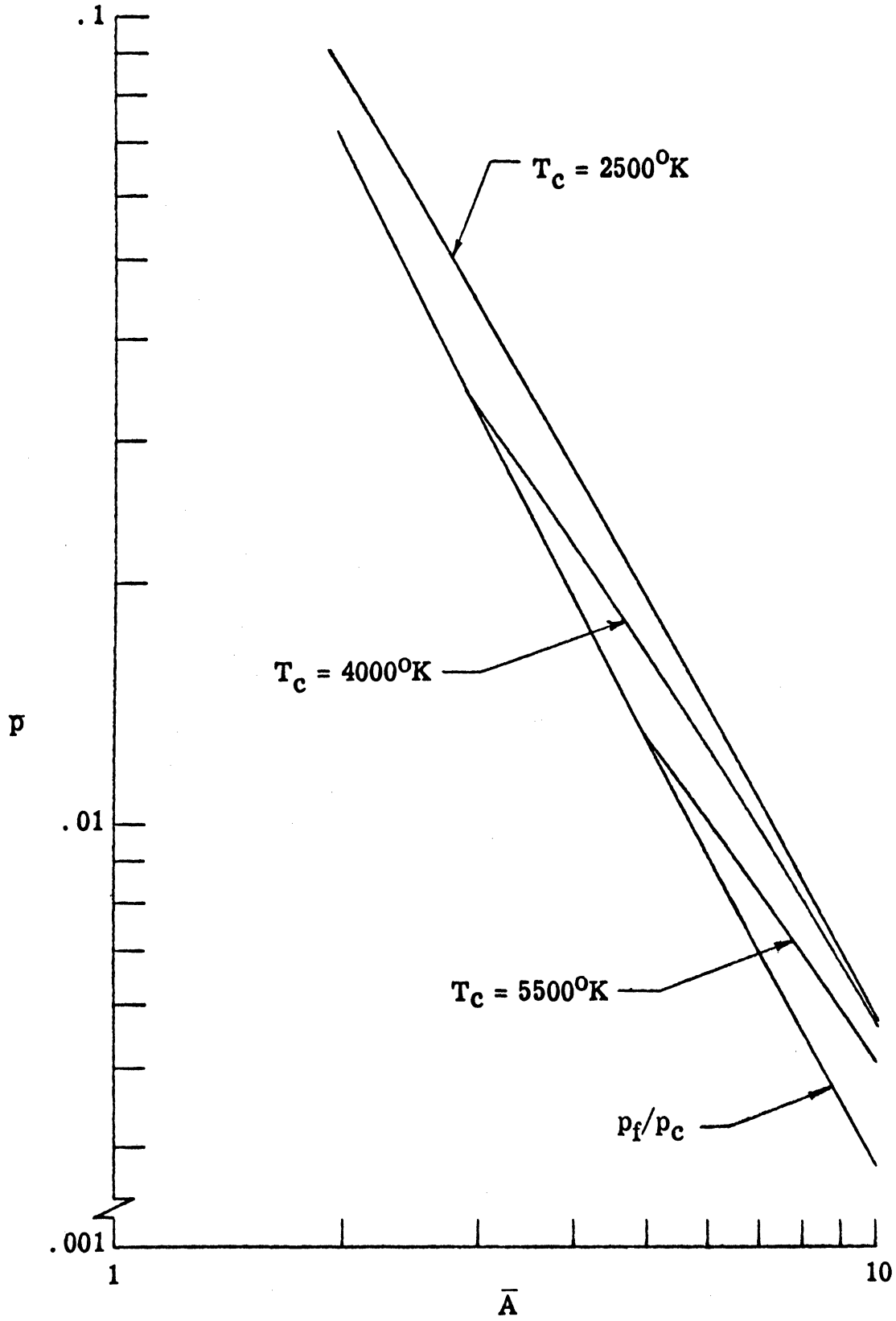

Figure 12. Saturated Equilibrium Expansion
(f = .55, p_c = 2500 psia, T_c = 2500°K, 4000°K, 5500°K)

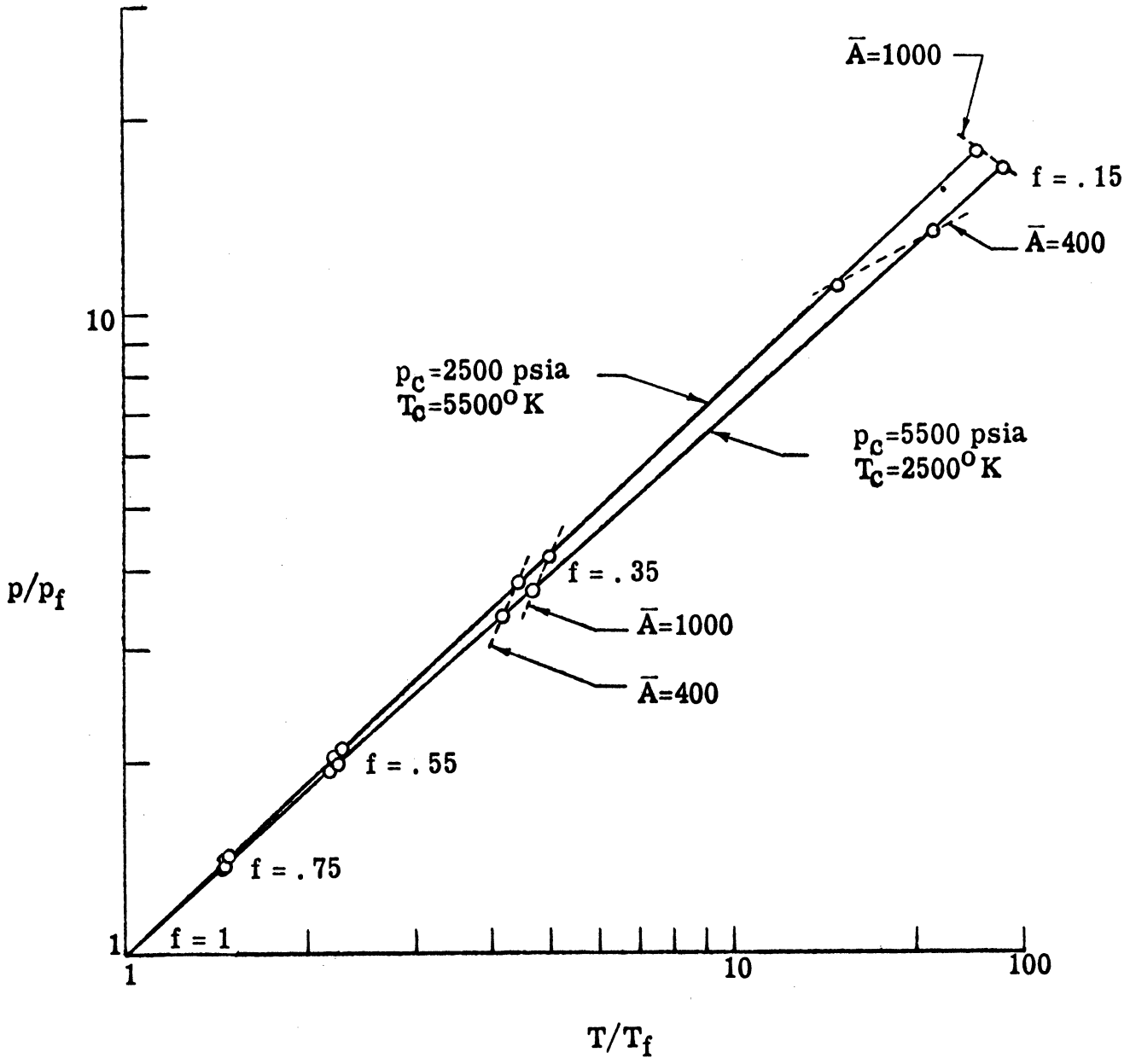

Figure 13. Comparison of Pressures and Temperatures for Frozen and Equilibrium Flow for: $400 \leq \bar{A} \leq 1000$, $2500^{o}K \leq T_c \leq 5500^{o}K$, 2500 psia $\leq p_c \leq$ 5500 psia, $.15 \leq f \leq 1.0$.

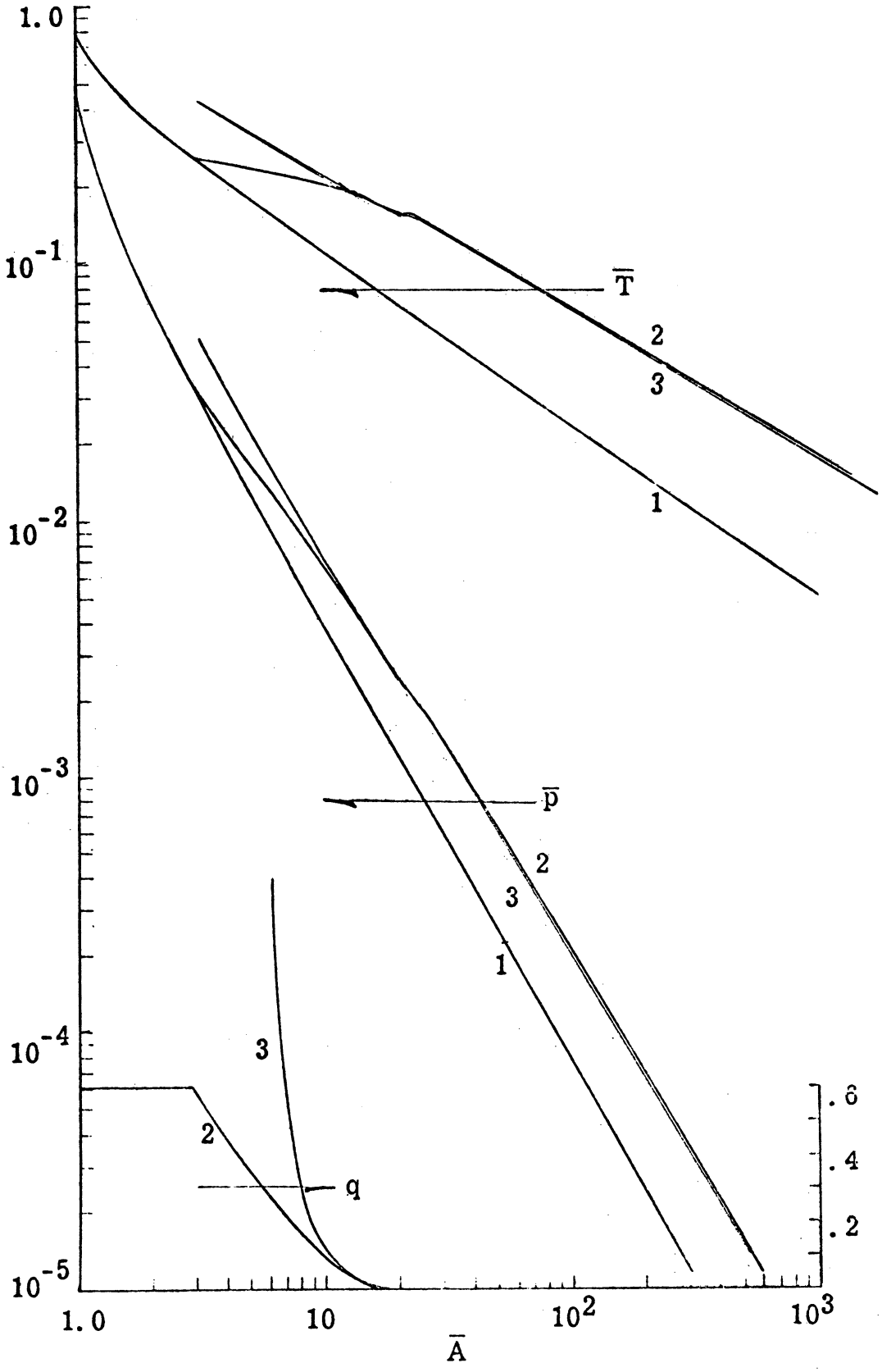

Figure 14. Comparison of Various Saturated Equilibrium Expansions (p_c = 4500 psia, T_c = 4500 °K, f = 0.40); Curves 1) frozen flow, 2) "exact" solution and Eq. D-21, 3) Eq. D28.

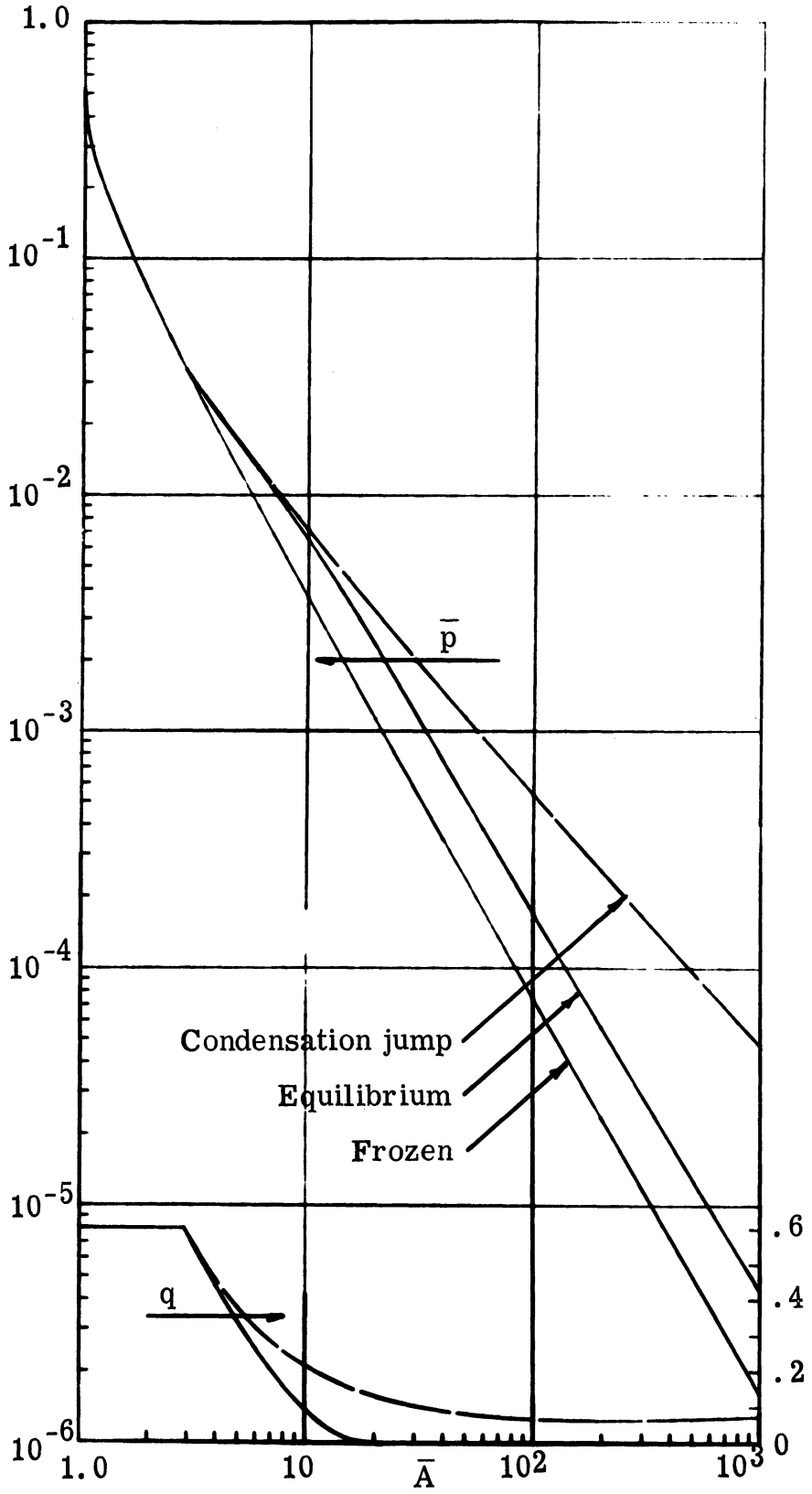

Figure 15. Comparison of Condensation Jump Locus of Solutions with Saturated Equilibrium Expansion (p_c = 4500 psia, T_c = 4500°K, f = 0.40)

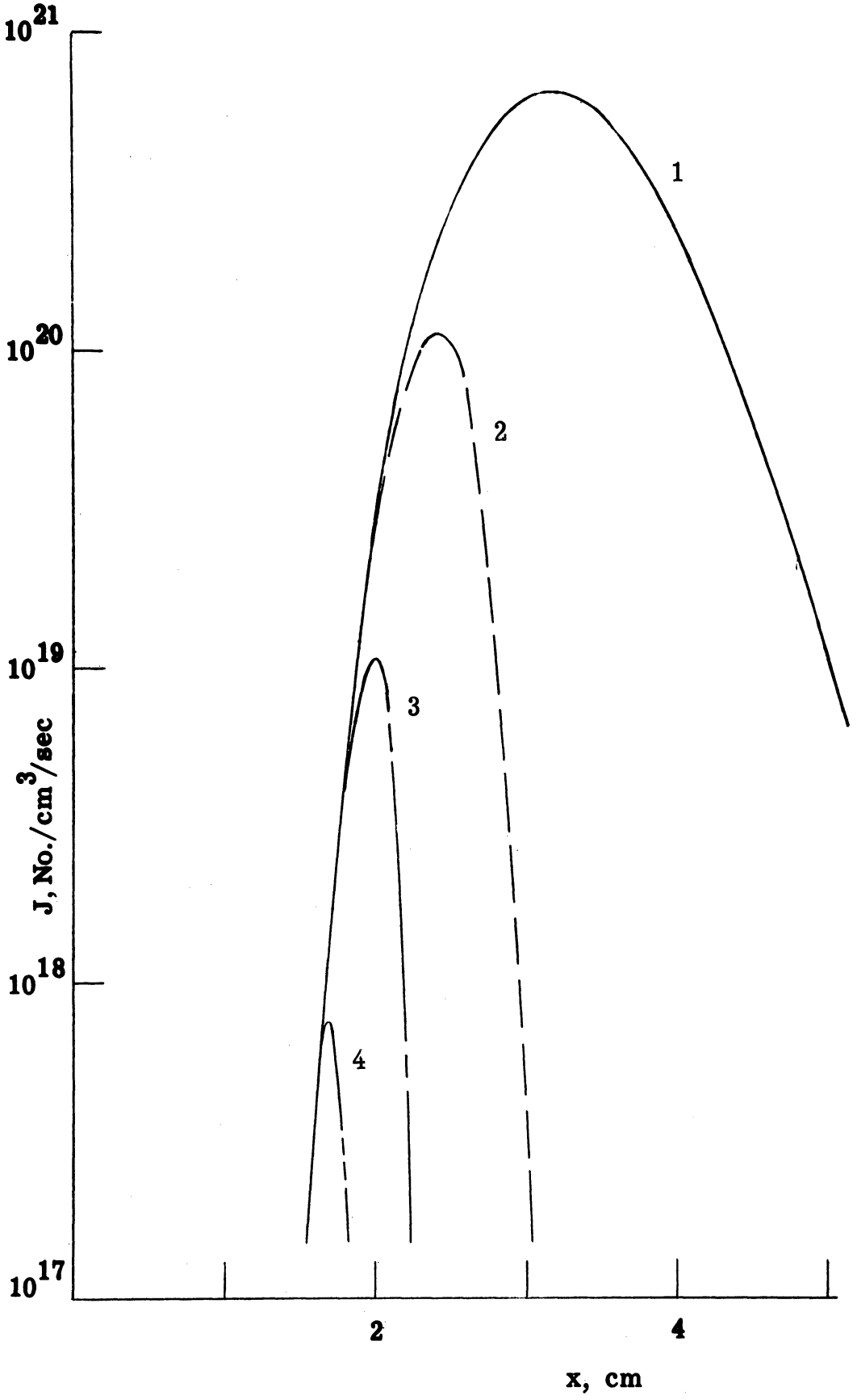

Figure 16. Effect of Growth Rate Equation for Constant p_c = 2500 psia, T_c = 2500°K, y = . 5. Curves are for Equations (F. 51), (F. 62), (F. 64), (F. 65) Respectively.

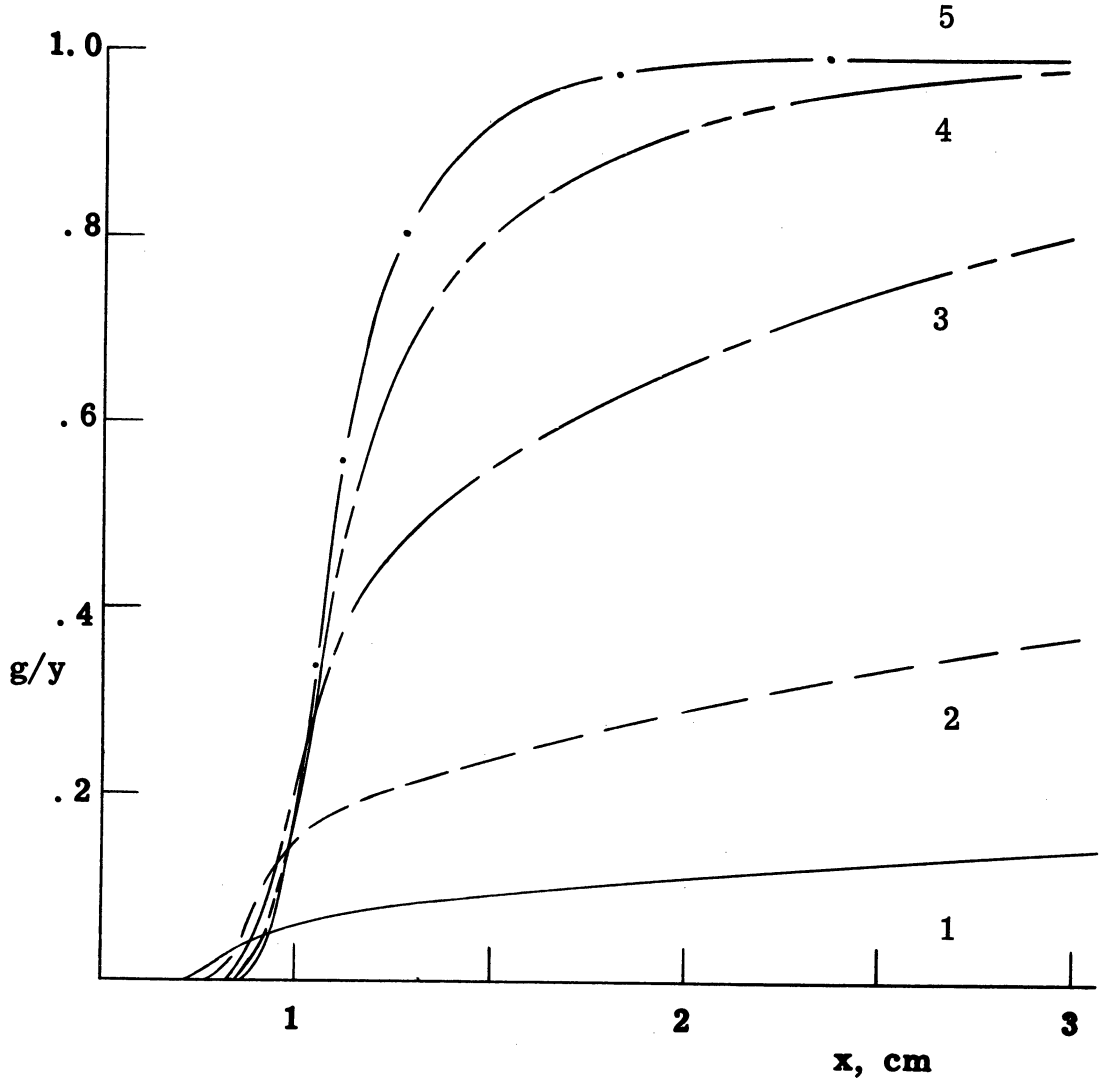

Figure 17. Effect of Initial Mass Fraction of Zinc on Fraction of Condensate for Constant p_{zo} = 888.2 psia, T_c = 2500°K. Curves are for y = 1.0, .9, .7, .5, and .3 respectively.

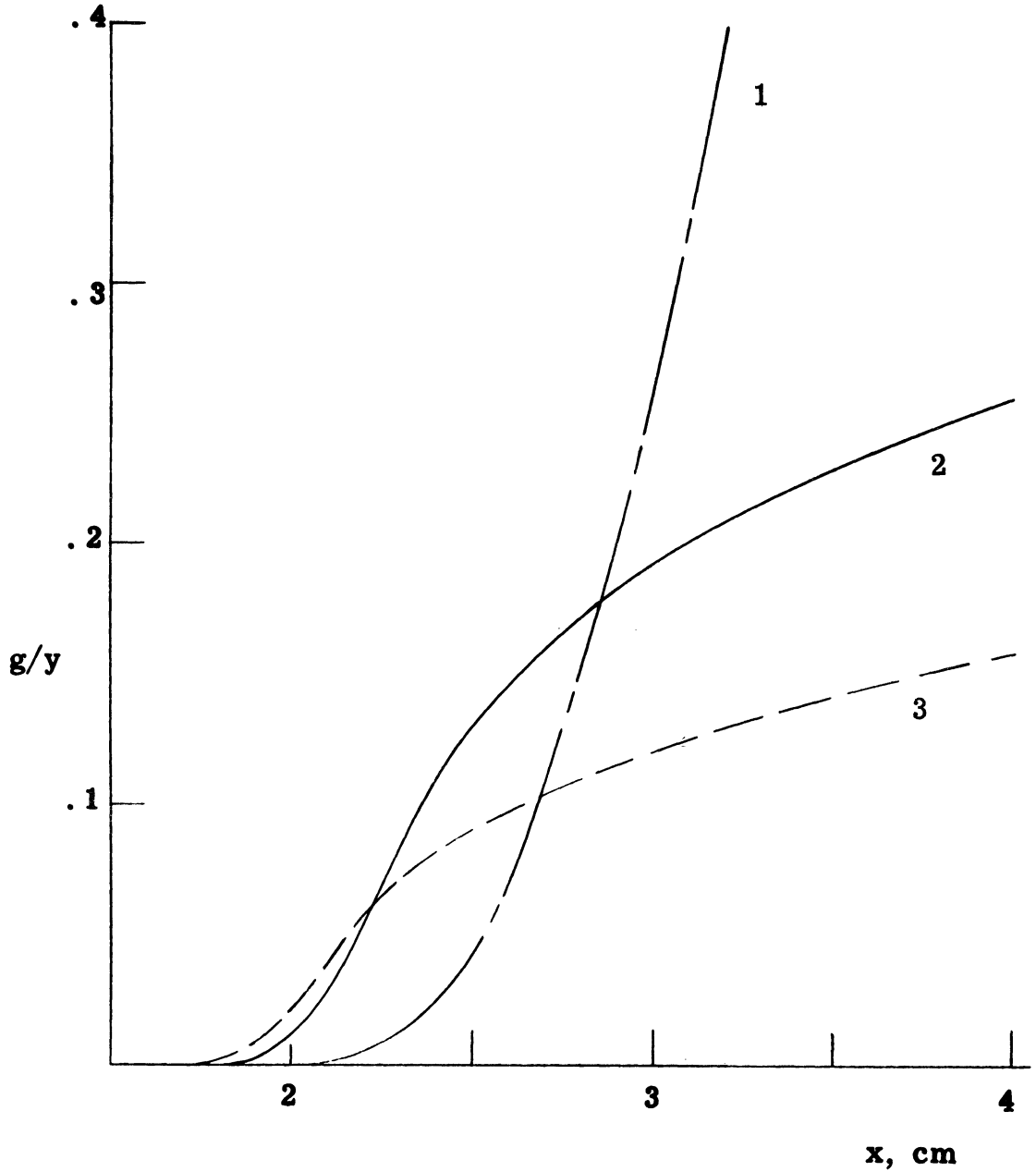

Figure 18. Effect of Molecular Weight of Carrier Gas on Fraction of Condensate for Constant p_{zo} = 144 psia, T_c = 2500°K, y = .5. Curves are for Carrier Molecular Weights of 4.003; 39.948; and 131.3 Respectively.

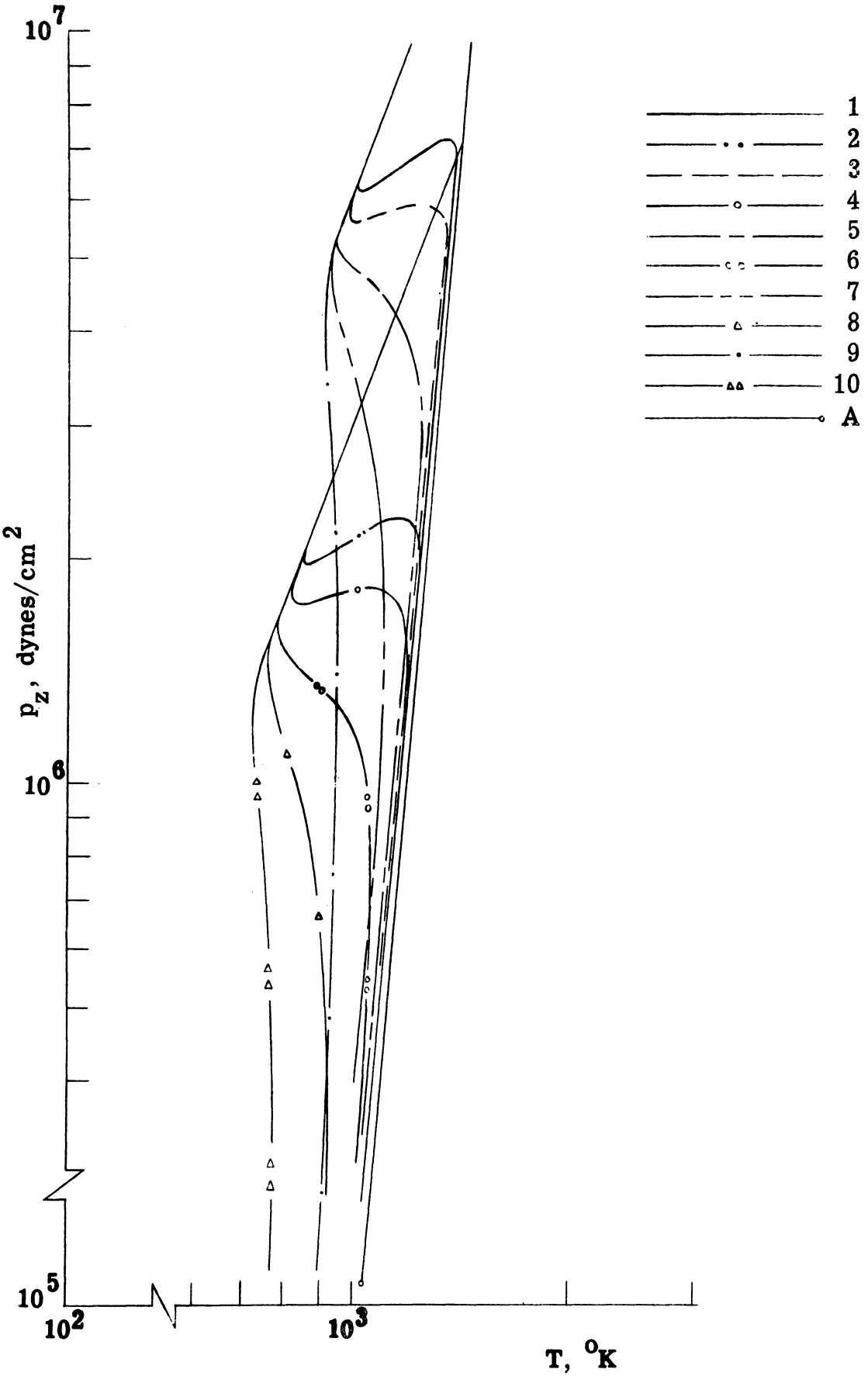

Figure 19. Effect of Initial Mass Fraction of Zinc for Two Sets of Constant Saturation Temperature and Partial Pressure. For Curves 1, 3, 5, 7, 9, T_c = 2500°K, p_{zo} = 882.2 psia; Curves 2, 4, 6, 8, 10, T_c = 4000°K, p_{zo} = 1421 psia, (y = 1.0, .9, .7, .5, .3 respectively). Curve A is Saturation Curve.

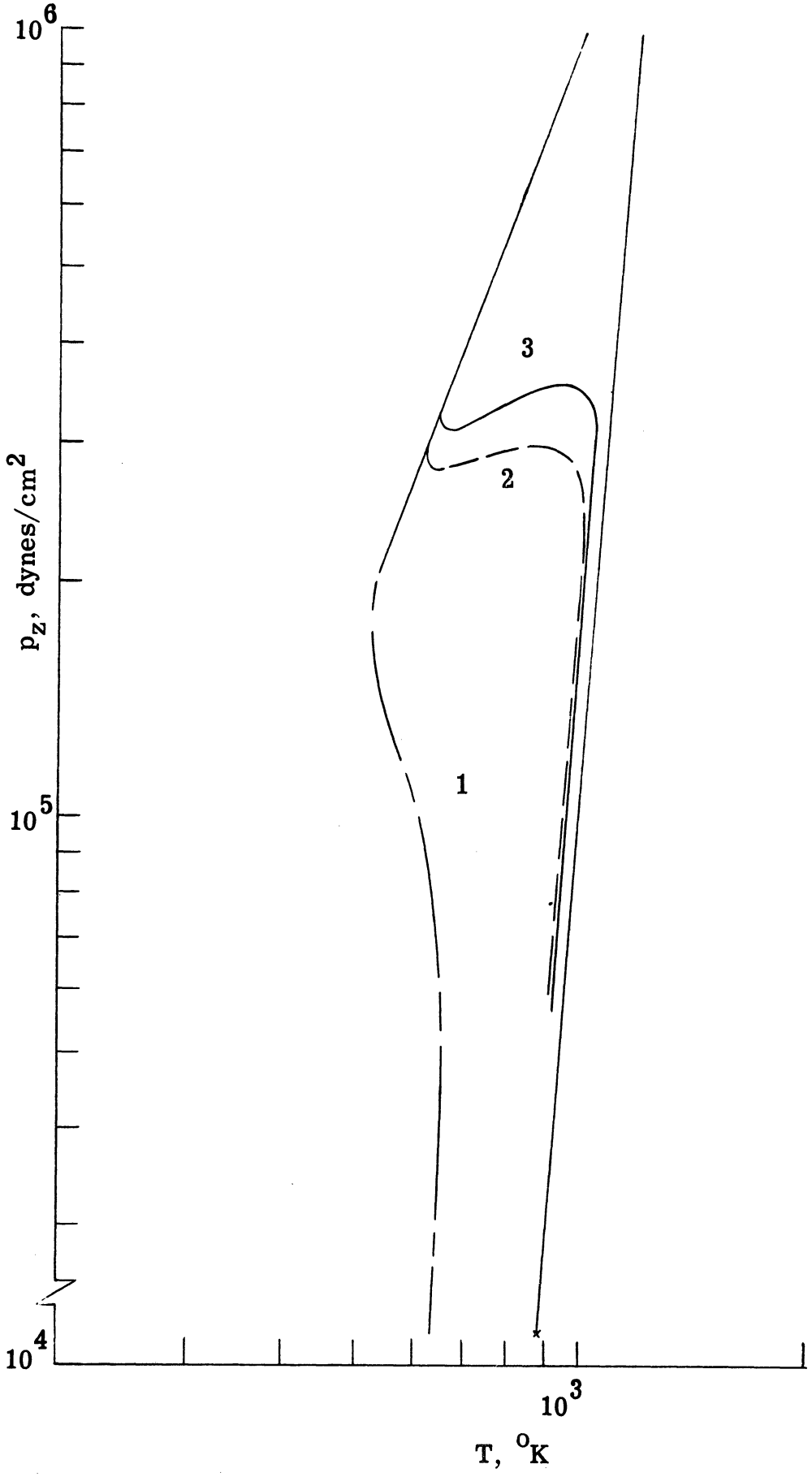

Figure 20. Effect of Molecular Weight of Carrier Gas on Start of Condensation for Constant T_c = 2500°K, p_{zo} = 144 psia, y = .5. Curves are for Carrier Molecular Weight of 4.003, 39.948, and 131.3 Respectively.

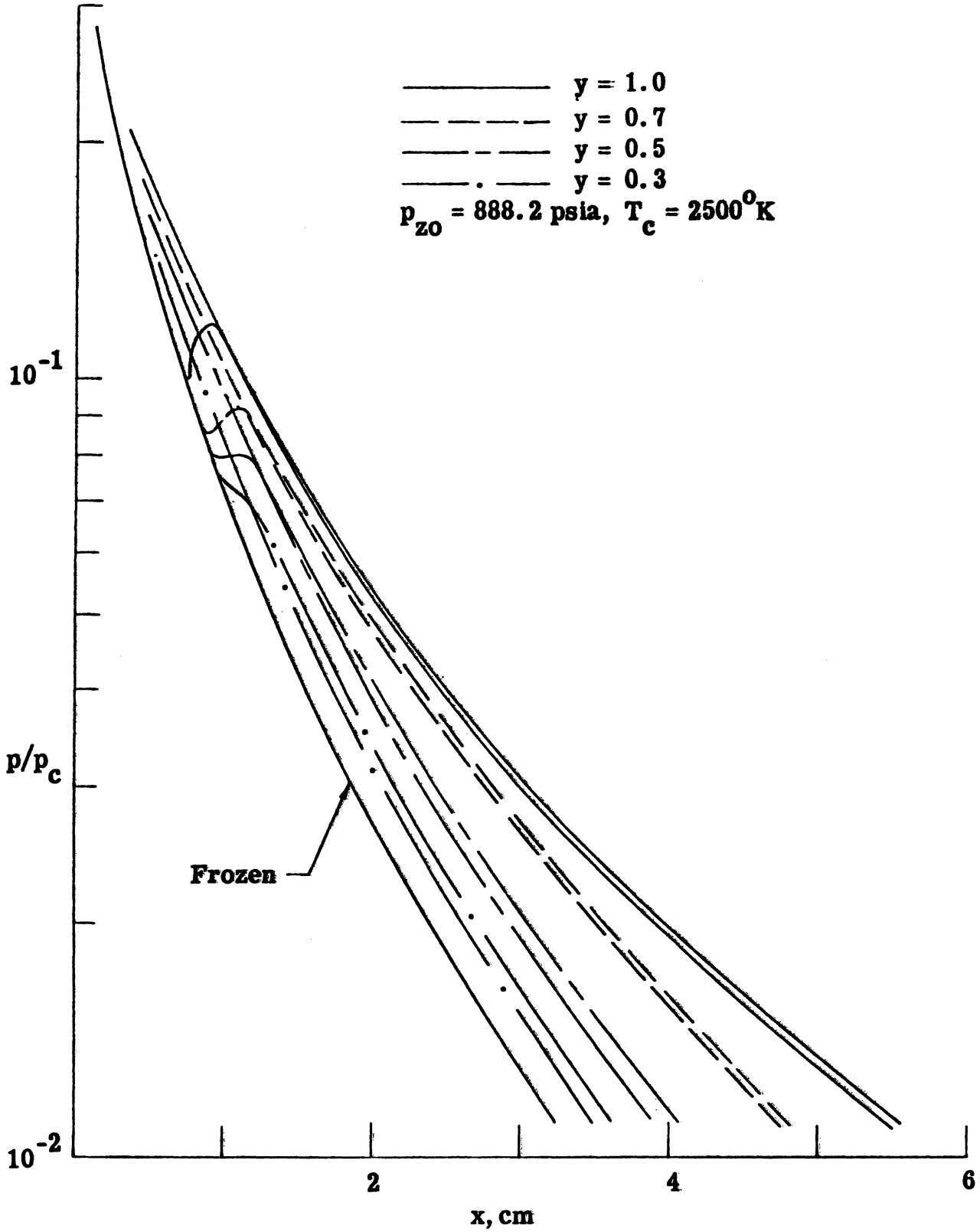

Figure 21. Effect of Initial Mass Fraction of Zinc on Pressure for Constant Initial Partial Pressure. (Expansion for equilibrium condensation is included in each case.)

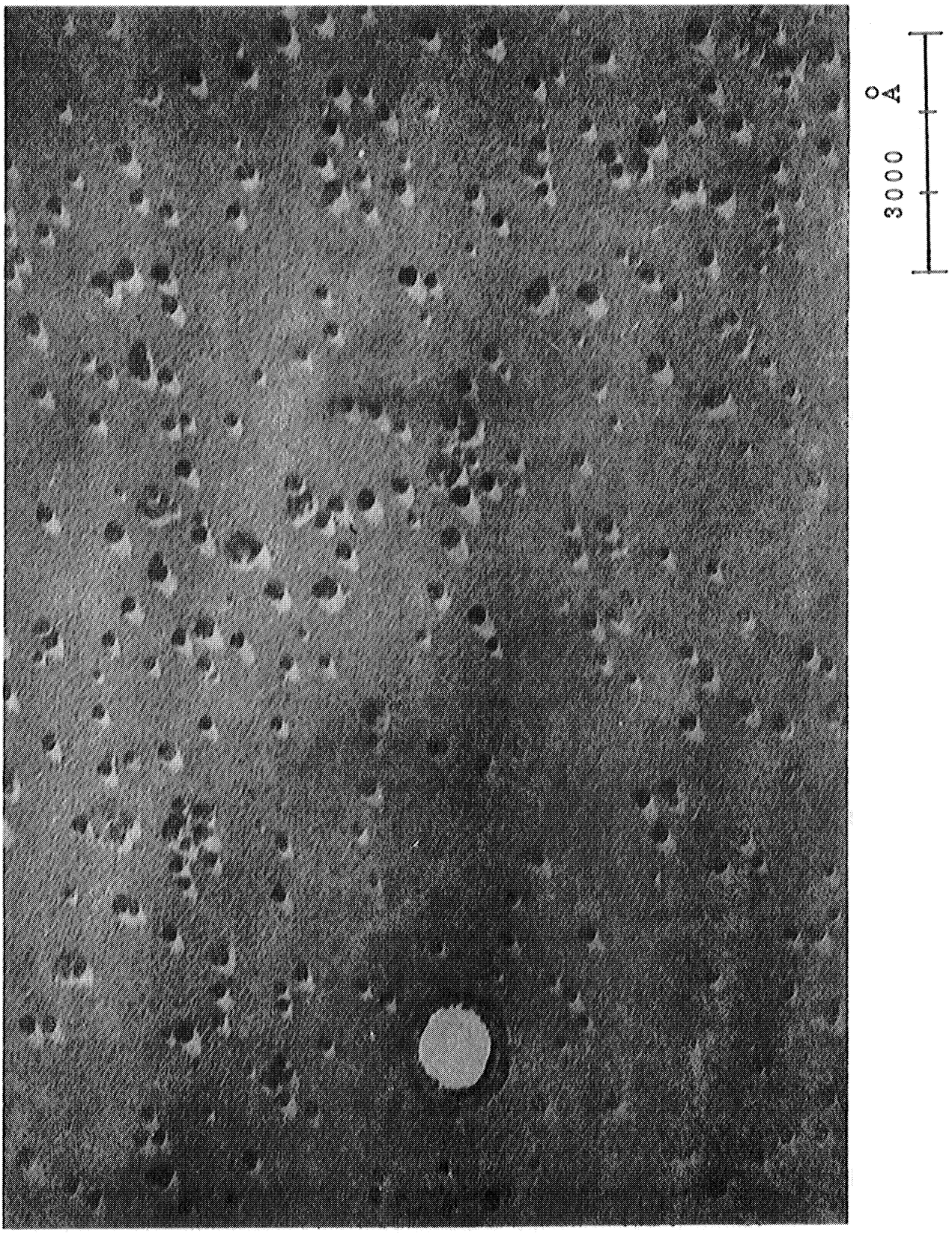

Figure 22. Photomicrograph of Collected Particles; 132,000X (Run 80514, 22.4 msec, p_c = 2259 psia, T_c = 2338°K, f = 0.215)

Figure 23. Photomicrograph of Collected Particles; 33,000X (Run 80514, 22.4 msec, p_c = 2259 psia, T_c = 2338 °K, f = 0.215)

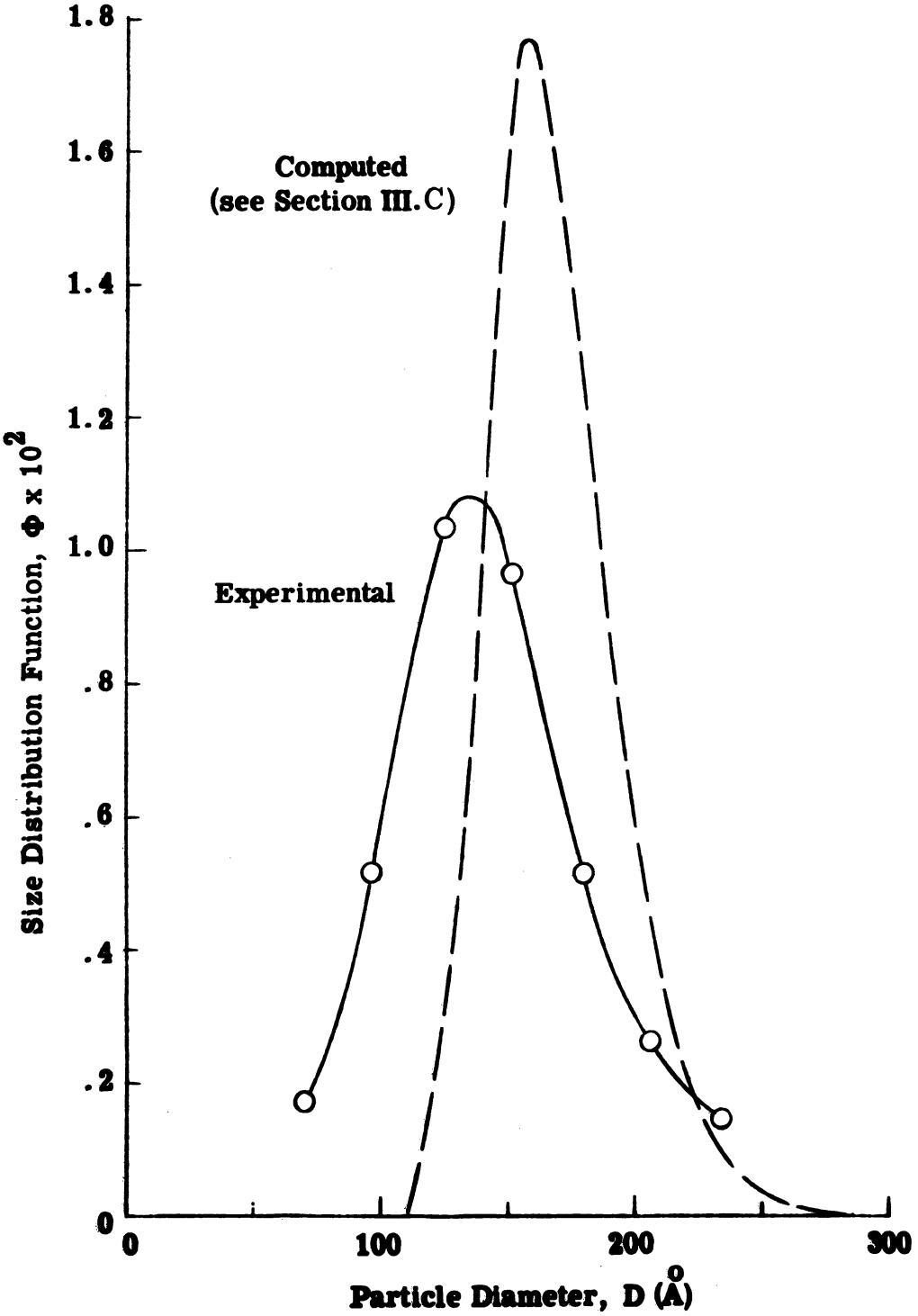

Figure 24. Particle Size Distribution (Run 80514, 22.4 msec, p_c = 2259, T_c = 2338 °K, f = 0.215)

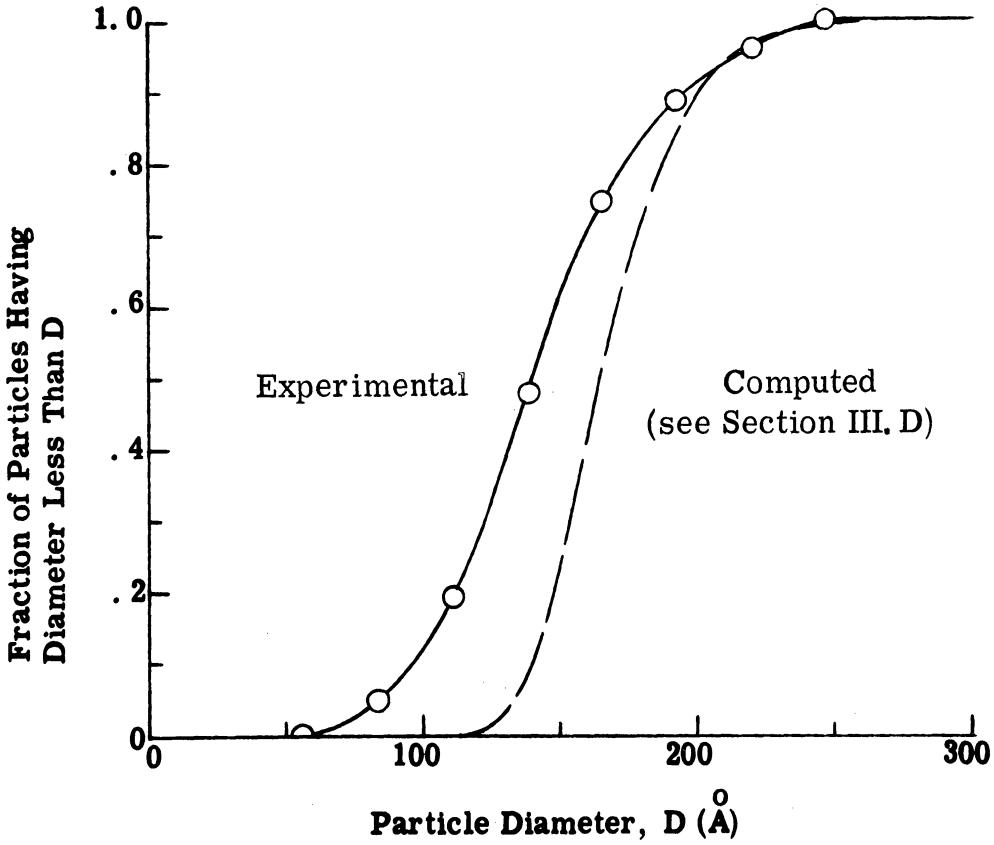

Figure 25. Fraction of Particles Smaller than D vs. D (Run 80514, 22.4 msec, p_c = 2259 psia, T_c = 2338 °K, f = 0.215)

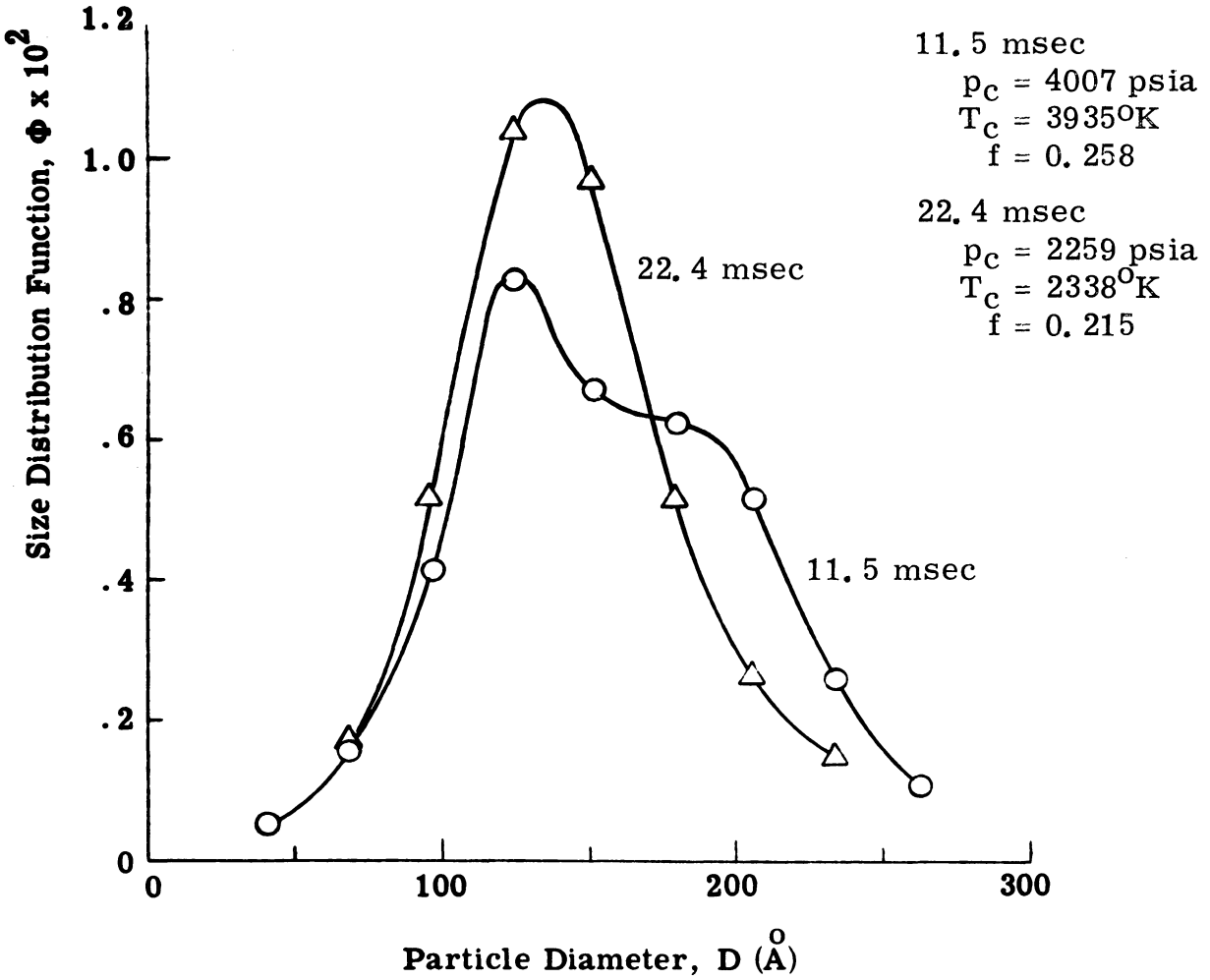

Figure 26. Particle Size Distribution (Run 80514, 11.5 msec, p_c = 4007 psia, T_c = 3935 °K, f = 0.258)

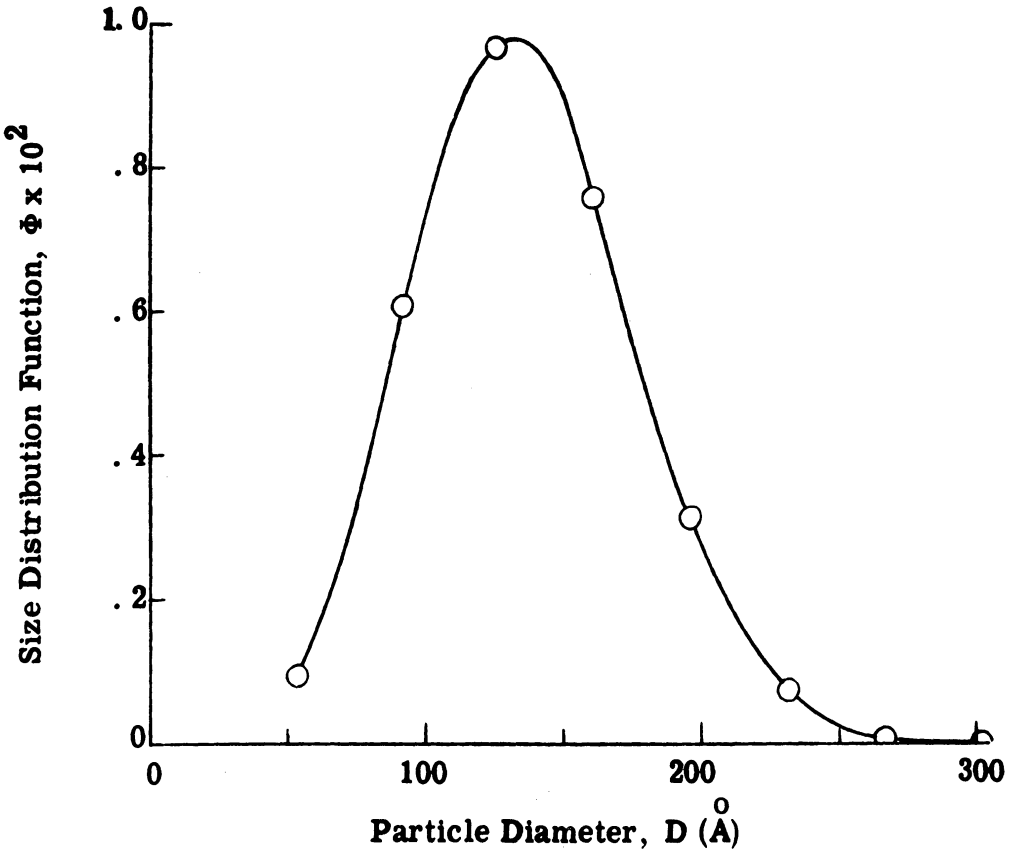

Figure 27. Particle Size Distribution (Run 80115, 22.8 msec, p_c = 2453 psia, T_c = 2644 °K, f = 0.280)

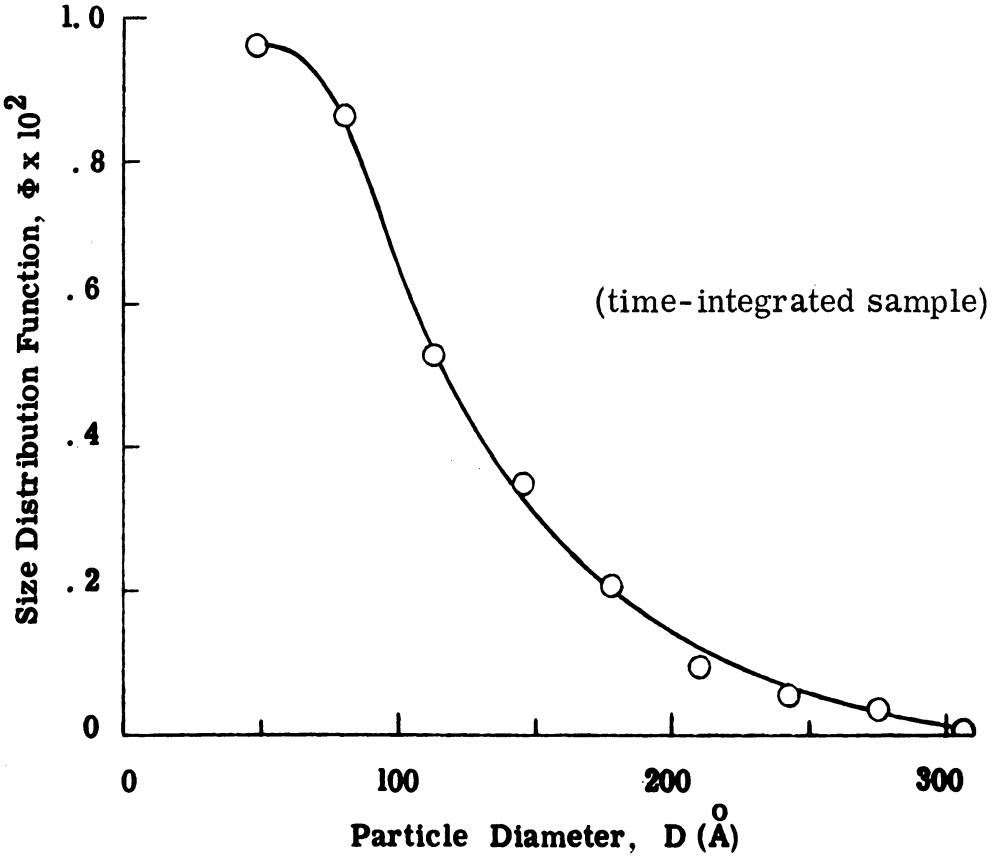

Figure 28. Particle Size Distribution of Particles Obtained Using the Mach 5 Nozzle; Sample Located on Rear of Pitot Sting

Figure 29. Photomicrograph of Particles Obtained Using the Mach 5 Nozzle; Sample Located Far Downstream of Nozzle Exit; 132,000X

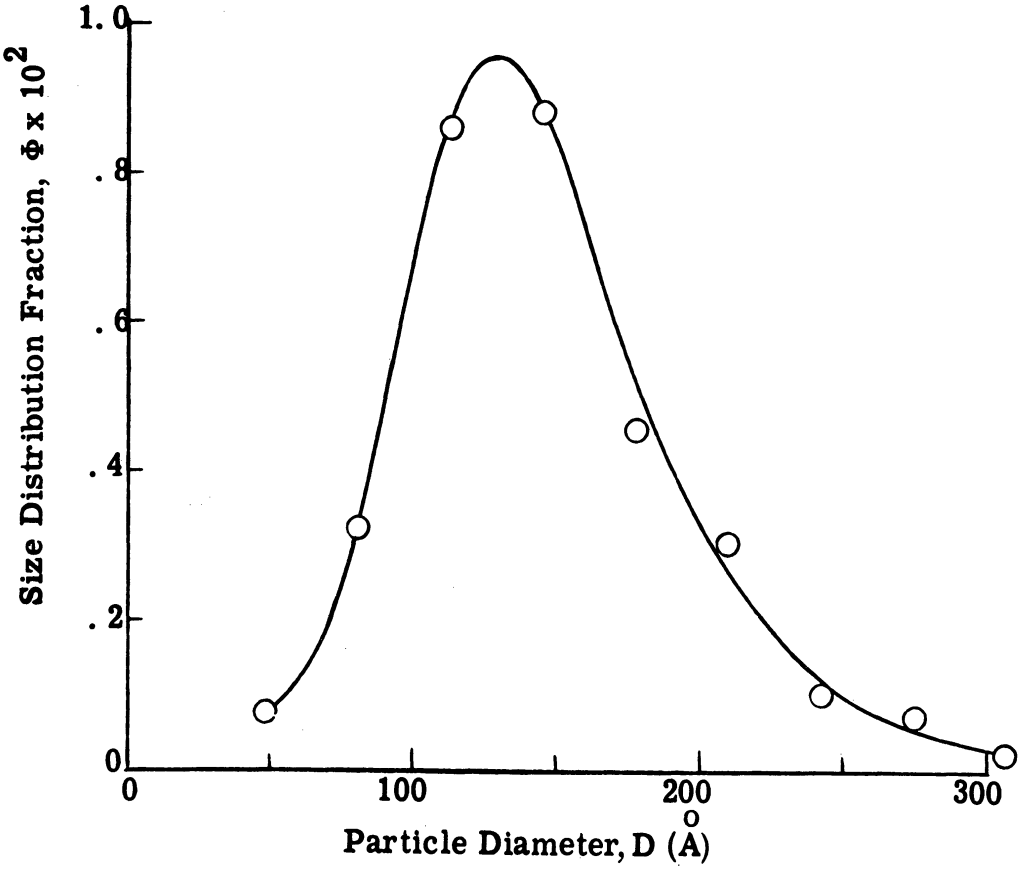

Figure 30. Particle Size Distribution of Particles Obtained on the Inside Wall of the Sampler (Run 80514)

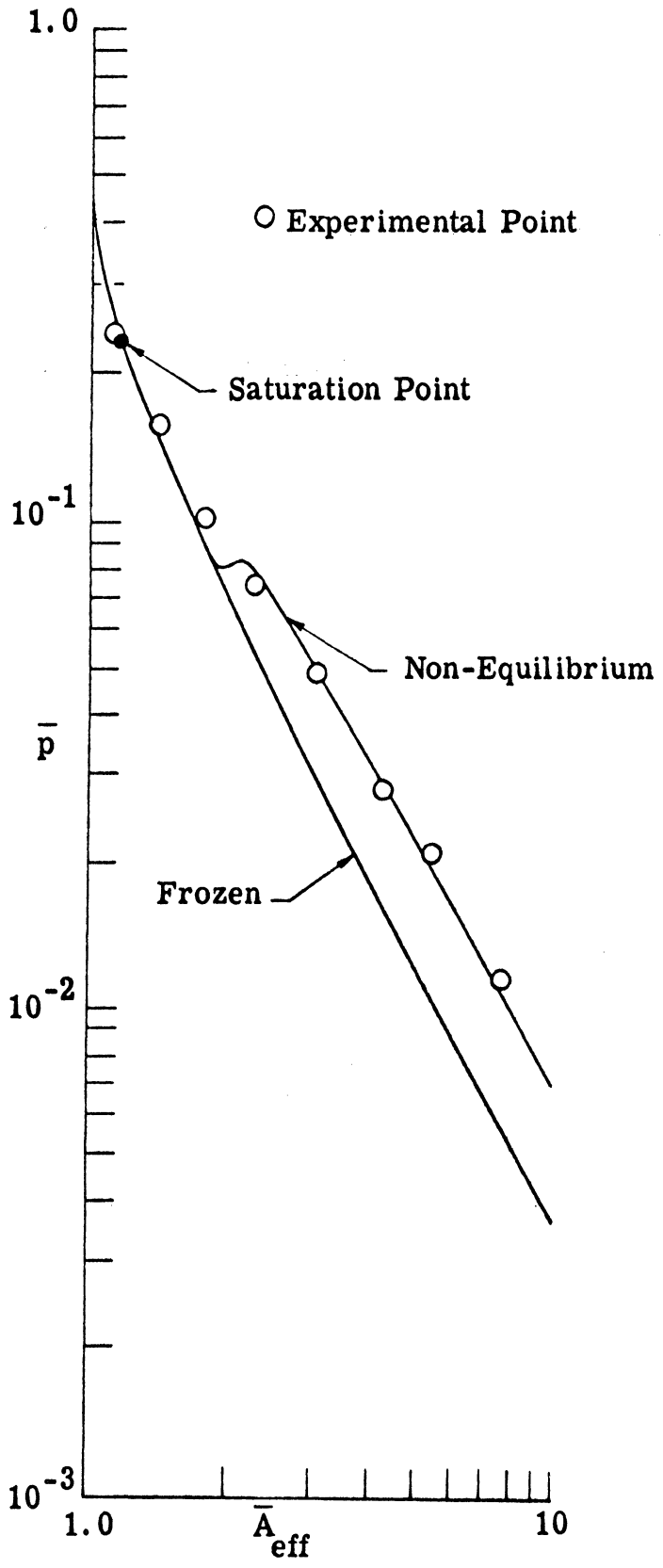

Figure 31. Static Pressure Expansion Profile (Run 80904, 22.5 msec, p_c = 1772, T_c = 2273°K, f = 0.409)

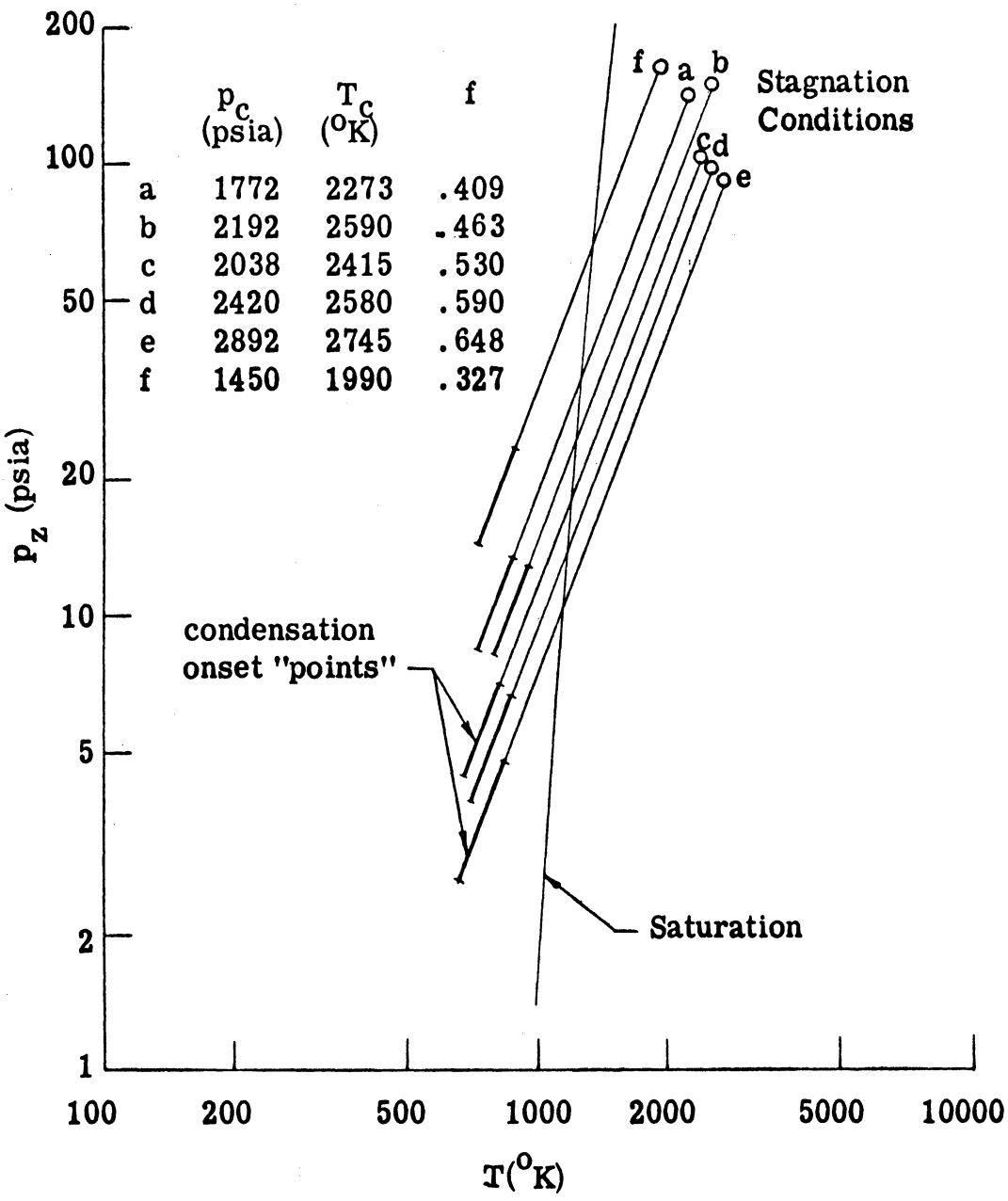

Figure 32. Region of Onset of Condensation.

$$T_o - T = \frac{2\sigma T_o v_B}{\lambda r}$$

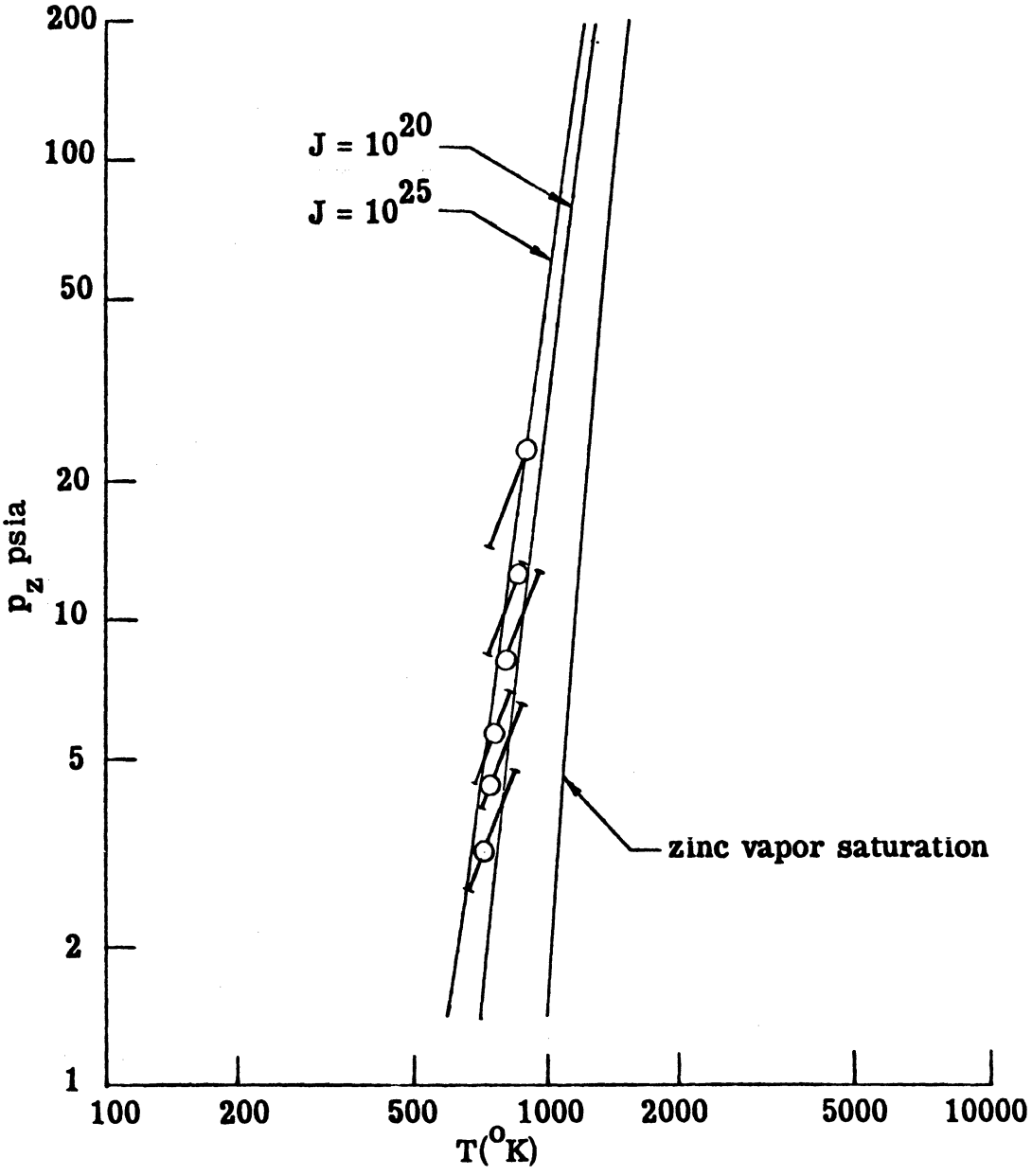

Figure 33. Condensation Onset Locus Shown with Constant J Curves. (Circles are computed location of condensation onset.)

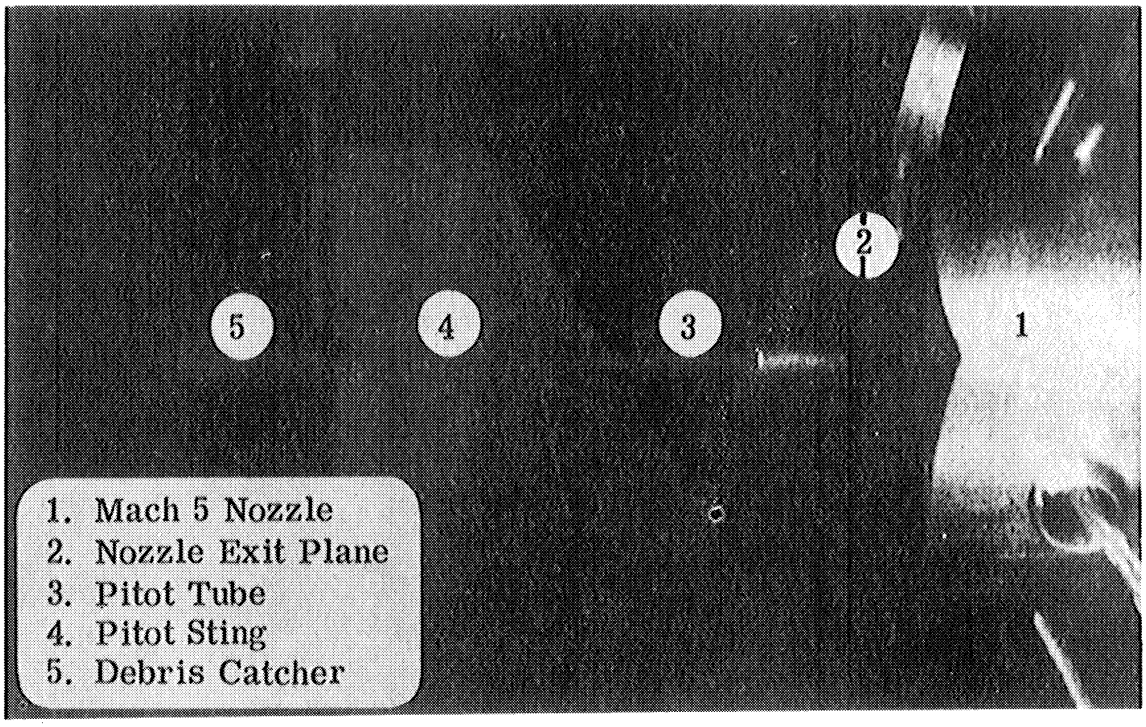

(a) Prior to Run

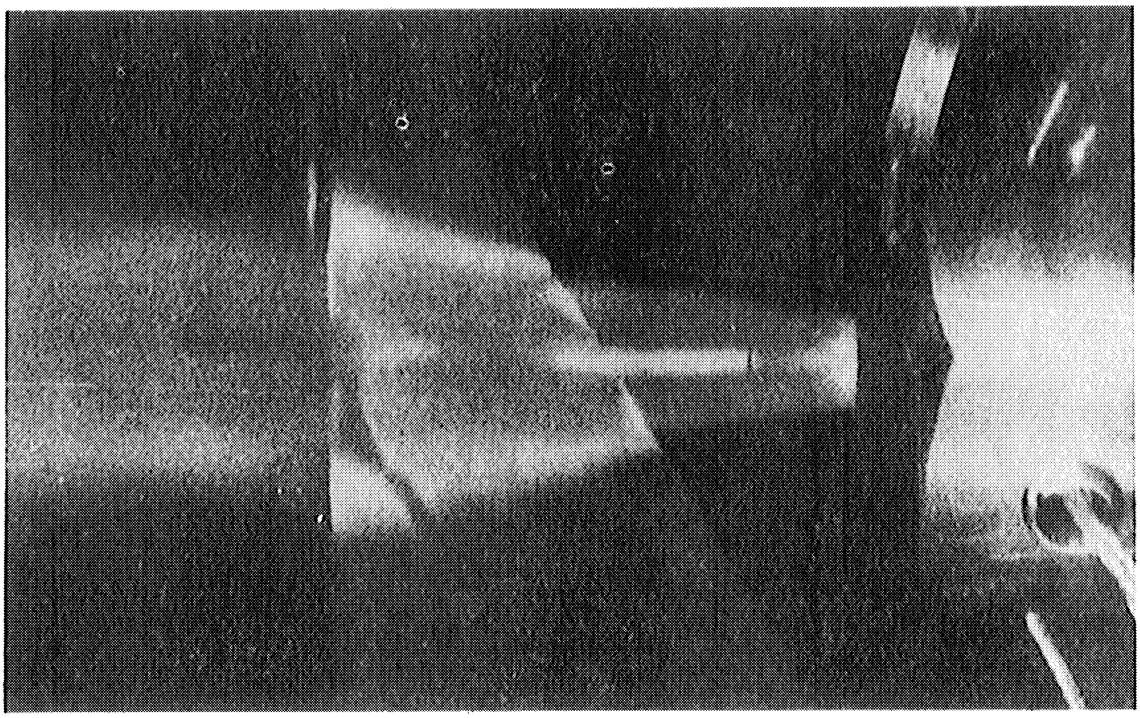

(b) During Run (t = 17.5 msec)

Figure 34. Light Scattering in the Mach 5 Nozzle Flow Field (Run 80904, 17.5 msec, p_c = 2192 psia, $T_c = 2590^{o}K$, f = 0.463)

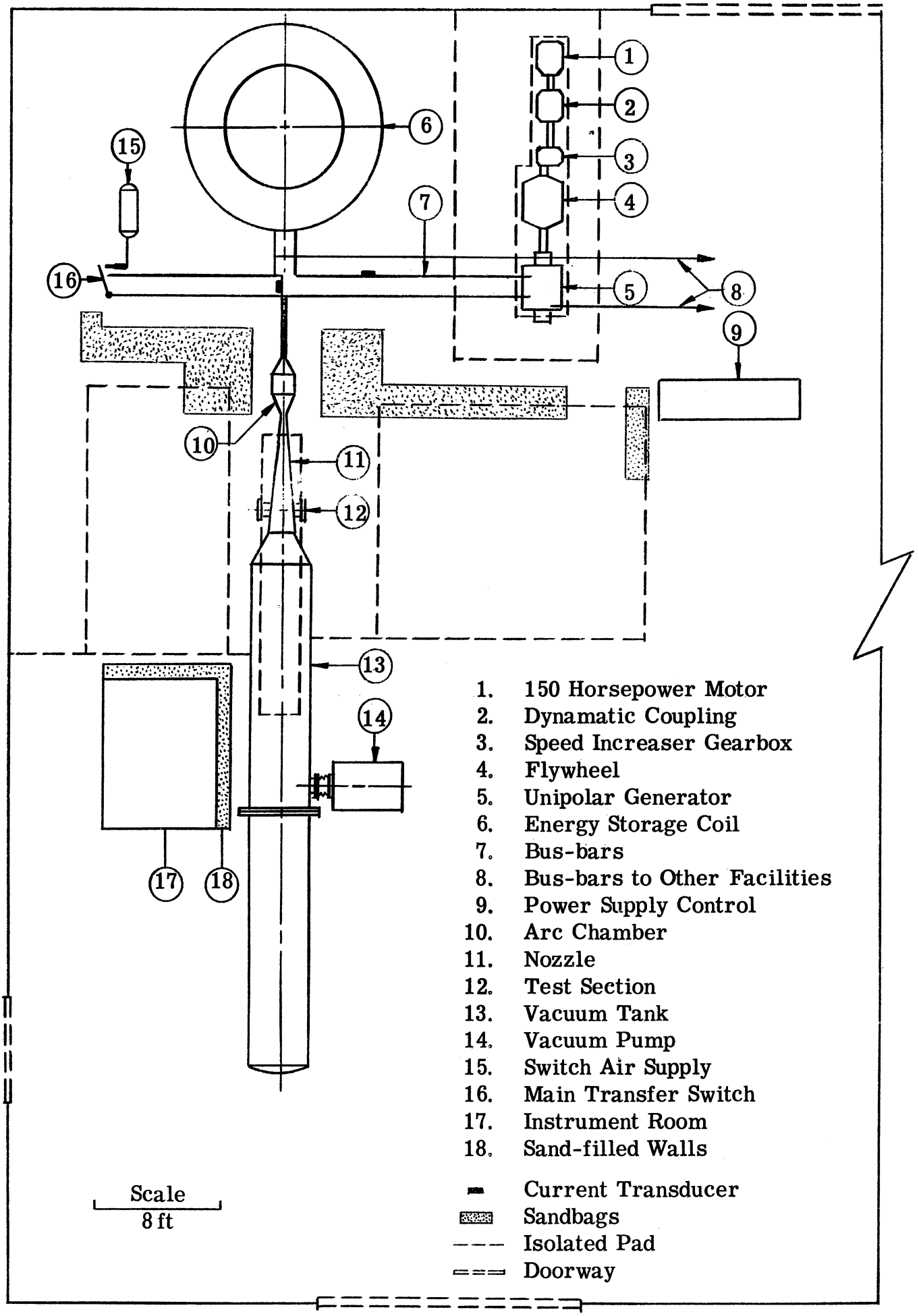

Figure A-1. Laboratory Layout

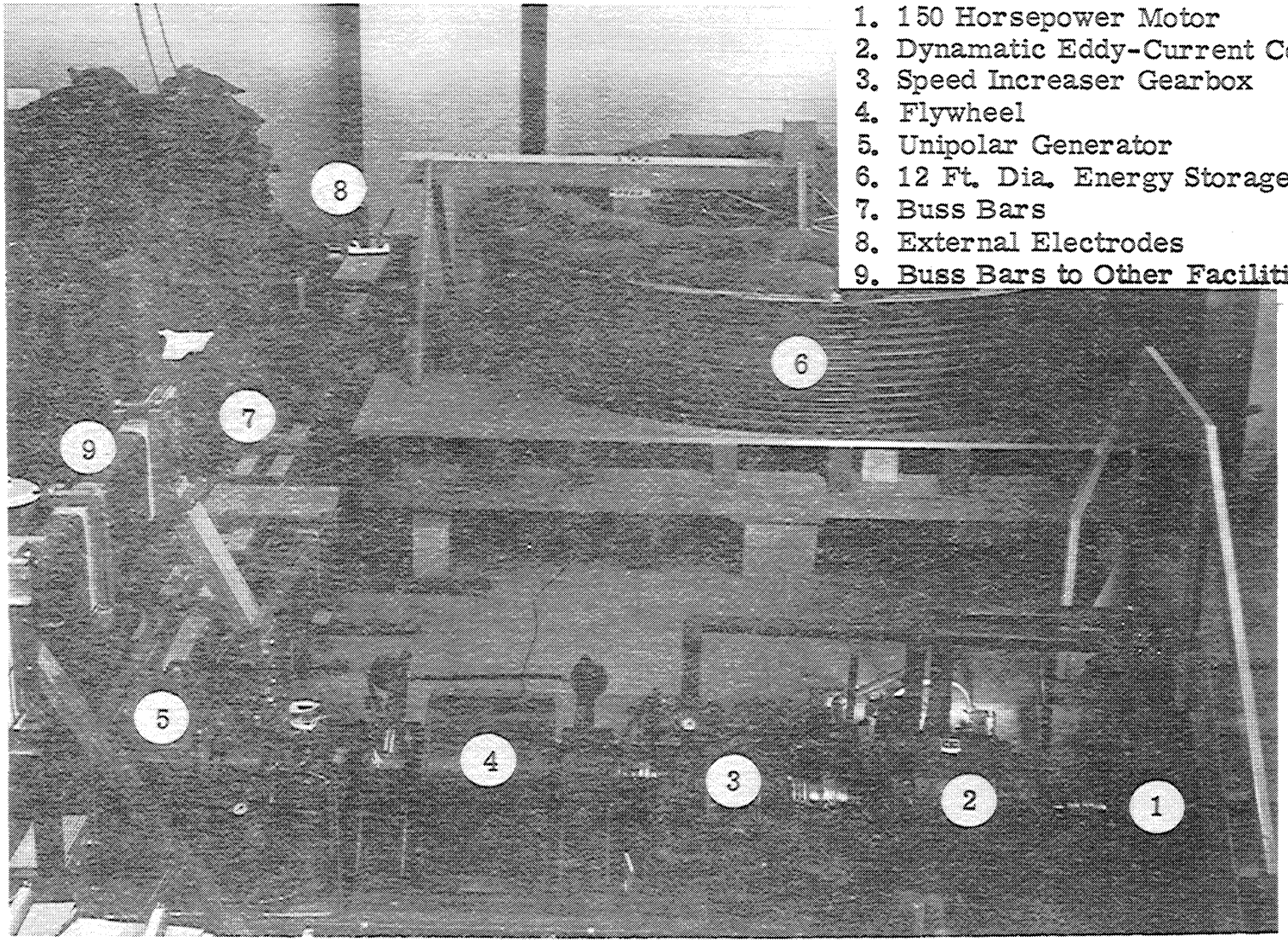

Figure A-2. Energy Supply System

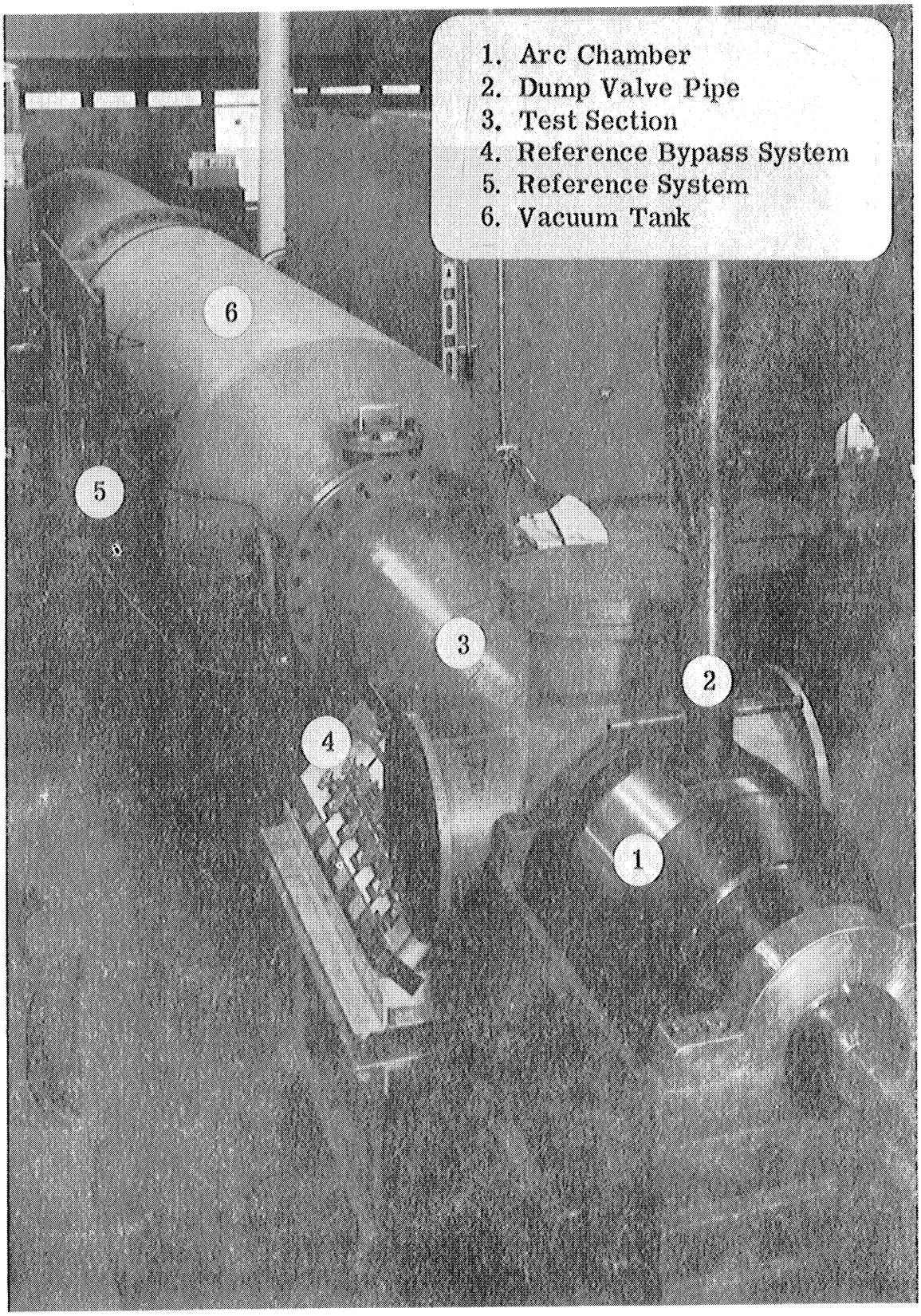

Figure A-3. Arc Chamber, Test Section, and Vacuum Tank

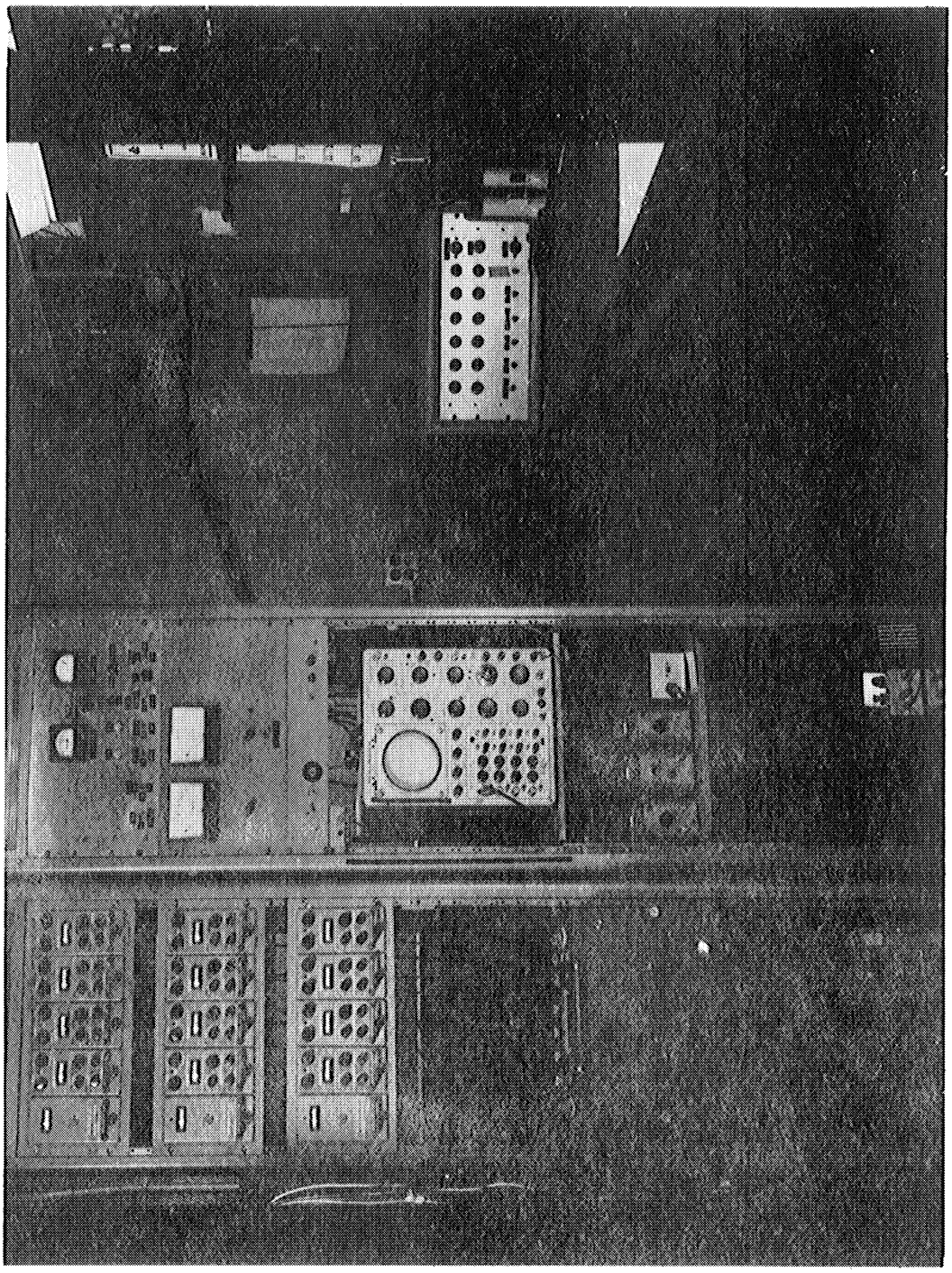

Figure A-4. Instrument Room

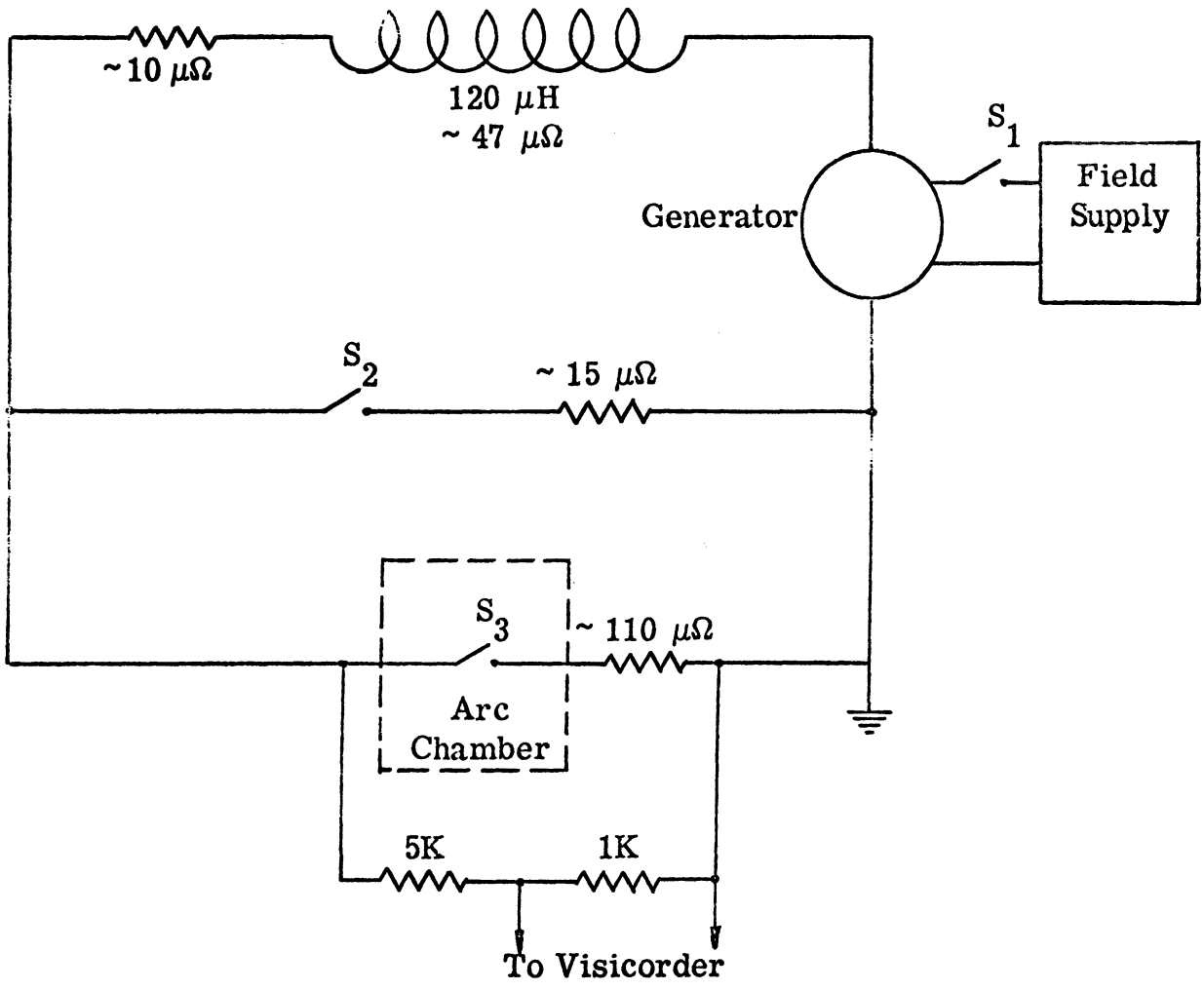

Figure A-5. Energy Supply Schematic

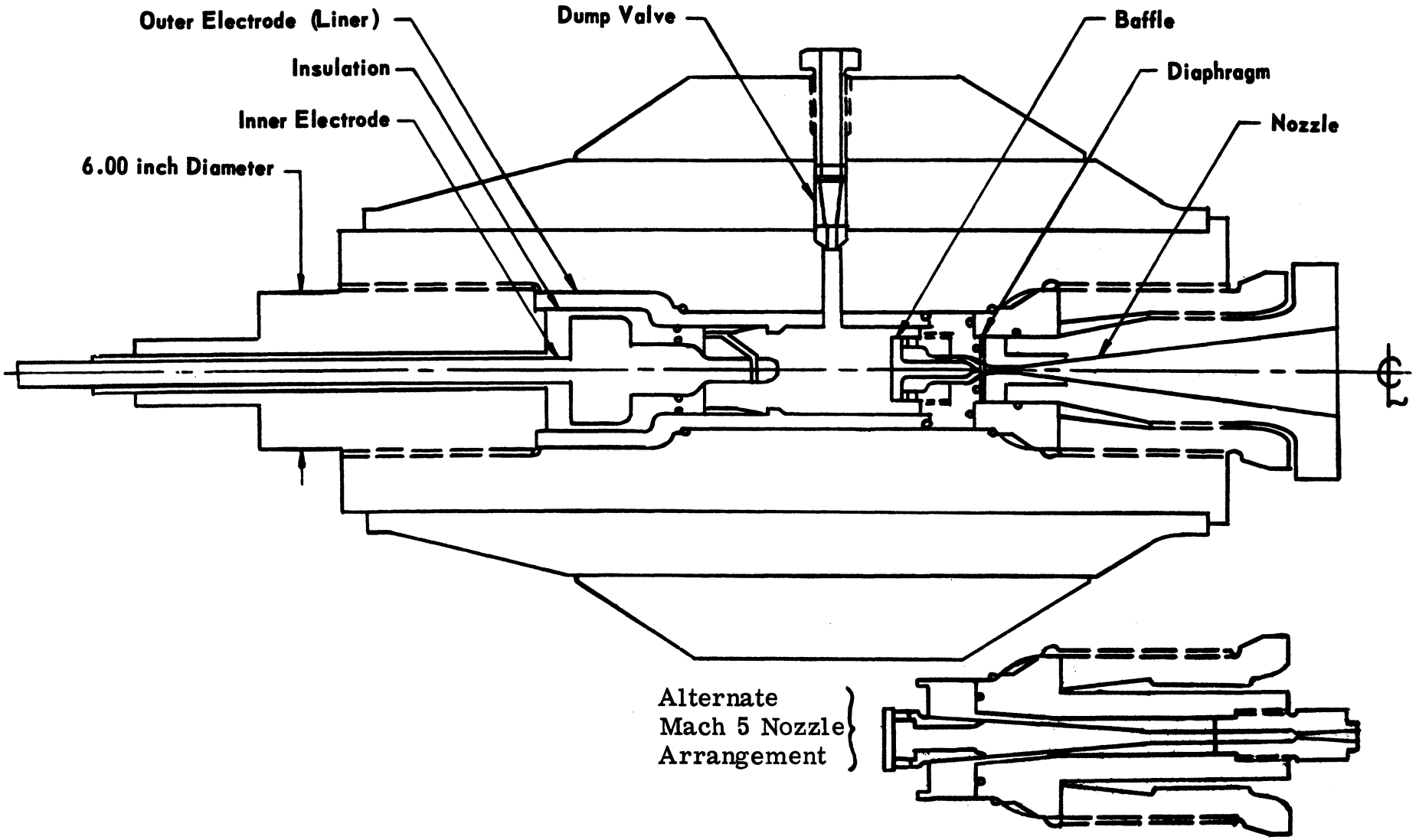

Figure A-6. **Sketch of the Hotshot Arc Chamber Assembly**

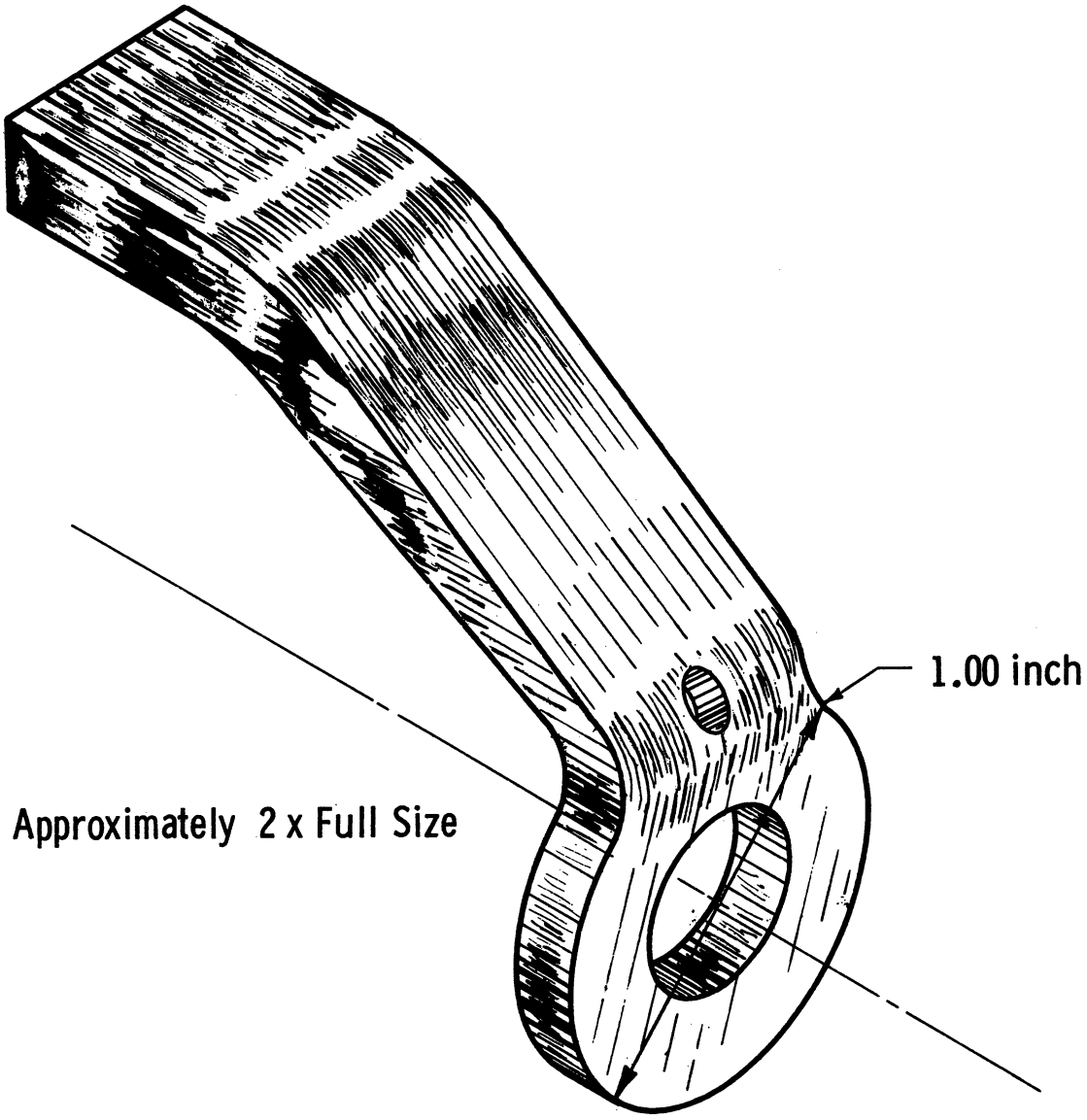

Figure A-7. Zinc Fuse Configuration

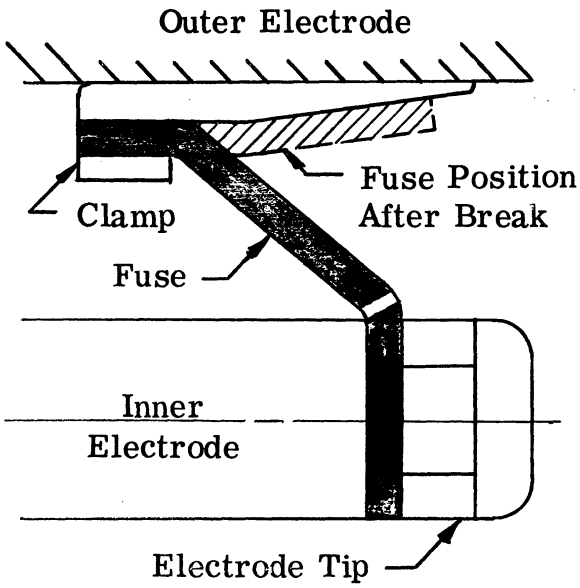

Figure A-8. Fuse Configuration

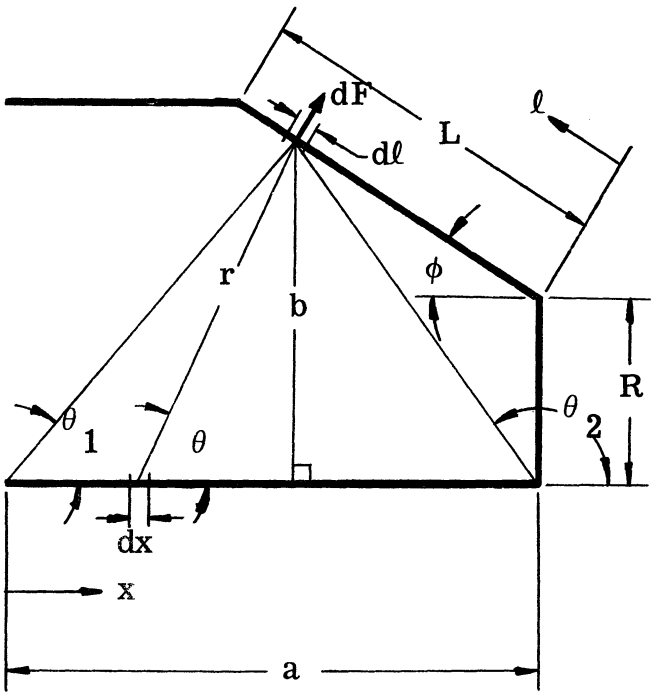

Figure A-9. Fuse Schematic and Nomenclature

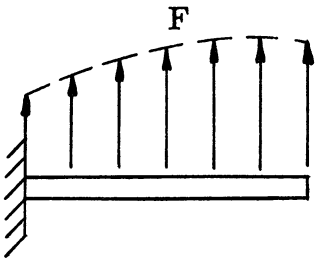

Figure A-10. Actual Force Distribution on Fuse

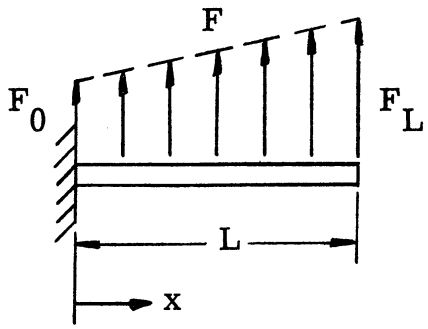

Figure A-11, Linearized Force Distribution on Fuse

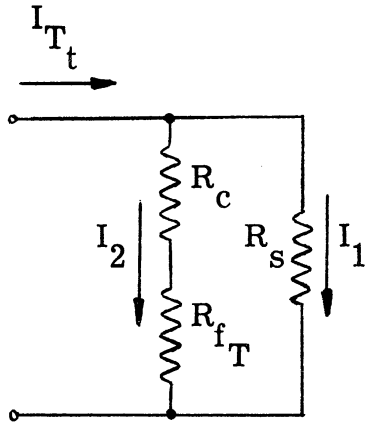

Figure A-12. Main Bus Bar Current Circuit Schematic Prior to Main Switch Opening

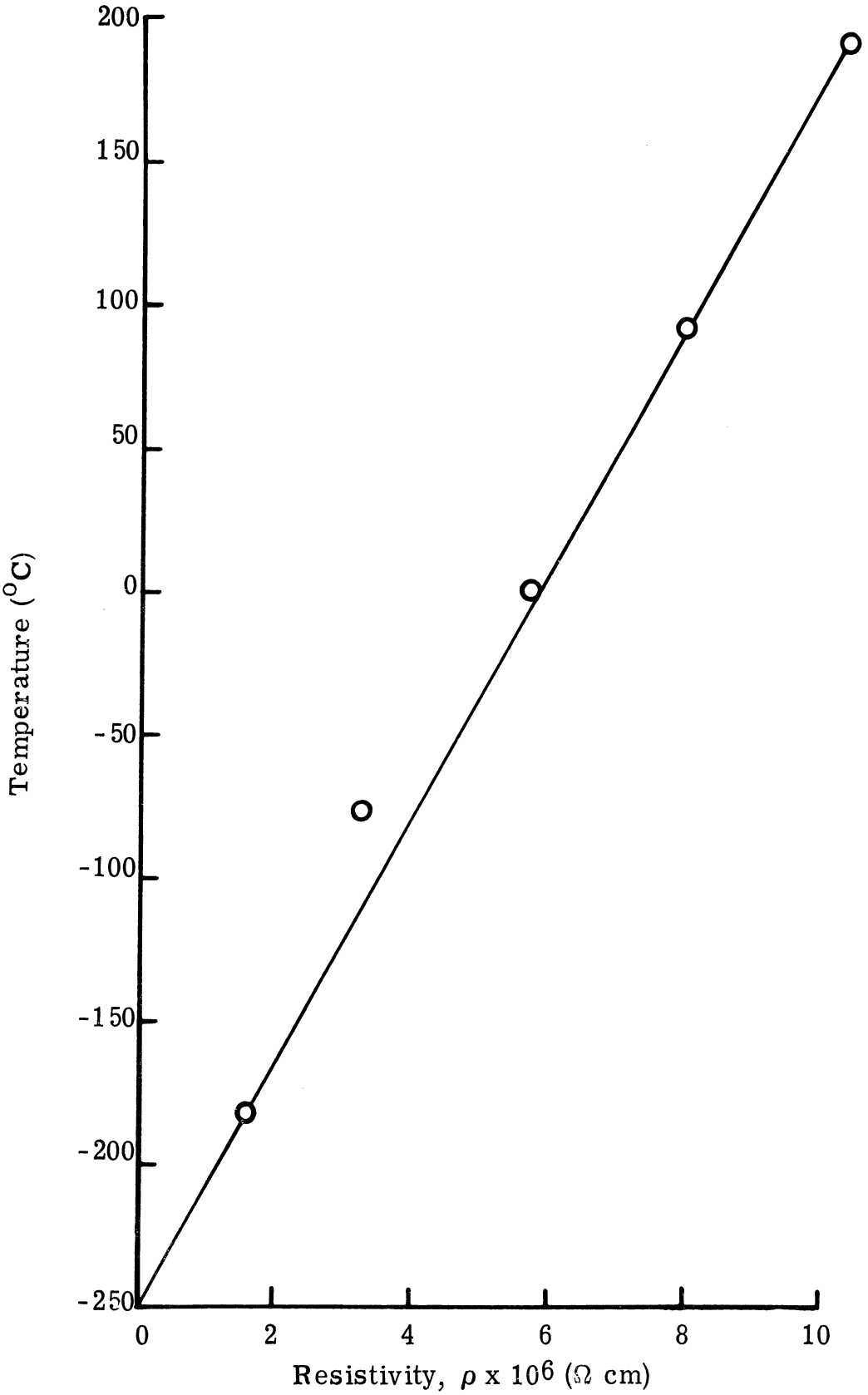

Figure A-13. Resistivity of Zinc vs. Temperature

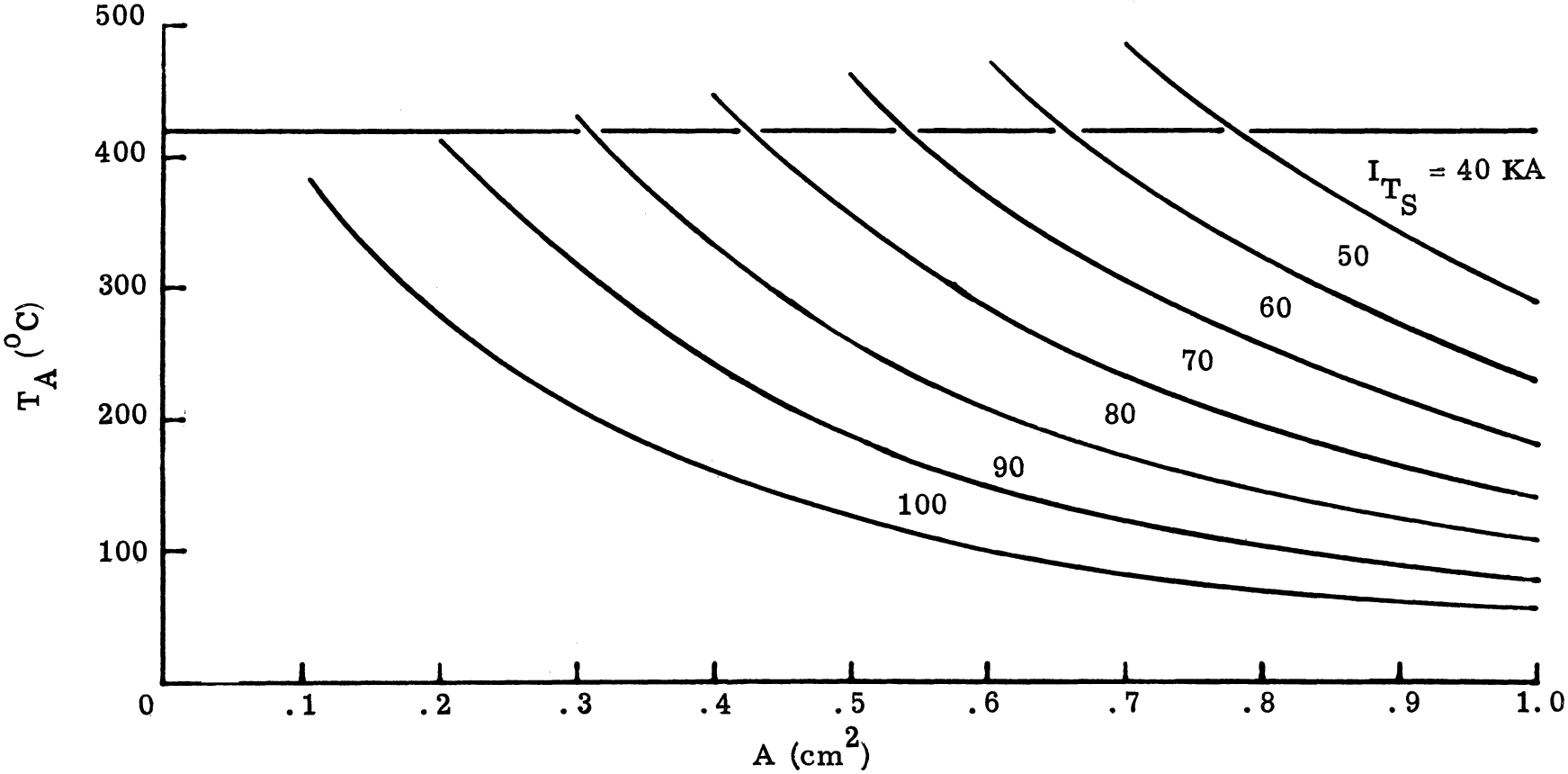

Figure A-14. Fuse Heating Prior to Main Switch Opening

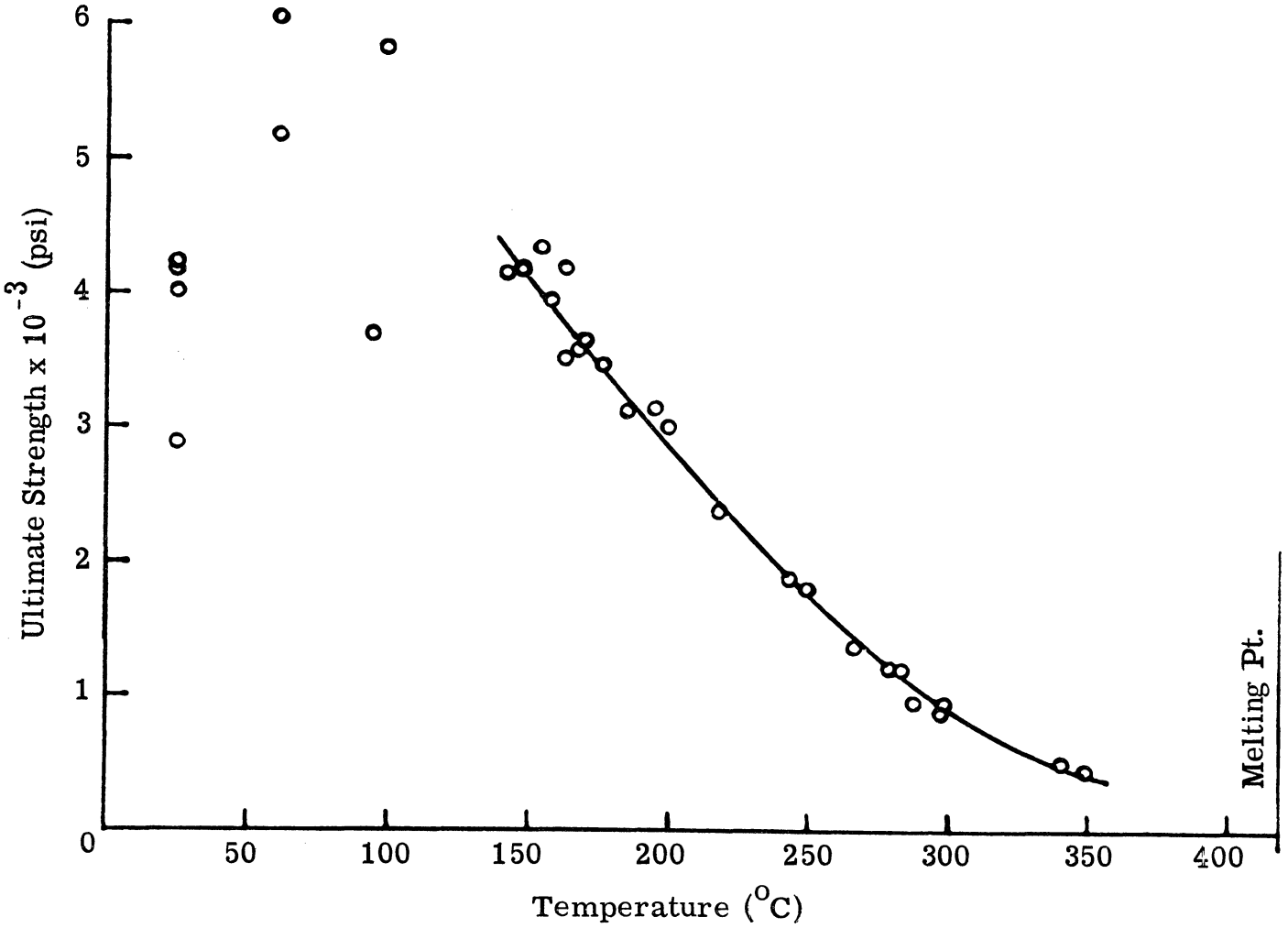

Figure A-15. Rupture Stress of Zinc vs. Temperature

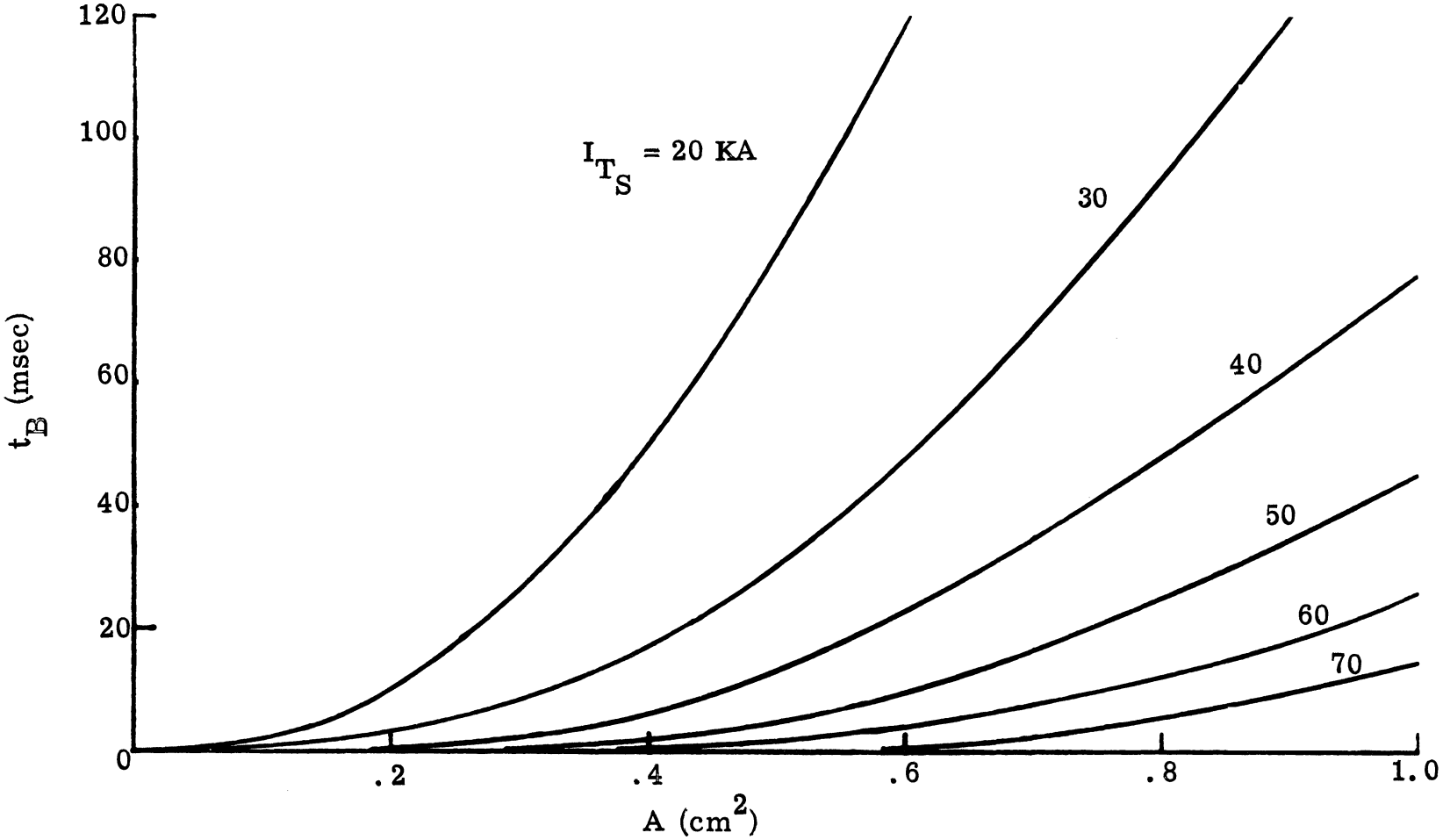

Figure A-16. Fuse Breakage Time vs. Fuse Cross-Sectional Area

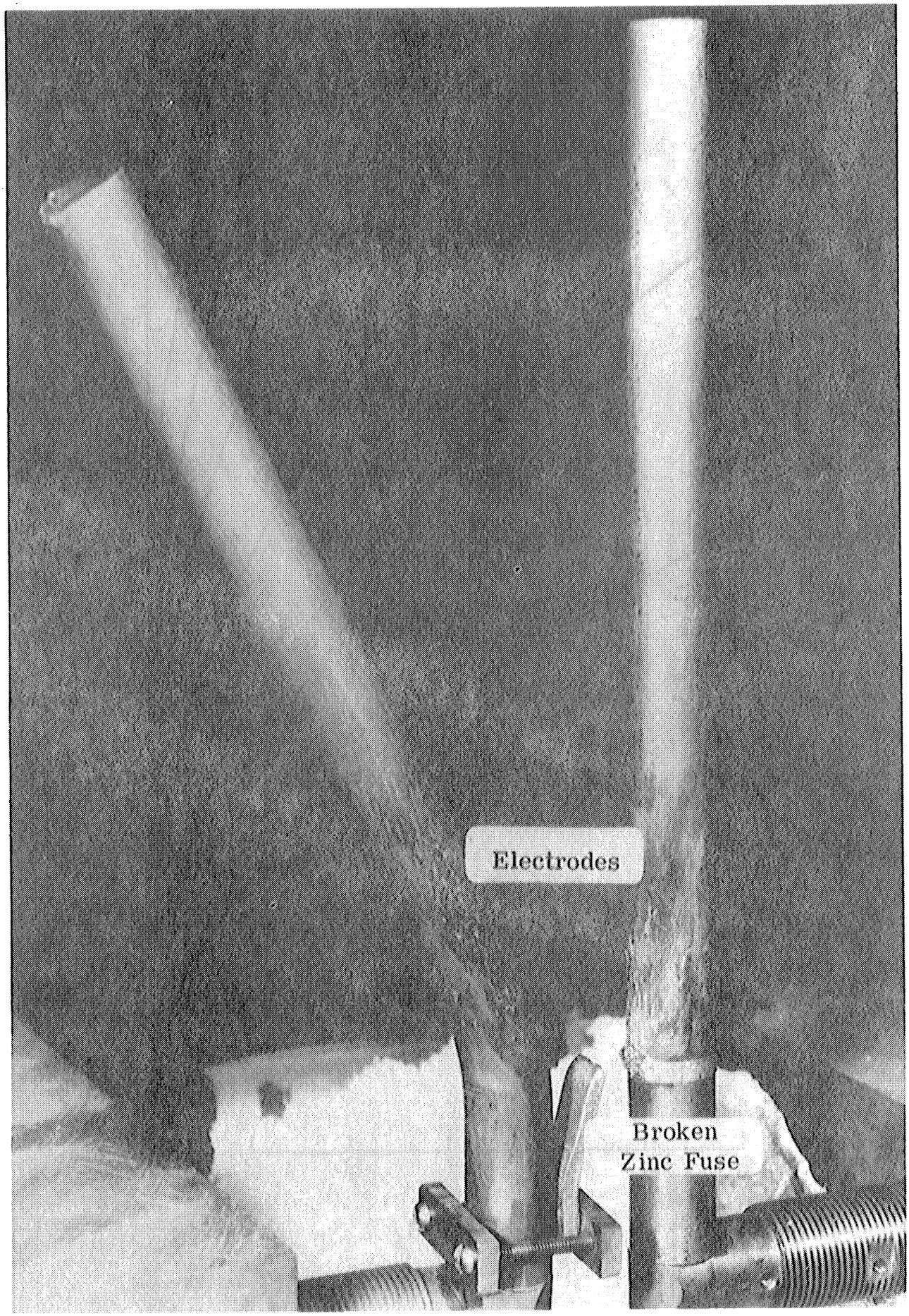

Figure A-17. External Electrodes After Zinc Fuse Test.

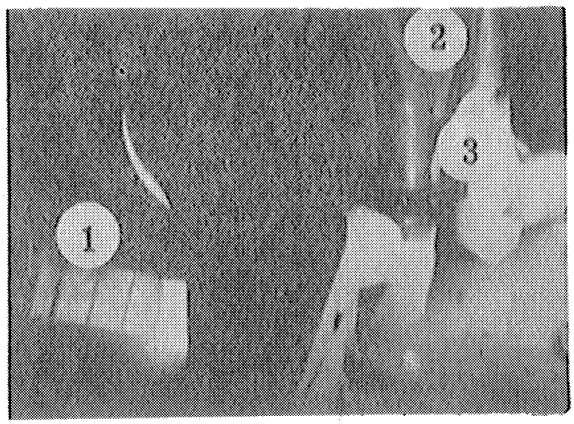

a.) Prior to Run
1.) Main Transfer Switch
2.) Electrodes
3.) Fuse

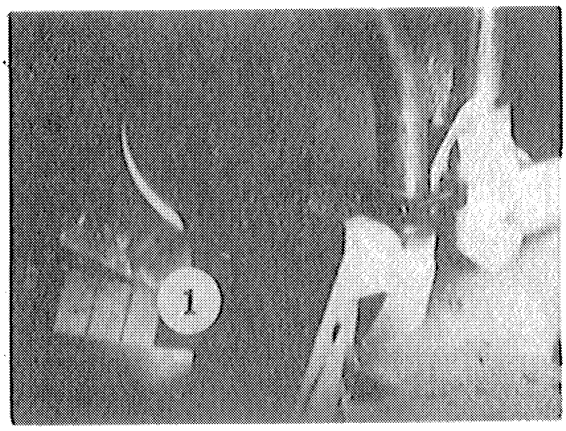

b.) t = 0
1.) Switch Breaks Contact

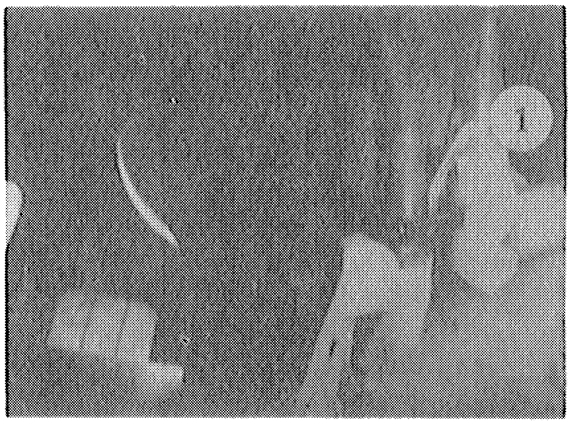

c.) t = 40 milliseconds
1.) slight wisp of smoke from fuse

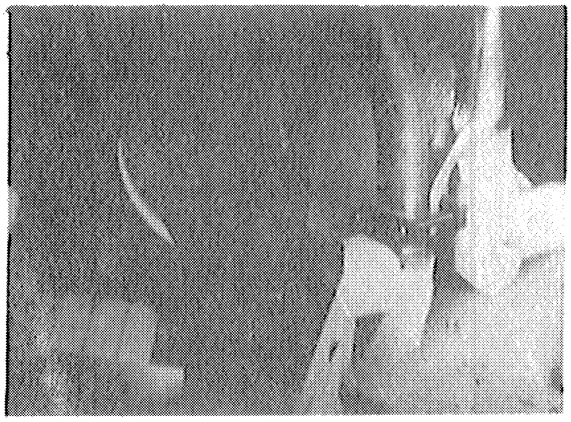

d.) t = 45 milliseconds
(Fuse Still Mechanically Intact)

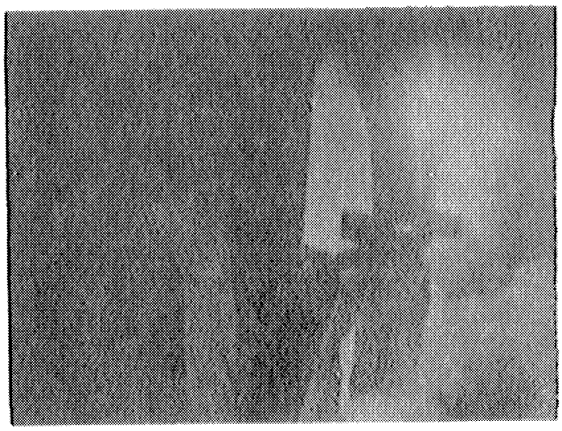

e.) t = 48 milliseconds
(Fuse Breaks Initiating Arc)

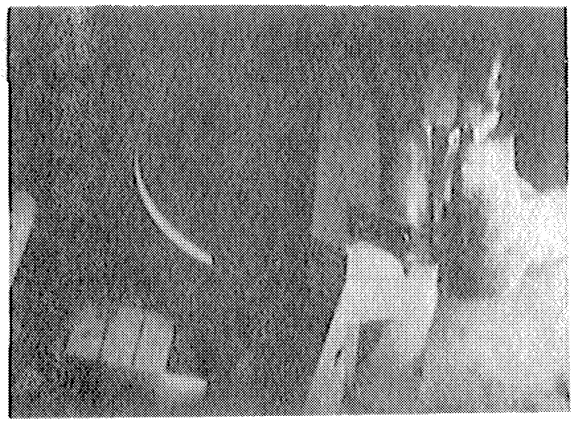

f.) After Run

Figure A-18. Fuse Test Sequence

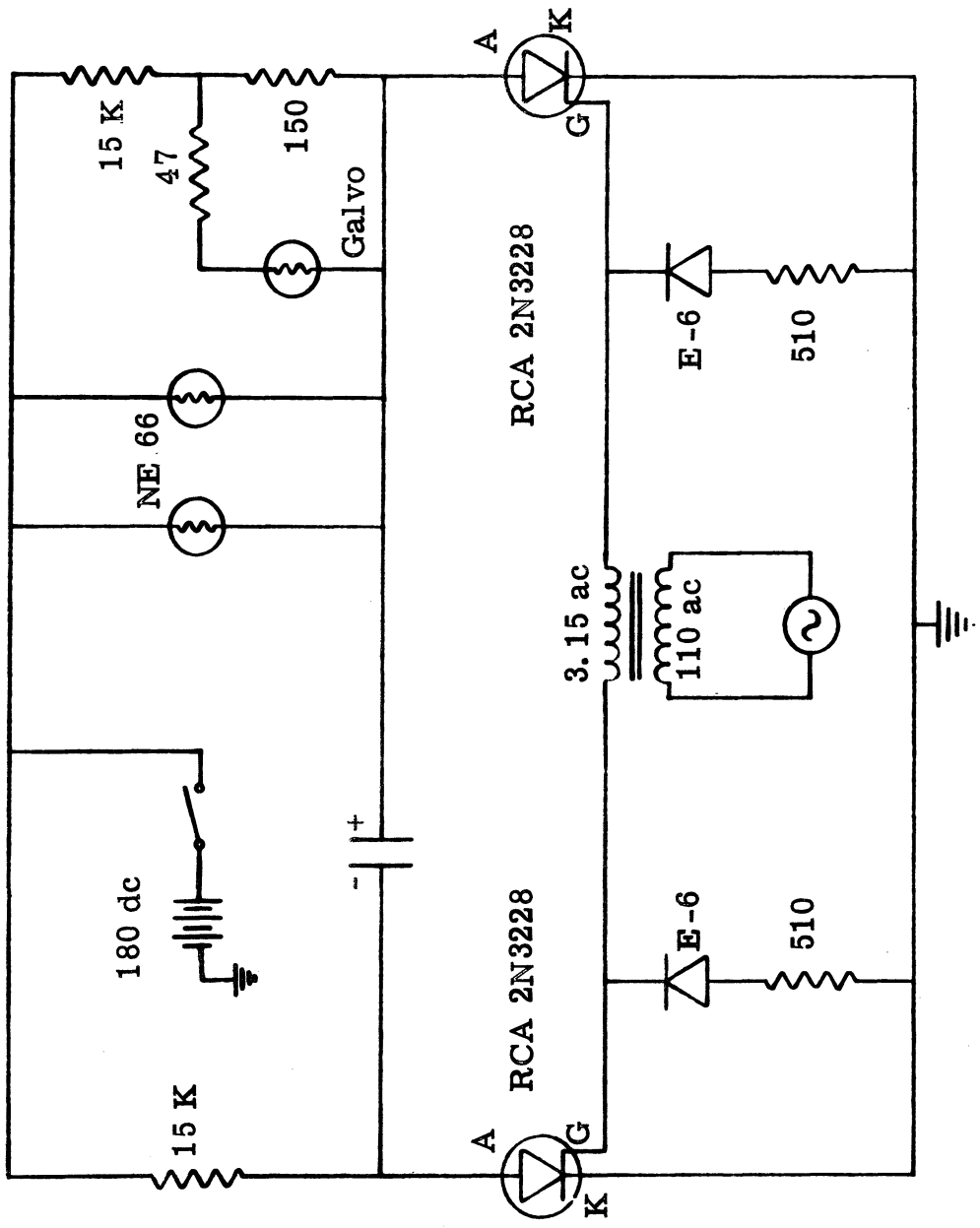

Figure B-1. Schematic of Square Wave Generator for Fastax Timing Marks

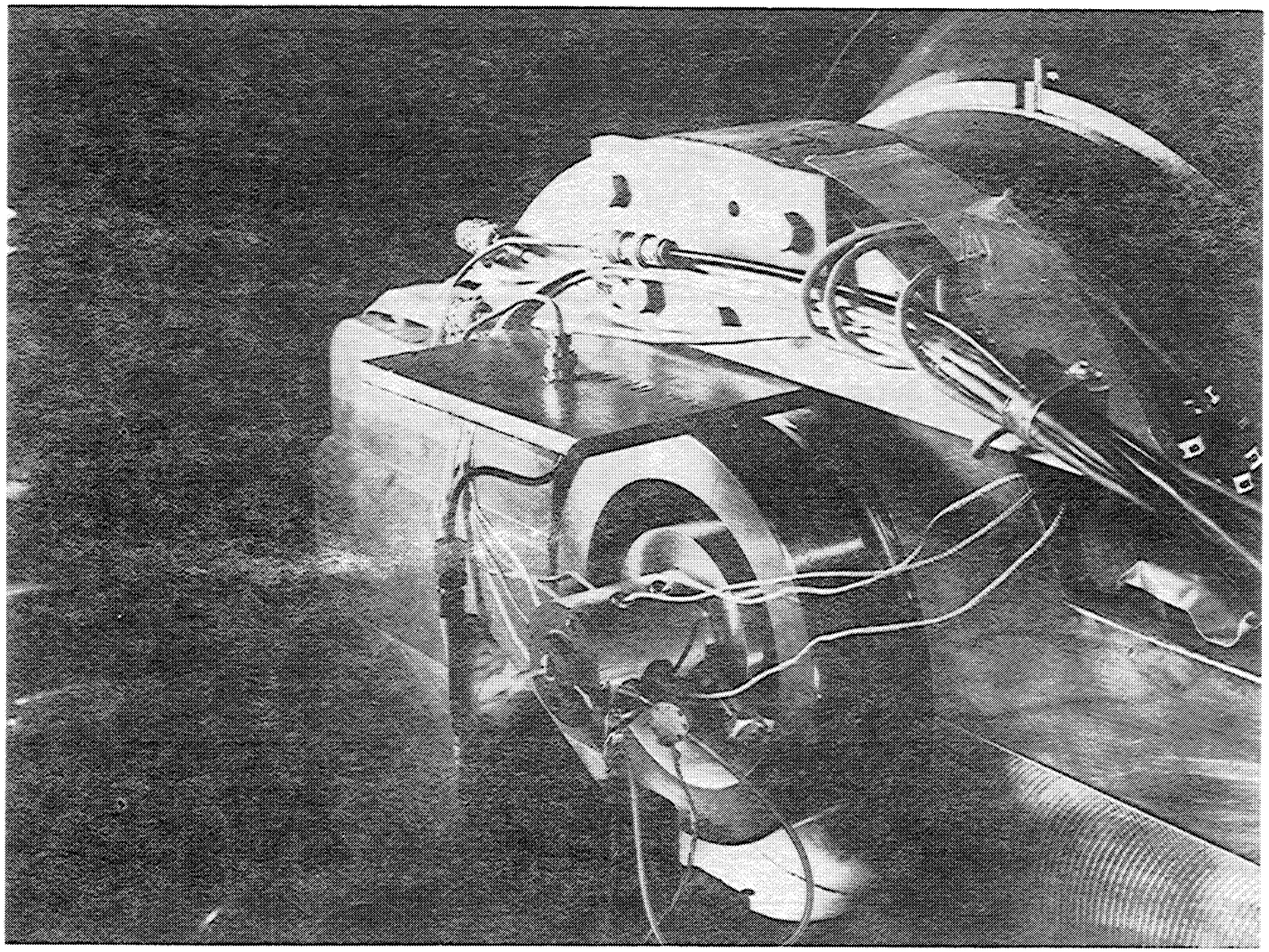

Figure B-2. Mach 5 Nozzle Installation

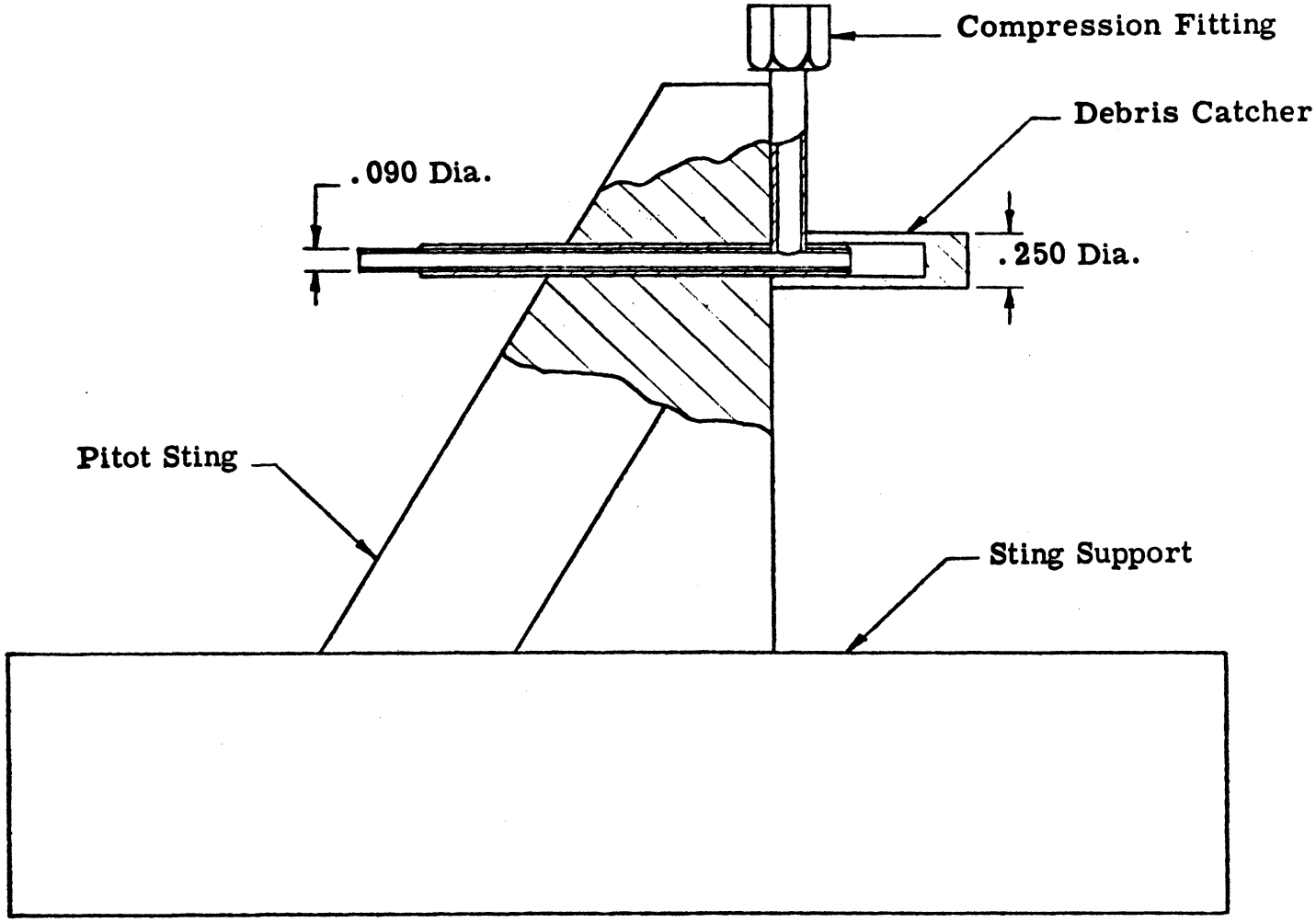

Figure B-3. Sketch of Mach 5 Nozzle Pitot and Sting

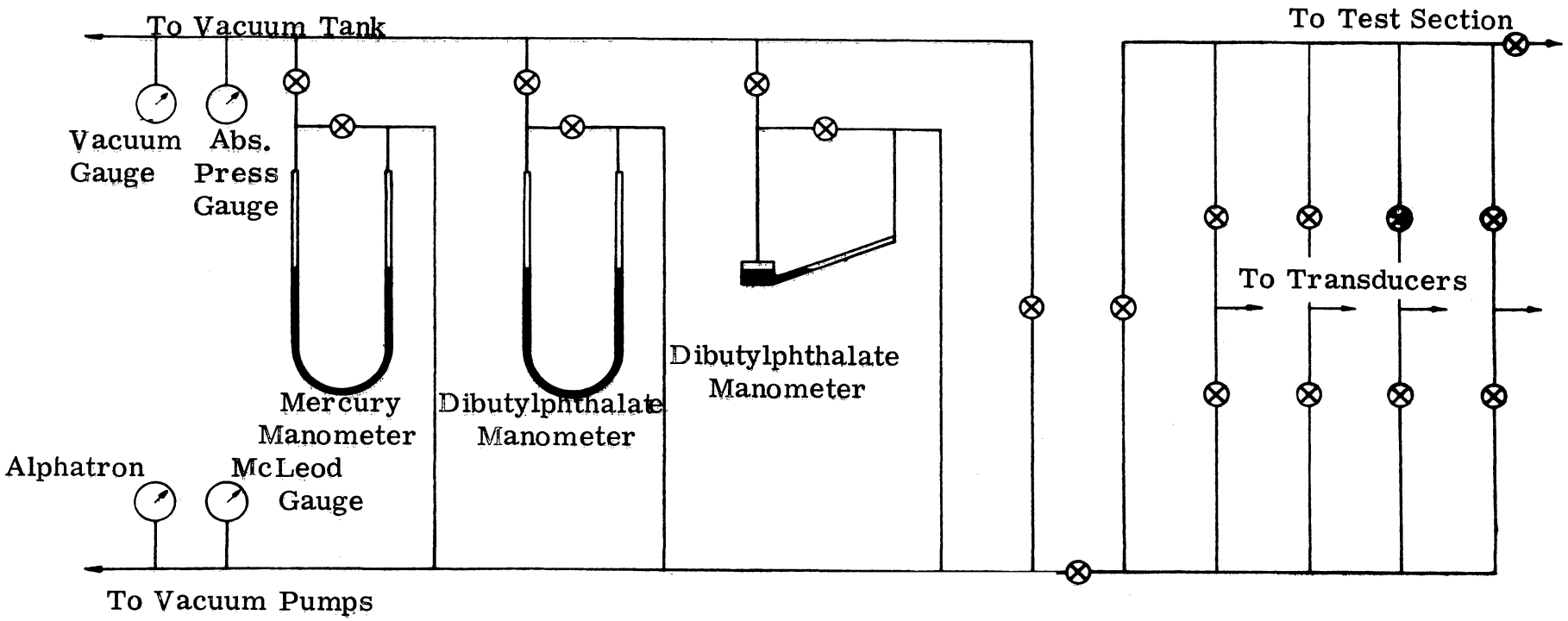

Figure B-4. Schematic of Vacuum Reference System

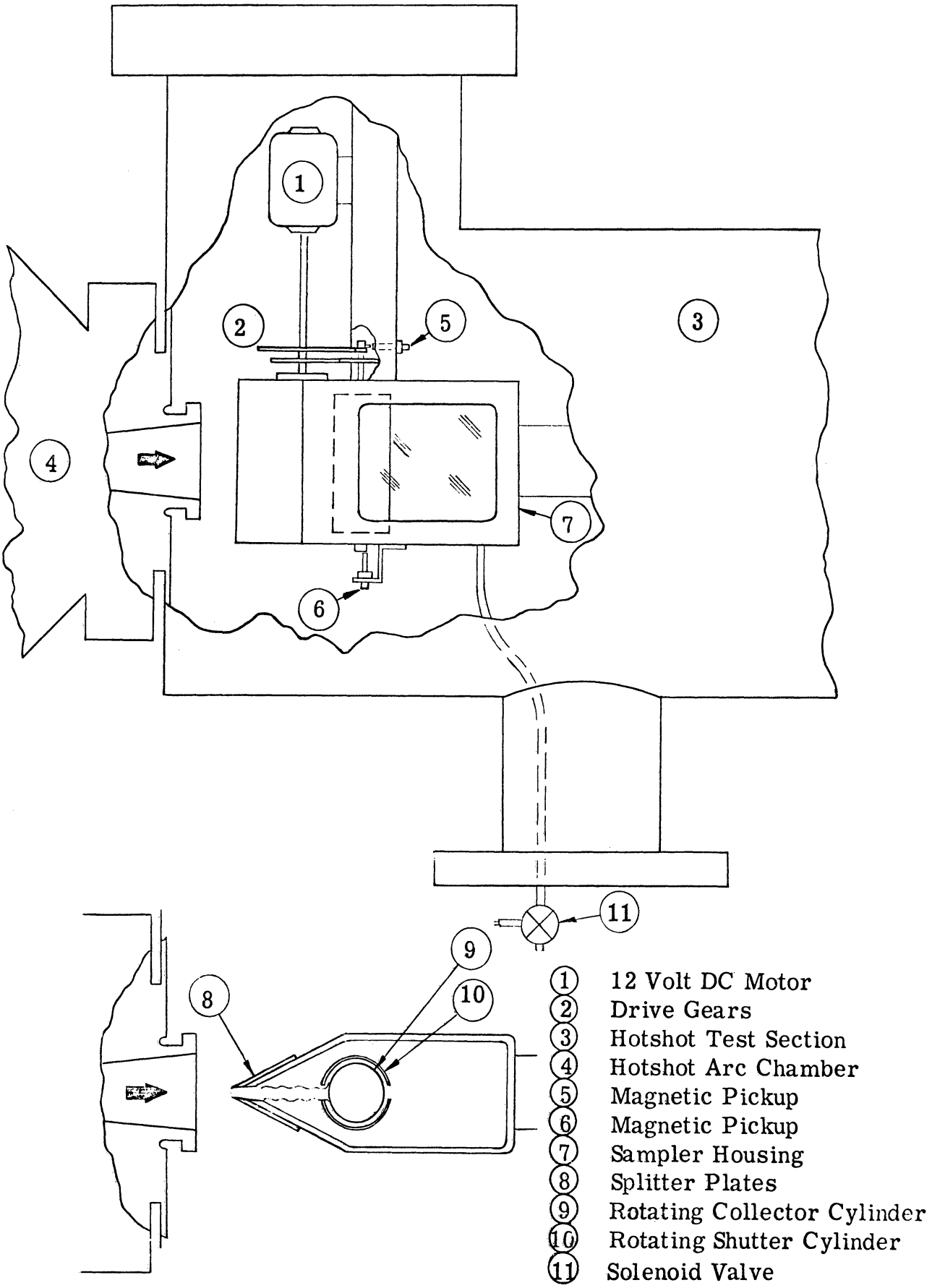

Figure C-1. Schematic of Rotating Shutter Sampling Apparatus Mounted in Hotshot Tunnel Test Section.

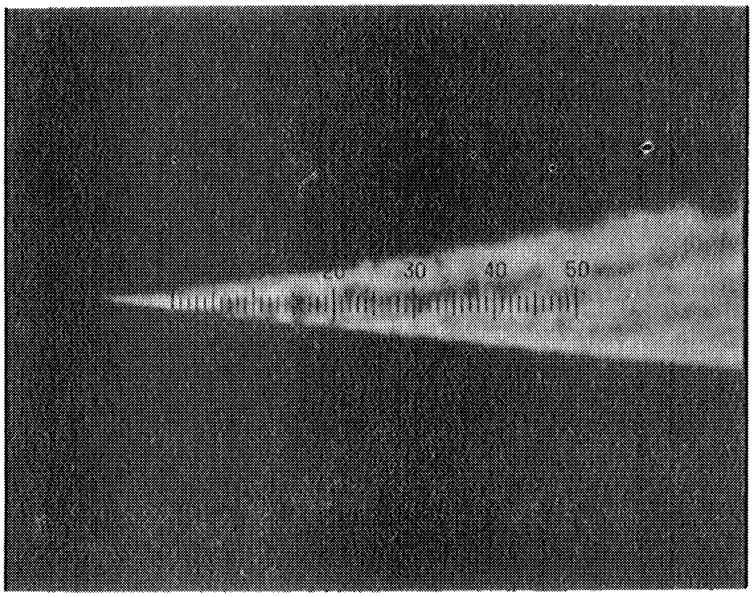

.05 mm

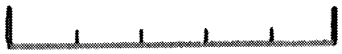

Figure C-2. Photomicrograph of Cross-Section of Gillette Super Stainless Razor Blade Edge. 875 X.

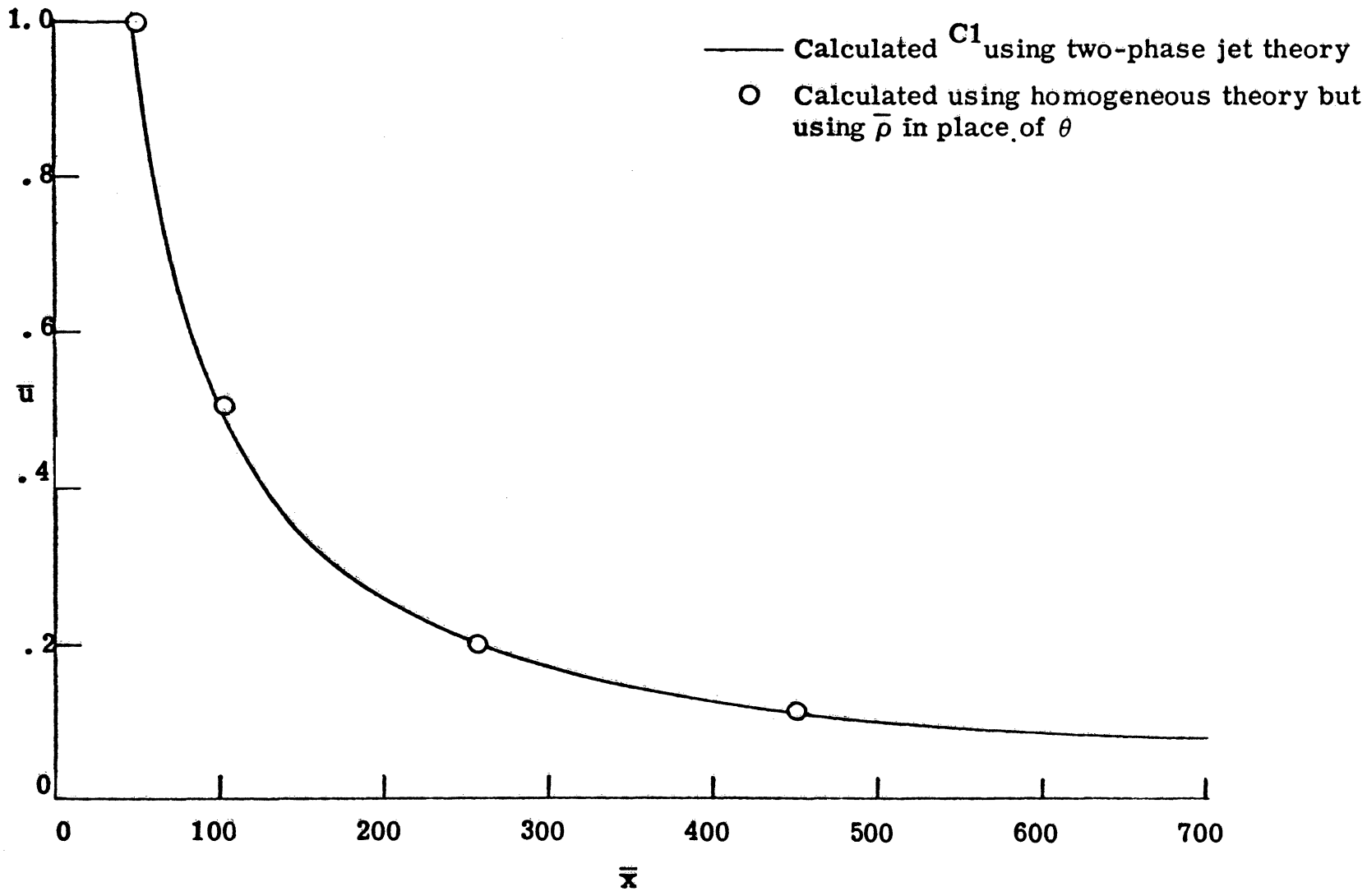

Figure C-3. Velocity Variation in a Two Phase, Water-Air Jet: A Comparison of Solutions

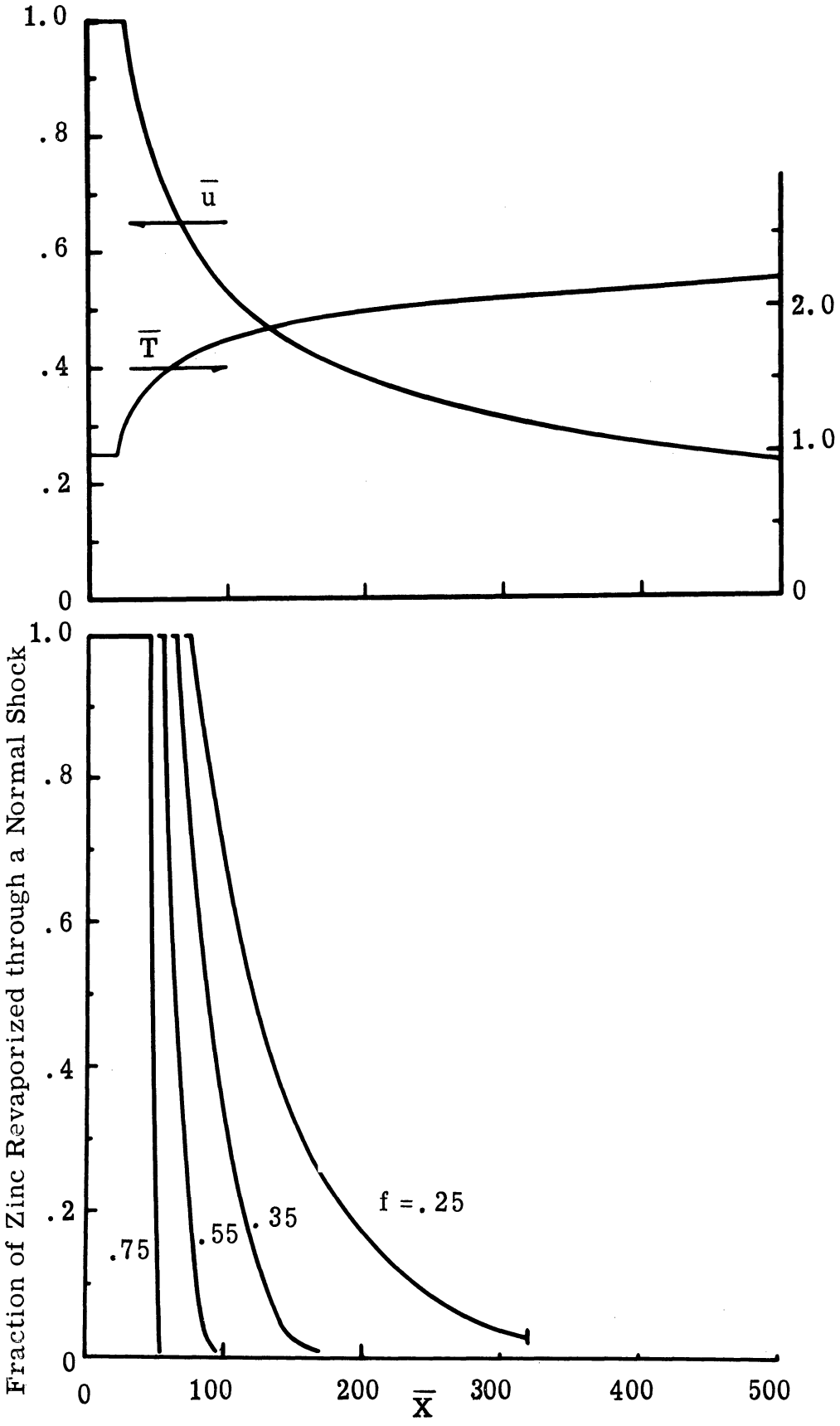

Figure C-4. Variation of Flow Properties in the Two-Dimensional Jet Inside the Sampler

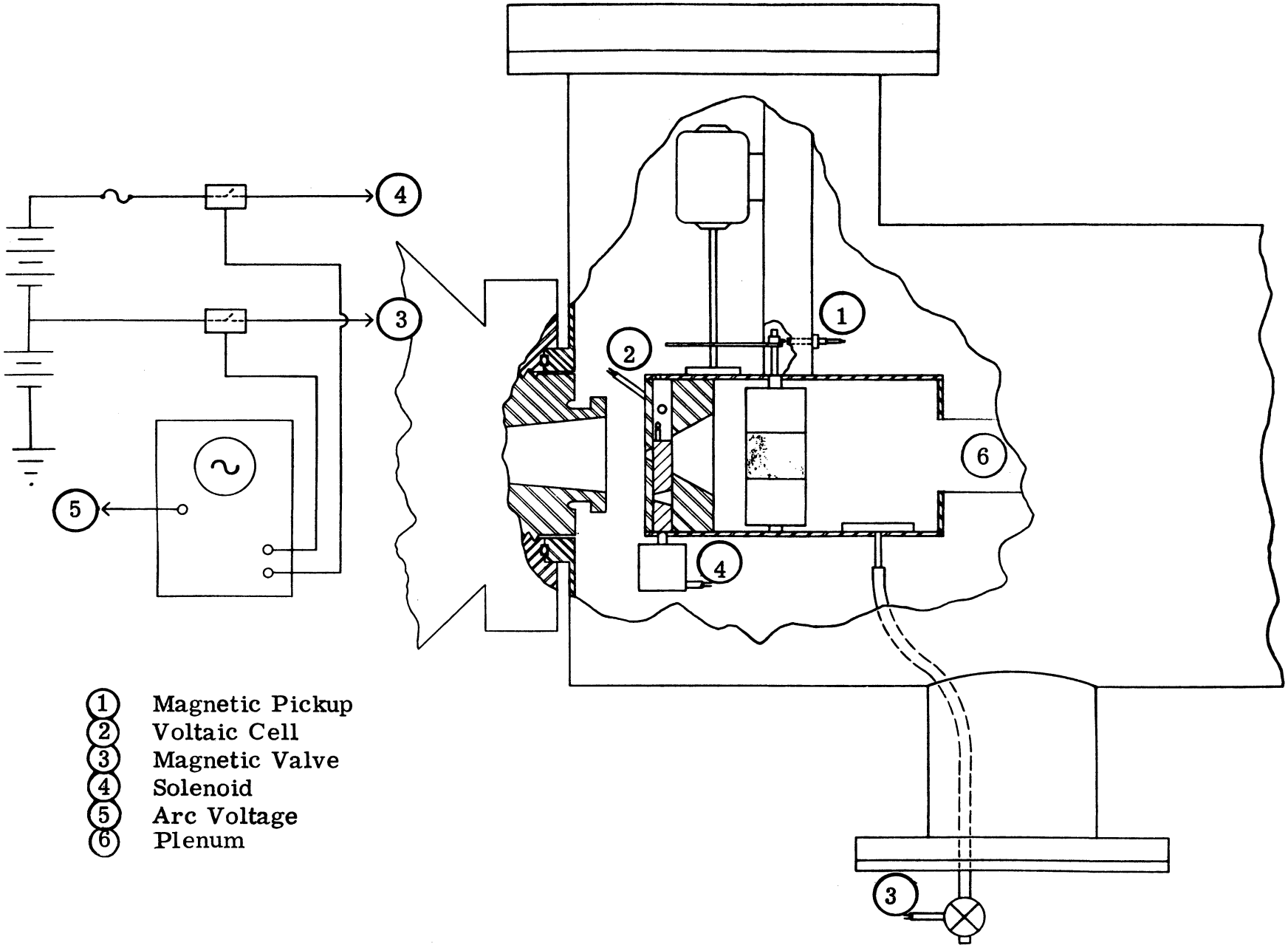

Figure C-5. Schematic of Linear Shutter Sampling Apparatus Mounted in Hotshot Tunnel Test Section.

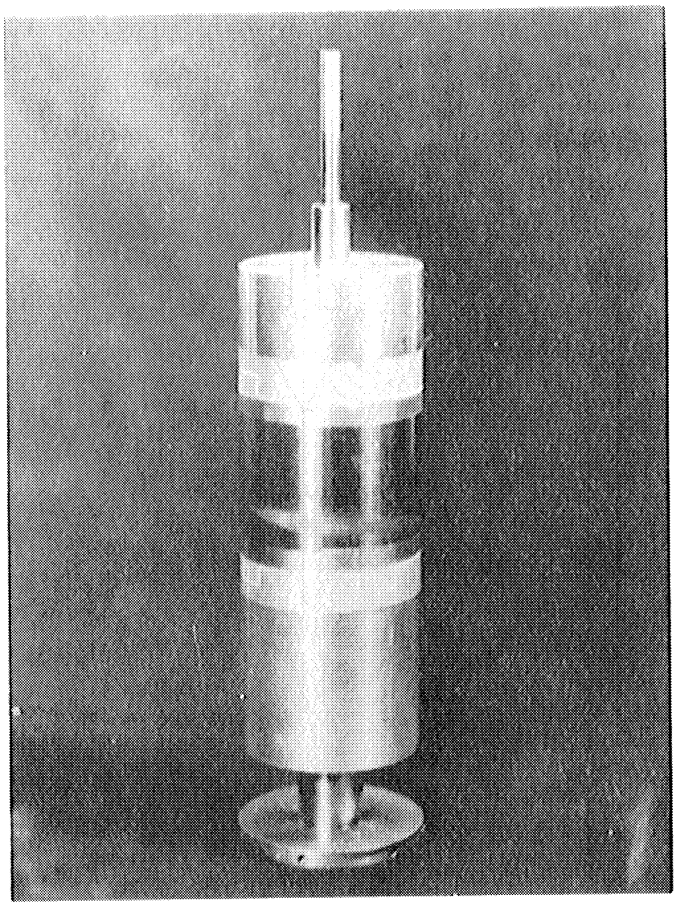

Figure C-6. Exposed Mica Tape on Collector Cylinder

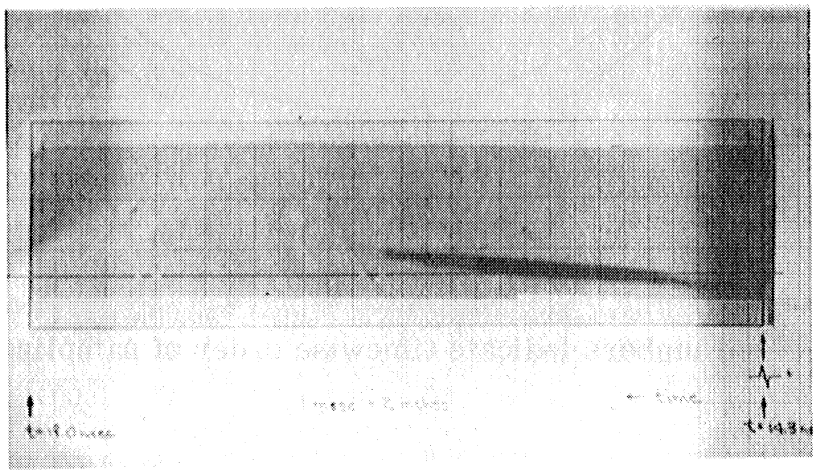

Figure C-7. Exposed Mica Tape Removed and Ready for Electron Microscope Analysis.

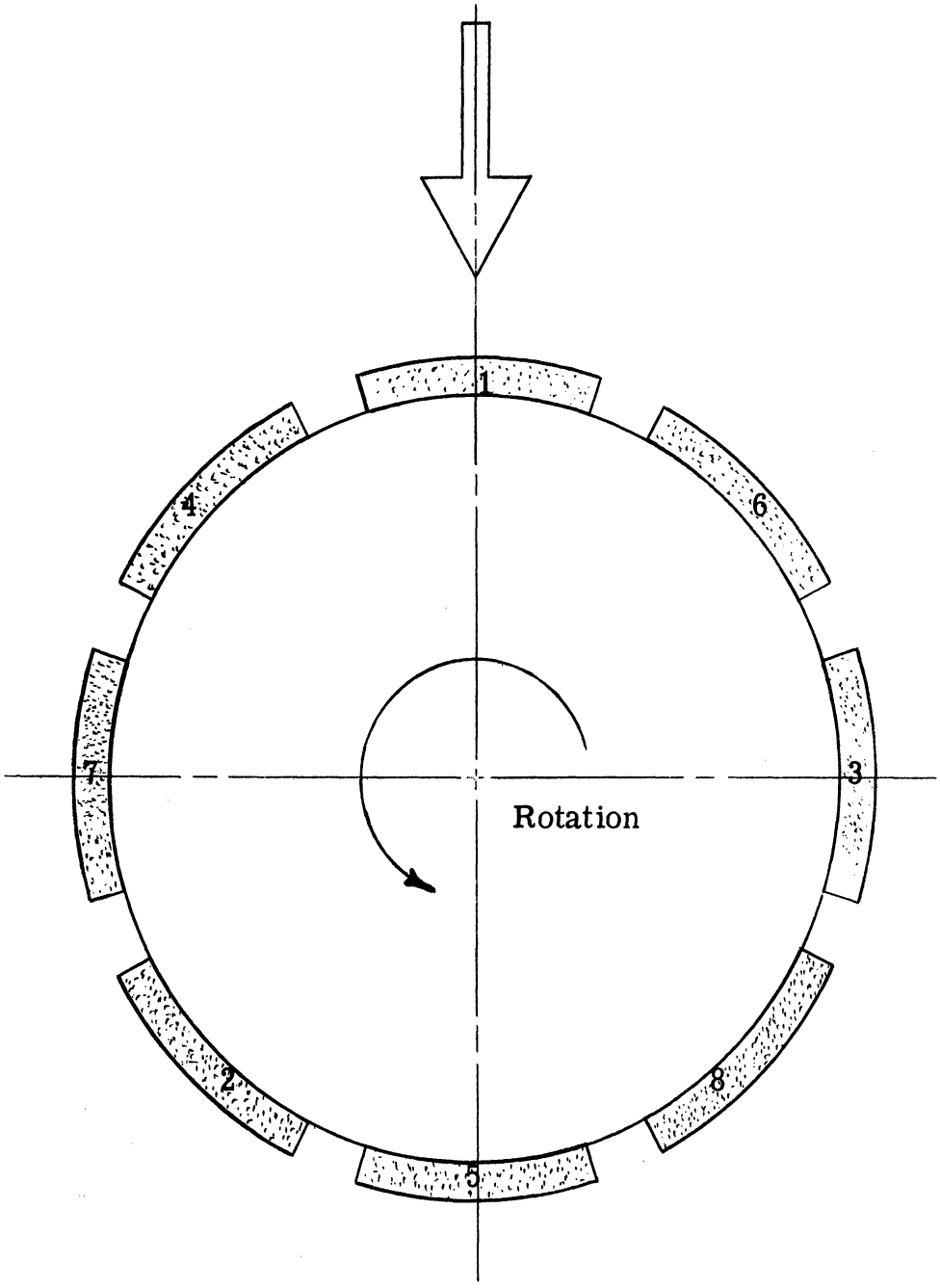

(Numbers indicate timewise order of sampling.)

Figure C-8. Collector Cylinder Sample Location Diagram (Rotating Shutter).

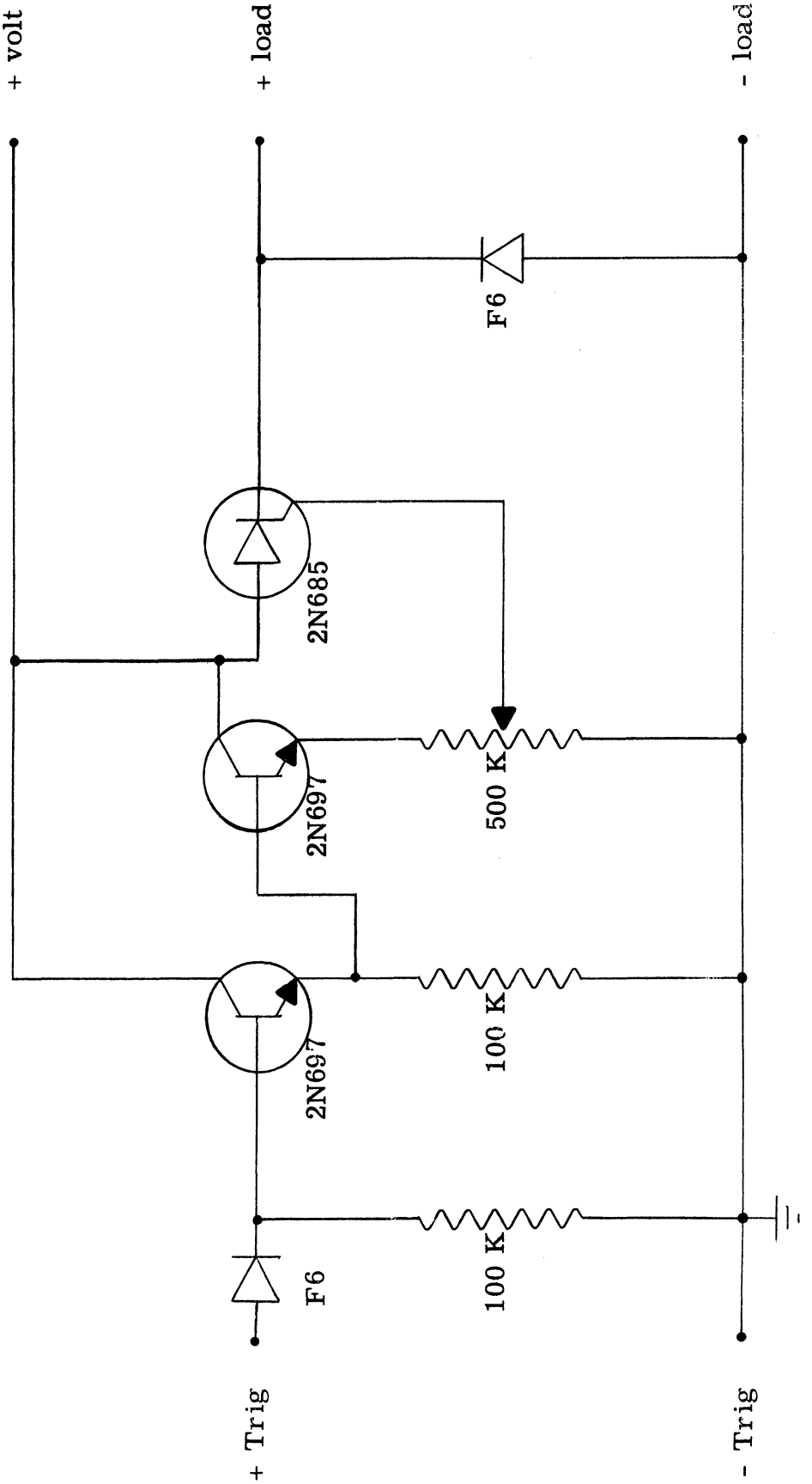

Figure C-9. Schematic of Silicon-Controlled-Rectifier Circuit.

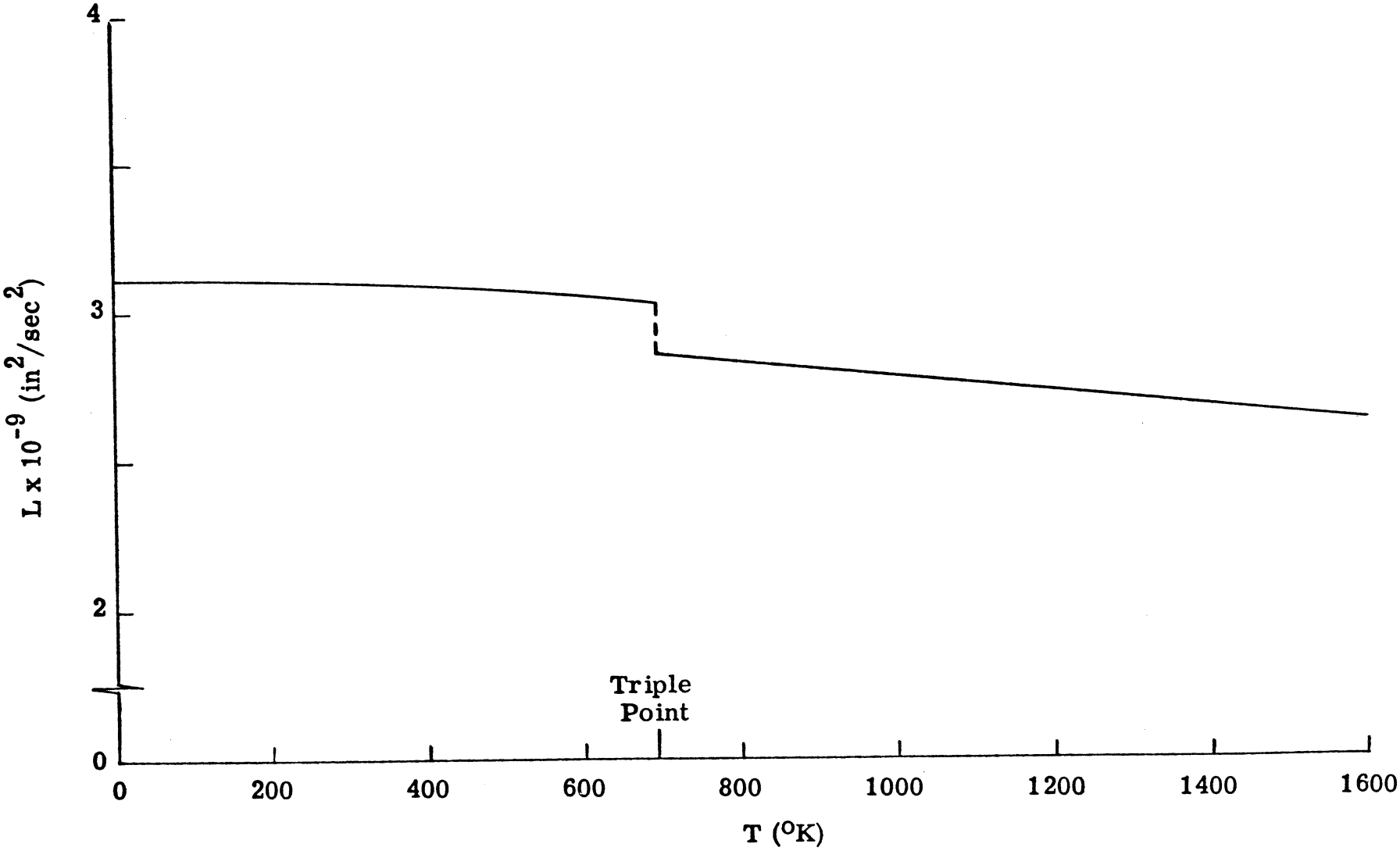

Figure D-1. Latent Heat of Zinc vs. Temperature

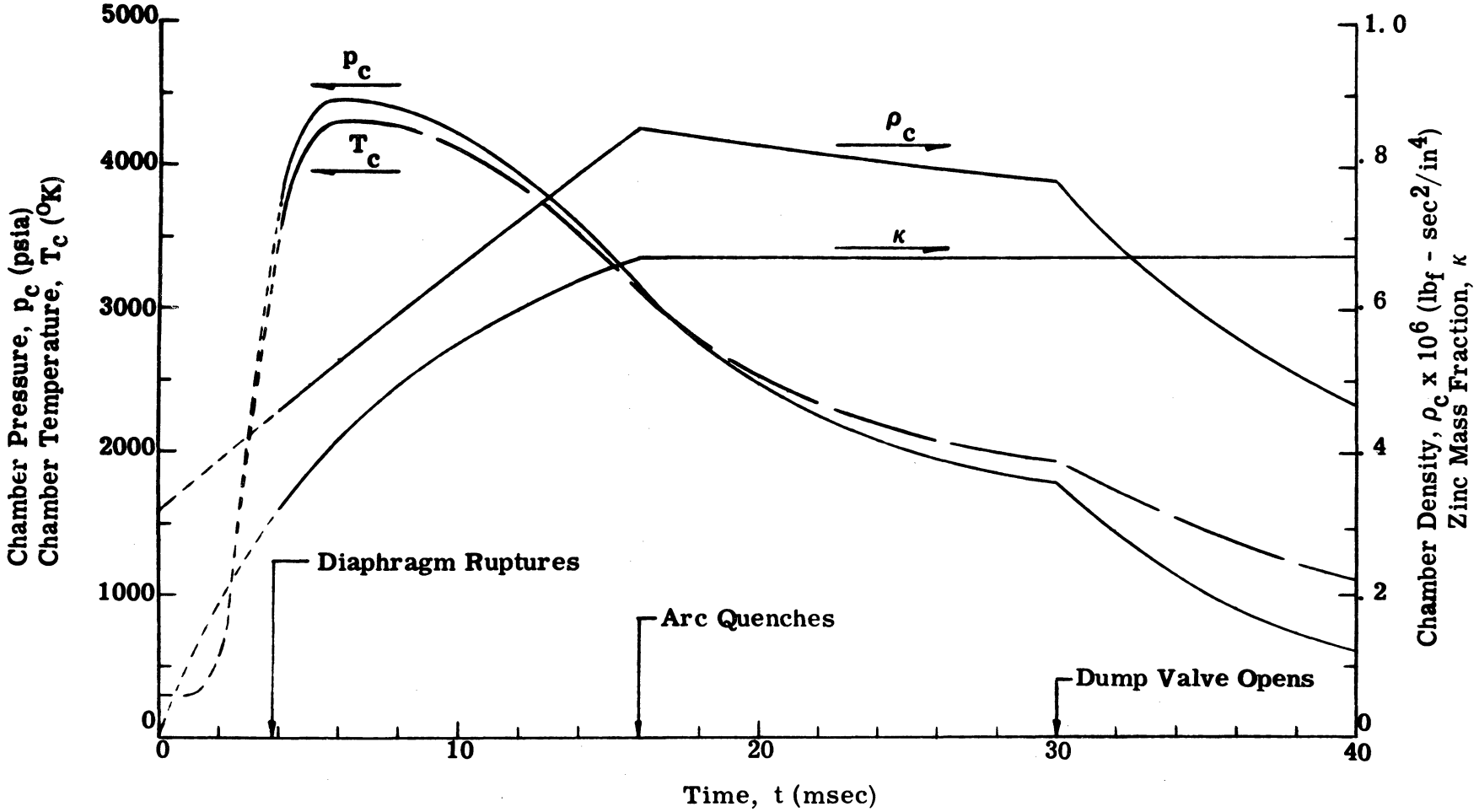

Figure G-1. Stagnation Chamber Conditions During a Typical Run; Determined from Equilibrium Isentropic Blowdown Considerations.

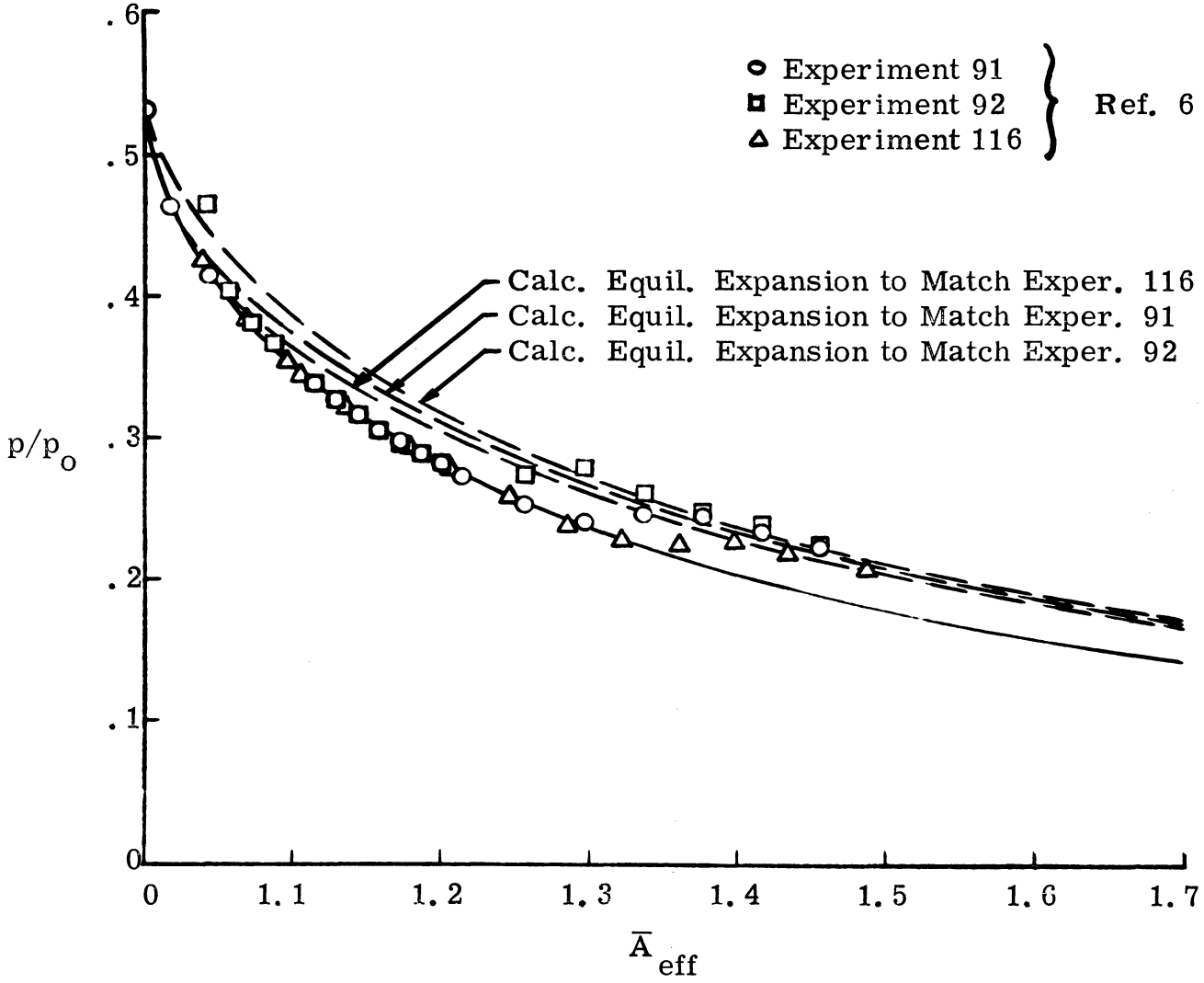

Figure G-2. Pressure Profile Calculated from Saturated Equilibrium Theory Compared to Experimental Data[6] for Condensing Steam

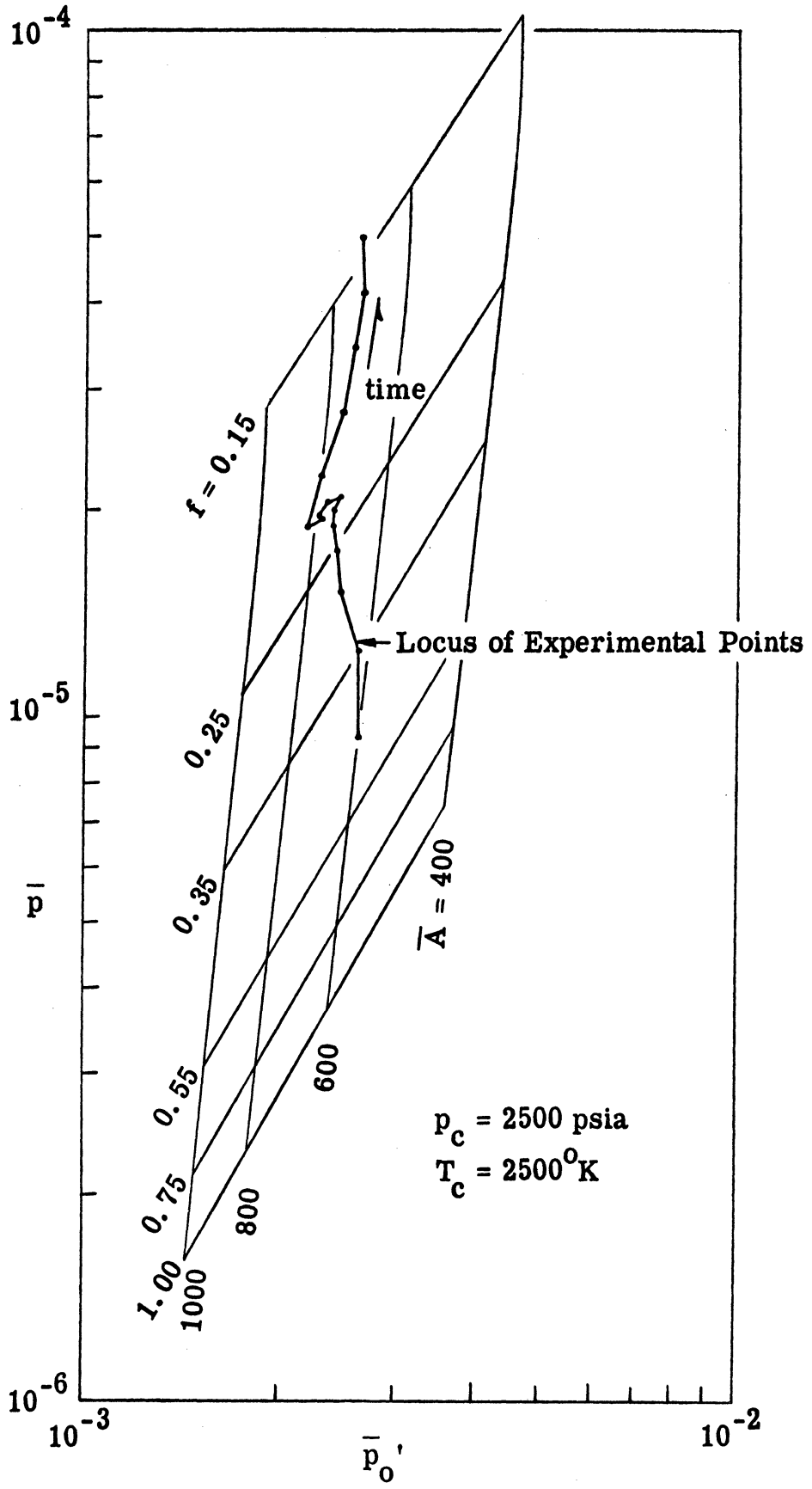

Figure G-3. Static Pressure — Pitot Pressure Grid from Parametric Saturated Equilibrium Theory; Experimental Points from Typical Zinc-Helium Run

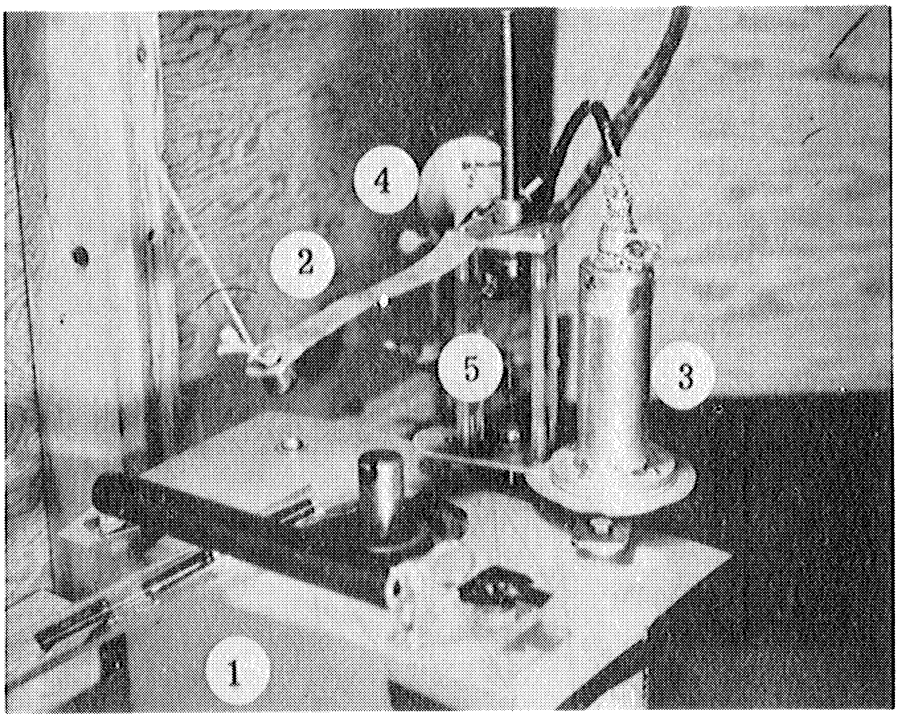

Figure H-1. Exploding Wire System

1. Capacitor
2. "Drop" Switch
3. Current Shunt
4. Voltage Probe
5. Exploding Wire

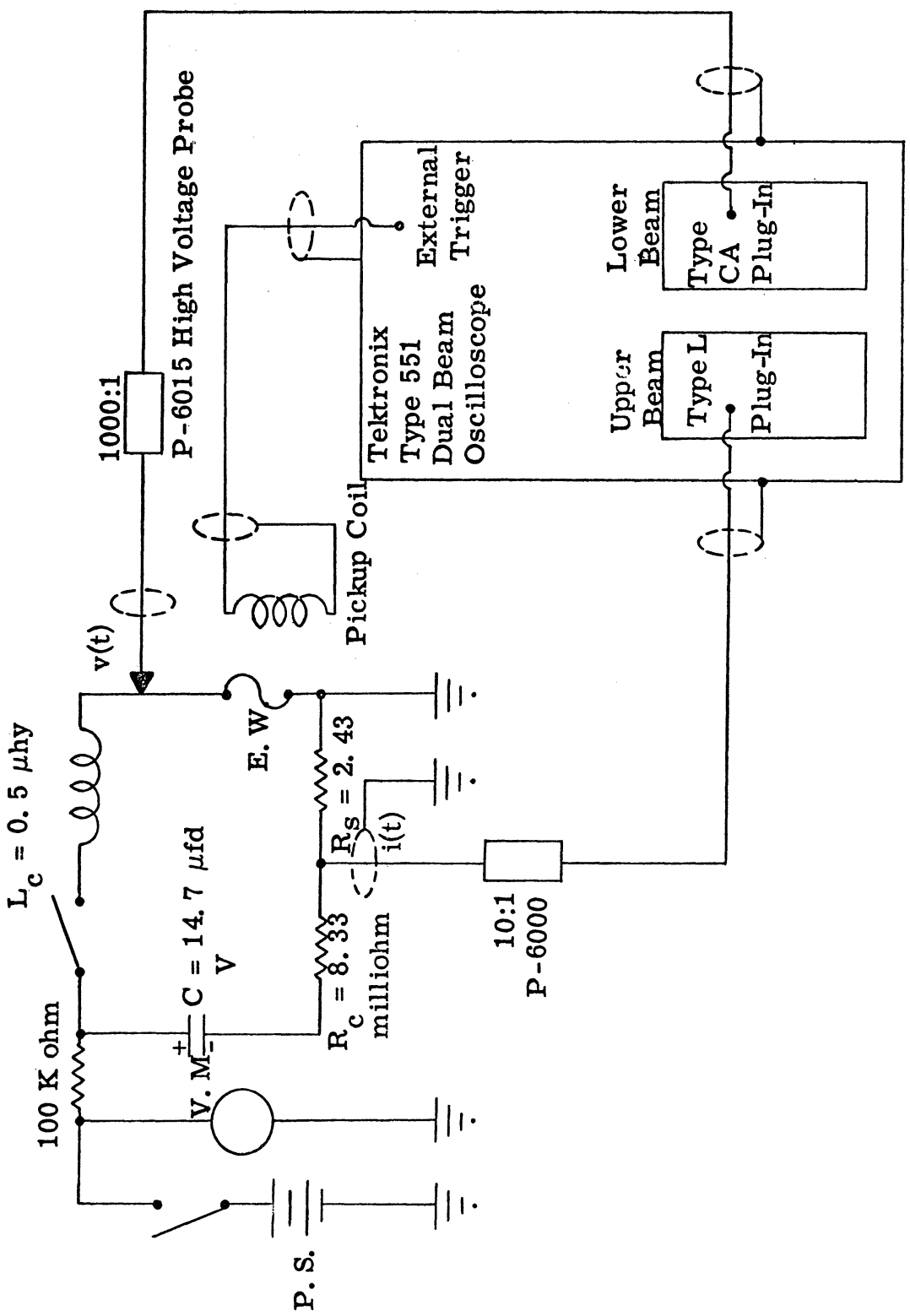

Figure H-2. Exploding Wire Circuitry

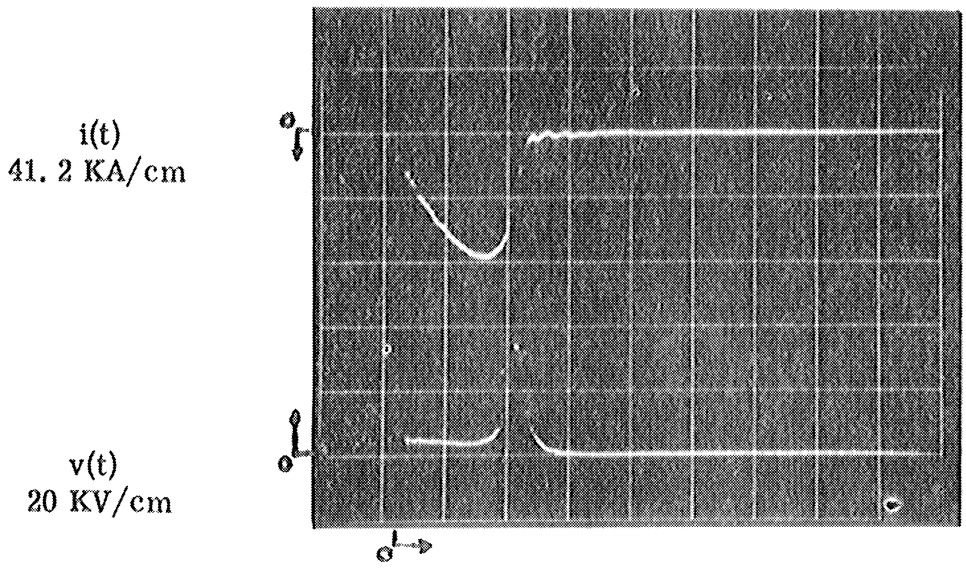

Figure H-3. Voltage and Current Traces for an Optimum Discharge (3 in. long, No. 22 Ag Wire, C = 14.7 μfd, V_o = 15 KV)

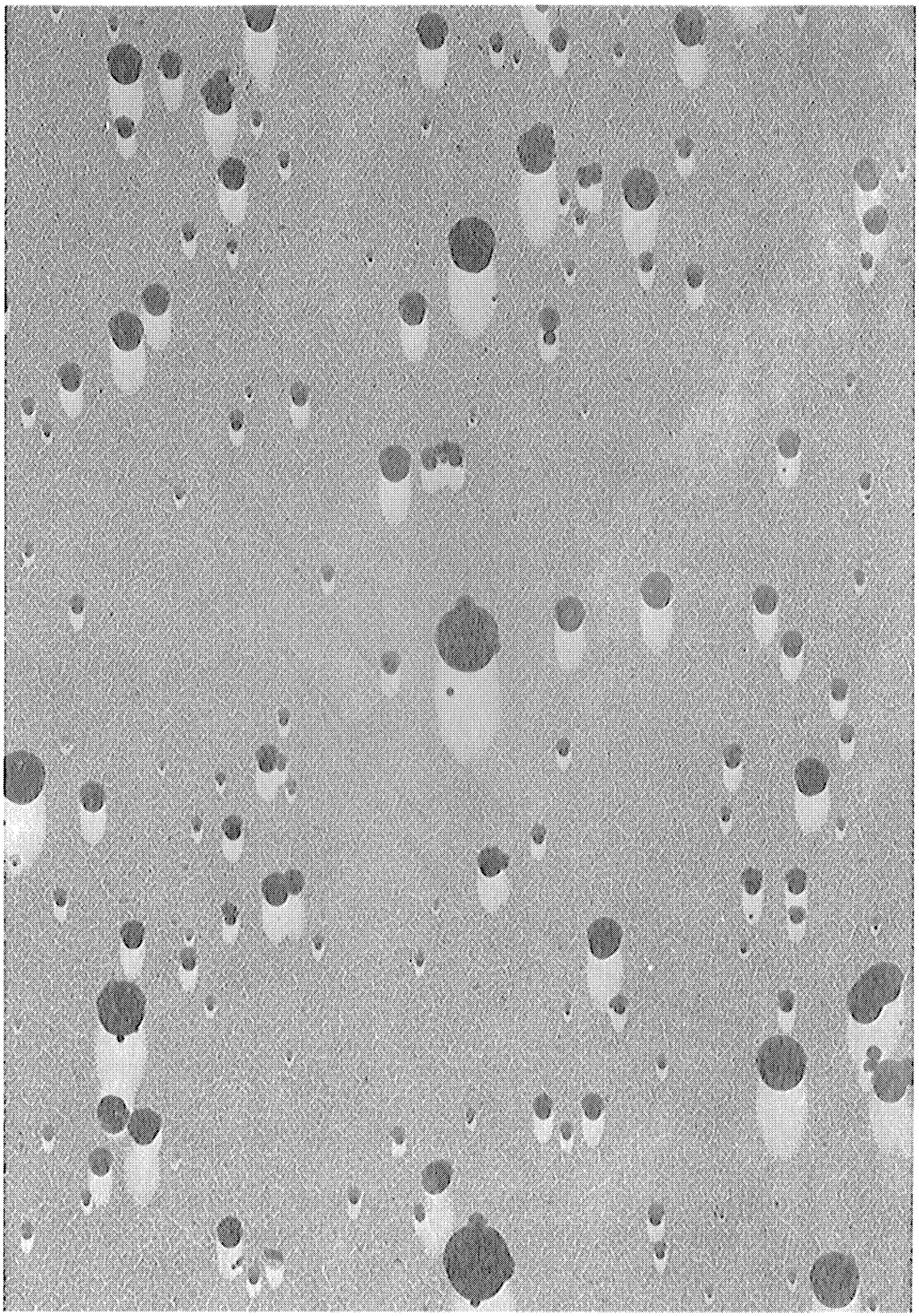

Figure H-4. Photomicrograph of Particles Obtained from a Platinum Wire Exploding in the Atmosphere; 132,000X

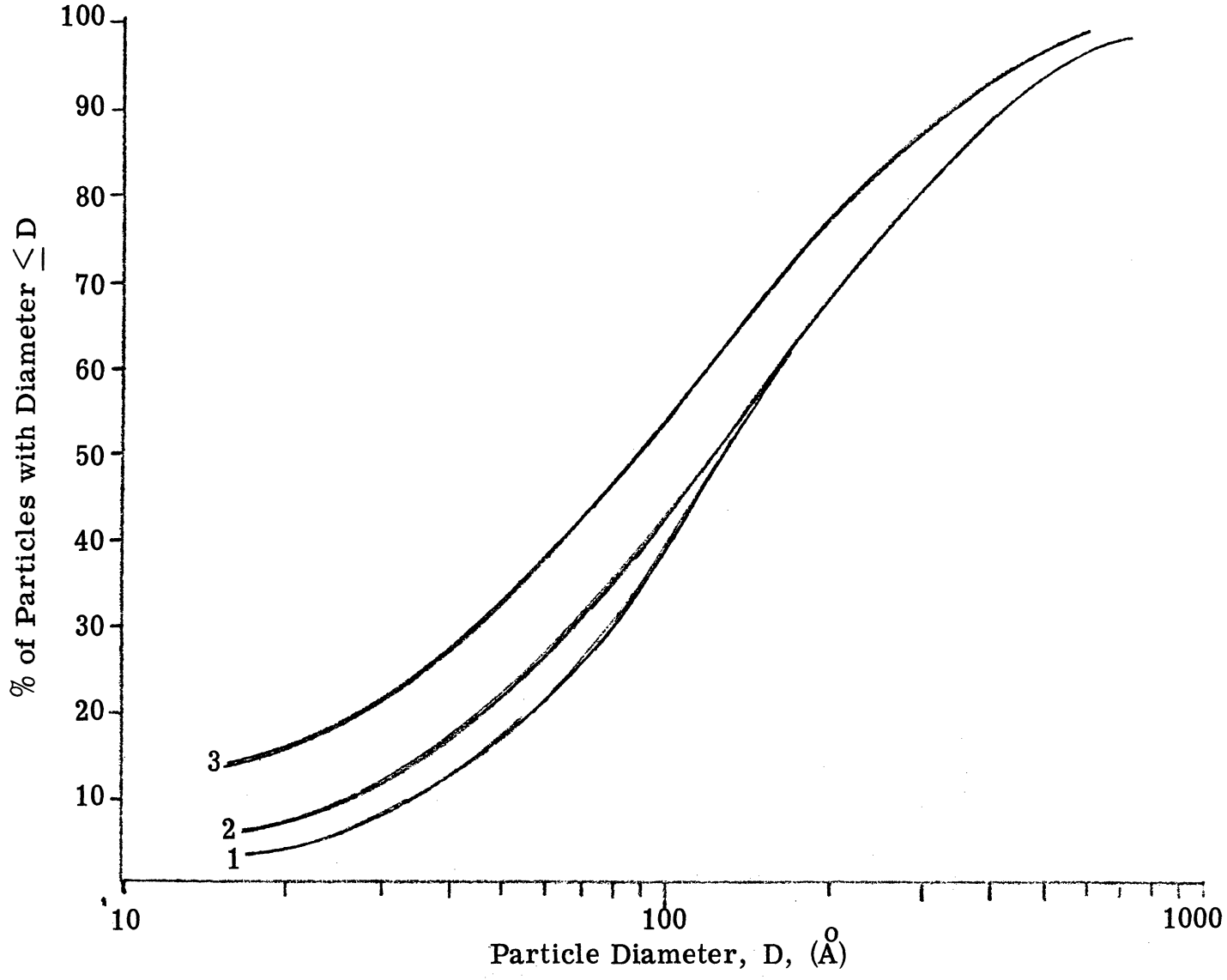

Figure H-5. Particle Size Distribution, Platinum.
1, 2 - Stored energy 5270 joules/gm. Collection 2" and 4" from wire respectively; 3 - stored energy 10,600 joules/gm."

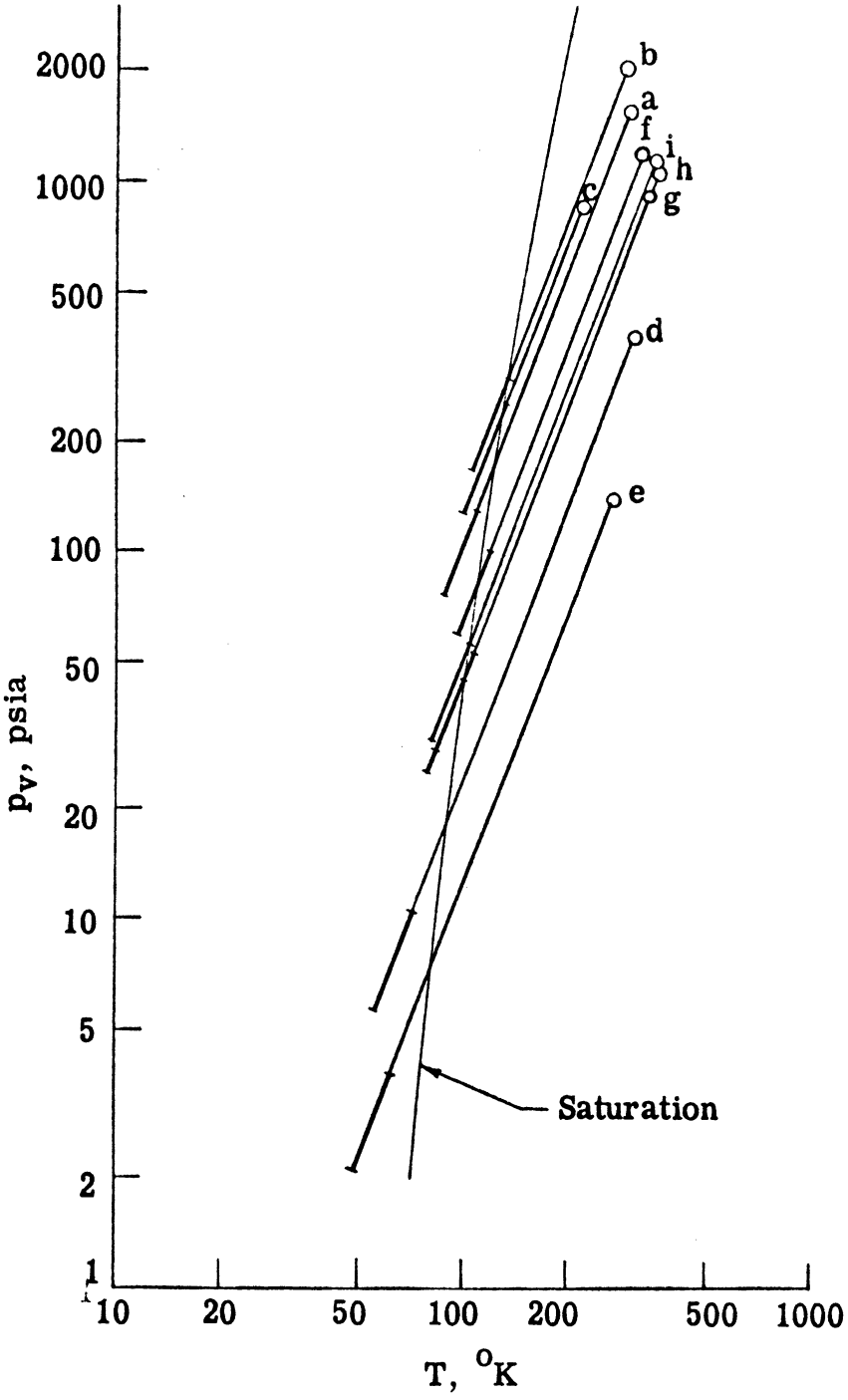

Figure I-1. Region of Onset of Condensation.
(See Table I-1 for Flow Conditions.)

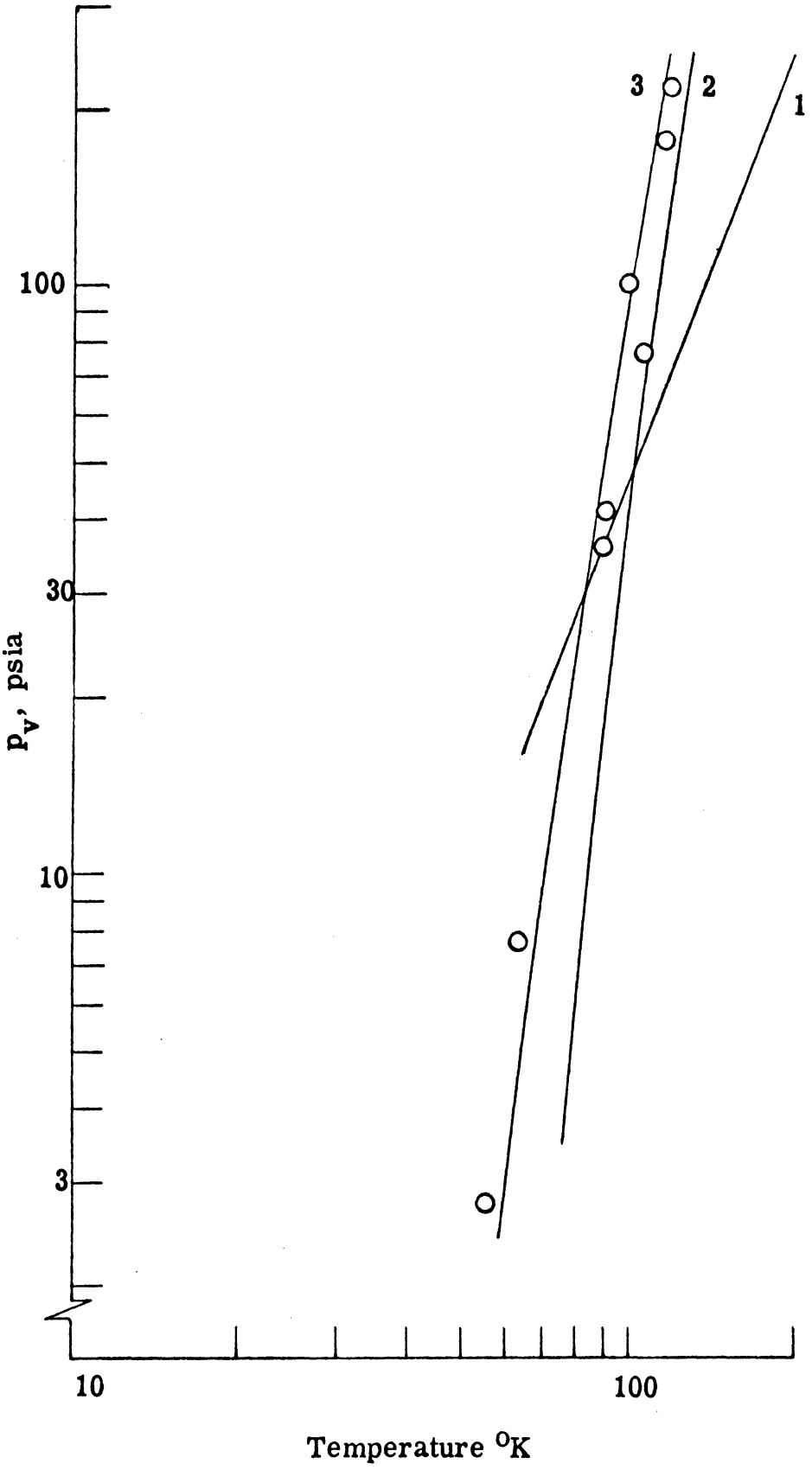

Figure I-2. Computed and Measured Onset. 1 - Typical Frozen Isentrope, 2 - Saturation Curve, 3 - Computed Locus of Condensation Onset. Points are Mid-interval Points from Experimental Measurements.

Table I-1. Stagnation Chamber Conditions

Run	Temperature	Partial Pressure of Argon	Mass Fraction of Argon
(a)	293°K	1555 psia	1.0
(b)	288	2016	1.0
(c)	214	859	1.0
(d)	304	379	.65
(e)	267	139	.5
(f)	317	1195	.937
(g)	331	914	1.0
(h)	352	1068	1.0
(i)	347	1138	1.0

REFERENCES

1. Wegener, P. P. and Mack, L. M., "Condensation in Supersonic and Hypersonic Wind Tunnels," Advances in Applied Mechanics, Vol. V, Academic Press, 1958, pp. 307-447.

2. Frenkel, J., Kinetic Theory of Liquids, Clarendon Press, Oxford, 1956, pp. 366-400. (Also published by Dover Publications, Inc., New York.)

3. Stever, H. G., "Condensation in High Speed Flows," High Speed Aerodynamics and Jet Propulsion, Vol. III, Princeton University Press, Princeton, N. J., 1958, pp. 526-573.

4a. Courtney, W. G., "Condensation During Heterogeneous Combustion," Eleventh Symposium (International) on Combustion, The Combustion Institute, Pittsburgh, Pennsylvania, 1967, pp. 237-244.

4b. Courtney, W. G., "Re-examination of Nucleation and Condensation of Water," Technical Report, Thiokol Chemical Corporation, Reaction Motors Division, Denville, New Jersey, July 1964.

5. Stodola, A., Steam and Gas Turbines, McGraw-Hill Book Company, New York, 1927.

6. Binnie, A. M. and Woods, M. W., "An Electrical Detector of Condensation in High Velocity Steam," Proc. Roy. Soc. A, No. 181, 1943 p. 134.

7. Binnie, A. M. and Woods, M. W., "The Pressure Distribution in a Convergent-Divergent Steam Nozzle," Proc. Inst. Mech. Engrs., No. 138, London, 1938, p. 229.

8. Yellott, J. I., "Supersaturated Steam," Engineering, No. 137, 1934, p. 303.

9. Head, R. M., Investigations of Spontaneous Condensation Phenomena, Ph. D. Thesis, California Institute of Technology, Pasadena, California, 1949.

10. Willmarth, W. W. and Nagamatsu, H. T., "Condensation of Nitrogen in a Hypersonic Nozzle," GALCIT Hypersonic Wind Tunnel Memorandum No. 6, January, 1952.

11. Buhler, R. D., Condensation of Air Components in Hypersonic Wind Tunnels. Theoretical Calculations and Comparison with Experiment, Ph. D Thesis, California Institute of Technology, Pasadena, California, 1952.

12. Daum, F. L., "Air Condensation in a Hypersonic Wind Tunnel," AIAA Journal, Vol. 1, No. 5, May 1963, pp. 1043-1046.

13. Duff, K. M., Non-Equilibrium Condensation of Carbon Dioxide in Supersonic Nozzles, Ph. D. Thesis, Massachusetts Institute of Technology, Cambridge, Massachusetts, January 1966.

Also: Duff, K. M. and Hill, P. G., "Condensation of Carbon Dioxide in Supersonic Nozzles," Proc. 1966 Heat Transfer and Fluid Mechanics Institute, Stanford University Press, 1966.

14. Kremmer, M. and Okurounmu, O., "Condensation of Ammonia Vapor During Rapid Expansion," Gas Turbine Laboratory Report No. 79, Massachusetts Institute of Technology, 1965.

15. Hill, P. G., Witting, H., and Demetri, E. P., "Condensation of Metal Vapors During Rapid Expansion," Journal of Heat Transfer, Vol. 85, No. 4, November 1963, pp. 303-317.

16. Glassman, A. J., "Analytical Study of the Expansion and Condensation Behavior of Alkali-Metal and Mercury Vapors Flowing Through Nozzles, NASA Lewis Research Center, Cleveland, Ohio, September 1964.

17. Solbes, A. and Kerrebrock, J. L., "Condensation and Electrical Conduction in Metallic Vapors," The Physics of Fluids, Vol. 10, Massachusetts Institute of Technology, Cambridge, Massachusetts, October 1967, pp. 2179-2198.

18. Goldin, D. S., "A Thermodynamic Flow Analysis of Particle Formation Efficiency in a Mixed Flow Colloid Thrustor," NASA Lewis Research Center, Cleveland, Ohio.

19. Cox, A. L., "Colloidal Electrohydrodynamic Energy Converter," AIAA Journal, Vol. 1, No. 11, November 1963, pp. 2491-2497.

20. Norgren, C. T., "Onboard Colloidal Particle Generator for Electrostatic Engines," Progress in Astronautics and Aeronautics, Vol. 9, Academic Press, New York, 1963, pp. 407-434.

21. Wegener, P. P. and Stein, G. D., "Light Scattering Experiments and The Theory of Homogeneous Nucleation in Condensing Supersonic Flow," Yale University, New Haven, Connecticut, March 1968.

22. Dobbins, R. A., "Applications of Light Scattering in Research and Technology," AIAA Paper No. 67-35, AIAA 5th Aerospace Sciences Meeting, New York, January 1967.

23. Thomann, H., "Determination of the Size of Ice Crystals Formed During Condensation of Water in Wind Tunnels and of Their Effect on Boundary Layers," FFA Report No. 101, The Aeronautical Research Institute of Sweden, Stockholm, July 1964.

24. Merritt, G. E. and Weatherston, R. C., "Condensation of Mercury Vapor and Drop Growth Processes in a Nitrogen Flow," AIAA Journal, April 1967, pp. 721-728.

25. Linhardt, H. D., "Potassium Condensate Droplet Size Determination," Aeronutronic Division, Philco Corporation, August 1, 1966.

26. Hoglund, R. F., "Recent Advances in Gas-Particle Nozzle Flows," ARS Journal, Vol. 32, No. 5, May 1962, pp. 662 671.

27. Sivier, K. R., Lu, P. L., McBride, D. D., and Oktay, E., "Initial Studies of Condensing Metal Vapors Carried by Expanding Inert Gases," ARL Report 65-59, March 1965.

28. Sherman, P. M., "Development and Operation of an Arc Heated Hypersonic Tunnel," University of Michigan Report 02953 3-F, July 1963.

29. Marble, F. R., "Dynamics of a Gas Containing Small Solid Particles," Guggenheim Jet Propulsion Center, California Institute of Technology, Pasadena, California, 1962.

30. Lu, H. Y. and Chiu, H. H., "Dynamics of Gases Containing Evaporable Liquid Droplets under a Normal Shock," AIAA Journal, June 1966, pp. 1008-1011.

31. Sherman, P. M., McBride, D. D., and Oktay, E., "Condensation in a Rapidly Expanding Metal Vapor-Inert Gas Mixture," ARL Report 67-0071, April 1967.

32. Daum, F. L. and Gyarmathy, G., "Air and Nitrogen Condensation in Hypersonic Nozzle Flow," ARL Report 65-159, March 1967.

33. Griffin, J. L., "Digital Computer Analysis of Condensation in Highly Expanded Flows," ARL Report 63-206, November 1963.

Also: Griffin, J. L. and Sherman, P. M., "Computer Analysis of Condensation in Highly Expanded Flows," AIAA Journal, Vol. 3, No. 10, October 1965, pp. 1813-1819.

34. Pouring, A. A., "Thermal Choking and Condensation in Nozzles," The Physics of Fluids, Vol. 8, No. 10, American Institute of Physics, New York, October 1965, pp. 1802-1810.

35. Hill, P. G., "Condensation of Water Vapour During Supersonic Expansion in Nozzles," Journal of Fluid Mechanics, Vol. 25, Part 3, Great Britain, 1966, pp. 593-620.

36. Sivier, K. R., "Digital Computer Studies of Condensation in Expanding One-Component Flows," ARL Report 65-234, November 1965.

37. Tolman, R. C., "The Effect of Droplet Size on Surface Tension," Journal of Chemical Physics, Vol. 17, No. 3, March 1949, pp. 333-337.

38. Jirgensons, B. and Straumanis, M. E., A Short Testbook of Colloid Chemistry, John Wiley and Sons, Inc., New York, 1954.

REFERENCES

APPENDIX A

A1. Sherman, P.M., "Development and Operation of an Arc Heated Hypersonic Tunnel," University of Michigan Report 02953-3-F, July 1963.

A2. Krause, J.D., Electromagnetics, McGraw-Hill, Inc., 1953, pp. 145-167.

APPENDIX C

C1. Townsend, A.A., "Turbulence," Handbook of Fluid Dynamics, (Streeter, V.L. —Editor-in-Chief), McGraw-Hill Book Company, New York, 1961, p. 10-1.

C2. Abramovich, G.N., The Theory of Turbulent Jets, M.I.T. Press, Massachusetts Institute of Technology, Cambridge, Massachusetts, 1963 (translation from Russian by Scripta Technica).

APPENDIX D

D1. Wegener, P.P. and Mack, L.M., "Condensation in Supersonic and Hypersonic Wind Tunnels," Advances in Applied Mechanics, Vol. V, Academic Press, 1958, pp. 307-447.

D2. Goldin, D.S., "A Thermodynamic Flow Analysis of Particle Formation Efficiency in a Mixed Flow Colloid Thrustor," AIAA Paper No. 67-85; 5th Aerospace Sciences Meeting, N.Y., Jan. 1967.

APPENDIX E

E1. Wegener, P.P. and Mack, L.M., "Condensation in Supersonic and Hypersonic Wind Tunnels," Advances in Applied Mechanics, Vol. V, Academic Press, 1958, pp. 307-447.

E2. Goldin, D.S., "A Thermodynamic Flow Analysis of Particle Formation Efficiency in a Mixed Flow Colloid Thruster," AIAA Paper No. 67-85; 5th Aerospace Sciences Meeting, N.Y., Jan. 1967.

REFERENCES

APPENDIX F

F1. Sivier, K.R., "Digital Computer Studies of Condensation in Expanding One-Component Flows," ARL 65-234, Nov. 1965.

F2. Tolman, R.C., "The Effect of Droplet Size on Surface Tension," J. Chem. Physics, Vol. 17, No. 3, Mar. 1949, pp. 333-337.

F3. Shapiro, A.M., The Dynamics and Thermodynamics of Compressible Fluid Flow, The Ronald Press Co., New York, 1953.

F4. Liepman, H.W. and Roshko, A., Elements of Gas Dynamics, John Wiley and Sons, Inc., New York, 1958.

F5. Wegener, P.P. and Mack, L.M., "Condensation in Supersonic and Hypersonic Wind Tunnels," Advances in Applied Mechanics, Vol. V, Academic Press, 1958, pp. 307-447.

F6. Frenkel, J., Kinetic Theory of Liquids, Clarendon Press, Oxford, 1956, pp. 366-400.

F7. Stever, H.G., "Condensation in High Speed Flows," High Speed Aerodynamics and Jet Propulsion, Vol. III, Princeton University Press, Princeton, N.J., 1958, pp. 526-573.

F8. Kennard, E.H., Kinetic Theory of Gases, McGraw-Hill Book Co., 1938.

F9. Hill, P.G., "Condensation of Water Vapour During Supersonic Expansion in Nozzles," J. Fluid Mech., Vol. 25, pp. 593-620, 1966.

F10. Dufour, L. and Defay, R., Thermodynamics of Clouds, Academic Press, New York, 1963.

REFERENCES

APPENDIX H

H1. Oktay, E., "Effect of Wire Cross Section on First Pulse of an Exploding Wire," The Review of Scientific Instruments, Vol. 36, No. 9, September 1965.

H2. Sherman, P. M., McBride, D. D., Oktay, E., "Condensation in a Rapidly Expanding Metal Vapor—Inert Gas Mixture," ARL Report 67-0071, April 1967.

H3. Stull and Sinke, "Thermodynamic Properties of the Elements," Amer. Chem. Soc., 1956.

Unclassified
Security Classification

DOCUMENT CONTROL DATA - R & D

(Security classification of title, body of abstract and indexing annotation must be entered when the overall report is classified)

1. ORIGINATING ACTIVITY *(Corporate author)*
University of Michigan
Department of Aerospace Engineering
Ann Arbor, Michigan 48105

2a. REPORT SECURITY CLASSIFICATION
Unclassified

2b. GROUP

3. REPORT TITLE
Condensation of Metal Vapor in a Supersonic Carrier Gas

4. DESCRIPTIVE NOTES *(Type of report and inclusive dates)*
Scientific. Final.

5. AUTHOR(S) *(First name, middle initial, last name)*
P.M. Sherman, D.D. McBride, T. Chmielewski, T.H. Pierce, E. Oktay

6. REPORT DATE
June 1969

7a. TOTAL NO. OF PAGES
252

7b. NO. OF REFS
59

8a. CONTRACT OR GRANT NO. AF 33(615)-67c-1197

b. PROJECT NO. 7116

c. DOD Element 61445014

d. DOD Subelement 681308

9a. ORIGINATOR'S REPORT NUMBER(S)

9b. OTHER REPORT NO(S) *(Any other numbers that may be assigned this report)*
ARL69-0089

10. DISTRIBUTION STATEMENT

1. This document has been approved for public release and sale; its distribution is unlimited.

11. SUPPLEMENTARY NOTES
TECH OTHER

12. SPONSORING MILITARY ACTIVITY
Aerospace Research Laboratory (ARE)
Wright-Patterson AFB 45433

13. ABSTRACT A study of the condensation of metal vapor in an inert carrier gas was made with primary emphasis on the size of the particles formed and the location of the onset of the condensation. Superheated zinc vapor was generated in a hotshot wind tunnel in a helium carrier gas and expanded in a converging-diverging nozzle. Static pressure measurements were made to determine the location of the onset of condensation. A sampling method was developed and used to determine the size of the condensed particles. An exploding wire arrangement was also used in a few additional studies and condensed platinum and other metal particles were obtained. A few measurements were also made of the condensation of argon.

It was found that decelerating a skimmed part of the nozzle flow by mixing with air at matched pressure was an effective way of sampling. Electron microscope analysis of the particles sampled showed a narrow distribution of sizes with 80% of the particles having diameters within a 100 A° range, and a peak number of particles about 135 A° in diameter. The amount of supercooling before onset of condensation was found to be approximately 430°K (measured along the isentrope) over a range of zinc mass fractions of .35 to .70 for saturation partial pressure of zinc between 10 psia and 70 psia. Pitot pressure was found to be a function of the size of the pitot tube up to a critical diameter.

A classical non-equilibrium liquid drop analysis predicted values of both particle size and condensation onset in moderately good agreement with the measurements. The analysis was also used to determine the qualitative efforts of rate of expansion, amount of carrier gas and molecular weight of carrier gas.

An equilibrium analysis yielded useful algebraic approximations for conditions far downstream of the onset of condensation.

DD FORM 1 NOV 65 1473

Unclassified
Security Classification

14. KEY WORDS	LINK A		LINK B		LINK C	
	ROLE	WT	ROLE	WT	ROLE	WT
Metal vapor condensation						
Spontaneous condensation						
Condensation particles						
Hotshot tunnel						
Non-equilibrium expansion						
Particle sampling						
Particle size determination						
Two-phase flow						
Condensation in inert carrier gas						
Exploding wire						
Superheated zinc vapor						
Electron-microscope particle analysis						